POLITECNICO
MILANO 1863

DEPARTMENT OF ENERGY
DOCTORAL PROGRAM IN ENERGY AND NUCLEAR SCIENCE AND TECHNOLOGY

THERMOMECHANICAL CHARACTERIZATION OF FUSION-RELEVANT NANOSTRUCTURED COATINGS

Doctoral Dissertation of:
Edoardo Besozzi

Supervisor:
Prof. Marco Beghi
Dr. David Dellasega

Tutor:
Prof. Matteo Passoni

The Chair of the Doctoral Program:
Prof. Carlo E. Bottani

Year 2018 – Cycle XXX

Abstract

Plasma Facing Components (PFCs) must withstand extreme conditions of particles and heat fluxes in future fusion reactors such as ITER. In particular, tungsten (W), thanks to its attractive properties, such as high melting point, good thermal conductivity and high sputtering yield, has been chosen as the candidate material for the divertor region of ITER, where the most extreme conditions are expected. Due to plasma-wall interactions, W plasma facing components can be severely damaged, undergoing exstensive erosion with consequent formation of thick co/re-deposited layers with complex and hardly predictable morphology, structure and composition. The presence of these layers and their properties drastically affect the overall performances of PFCs, so that they must be deeply investigated. Moreover, as a consequence of the extreme thermal loads expected under steady and transient operating conditions, both pristine PFCs and co/re-deposited layers will suffer from severe thermal effects (e.g. recrystallization, surface melting, delamination) that unavoidably alter the properties of the materials. These effects must be opportunely understood, in order to become predictable in the future ITER environment, ensuring its operational stability.
The main goal of this Ph.D thesis is to provide, following an advanced laboratory scale materials science approach, a thermomechanical characterization of fusion-relevant nanostructured coatings. To this purpose, a novel lab-scale thermomechanical investigation method is developed. In particular, since the thermomechanical properties of coatings strictly depend on the specific nanostructure, morphology and composition, a suitable characterization setup, sensitive to these features, is developed. This system relies on the combined use of Brillouin spectroscopy and the substrate curvature method, providing, non-destructively, information about the elastic moduli, residual stresses, thermal stresses and coefficient of thermal expansion of various nanostructured films. The analyzed samples are deposited by Pulsed Laser Deposition, a PVD technique that, thanks to its high versatility in tailoring many process parameters, allows to obtain films with desirable properties, in particu-

lar suitable for mimicking different coatings scenarios in tokamaks (e.g. coated PFCs or co/re-deposits). The samples are thus characterized and the obtained properties are deeply discussed in terms of their relation with nanostructure. In the last part of the thesis, the samples are exposed to ITER-relevant thermal loads by annealing treatments at temperatures proxy of ITER steady operating temperatures, and by nanosecond laser irradiation, exploited for mimicking thermal effects induced by ITER-relevant transient heat fluxes. A numerical code is also developed for predicting the thermal effects of various nanostructured coatings after nanosecond laser pulses, with the aim of extending it also to realistic tokamak scenarios.

The obtained results provide valuable, quantitative, fruitful and tangible insights into a better comprehension of the relationship between thermomechanical properties and the nanostructure, morphology and composition of fusion-relevant coatings. In addition they can help in understanding the unknown behavior of co/re-deposited layers under extreme thermal loads conditions characteristics of tokamak environments.

Sinossi

I componenti di prima parete, dall'inglese plasma facing components (PFCs), di un reattore a fusione nucleare come ITER dovranno lavorare in condizioni critiche di elevati flussi di particelle e carichi termici per via della loro diretta esposizione al plasma. In ITER, le condizioni più estreme sono attese nella zona del divertore, dove il plasma termonucleare impatta direttamente su questi componenti. Il divertore di ITER sarà realizzato in tungsteno (W), scelto per via delle sue peculiari proprietà, come un'alta temperatura di fusione, una buona conducibilità termica e un'alta soglia di erosione. Tuttavia, a seguito delle interazioni plasma-parete, intensi fenomeni di erosione con conseguente formazione di co/re-depositi dalla morfologia, struttura e composizione chimica complessa e difficilmente prevedibile, potranno modificare drasticamente lo scenario iniziale dei materiali di prima parete e le loro proprietà. In aggiunta, a seguito dell'esposizione ad estremi carichi termici durante sia condizioni stazionarie che transitorie, sia i PFCs nativi che i co/re-depositi saranno soggetti a fenomeni di fusione, ricristallizzazione o delaminazione, che inevitabilmente modificheranno le proprietà dei materiali, riducendone le prestazioni e compromettendo la stabilità del reattore. Questi effetti e le modifiche indotte ai vari materiali devono quindi essere opportunamente studiate per poter essere prevedibili in scenari estremi come quelli attesi per ITER, così da poterne garantire la stabilità operativa.

Il principale obiettivo di questa tesi di dottorato è quello di fornire, seguendo un approccio innovativo di scienza dei materiali alla scala di laboratorio, una caratterizzazione termomeccanica di fillm nanostrutturati di interesse fusionistico. Dal momento che le proprietà dei film possono dipendere fortemente dalla specifica nanostruttura, morfologia e composizione chimica, per caratterizzare opportunamente i campioni è stato necessario sviluppare un metodo di investigazione sperimentale basato sulla realizzazione di un set-up innovativo, che risultasse sensibile alla variazione di queste proprietà. Questo set-up si fonda sull'utilizzo combinato della spettroscopia Brillouin e del metodo di analisi della curvatura

del substrato, permettendo un'indagine non distruttiva di diverse proprietà di coating dalla nanostruttura complessa, come moduli elastici, stress termici, stress residui e coefficiente di dilatazione termica. I campioni analizzati sono ottenuti mediante la Pulsed Laser Deposition, una tecnica PVD molto versatile che permette di depositare film con le proprietà desiderate, che simulino, ad esempio, diversi scenari di coating in tokamaks (come possono essere PFCs rivestiti o co/re-despositi). Utilizzando il set-up sviluppato si è quindi caratterizzata una vasta famiglia di campioni, discutendo in dettaglio il legame tra le proprietà termomeccaniche e la specifica nanostruttura, composizione chimica e morfologia. Successivamente, si è investigato il comportamento di questi coating quando esposti a carichi termici di rilevanza fusionistica. A tale scopo, si è seguito un duplice approccio, consistente in trattamenti termici di annealing a temperature prossime alle temperature operative stazionarie previste per ITER, e irraggiamento con laser al nanosecondo, per simulare, invece, gli effetti indotti sui materiali da carichi termici estremi come quelli generati da transitori di plasma. Infine, si è sviluppato un modello numerico per simulare e predire gli effetti termici indotti da impulsi con durata temporale del nanosecondo su coating nanostrutturati, con la possibilità, poi, di un'ulteriore estensione a situazioni più caratteristiche di scenari tokamak.

In generale, i risultati ottenuti in questa tesi possono fornire un consistente contributo per comprendere meglio il legame, non ancora completamente chiarificato, tra le proprietà termomeccaniche e la specifica nanostruttura, morfologia e composizione chimica di coating di interesse fusionistico. In aggiunta, per via del test diretto a carichi termici ITER-relevant, tali risultati possono essere utili per iniziare a chiarire il comportamento, fino ad ora ignoto, di co/re-depositi quando esposti a condizioni critiche caratteristiche di ambienti tokamak.

Contents

Introduction and Thesis goals

The World's energy problem has been among the most debated causes for the last years. Over 15 terawatts a year are consumed by human beings, and this requirement increases every year as more people have access to technological innovations. About 80% of the total electric power demand is nowadays covered by fossil fuel. This obviously results in severe problems related to greenhouse emissions, which in turn are associated to the global warming and its harmful effects. In addition, the limited fossil fuel availability on earth is also of potentially interest for geopolitical conflicts due to escalating competition for energy resources.

As the technological progress evolves, many new solutions for going beyond our dependence on fossil energy sources are proposed. These solutions concern the exploitation of solar energy, hydro-power, wind power and nuclear power. A lot of research is focused on improving as much as possible the performances of the devices targeted to the energy production, obviously limiting possible side effects on the environment. Among them, nuclear fusion energy is one of the most promising and, at the same time, one of the most questioned renewable source of energy. It is believed to show the main advantages of other renewable sources, such as unlimited fuel availability and zero greenhouse emissions, but, in addition, it can provide continuous power delivery with very high power densities.

The exploitation of this source of energy basically relies on the ability to recreate a small star in a "box". Nuclear fusion, indeed, is the physical process that is at the base of a star's life, and it consists on the fusion of two light nuclei into heavier products (this is the opposite case to nuclear fission, where heavy nuclei are broken into lighter products). During this process, other particles/nuclei and a high amount of energy can be released. Even if the basic idea is very simple, the extreme physical and technological issues (and economical costs) that concern the realization of a nuclear fusion power plant, have always slowed the achievement of the opportunity to exploit this unique source of energy.

First of all, in order to promote fusion reactions, the interacting nuclei must be sufficiently energetic to overcome their reciprocal Coulomb repulsion energy. This is possible if the system operates at extreme temperatures. For example, let us consider the fusion process between two isotopes of hydrogen, namely deuterium (D) and tritium (T). In this case, the Coulomb barrier energy is of the order of 100 keV; this means that the system has to be heated up to about 100 milions degrees °C in order to promote fusion processes. At these temperatures, which are approximately ten times the temperature of the Sun core, D and T atoms are completely ionized forming the so called *thermonuclear plasma* state. To have a net energy gain from fusion reactions, the thermonuclear plasma must be sustained at these conditions for suitable long times. This can be done by properly confining the plasma. The strategy adopted for plasma confinement divides into two main different solutions, namely the *magnetic* and the *inertial* fusion confinements. In the former case, intense magnetic fields are exploited to force the electrically charged particles of the plasma to move along imposed trajectories (i.e. the magnetic field lines), while, in the latter case, the confinement is guaranteed only by the atoms inertia which counteracts their thermal expansion upon heating.

At the moment, the *Tokamak* configuration, where the plasma is confined in a toroidal shape by intense magnetic fields (here comes the acronym ***To****roidal* ***cha****mber with* ***ma****gnetic* ***c****oils*), is regarded as the reference design for nuclear fusion power plants. Until now, 221 tokamak machines, of which 45 are operating today, have been built by men around the world. All these reactors are experimental devices and do not produce more energy than what they actually consume. The experience gained with these machines has opened the way to ITER, the most advanced tokamak experiment that is currently under construction in the french site of Cadarache. Thanks to ITER (see the acronym *the way* in latin), we will be finally able to prove the feasability of nuclear fusion from magnetic-confined devices as an alternative source of energy (ITER will operate with Q = 10, which means a net production of energy equal to 10 times the energy required to turn the plasma on). In addition, it will give us all the technological knowledge necessary for the development of the first demonstrative nuclear fusion power plant DEMO, targeted to the production of electrical power.

It is now evident that, in all its technological complexity, ITER represents one of the greatest challenges of the mankind. As a result, it encloses the collaboration of seven member entities (i.e. EU, India, China, Japan Russia, South Korea and USA) with an overall cost that approximately sets to more than 14 billions dollars (second most expensive project ever beyond International Space Station). This facility is expected to start its first operations of commissioning in 2025, but the first D-T plasma will be burned not before 2035. With a net fusion power of 500 MW and a plasma volume of 840 m^3, when in operation, it will become the largest tokamak experiment, surpassing by ten times the at the moment largest tokamak JET.

Among all the possible issues that are still open questions for ITER, the comprehension of

the plasma-wall interactions (PWIs) is one of the most critical. PWIs have a double side effect both on the plasma facing materials (PFMs) and the burning plasma itself. In particular, during plasma discharges, the extreme flux of energetic particles (up to 10^{24} m^{-2} s^{-1}) coming from the plasma, striking on the PFMs, result in the erosion and radiation damaging of the PFMs. This particles flux is accompained by extreme thermal loads, that can reach 20 MW m^{-2} during standard operating conditions but that can rise to 25 GW m^{-2} during off-normal events, leading to severe PFMs surface melting and modifications. All these effects, obviously, lead to unwanted loss of materials performances. Moreover, the eroded particles can then migrate, entering the plasma and inducing loss of plasma quality and stability, and form co/re-deposits above the PFMs. These layers usually show different properties with regards to the ones of native PFMs, being severely affected by the specific structure, morphology and chemical composition. Moreover, their behavior, when facing to the extreme plasma conditions, can be totally different and unpredictable.

Following an advanced materials science approach, this doctoral thesis provides an experimental and numerical investigation, at the laboratory scale, of the thermomechanical properties of nanostructured coatings. In particular, the target samples are tungsten (W) based coatings and boron (B) coatings that are relevant for nuclear fusion research. Since the thermomechanical properties of coatings strictly depend on the peculiar structure, morphology and composition, a novel characterization method, sensitive to these features, is developed. This method relies on the combined use of Brillouin spectroscopy, whose data analysis is optimized to consistently derive the elastic moduli of the coatings, and an ad-hoc developed experimental apparatus based on the substrate curvature method, which is exploited for the determination of the residual and thermal stresses and the thermal expansion coefficient of the coatings. Knowing these properties is fundamental to understand the behavior of the coatings under extreme fusion thermal loads. W coatings are thus tested under fusion-relevant thermal loads through thermal annealing at ITER-relevant steady operating temperatures and nanosecond laser irradiation, that mimic transient heat load conditions expected in ITER. In addition, a numerical code is also developed for predicting the thermomechanical behavior of various nanostructured coatings during nanosecond laser pulses, with the aim of extending it also to realistic tokamak scenarios.

All the research activities reported in this work were developed within the framework of the Nuclear and Energy Science and Technology (STEN) Ph.D. program at the Micro and Nanostructured materials Laboratory of Politecnico of Milan (Italy). Part of the work has been funded by EUROfusion WP EDU and by ENEA (PAR2015) research projects. The thesis is divided into six chapters as follows.

Chapter 1 : In the first chapter, a brief introduction about the principles of nuclear fusion energy is given. After the basis of nuclear fusion reactions and how to obtain energy from them, the focus is shifted to the different plasma confinement strategies. The Tokamak design is then described and finally the main features of the ITER project

are highlighted.

Chapter 2 : chapter 2 describes all the main issues regarding plasma-wall interactions that are useful for the contextualization of this thesis work. Suitable materials candidate as PFMs are then analyzed. The choice of W as PFM is thus motivated, and the main results on its behavior under fusion-relevant conditions are summarized. The laboratory scale approach for mimicking ITER-relevant thermal loads is presented. At the end of the chapter, before introducing the specific goals of the thesis, the experimental apparatus exploited for the deposition of all the analyzed coatings is also briefly introduced.

Chapter 3 : in this chapter, the development of the thermomechanical characterization method for nanostructured coatings is proposed. This chapter comprehends the description of the elastic properties derivation method from Brillouin spectroscopy, the realization of the experimental apparatus for the substrate curvature measurements, the exploitation of nanosecond laser irradiation for mimicking fusion-relevant transient conditions and the development of the numerical code for laser-matter interaction.

Chapter 4 : chapter 4 shows the thermomechanical characterization results of the as-deposited coatings. All the thermomechanical properties are investigated and deeply discussed as function of the specific nanostructure, morphology and composition of the coatings.

Chapter 5 : strictly correlated to the previous chapter, in chapter 5 the behavior of W coatings under fusion relevant thermal loads is analyzed. The coatings are firstly annealed at ITER relevant steady operating temperatures. The crystallization behavior and the coating stress evolution are investigated. Secondly, the coatings are irradiated by nanosecond laser pulses, and their damage thresholds are studied as function of the specific irradiation conditions and materials properties. Finally, the developed numerical code is exploited to predict the damage thresholds of various nanostructured coatings. The obtained numerical and experimental results are compared and the code is preliminarly extended to tokamak scenarios.

Chapter 6 : finally, the sixth chapter presents the main conclusions of this Ph.D. work and the possible future developments that can be investigated from the obtained results.

The original contributions of this thesis acitivities have led to the publication of the following papers:

- **E. Besozzi** D. Dellasega, A. Pezzoli, C. Conti, M. Passoni, M.G. Beghi, *Amorphous, ultra-nano- and nano-crystalline tungsten-based coatings grown by Pulsed Laser Deposition: mechanical characterization by Surface Brillouin Spectroscopy*, Materials and Design 106, (2016) 14 -21.

- D. Dellasega, V. Russo, A. Pezzoli, C. Conti, N. Lecis, **E. Besozzi**, C.E. Bottani, M.G. Beghi and M. Passoni, *Boron films produced by high energy Pulsed Laser Deposition*, Materials and Design 134, (2017) 35 - 43.
- **E. Besozzi**, D. Dellasega, A. Pezzoli, A. Mantegazza, M. Passoni and M. G. Beghi, *Coefficient of thermal expansion of nanostructured tungsten based coatings assessed by substrate curvature method*, Materials and Design 137, (2018) 192 - 203.
- **E. Besozzi**, A. Maffini, D. Dellasega, V. Russo, A. Pazzaglia, A. Facibeni, M.G. Beghi and M. Passoni, *Nanosecond laser pulses for mimicking thermal effects on nanostructured tungsten-based materials*, Nuclear Fusion 58, (2018) 036019.

In addition, the work has been presented at the following national, international conferences and schools:

- D. Dellasega, A. Pezzoli, V. Russo, **E. Besozzi**, A. Maffini, M. Passoni, *Synthesis of metastable W-O and W-N films and nanostructure growth induced by thermal and laser annealing*, International Conference on Laser Ablation, COLA 2017, Marseil, France, September 2017. Poster presentation by D. Dellasega.
- E. Besozzi, et al., *Thermomechanical properties of W coatings grown by Pulsed Laser Deposition and exposed to ITER-relevant thermal loads*, 2017 IEEE 27th Symposium on Fusion Energy (SOFE), Shangai, June (2017). Oral presentation.
- E. Besozzi et al., *Thermomechanical behaviour of W under nanosecond laser induced thermal loads*, 16th International Conference on Plasma-Facing Materials and Components for Fusion Applications (PFMC16), Dusseldorf-Neuss, May (2017). Poster presentation.
- E. Besozzi et al., *Amorphous-like tungsten coatings: deposition, processing and thermomechanical characterization under thermal loads*, MRS fall meeting, Boston, November (2016). Poster presentation.
- E. Besozzi and M.G. Beghi, *Thermomechanical characterization of coatings for nuclear energy applications*, ENEA kick-off meeting PAR2015, Bologna, June (2016). Oral presentation.
- E. Besozzi et al., *Thermomechanical properties of nanostructured tungsten coatings grown by Pulsed Laser Deposition*, 22nd Interneational Conference on Plasma Surface Interactions in Controlled Fusion Devices (PSI-22), Roma, June (2016). Poster presentation.
- E. Besozzi *Thermomechanical characterization of coatings for harsh temperature and irradiation environments*, 5th PhD Fusenet Event, Prague, November (2015). Poster presentation.

- E. Besozzi *Thermomechanical properties of novel coatings designed for high temperatures and irradiation conditions of fusion reactors*, The 56th Course on Atoms and Plasmas in Super-Intense Laser Fields, Erice, July (2015). Poster presentation.

CHAPTER 1

Principles of Nuclear Fusion Energy

In this first chapter, the basic principles of nuclear fusion energy are presented. The main fusion reactions and the way to obtain them are discussed (section 1.1). In section 1.2, the requirements mandatory to obtain energy from these reactions are introduced. If these requirements are satisfied, the *thermo-nuclear plasma* state is obtained. This plasma must be opportunely confined, so, in section 1.3, the two main plasma confinement strategies are shown: the *inertial* (section 1.3.1) and the *magnetic* (section 1.3.2) confinements. Particular emphasis is thus given in section 1.4 to the description of the *tokamak* design, based on the magnetic confinement. Finally, the ITER project is briefly presented (section 1.4.4).

1.1 Fusion Reactions and Thermonuclear Plasmas

Chemichal, nuclear and other types of reactions may cause a system to change some of its corresponding mass and, consequently, some of its energy content as stated by the famous Einstein's mass-energy equivalence formula:

$$E = \Delta M c^2 \tag{1.1}$$

where ΔM is the difference between the rest mass of reactans and products (i.e. *mass defect*) and c is the speed of light. In the case of nuclear reactions, if, instead of the mass, the binding energies are considered, exoenergetic reactions (i.e. $E > 0$) are obtained if the average binding energy per nucleon increases after the process. This is well explained by figure 1.1, that shows the binding energy per nucleon (BIA) versus the mass number (A). To obtain $E > 0$, fusion reactions are considered for $A < 56$ (while fission reactions are of interest for $A > 56$).
In order to fuse, the charged nuclei must win the Coulomb barrier. Therefore, they must

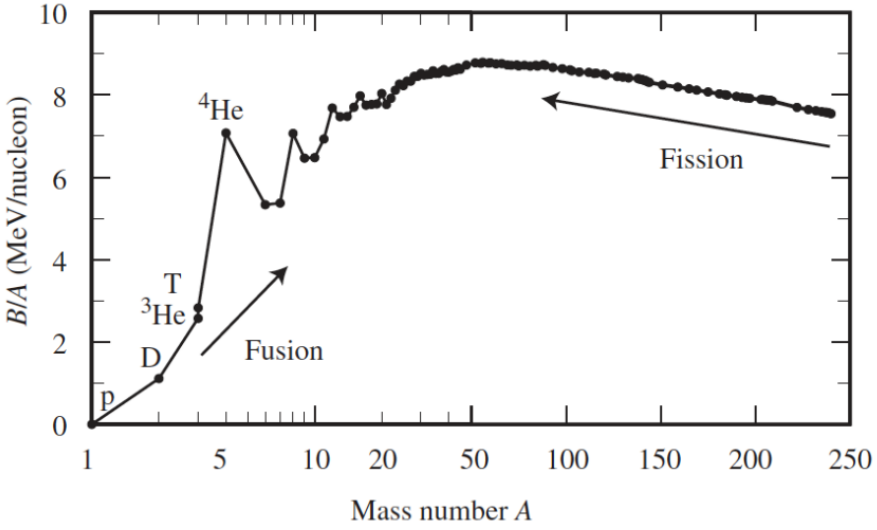

Figure 1.1: Average binding energy per nucleon (BIA) versus mass number (A).

be sufficiently energetic so that their kinetic energy allows them to be close enough for the strong interaction to take place and bind them together. This working distance is strictly correlated to the mass number of the interacting nuclei and it can be estimated as $r_{cr} \approx 1.44 \times 10^{-15}(A_1^{1/3} + A_2^{1/3})$ [m]. The Coulomb barrier (V_c) evaluated at r_{cr} is expressed as:

$$V_c(r_{cr}) = k\frac{Z_1 Z_2 e^2}{r_{cr}} \approx \frac{Z_1 Z_2}{A_1^{1/3} + A_2^{1/3}} \qquad [MeV] \tag{1.2}$$

where k is the Coulomb's constant, Z_1 and Z_2 the atomic numbers of the colliding nuclei. Under a classical mechanics point of view, only the particles that can overcome the Coulomb barrier start then to feel the attractive nuclear force. As it can be seen in equation 3.4, since $V_{\propto} Z_1 Z_2$, the lighter the interacting nuclei, the lower the V_c, the higher the probability to have fusion reactions. This constraint thus limits the occurance of fusion reactions only between a small class of nuclei.
This is better highlighted by considering also the fact that, under a quantum mechanics description, the tunneling probability can be taken into account, so that also nuclei with an energy below V_c can pass the Coulomb barrier.
Considering these aspects, the total cross section σ_{fusion} (i.e. the probability of occurence of a reaction) for a fusion reaction can be parametrized as:

$$\sigma_{fusion}(\epsilon) \approx \sigma_{geometrical}(\epsilon) \times T(\epsilon) \times R \tag{1.3}$$

where $\sigma_{geometrical}$ is the geometrical cross section, T the barrier transparency (i.e. tunneling probability) and R the reaction characteristics that is strictly correlated to the different types of interactions characterizing the reaction (e.g. weak or strong interactions). Taking into account the dependences of these factors by the center of mass energy ϵ and the Gamow

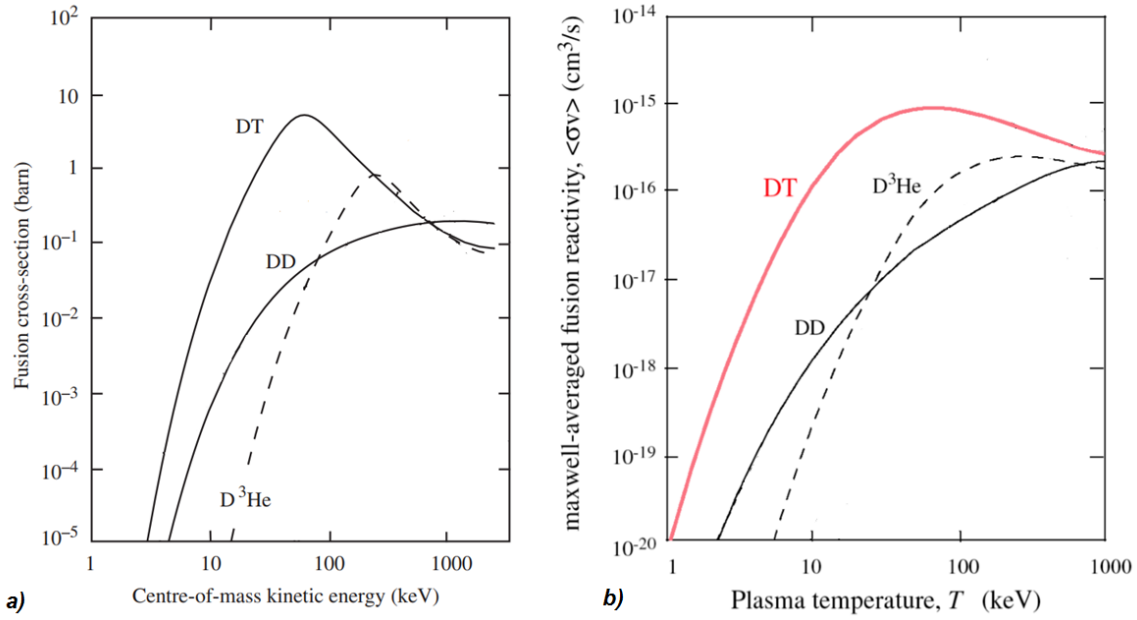

Figure 1.2: a) Nuclear fusion cross section $\sigma(\epsilon)$ for the different fusion reactions involving hydrogen isotopes. b) Maxwell-averaged fusion reactivity $< \sigma v >$ for the different reactions

energy ϵ_G, the total cross section can be then expressed as:

$$\sigma_{fusion}(\epsilon) \approx \frac{S(\epsilon)}{\epsilon} exp(-\sqrt{\epsilon_G/\epsilon}) \tag{1.4}$$

S, known as the *astrophysical S factor*, is nothing else a rescaled variant of the total cross section for Coulomb repulsion between charged particles. Since $\epsilon_G \propto (Z_1 Z_2)^2 m_r$, where m_r is the reduced mass of the system, this parametrization of the total cross section provides an explanation for the fact that nuclear fusion is cosidered only between light nuclei.
For these reasons, fusion reactions involving hydrogen isotopes are usually investigated. They concern the exploitation of deuterium (D) and tritium (T) as nuclear fuel, as described by the following reactions:

$$D + T \rightarrow \alpha(3.5\ MeV) + n(14.1\ MeV)$$

$$D + D \rightarrow \begin{cases} T(1.01\ MeV) + p(3.03\ MeV) & 50\% \\ {}^3He(0.82\ MeV) + n(2.45\ MeV) & 50\% \end{cases}$$

$$D + {}^3He \rightarrow \alpha(3.67\ MeV) + p(14.7\ MeV)$$

These fusion reactions, are not equally probable. Their cross sections are shown in figure 1.2a as function of the center of mass kinetic energy ϵ. As it can be seen, the D-T reaction shows the highest cross section at the lowest energy. In addition, D-T is characterized by the highest energy yield for the reactions involving only hydrogen isotopes (i.e. 17.6 MeV). Finally, considering the Maxwellian averaged reactivity $< \sigma v >$, defined as the product of the

cross-section times the relative velocity of the reacting nuclei averaged over the Maxwellian velocity distribution, the D-T reaction is again the most promising with respect to the other reactions (see figure 1.2b). For these reasons, the first generation of nuclear fusion power plants will be based on the D-T reaction. However, critical drawbacks are correlated to the use of D-T as nuclear fuel. First of all, the high energy amount is shared between an α particle and a neutron (n). The really energetic fast neutron field (i.e. 14.1 MeV) is then associated to several issues concerning radiation damage and neutronic activation of all the reactor components. Secondly, the use of T, due to its high intrinsic activity, is related to radiation protection concerns as well. In addition, T must be artificially produced, with connected technological issues (e.g. use of lithium (Li) blanket as a T breeder, moderator for fast neutrons and also primary coolant).
From now on, let us consider only the D-T reaction. Remembering eq. 3.4, V_c can be estimated to be around 0.1 MeV. This value can be decreased down to $\approx$ 10 keV if barrier tunneling probability is taken into account [1]. This means that, assuming the D-T mixture as an ideal gases mixture, so that $\epsilon = 3/2k_BT$, to overcome a barrier of $\approx$ 10 keV, the system must reach a temperature of about 10^8 K. At these temperatures the atoms are completely ionized, so that the matter is in the state of plasma. In this peculiar case, the plasma is called *thermonuclear plasma*. In order to have a net energy gain from the fusion reactions, the thermonuclear plasma must be sustained for suitable time by satisfying different criteria. These criteria are briefly described below.

1.2 Energy Balance for a Nuclear Fusion System

Referring to figure 1.3, let's consider a D-T steady plasma as a system open to energy exchange. Under the steady condition, it must be satisfied that:

$$P_{Loss} = P_{input} \tag{1.5}$$

which means that, by taking into account the different contributions highlighted in figure 1.3:

$$P_R + P_Q = P_{ext} + P_{fusion} \tag{1.6}$$

In this equation, P_{ext} refers to the power gained by the plasma from external sources, such as heating systems, while P_{fusion} is the power associated to fusion reactions occurring in the plasma. P_{fusion} is thus related to the energy deposited by the α particles inside the plasma, and it can be expressed as:

$$P_{fusion} = \frac{n^2}{4} < \sigma v > E_\alpha \tag{1.7}$$

where n is the plasma density and E_α is the energy of the α particles (i.e. 3.5 MeV). The neutrons produced by the reaction, due to their neutral charge nature, can easily escape from

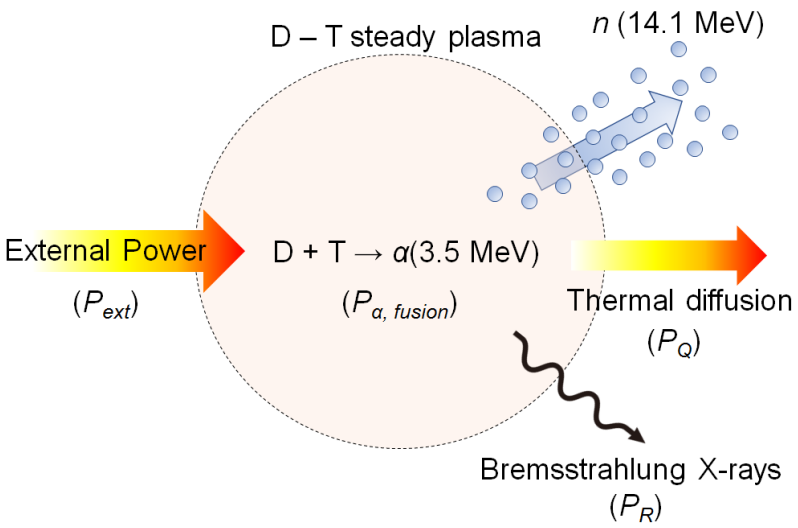

Figure 1.3: Schematic rapresentation of a steady D-T thermonuclear plasma. The different contributions to the plasma energy balance are highlighted.

the system without loosing a consistent fraction of their energy, so they are not considered in the balance equation.

In equation 3.6, P_R and P_Q stand for the radiative losses and the thermal diffusion losses respectively. The radiative losses are mainly related to the Bremsstrahlung effect, due to the scattering events between the ions and the electrons inside the plasma, and they can be defined as:

$$P_R = c_B Z_{eff}^2 n^2 \sqrt{T} \tag{1.8}$$

where c_B is the Bremsstrahlung constant (i.e. $c_B \approx 10^{-34}$ W cm^{-2}), Z_{eff} is the effective atomic number of the plasma and T the plasma temperature. The dependence of P_R by the square power of Z_{eff} highlights the fact that only low Z atoms can minimize the P_R contribution in the energy balance equation. High Z impurities, that usually come from plasma surrounding materials, can thus have a severe impact on the steady plasma condition stability. Therefore, a crucial aspect regards the choice of suitable materials for the plasma chamber in order to minimize the P_R contribution. This fundamental aspect will be further investigated in the next chapter.

Finally, if the expansion work of the plasma is neglected and equal densities and temperatures are assumed for electrons and ions, the last term P_Q can be written as a ratio between the mean plasma energy and a characteristic time as:

$$P_Q = \frac{3nk_BT}{\tau_E} \tag{1.9}$$

where τ_E is the plasma confinement time.

Now, considering a plasma in a steady state condition with no external inputs (i.e. P_{ext} = 0), and substituting all the contributions of equations 3.7, 3.8 and 3.9 into equation 3.6, it

holds:

$$c_B Z_{eff}^2 n^2 \sqrt{T} + \frac{3nk_B T}{\tau_E} = \frac{n^2}{4} < \sigma v > E_\alpha \tag{1.10}$$

Here, starting with an ideal equimolar pure D-T steady plasma with no diffusive losses (i.e. P_Q = 0), equation 1.10 says that the plasma is *self-sustained* if:

$$c_B Z_{eff}^2 n^2 \sqrt{T} = \frac{n^2}{4} < \sigma v > E_\alpha \tag{1.11}$$

so, when the fusion energy production itself (i.e. energy deposited by α paricles) is able to compensate the radiative losses. This ideal condition of plasma self-sutainement, in turn defines a specific criterion for temperature, which can be written as:

$$T_{id} = \frac{< \sigma v >^2 E_\alpha^2}{16 c_B^2 Z_{eff}^4} \tag{1.12}$$

T_{id} is known as the *ideal ignition temperature*, and, due to its dependence by $< \sigma v >$, it can be exploited as a first parameter to evaluate the feasability of different nuclear fusion reactions under an energetic point of view. For example, comparing the T_{id} values obtained for the different reactions between hydrogen isotopes, it results that the D-T one is again the most promising, showing the lowest $T_{id} \approx$ 4.3 keV (i.e. $T_{id} \approx 32$ keV for D-D).
However, in order to have a more realistic approach to the plasma ignition problem, also the thermal diffusive losses must be taken into account. So, considering again equation 1.10, it is possible to write a new criterion for the ignition condition as:

$$n\tau_E \geq \frac{12 k_B T}{E_\alpha < \sigma v > - 4 c_B Z_{eff}^2 \sqrt{T}} \tag{1.13}$$

This product between plasma density and confinement time is a plasma temperature dependent parameter, and it has a minimum for a specific value of T for each specific reaction (so each specific $< \sigma v >$). In the case of the D-T, for example, this minimum results to be around 25 keV, so that the $n\tau_E$ product assumes a well-determined value of:

$$n\tau_E \geq 2 \times 10^{20} \quad \mathrm{m^{-3}s} \tag{1.14}$$

Equation 1.14 is known as the *Lawson criterion* [2]. Following this criterion, the ignition condition can be achieved both for a dense plasma confined for a short time and viceversa. As a result of these two opposite ignition conditions, two main strategies are adopted for the sustainment of a thermonuclear plasma: the *inertial confinement*, which exploits a very dense plasma confined for very short times, and the *magnetic confinement*, based on less dense plasmas but confined for much higher times. These two confinement strategies are discussed in the next section.
Before going ahead, it is useful to introduce a key parameter for the estimation of the

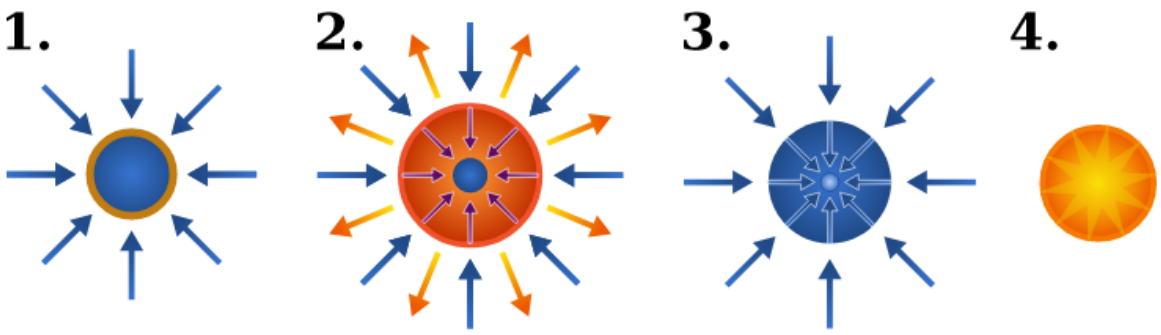

Figure 1.4: Schematic rapresentation of the processes involved in ICF. a) heating by lasers and formation of a plasma shell, b) compression of the pellet, c) rise of the core density by shock waves and d) ignition condition.

performance of a fusion power plant. To this purpose, it is possible to define the *gain factor* Q as:

$$Q = \frac{nuclear\ fusion\ power}{input\ power} \tag{1.15}$$

In the case of $Q = 1$, so when the power produced by nuclear fusion equals the input power, the system is said to operate at the *break-even* point. However, to have a system which can be exploited for energy production, the condition $Q = 1$ is not clearly sufficient. Future fusion reactors are expected to operate with $Q > 5$, so that the energy produced by the plasma itself and that remains in the plasma can compensate all the energy provided by external systems. Finally, if the plasma provides alone the amount of energy suitable to compensate all the energy losses, $Q = \infty$, and the ignition condition is reached.

1.3 Plasma Confinement Strategies

As already mentioned, in order to have a net energy gain from nuclear fusion reactions, the thermonuclear plasma must be sustained for suitable times. This, in turn, is related to the problem of plasma confinement, which, up to now, has not a unique and simple solution. The two most investigated plasma confinement strategies are based on the confinement of the electrical charged particles of the plasma by intense magnetic field (i.e. *magnetic confinement* fusion (MCF)) or by the inertia of the plasma (i.e. *inertial confinement* fusion (ICF)). They are briefly described in the following sections.

1.3.1 Inertial Confinement

The idea of *ICF* was initially proposed by *Nuckolls* in 1972 [3], considering high-power lasers to bring the nuclear fuel to the ignition conditions. In this design, the lasers are focused on a small D-T sphere that is rapidly compressed to reach the ignition condition, obtaining very high particle density (i.e. $\approx 10^{24}$ cm^{-3}) with very short confinement times (i.e. nanoseconds). Even if the physical process exhausts in a very short time, in the com-

pressed core, the plasma inertia confines the plasma pressure for sufficiently long times for nuclear fusion reactions to occur. This process can be divided into four steps, that are summarized in figure 1.4. At a first stage, the laser beams heat the surface of the fusion fuel sphere, rapidly forming a surrounding plasma (step 1). Subsequently, the material exploding off the surface with a *rocket-like* blowoff induces a great force on the inside of the material, resulting in high compression of the fuel (step 2). During the collapse, shock waves are formed. They propagates inside the material towards the center of the sphere leading to a sudden rise of the core density so that fusion reactions can take place (step 3). Due to the extreme pressure and the high density gradient, the α particles produced during the D-T reactions can slightly move from around the center and they are suddenly thermalized, releasing additional energy to the fuel pellet. This process, finally spreads outward from the center giving the self-sustained plasma condition (step 4).
Remembering equation 1.14, for ICF the Lawson's criterion can be rewritten in terms of a critical dimension of the fuel sphere and its density. So, starting from the fact that the confinement time must be greater than the reaction time (i.e. $\tau_E > \tau_{reaction}$), it is possible to express τ_E in terms of a characteristic dimension (i.e. the radius of the fuel sphere) and the sound velocity C_s in the plasma as [7]:

$$\tau_E = \frac{R}{C_s} \tag{1.16}$$

where C_s depends both on the temperature and the specific nuclear fusion reaction. The reaction time, instead, can be written as:

$$\tau_{reaction} \approx \frac{m_i}{\rho < \sigma v >} \tag{1.17}$$

where ρ is the density of the plasma core and m_i the ions mass. This leads to the following inequality:

$$\rho R \geq \frac{C_s m_i}{< \sigma v >} \tag{1.18}$$

This new ignition condition says that, in the case of the D-T reaction, the areal density ρR of the compressed core must be at least 2 - 3 g cm^{-2}. However, since the laser heating process results in a fast explosive process, only few mg of fuel per ignition can be exploited in order to contain the energy of the explosion. For example, considering only 3 mg of fuel, this requires $\rho > 100$ g cm^{-3}. With this density value, hydrodynamic instabilites easily grow, resulting in the quenching of the ignition process [6]. A lot of effort is thus driven to achieve the Lawson's criterion with a balanced compromise between compression and stability [5].
At the moment, the most advanced facility that investigates the ICF strategy is the *National Ignition Facility* (NIF), located at the Lawrence Livermore National Laboratory (USA). At NIF, in 2014, the scientists reported the achievement of $Q \approx 1.2$ (i.e. excluding the power

needed for the laser system to operate) [8]. This facility operates with the so-called *indirect drive* approach, where the fuel sphere (approximately 1 mm in diameter), instead of being directly heated by the laser, is contained inside a *hohlraum* that collects all the laser beams. In this way, the sphere is immersed in a X-rays bath, produced by the fast heating of the hohlraum walls, that guarantees a uniform heating. The spherical capsule is made by an outer plastic shell, which is called the *ablator*, that encloses a layer of cryogenic solid D-T, while the hohlraum material is usually a high Z and high density material, such as gold, in order to minimize the diffuson of the radiant energy through its walls and maximize the opacity to X-rays. This indirect-drive approach is opposite to the *direct drive* ICF, where the fuel sphere is directly heated by the laser driver. With respect to indirect-drive, with direct-drive a higher fuel mass implosion can be achieved thanks to a higher conversion efficiency of laser energy into shell kinetic energy. However, direct-drive, at the moment, does not allow a uniform illumination of the fuel target, resulting in hydrodynamic instabilites that can break the shell before the ignition conditions are achieved.
Finally, it has to be mentioned that other advanced ignition ICF schemes are currently under development. Among them *Fast Ignition* and *Shock Ignition* are considered as valid alternative to the indirect and direct drive schemes [4].

1.3.2 Magnetic Confinement

Magnetic confinement fusion relies on the fact that the charged particles of the plasma easily interact with magnetic fields. This interaction gives the opportunity to confine the plasma for longer confinement times with respect to ICF (i.e. seconds vs nanoseconds) and thus to work with lower density plasmas (i.e. $n \approx 10^{14}$ cm^{-3}).
In order to understand how this magnetic confinement works, let's consider a charged particle that, moving in a strong magnetic field, is bound to the magnetic field lines as a result of the Lorentz force. The resulting motion, called *Larmor motion*, consists in a superposition of a circular motion, characterized by a gyration radius $r_L = v_\perp/\omega_c$, where $v_\perp$ is the velocity perpendicular to the field line and ω_c the cyclotron frquency, and a linear motion of the guiding centre, characterized by a velocity parallel to the field lines $v_\parallel$. The Larmor radius r_L linearly depends by the charged particles masses, being higher for ions than for electrons. Real MCF devices exploit magnetic fields that opportunely tailor the Larmor radii of the ions and the electorns of the plasma, such that they both result to be much smaller than the dimension of the device.
The magnetic field geometry, in turn, determines the shape of the confined plasma. For this reason many different plasma configurations have been investigated in the last years. The simplest geometry one can think of, is represented by a straight cylinder magnetic field, which is intensified by suitable additional coils (i.e. mirrors) at the both ends. Besides minimizing particles losses through these surfaces, the use of magnetic mirrors results in a plasma confined in a sort of magnetic bottle. Machines that rely on this particular configu-

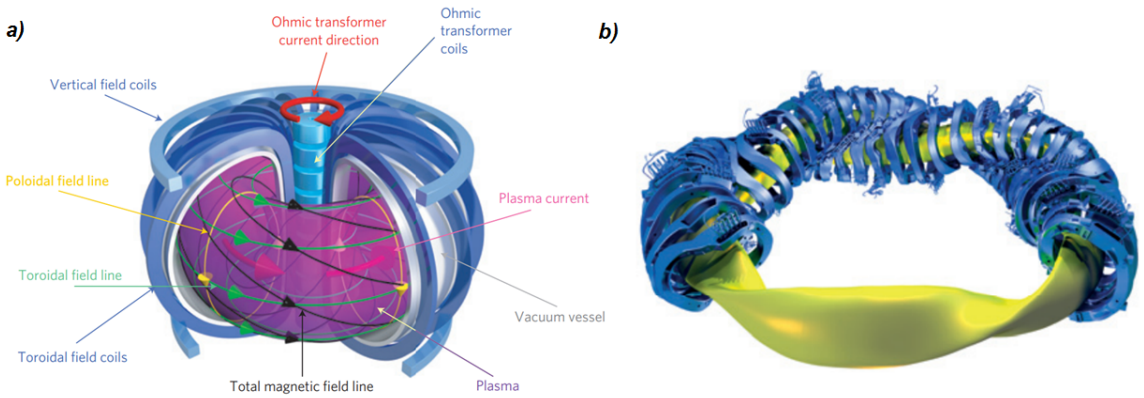

Figure 1.5: a) Schematic of a Tokamak configurations. The toroidal, poloidal and total magnetic fields and the coils are represented. b) Schematic of a Stellarator configuration of the magnetic coils and the plasma shape. Figure adopted from [9].

ration are the so-called *mirror machines*. Unfortunately, the end mirrors can not reflect all particles, giving rise to plasma instabilites and particles losses that drove the scientists to abandon this MCF strategy so far in 1986.

To prevent the particles loss, an obvious solution is to wind the cylinder onto itself, obtaining the so-called *toroidal plasma*. To obtain this configuration the magnetic field (i.e. *toroidal field* $\mathbf{B}_T$) has to be generated. This is achieved by suitable winding coils, which are placed outside the machine. However, the toroidal field alone is not able to properly confine the plasma. The magnetic field is a solenoidal field, being the field lines more concentrated near the inner part of the torus. This results in a gradient of $\mathbf{B}$, likely inducing a vertical drift of the charged particles, with a consequent charge build-up (i.e. the formation of a vertical electric field) and plasma loss. In order to prevent this drift (i.e. $\mathbf{E}$ x $\mathbf{B}$ drift), an additional magnetic field, the so-called *poloidal field* $\mathbf{B}_P$, has to be added to the system. In this way, the resulting total magnetic field $\mathbf{B} = \mathbf{B}_P + \mathbf{B}_T$ shows field lines that wound around the torous so that the particles drift in the inner and the outer part of the trajectory is compensated. The amount of these wrapping field lines is called the *rotational transform*, while the number of field lines turns in the toroidal direction per turn in the poloidal direction on each magnetic surface is called the *safety factor* (q).

Among the different schemes proposed to generate the rotational transform, the two main strategies that are currently exploited are the *Tokamak* and the *Stellarator* configurations. The schematics of these two MCF devices are shown in figure 1.5. In Tokamak devices, toroidal coils are exploited to generate $\mathbf{B}_T$. The toroidal magnetic field induces inductively a toroidal current inside the plasma, as in a simple transformer, varying the magnetic flux in the primary transformer coils (i.e. *ohmic* transformer). The toroidal current promotes itself the poloidal component of the total magnetic field. In addition, since the plasma has an own non-zero electrical resistivity, the plasma current is also exploited to heat the plasma in the first stages of plasma heating (i.e. ohmic heating). Additional vertical coils are added to

counteract the expansion forces related to the plasma current and plasma pressure, to shape the plasma and to create a divertor [9].
To have a constant plasma current, all the tokamaks must operate within a pulsed regime. This means that after each plasma discharge the primary ohmic system must be reacharged. Continuous operation can be achieved if, instead of using the principles of a transformer to induce the poloidal component of the magnetic field, currents external to the plasma are exploited. The Stellarator, which is shown schematically in figure 1.5b, relies on this principle. Here, the addition of extra helical coils provides the missing part of the magnetic field necessary to obtain final helicoidal shape.
Due to technological issues mainly related to the complex shape coils design and realization, the Stellarator technology has been gaining interest for the generation of fusion power only since 1998, when the first large Stellarator LHD was built and put in operation in Japan. In 2015, W7-X, the largest Stellarator on Earth which is sited in Greifswald (Germany), produced its first plasma. On the other hand, by the mid of the 70s, most of the fusion research programs were running Tokamak experiments. In 1997, for example, the largest operating tokamak JET (*Joint European Torus*) in Culham (UK), operating with D-T achieved $Q \approx 0.7$, the all time record for controlled fusion power production from MCF devices [12].
For this reason, the tokamak configuration has been chosen as the reference design for the future first generation of nuclear fusion power plants, passing through the realization of the experimental reactor ITER and culminating with the demonstrative reactor DEMO. In this thesis only the tokamak configuration is thus taken into account. A complete description of stellarator devices goes beyond the purposes of the thesis work. The interested readers may refer to [10, 11] for more specific information.

1.4 The Tokamak

As already mentioned in the previous section, the tokamak configuration is regarded as the reference design for the first generation of nuclear fusion power plants. In a tokamak, the plasma is contained in a toroidal vaccum chamber and it is confined, as said in the previous section, by intense toroidal and poloidal magnetic fields. However, it is not trivial to reach the thermonuclear plasma state, and many components, from heating to diagnostic systems, have to be optimized. In this section, the key aspects concerning tokamak devices are briefly discussed. They consist in: plasma confinement and heating systems (sec 1.4.1), plasma stability and plasma control by diagnostic systems (sec 1.4.2), and plasma facing components (sec 1.4.3). Finally a general overview on the ITER project is given in sec 1.4.4.

1.4.1 Plasma Heating and Confinement

As discussed in section 1.3.2, in tokamak devices a set of external magnetic coils is exploited to induce the toroidal magnetic field $\mathbf{B}_T$. This coils can be made by standard conducting materials (e.g. copper) or by superconducting materials (e.g. NbTi or Nb_3Sn). In general, $\mathbf{B}_T$ can be of several tesla, reaching in the largest machines 12 - 13 T. The poloidal field $\mathbf{B}_P$, which is generated inductively by the toroidal plasma current, instead is approximately ten times lower than $\mathbf{B}_T$. To finely tune the $\mathbf{B}_P$ additional coils are usually added to the system.
In order to promote fusion reactions, the plasma must be heated to tens of keV. The first source of heating is provided by the plasma current itself (I_T) through the principle of ohmic heating as:

$$P_{ohminc} = R_{plasma} I_T^2 \tag{1.19}$$

where R_P is the electrical resistance of the plasma. One can think that, to reach 100 milions of K, it is sufficient to increase the I_T value, and relying on the ohmic heating only. However, increasing I_T over certain values leads to plasma instabilites that can destroy the plasma confinement. In addition, $P_{ohmic} \propto T^{-3/2}$, so, the higher the plasma temperature, the lower the particles collisions, so the electrical resistance and thus the heating power. For these reasons, the ohmic heating alone can not provide all the sufficient energy to reach ignition conditions. For temperatures usually above $\approx$ 10 milions K other external input sources must be exploited. One of them consists in the injection of neutral particles (i.e. neutral beam injection) $P_{neutral}$ that, through collisions with other particles in the plasma, get ionized and become part of the plasma itself transferring a certain amount of energy [13, 14]. Another way is to use the so-called radio-frequency heating (P_{RF}), that exploits electromagnetic waves that, coupling with plasma particles, transfer a certain amount of energy [13, 15]. In order to guarantee an efficient energy transfer, this coupling must be performed at frequencies around the ion cyclotron plasma resonance (i.e. *ICR heating*, $\approx$ MHz) or at around the electron cyclotron plasma resonance (i.e. *ECR heating*, $\approx$ GHz). These heating sources are summarized in figure 1.6. Remembering the energy balance equation 3.6, the term P_{ext} can now be written as:

$$P_{ext} = P_{ohmic} + P_{RF} + P_{neutral} \tag{1.20}$$

such that the increasing rate of the total energy below the ignition temperature is:

$$\frac{d\epsilon}{dt} = R_P I_T^2 + P_{RF} + P_{neutral} - c_B Z_{eff}^2 n^2 \sqrt{T} - \frac{3nk_BT}{\tau_E} - \frac{\epsilon}{\tau_E} \tag{1.21}$$

When the plasma steady state is reached (i.e. $d\epsilon/dt = 0$), the heat coming from external sources and from α particles produced by D-T reactions has to be exhausted to mantain constant plasma temperature. Moreover, the fuel must be injected as it is progressively

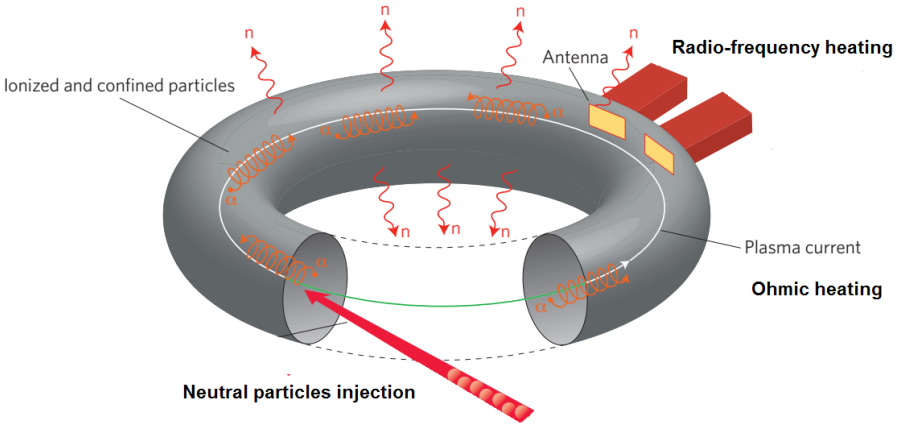

Figure 1.6: Schematic of the different plasma heating strategies in tokamaks. Figure adopted from [16].

burned. All these aspects are only some of the total critical issues that have to be still solved in order to guarantee stable operating fusion reactors.

1.4.2 Plasma Stability and Diagnostics

When the thermonuclear plasma reaches the ignition condition and starts to burn, many other aspects, in addition to the power losses described in the previous sections, have to be taken into account in order to guarantee plasma stability. The *magnetohydrodynamic* description (MHD) of the plasma is regarded as a good approach to properly investigate plasma stability conditions. It relies on a hydrodynamic description of the plasma that is treated as an ideal gas with infinite electrical conductivity. This model is valid when the plasma is sufficiently hot such that the electrical resistivity can be neglected, but also for sufficiently short timescales, so that current redistribution can be disregarded. Under the MHD approach, the force balance for a toroidal plasma can be described in terms of the plasma current density, the plasma pressure and the magnetic field. By the linearization of the ideal time-dependent MHD equation, the plasma stability can be assesed. A rigorous discussion on MHD is not presented here. A detailed description of the model can be found in several works, such as in [17]. For the purpose of this thesis work, it is important to consider the fact that MHD instabilities severly affect the operational range of fusion devices [18]. An important parameter that can be exploited to set a limit on the insurgence of MHD instabilites is the ratio β, defined as the ratio between the plasma pressure (p) and the magnetic field pressure ($B^2/2\mu_0$):

$$\beta = \frac{p}{B^2/2\mu_0} \tag{1.22}$$

where the plasma pressure p is related to the plasma temperature as $p = 2nk_BT$. When β exceeds a critical value of a few percent MHD instabilities are likely to occur. This β limit can be further decreased by the occurance of the so-called *tearing modes*, that induce

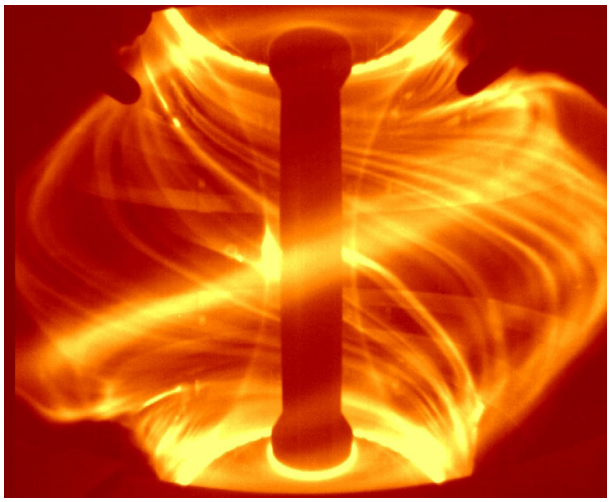

Figure 1.7: Plasma discharge in the Tokamak MAST. ELMs are identified by the plasma filaments that are visible in the image. Figure taken from [19].

the formation of magnetic islands, which increases heat and particles flow accross plasma cross section in the island region. Among the various MHD instabilities, the ones most noteworthy are:

Disruptions : Disruptions occur when different magnetic islands interact. This interaction leads to the loss of plasma insulation on a timescale of hundreds of microseconds, so a decrease of plasma temperature that increases plasma electrical resistivity, affecting the plasma current that can no longer be sustained. In this way, the plasma current is redistributed firstly over the plasma cross section, and then on the vacuum vessel, with consequent critical effects on the surrounding materials.

Edge Localized Modes (ELMs) : ELMs instabilities are not always an unwanted type of plasma instability, because they provide a self-limited operation of the device when operating under a non linear plasma behavior. During ELMs the regulation of the plasma edge pressure gradient is achieved. Moreover, they are at the basis of different plasma mode operations (e.g. *H-mode*). Thousands of ELMs can likely occur during a single plasma discharge, delivering a high amout of energy to the plasma surrounding materials. For this reason, ELMs have to be mitigated in order to ease these loads on plasma facing components. Figure 1.7 shows ELMs instabilities during a plasma discharge in the tokamak MAST (China).

Vertical Displacement Events (VDEs) : VDEs occur in vertically elongated plasmas, when the plasma current increases in a certain region of the plasma due to a vertical displacement of the plasma itself. This displacement is caused by a coupling between unstable helical modes and asymmetries in the magnetic field configuration. VDEs are usually accompained by the transmission of part of the current to the so-called *runaway electrons*, that leave the plasma and impinge on the first wall materials.

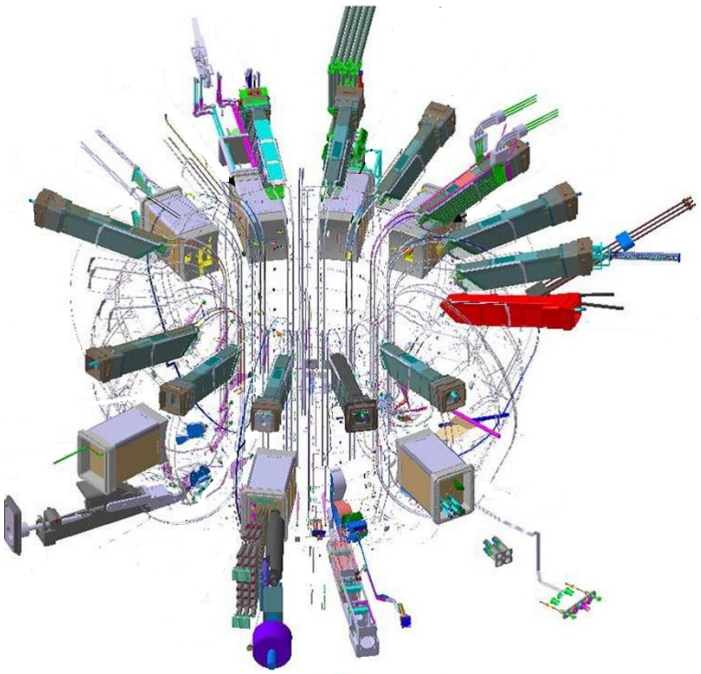

Figure 1.8: Plasma diagnostics positions in a Tokamak (ITER). Figure taken from [22].

As it will be discussed in details in the next chapter, all these instabilites, besides being critical aspects of plasma sustainement conditions, have also a severe impact on the plasma facing materials, inducing a high radiation damage and delivering extreme thermal loads. In the recent years [9], a lot of effort is driven to investigate the possibility to avoid or mitigate them. For example, ELMs and VDEs can be mitigated by massive injection (i.e. 10^{22} atoms in tens of ms) or pellet injection of impurities gases (e.g N, H). ELMs can also be suppressed by using suitable magnetic coils that tailor the magnetic field shape in the critical region of the plasma where instabilities are expected. However, plasma instabilities mitigation or avoidance is still an active research topic, being one of the most challenging fusion-related problem that must will be investigated directly in ITER [20].

It is evident that, when the tokamak starts its operations, it is fundamental to accurately monitor various plasma parameters. This concerns, for example, plasma temperature, density, impurity content, current measurements, but also the state of the plasma facing materials. All this information is obtained by suitable plasma diagnostic systems. A schematic representation of the complex map of diagnostics system position in a tokamak is shown in figure 1.8. Even the design of these probing systems is challenging, because any standard probe would be destroyed if it enters in contact with the plasma. A more complete description of the different plasma diagnostic is reported elsewhere [21]. Here, only a brief summary of some of them is proposed.

Plasma temperature: Plasma temperature can be estimated by measuring ions and electrons temperatures. For the ions temperature, spectroscopic systems based on both active beams (i.e. injection of neutral particles (H_2 or D_2)) and passive emission (i.e. analysis of

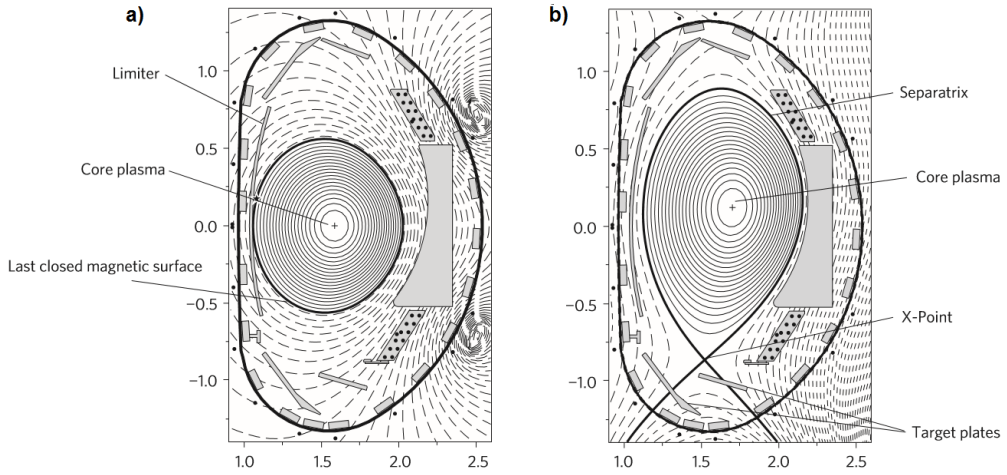

Figure 1.9: a) *Limiter* configuration, b) *Divertor* configuration. Figure taken from [9].

plasma radiative losses) are exploited. These methods relies on the detection of the Doppler broadening of plasma ion emission spectral lines. For electron temperature measurement, instead, mainly *Langmuir* probes and *Thomson scattering* or *microwave radiometry* are exploited for the analysis of the plasma edge and core properties respectively.

Plasma current: Plasma current and its distribution can be measured by electric and magnetic diagnostics. Basically, introducing elecrodes or coils of wires in the plasma region with a constant or time-varying electric potential between electrodes, or them and the ground, results in induced currents or voltage, that, in turn, are associated to the plasma properties.

Neutron Diagnostics: the neutron diagnostics are among the most important diagnostics systems for tokamaks, since they allow the evaluation of the neutron emissivity, which is strictly related to the fusion power. In addition, the neutron fluence at the plasma facing materials gives an idea of the expected radiation damage. These diagnostics are also exploited to derive information, from neutron emission profiles, about the α particles birth source, which is fundamental to assess the role of plasma self-heating by particles in self-sustained thermonuclear plasmas.

1.4.3 Plasma Facing Components

Plasma Facing Components (PFCs) are the systems directly exposed to the thermonuclear plasma. They are the dowels of the so-called First Wall (FW). Due to their direct exposure to the plasma they operate under extreme conditions of both particles and heat fluxes. At the same time, they must withstand their functional properties during all the operation history. In order to mitigate the possible effects on the components induced by the direct exposure to the plasma, the magnetic field is usually opportunely shaped, so that only some of the total PFCs are directly touched by the plasma. Two strategies are proposed: the *limiter* and the *divertor* configurations (see figure 1.9). Limiters can be regarded as an extension

of the first wall, where the plasma can directly impinge. They can have different shapes, being like a toroidal ring (i.e. toroidal limiter) or like poloidal rings (i.e. poloidal limiter) placed in different positions of the first wall. As it can be seen in figure 1.9a, in this type of configuration the plasma is bounded by the limiter material, and the magnetic field lines from the hot plasma strike directly on the limiter itself. However, open magnetic field lines that are connected to first wall elements have resulted in a better confinement of the plasma. This is why the limiter configuration has become less important in favour of the divertor one (see figure 1.9b). In the divertor configuration, the *separatrix* field line separates the magnetic surfaces, where nuclear fusion takes place, from the outer plasma regions. The open field lines of the boundary plasma (i.e. *scrape of layer*) focus the particles on target areas (i.e. the divertor plate), which are quite far from the burning plasma and they are opportunely designed to withstand the high particles and heat loads. During standard operating conditions, typical power densities of 10 - 20 MW m^{-2} are expected on the divertor targets. This value is drastically increased up to tens GW m^{-2} during off-normal events (i.e. plasma instabilites). Different solutions are thus investigated in order to mitigate these extreme heat loads and to guarantee operational stability to the component. These solutions include *plasma detachment*, or introduction of impurities, such as noble gases, that promote periphery plasma radiation.
Among all the issues related to the PFCs behavior in Tokamak devices, the investigation of the effects induced on the materials by the extreme thermal loads are one of the most critical. Being one of the main topic of this thesis work, they will be discussed in details in the next chapter.

1.4.4 The ITER project

The last section of this first chapter could only be devoted to briefly introduce what is, at the moment, one of the greatest challenges of the mankind: the ITER project. ITER ("*the way*" to new energy), is a tokamak experiment whose main objective is to demonstrate the feasibility of nuclear fusion as an alternative source of energy. Even if the first design of ITER dates back to the 90s [23], the ITER project officialy began in 2006 as a joint venture between seven member entities (i.e. EU, India, China, Japan, Russia, South Korea and USA). This experiment will provide a thermonuclear burning plasma of D-T, that will be sustained by the α particles energy E_α for more than 10 minutes, with a gain factor $Q = 10$ and a total fusion power of ≈ 500 MW [24]. The tokamak is under construction in the french site of Cadarache. In details, the tokamak complex surrounding construction will be finished in 2021, while the tokamak assembly in 2025 with the starting of the first non-nuclear phase (i.e. first He or D plasmas). The first D-T plasma will be achieved not before 2035.
A schematic representation of the Tokamak ITER is presented in figure 1.10. This Tokamak will confine a ≈ 840 m^3 plasma, with a 6.3 m radius, by a 6 T toroidal field (up to 12 T

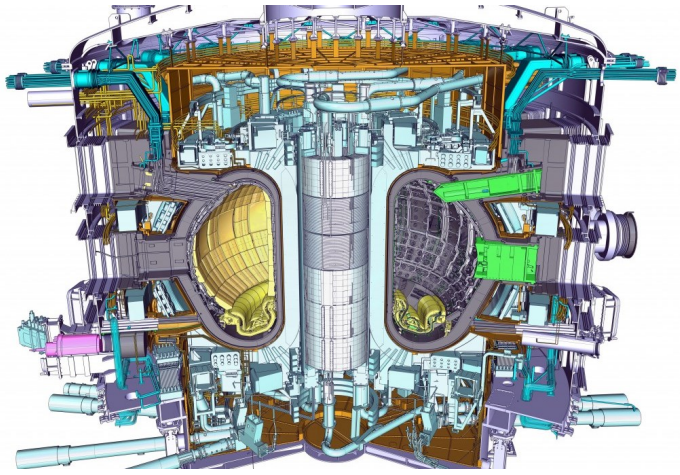

Figure 1.10: ITER Tokamak scheme. Figure taken from [25].

at the coils) provided by superconductive coils. Thanks to these superconducting magnets, it is possible to achieve a quasi-steady state regime. During this operating condition high heat fluxes (HHFs) are delivered to the PFCs (up to 20 MW m^{-2}). Neutral beam injection up to 1 MeV and radio-frequency heating will be exploited as auxiliary heating, for a total of 73 MW. The plasma current will be around 15 MA. The FW plasma facing components, as described in details in the next chapter, will be based on beryllium (Be), for the so-called main chamber region (i.e. the blanket), and tungsten (W), exploited for the divertor components, where the most critical conditions are expected.
Beside demonstrating the feasability of a D-T burning thermonuclear plasma, ITER would be the answer to a threefold physical problem:

- The ability of handling the energy of a burning plasma in completely new conditions never tested in other fusion experiments. This concerns the behavior of PFCs under the extreme ITER working conditions, in particular in the divertor region.
- The possibility to mitigate and control ELMs: in ITER there will be hundreds of ELMs per plasma discharge that deliver ≈ 1 MJ m^{-2} energy fluence on the PFCs in hundreds of microseconds. They must be thus mitigated in order to avoid an unaccetable deterioration of PFCs properties.
- The possibility to avoid disruptions, the most detrimental plasma insability that result in unacceptable mechanical and thermal effects on all the PFCs, not only on the divertor.

The realization of ITER is a necessary step towards the energy production from fusion reactions, but it is only the first one of this arduous path. Only with the first demonstrative reactor $DEMO$, whose building is set to around 2050, we will be able to answer to the final, but most important, question: are we ready to produce electricity from nuclear fusion reactions?

CHAPTER 2

Plasma Facing Materials issues in Magnetic Fusion Systems

As mentioned in the previous chapter, the D-T thermonuclear plasma in ITER must reach a temperature of about 100 million K to guarantee nuclear fusion reactions and plasma self sustainement. This temperature corresponds to an average kinetic energy of the hydrogen isotopes of about 10 keV. It has been shown how these energetic particles can be confined by intense magnetic fields. However, the plasma confinement is not perfect, in the sense that, during steady operating conditions, in specific first wall regions (i.e. divertor and limiters), the plasma delivers a high particles flux to the sorrounding materials. In addition, during off-normal transient events, the energetic particles can escape from the plasma, so that the particles flux increases and spreads around the first wall materials. Hence, these energetic particles deposit their kinetic energy on the first wall PFMs, with consequent severe effects on their properties, as well as on the thermonuclear plasma quality. The interactions between the particles and the PFMs, known as *plasma-wall interactions* (PWIs), are a crucial aspect of plasma physics in tokamaks and they must be opportunely understood to guarantee operational stability to the whole device.
In this chapter, the main PWIs are described in section 2.1. Then, in section 2.2, the focus shifts on the R&D about PFMs, where the main features of suitable PFMs are described. In current and future tokamaks, tungsten (W) is regarded as the main candidate for the most critical regions of the FW, where the highest particles flux is expected. In section 2.3, the use of W as PFM is thus highlighted. In particular, the exploitation of both bulk W and W coated PFCs in the recent tokamaks experiments is summarized. In section 2.4, the main effects of plasma interactions on W PFCs are analyzed. Finally, the laboratory investigation of W materials relevant for fusion applications is presented in section 2.5. In particular, the

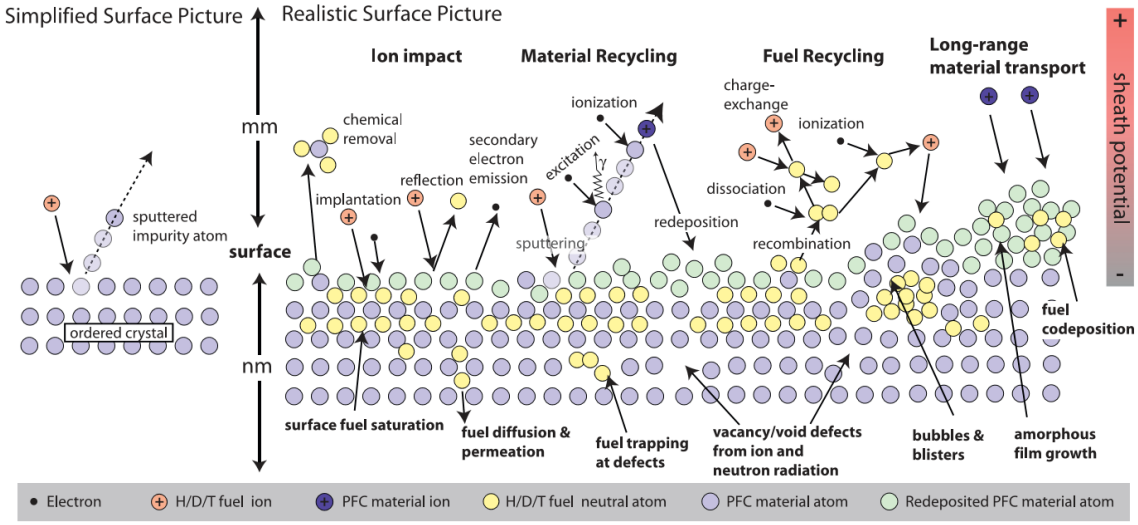

Figure 2.1: Schematic representation of PWIs. Figure taken from [26].

study of the behavior of W under fusion relevant thermal loads (section 2.5.1) and the mimicking at the lab-scale of W based coatings by Pulsed Laser Deposition (section 2.5.2) are discussed. These steps are crucial to consistently introduce, in section 2.6, the main goals of the thesis .

2.1 Plasma-Wall Interactions

Due to the direct exposure to the burning plasma, PFMs have to withstand extreme conditions. The energetic particles coming from the plasma can impinge on PFMs and give rise to a multide of effects (figure 2.1). PWIs have a double side effect on the PFMs properties, that can change radically from the ones of the pristine materials, and on the plasma quality as well, since, for example, the eroded particles can migrate, can enter the plasma and increase impurity losses. In addition, the tritium management, regarding co-deposition of T and D in the eroded and then redeposited materials, is a fundamental aspect for the radiation protection and activation of the PFCs. In general, these effects can exist at very different physical scales, from nanometers to millimiters, and from nanoseconds to years. For these reasons, it is crucial to understand what type of PWIs can be found in a tokamak device, and how they affect the overall properties of the system. In this thesis work, the main effects induced by PWIs on the PFMs are distinguished in *atomistic effects*, namely the effects related to particles bombardment (e.g. erosion, co/re-deposition, neutron damage), and *thermal effects*, which are related to the effects induced by the thermal loads that the edge plasma delivers onto PFCs. In the following sections some of the these effects are discussed.

2.1.1 Atomistic Effects

The D-T thermonuclear plasma produces extremely energetic neutrons, neutral and charged particles (i.e. ions, electrons) as a consequence of fusion reactions. In particular, for ITER, taking into account a plasma discharge of 400 s, with Q = 10, in the divertor area near the strike point, the particles flux reaches a typical value of about 10^{24} m^{-2} s^{-1}, with a plasma density of about 10^{21} m^{-3} and a plasma temperature of $\sim$3 eV. Around the first wall, instead, lower fluxes are expected between 10^{19} and 10^{23} m^{-2} s^{-1} [33, 34].
Generally, an impinging energetic particle can transfer part of its kinetic energy to the so-called *primary knok-out atom* (PKA), which then can eventually transfer its energy to other lattice atoms through collisions, giving rise to a collisional cascade. In this way, during a collisional cascade, a certain number of atoms is displaced from their lattice positions, thus generating lattice defects, such as vacancies and interstitials. The total radiation damage is usually reported in terms of the total *displacements per atom* (dpa), which statistically accounts for the times an atom is moved from its original lattice position. The interaction of the energetic particles flux with the PFM surface results thus in different radiation damage effects, that depend on the specific nature of the colliding particles, on their energy and chemical affinity with the target materials.
Neutrons damage is one of the most crucial aspects for PFMs radiation damage, since neutrons, due to their neutral charge, can penetrate deeply into the material, inducing bulk damage by collisional cascades and nuclear transumations of the target atoms. As a result of collisional cascades, the microstructure radically changes, and *swelling* phenomena associated to the formation of voids and helium (He) bubbles in lattice vacancies formed by (n, α) reactions and the formation of *dislocation loops* occur [28]. Nuclear transmutations reactions, instead, can result in the formation of multi-component alloys that can affect peculiar properties of the materials, fundamental for their use as PFMs, such as hardness, thermal conductivity and electrical resistivity [28, 29]. Finally, the activation of the PFCs leads to unwanted long-life nuclear waste, with problematic radiation protection concerns and handling of all the in-vessel components. For ITER, the radiation damage at the end of its lifetime has been estimated to be 0.6 dpa in the divertor region, while 1 dpa at the first wall [27].
In addition to neutrons damage, also the effects of **He impact** onto PFMs is fundamental, as He is a product of fusion reactions, so it is a consistent part of the total impinging plasma impurities. The surface of PFMs can be deeply affected by the exposure to energetic He atoms, that results in erosion phenomena, the growth of surface nanostructures (e.g. *fuzzy* structures) [30, 31], and implantation phenomena. Implanted He rapidly precipitates into He bubbles, that can accumulate at lattice defects, such as dislocations or grain boundaries [32], with consequent swelling phenomena and irradiation induced embrittlement of the material.

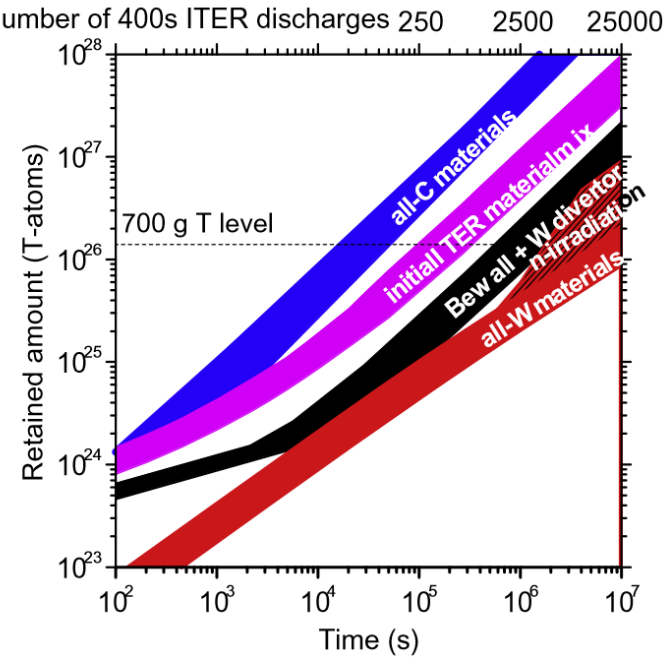

Figure 2.2: Tritium inventory in ITER for different PFMs choices after different plasma discharges with different particles fluxes and baseline temperatures. Figure taken from [33].

As it happens for He, **implantation of nuclear fuel** is in general a crucial aspect when discussing plasma-material interactions in a tokamak device. First of all, since the breeding of T necessary for the D-T reactions is one of the most critical issues for future fusion reactors, for each T atom used, another one must be produced by the system, also compensating all the possible losses that can be drastically increased by fuel retention in PFMs. Moreover, radiation protection concerns, related to the intrinsic activity of T, set several limits on the total amount of possible retained fuel by PFMs (i.e. the total T amount for ITER is set to 700 grams [33]). Figure 2.2 shows the T inventory of different ITER-relevant materials for an increasing number of 400 s plasma discharges. Once the H isotopes enter the PFMs they first thermalize, and then they start to accumulate at lattice defects. The higher the concentration of defects, which is raised by radiation damage, the higher the retention in the material. When the surface is completeley saturated, D and T atoms can diffuse and can be trapped by bulk lattice defects, increasing the trapped inventory. This explains the increasing trends of the curves in figure 2.2. Retention by bulk PFMs is not the unique source of fuel loss in tokamaks. As it is described below, the eroded particles can mix with fuel atoms, forming co-deposits rich of nuclear fuel above the FW materials.

The **erosion** of PFMs is the most fundamental effect of PWIs in tokamaks. Erosion can be driven by physical or chemical *sputtering* processes. **Physical sputtering** occurs when the kinetic energy of the colliding ions or neutral particles exceeds the surface binding energy of the atoms (i.e. 3 - 8 eV). In this condition, there is a finite probability that the scattered atoms, instead of forming a collisional cascade, are ejected from the surface. The amount

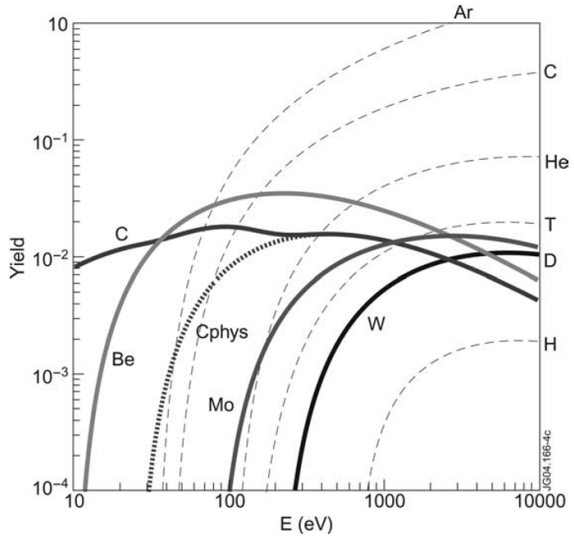

Figure 2.3: Physical sputtering yield for different fusion relevant materials bombarded with D. In the case of W, physical sputtering yield for different colliding particles are plotted by the dashed lines. Figure taken from [35].

of these sputtered atoms is proportional to the total energy deposited by the plasma particles within the surface. The threshold energy for physical sputtering (i.e. the *sputtering yield*) is not a constant value, but it is strictly correlated to the mass of the colliding and target particles (i.e. increases with target mass number and decreases with incident particles mass number) [35]. In figure 2.3 the physical sputtering yields for different fusion relevant PFMs are plotted. In each case, the sputtering curve increases, reaching a maximum, and then starts to decrease, as the impinging energy is so high that collisional cascades are favoured. This yield, moreover, can be severly affected by many other factors, such as surface roughness, crystallographic structure and scattering geometry. In contrast to physical sputtering, **chemical sputtering** occurs thanks to a chemical affinity between the colliding particles and the target atoms. Chemical sputtering is particularly relevant in tokamaks with high presence of low Z materials (e.g. carbon (C) and beryllium (Be)). The impinging species chemically interact with the target atoms, breaking the chemical bonds and forming new chemical composites. Generally, the presence of C, oxygen (O) or nitrogen (N) as plasma pollutions, can induce chemical sputtering of PFMs metals and the formation of new compounds, namely carbides, oxides and nitrides respectively.

The physically or chemically sputtered particles finally can undergo to **migration** processes inside the reactor, entering the plasma, contaminating it and increasing power losses (see section 1.2). In addition, since a tokamak is a closed system, each eroded particle must then **redeposit** somewhere over the FW. Eroded particles can promptly redeposit close to the regions where they are released, or they can enter the plasma and be transported around the machine. This process occurs several times during tokamak operations, with a net result of a growth of thick layers above the pristine PFMs. These coatings are usually composed by the various elements present in the machine, and show complex morphologies and structures.

In particular, the eroded PFMs particles can co-deposit with the hydrogen isotopes used as nuclear fuel, giving rise to additional fuel inventories, or with gas contaminants, such as O or N, forming oxides and nitrides layers. The presence, the composition and the form of these co/re-deposited layers are hardly predictable, depending on the specific type and regions of the tokamak, on the kind of PFMs that form the FW and on the overall operating conditions. In the case of a tokamak with a limiter configuration, the limiters are the main sources of impurities for the formation of co/re-deposits. In this case, the eroded particles are usually re-deposited in their proximity. In divertor configurations, instead, the situation is much more complex, since, in addition to the redeposition of eroded material from divertor plates, also redeposition of materials coming from the blanket can be observed. It has been found during the first *ITER-like wall* (ILW) campaigns at the Tokamak JET [36], that a large fraction (e.g. up to 90%) of divertor sputtered particles is promptly re-deposited in the outer regions of the divertor. The remaining part can undergo to migration through the scrape-off layer towards the inner regions of the divertor, where codeposited layers rich of many elements with thickness up to 30 μm are found in the upper and horizontal parts of the inner divertor.
In general, the thickness of these co/re-deposited layers, that ranges from nanometers to hundreds of micrometers, and their presence around the FW severely affects both the PWIs and the performances of pristine PFMs. The adhesion of the co/re-deposits to their substrates, indeed, can be weak, resulting in unwanted removal of the layers when facing the plasma and, consequently, the formation of **dust**, which is a critical aspect for machine operation and safety [36–38]. In addition, the usually unknown microstructure of co/re-deposits corresponds to unknown properties of the films, which, in turn, results in an unpredictable behavior of these layers when exposed to the plasma.

2.1.2 Thermal Effects

In addition to the particles flux, PFMs have to withstand extreme thermal loads during tokamak operations. For ITER, the divertor will be the most critical region of the FW, designed to operate, preserving its integrity, under steady and quasi-steady heat loads of about 10-20 MW m^{-2}. However, during off-normal events (i.e. plasma instabilities), power densities up to tens of GW m^{-2}, usually delivered within milliseconds, can be achieved. These extreme loads can have a severe impact on materials properties, leading to different thermal effects on the PFMs (see figure 2.4).
During ELMs, VDEs or disruptions, the surface temperature can rapidly increase, exceeding the recrystallization temperature of the material and thus leading to surface morphology and crystalline structure changes, that unavoidably result in local surface damage and change of PFMs properties. In addition, it is likely that, during the majority of plasma instabilities, surface temperature further increases and overcomes melting temperature. Predicting PFMs melting and understanding the melted layers motion are ones of the key issues

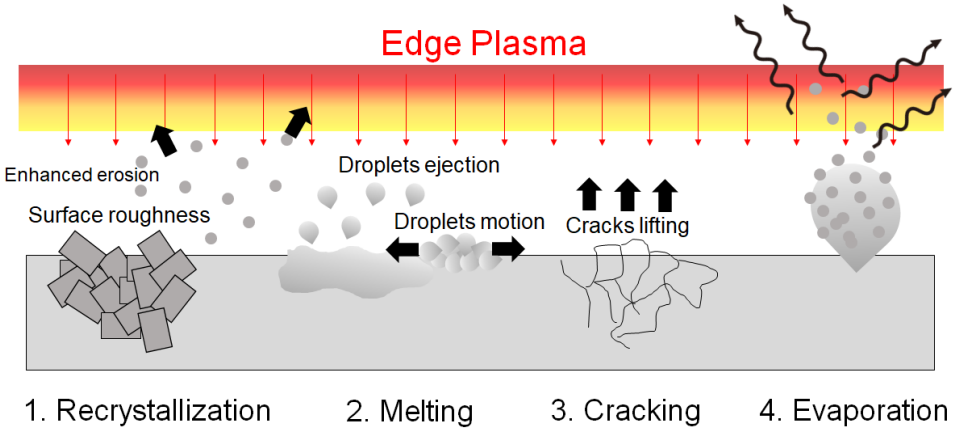

Figure 2.4: Schematic representation of different thermal effects on PFMs.

of recent R&D activities for ITER, especially for the divertor targets [39]. Divertor surface melting can lead to degradation of component lifetime and change of surface topology that may have a severe impact on plasma operation. The molten material can be either ejected from the surface in the form of droplets, that can eventually propagate, moving on the PFMs surface, or suddenly crystallize, forming new layers with different physical properties. In addition, the melt splashing can enhance the erosion of the material and the gaps between adjacent divertor blocks can be filled (i.e. *tiles bridging*), with consequent increasing electromagnetic forces (eddy current).

As ITER will be a pulsed-regime machine, every PFCs will be subjected to cycling thermal loads, with corresponding thermal fatigue effects. Thermal fatigue can result in the growth of a crack network, that, in turn, is strictly correlated to the degradation of material performances and to the formation of potential *leading edges*, that favour localized over-heating with enhanced erosion and melting. It has to be mentioned that cracks formation due to thermal fatigue is strictly correlated to the baseline temperature of the pristine PFMs (i.e. if above or below the ductile to brittle transition temperature (DBTT)).

Finally, if the heat load is such that the surface temperature overcomes the sublimation temperature, PFMs can be vaporized with a consequent severe dust formation that, enetering the core plasma, drastically increases radiative losses, undermining to the operational stability of the system. It must be remembered, as it will be discussed in the next chapters, that all these effects affect both pristine PFCs and co/re-deposited layers. In the latter case, the high induced thermal stresses can easily result in the complete delamination of the coatings, which, again, can drastically increase dust formation.

2.2 Suitable Materials for the First Wall

As it could be seen in the previous section, the PFMs are subjected to extreme conditions when facing the plasma. PWIs, indeed, can deeply affect the properties and the overall

functionality of the PFCs. The choice of suitable PFMs is thus crucial. The best PFM should show the following requirements:

- Low physical and chemical sputtering yields, in order to minimize erosion phenomena, that, in turn, correspond to lower plasma pollution contents and radiative power losses.
- Low nuclear fuel retention, so that problems concerning T inventory, sustainement and activation of FW materials can be minimized.
- Unique thermomechanical properties, i.e. high melting temperature, high thermal conductivity, high yield and ultimate strengths, in order to mitigate as much as possible all the thermal effects induced by the extreme thermal loads.
- High resistance to neutrons damage, so that low activation and formation of short-life products can be avoided.

Any known material can satisfy all these requirements at the same time. For this reason, the choice of PFMs is, up to now, a key topic for nuclear fusion research. Different solutions have been proposed and investigated in current day tokamaks, going from single element materials to multi-components and smart alloys designs. As a general rule of thumb, one can work with **low Z** materials (e.g. carbon (C)), to minimize plasma pollution, or with **high Z** materials (e.g. tungsten (W), molybdenum (Mo)), ensuring a low sputtering yield.
Among all the possible investigated solutions, **carbon** shows, in addition to the unique feature of low Z materials of minimized plasma pollutions, an excellent thermomechanical behavior, having no melting point, but showing a high sublimation temperature (i.e. 3915 K) and high thermal conductivity (i.e. 200 W m^{-1} K^{-1}). For these reasons, C, usually in the form of *carbon fiber composites* (CFC), has been widely exploited in past and present tokamaks (e.g. JET, ASDEX, TORE-SUPRA). However, its high chemical sputtering yield related to hydrogen isotopes bombardment, its affinity to form highly fuel enriched codeposits, its high fuel retention and irradiation induced deterioration of the thermomechanical properties severely limit its use in future fusion reactors as PFMs (e.g. only few designs of the divertor strike points tiles of ITER foresee CFC).
Beryllium is another fundamental low Z material, particularly interesting for its very low Z (i.e. Z = 4), its good thermal conductivity (i.e. 190 W m^{-1} K^{-1}), and, if compared to C PFMs, its lower fuel retention. In addition, due to its chemical affinity with O, it can be exploited as O getter. Unfortunately, its relatively low melting point (i.e. 1560 K) and its high toxicity set critical drawbacks to its use. A full blanket Be, made both by bulk Be limiters and Be coating on Inconel tiles has been tested during the ILW project at the tokamak JET [43, 44]. Thanks to these appealing properties, Be remains the reference design material for the entire blanket of ITER.
Finally, **tungsten** is a high Z metal (i.e. Z = 74) that shows the highest melting point among all metals (i.e. 3695 K), it has a good thermal conductivity (i.e. 174 W m^{-1} K^{-1}) and, if

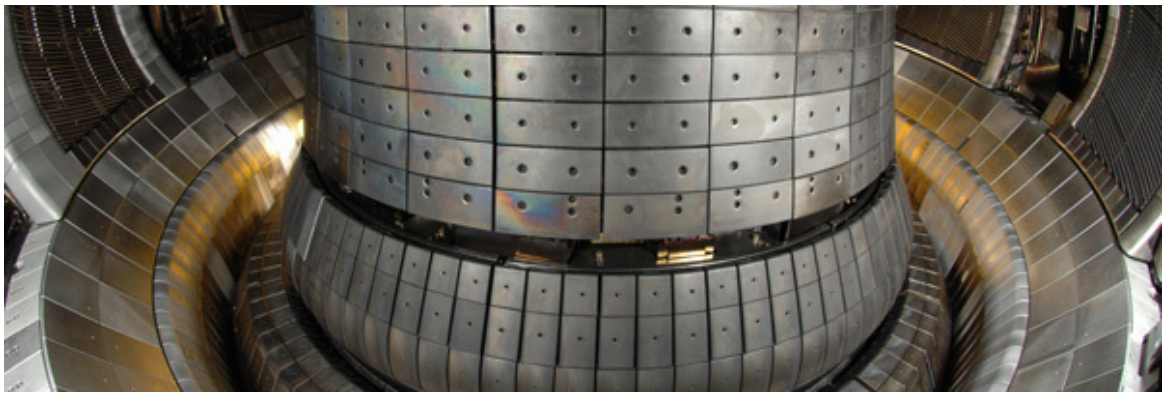

Figure 2.5: Internal view of the full W AUG Tokamak, equipped with the Div-III bulk W divertor. Image taken from [51]

compared to the above mentioned materials, it is of particular interest for its lowest sputtering yield and fuel retention (see figures 2.2, 2.3). For these reasons, W has been fully exploited in several tokamaks, for both only critical regions (i.e. divertor of JET-ILW) or the full machine (i.e. ASDEX-AUG). Its high Z, which is unavoidably related to large radiative losses due to plasma contamination, and its low DBTT (i.e. ≈ 400 °C), which results in unwanted fragile behavior at standard operating baseline temperatures, are the main drawbacks associated to its use as PFM. However, its benefits in limiting and mitigating the various thermal effects and surface erosion, consequently extending the PFC lifetime, made W the reference material for the divertor region of ITER, but also, up to now, for the whole FW of DEMO.
For this reason, W is taken as the material case of study of this thesis work. Its use in fusion research is presented in details in the next section.

2.3 Tungsten as Plasma Facing Material in Present-day Tokamaks

In current tokamaks experiments, W has been exploited as PFM both in the form of bulk and coatings. Here, some main R&D activities on W PFCs are summarized.
Even if the first attempts to use W based PFCs were proposed for the tokamaks JT-60 [46] and TEXTOR [47] at the beginning of the '90s, only in 1996 the first W based divertor was mounted in the medium size tokamak **ASDEX UpGrade** (AUG) [45]. With this upgrade, W coated graphite divertor tiles were mounted and tested under reactor relevant conditions, with the aim of investigating W erosion and deposition, as well as transport processes into the bulk plasma. The low sputtering yield, the negligible migration of W into the vessel and the almost negligible influence of the W divertor on the main plasma behavior encouraged the use of W PFCs for next experiments. For these reasons, in the 2007 campaign, all the CFC PFCs were covered by W coatings [48]. The thickness of W coatings was increased at maximum in order to accomodate the total expected erosion of several campaigns, but also limited to keep as low as possible the residual mechanical stresses associated to the

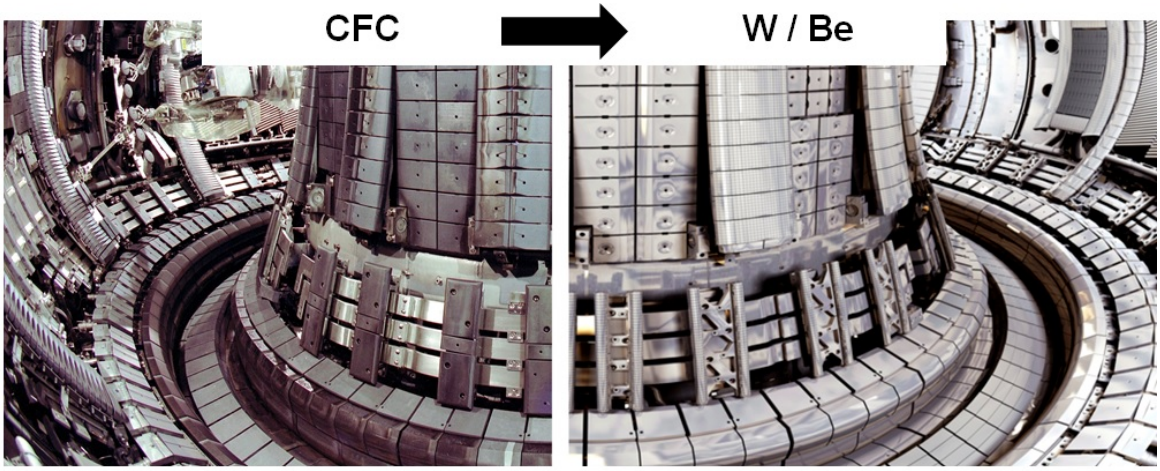

Figure 2.6: Internal view of the JET Tokamak, before (left) and after (right) the installation of the ILW. Image adapted from [52]

deposition process. Initially, the outer divertor region, where the highest erosion degree was previously observed, was covered by 200 μm W coatings. However, these thick coatings, delaminating after few plasma discharges, with consequent critical effects on plasma stability (i.e. disruptions), were replaced by thinner 10μm coatings. In the inner divertor, instead, 4 μm W coatings were exploited. In the first 2007 deposition campaigns, for the outer divertor thicker W coatings the *Vacuum Plasma Spray* (VPS) deposition technique was adopted, while *Physical Vapour Deposition* (PVD) techniques for the thinner coatings. *Magnetron sputtering* (MS) and *arc deposition* were successively tested [50]. The obtained results from coating, beside testing the effective capabilities of coated PFCs in tokamaks, helped in defining the best deposition procedure for future experimental campaigns. A further upgrade of AUG was obtained in 2013 by replacing the W coated divertor with a bulk W one (i.e. the Div-III divertor), non actively cooled, made by powder metallurgy W, in order to avoid coatings delamination and a frequent exchange of the targets plates with thin

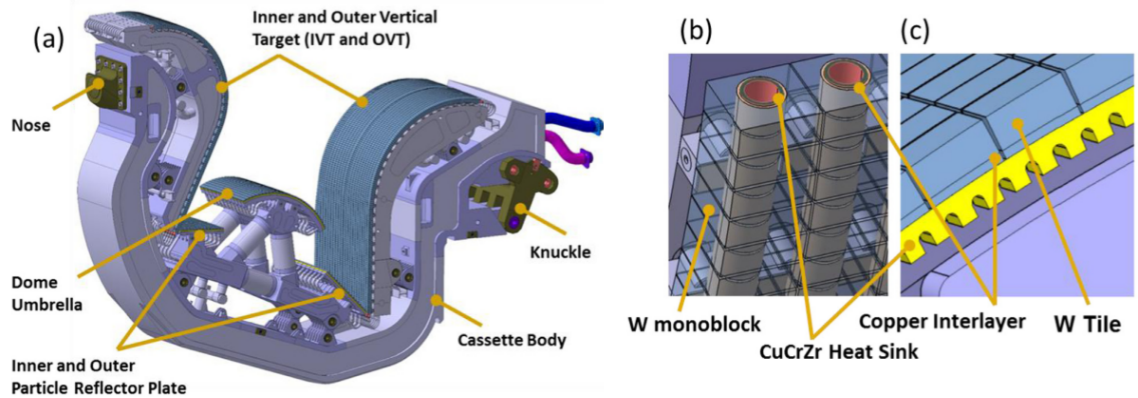

Figure 2.7: a) Schematic representation of ITER divertor. b) Monoblock geometry of the inner and outer vertical targets, c) flat tile geometry for the dome. Image adapted from [56]

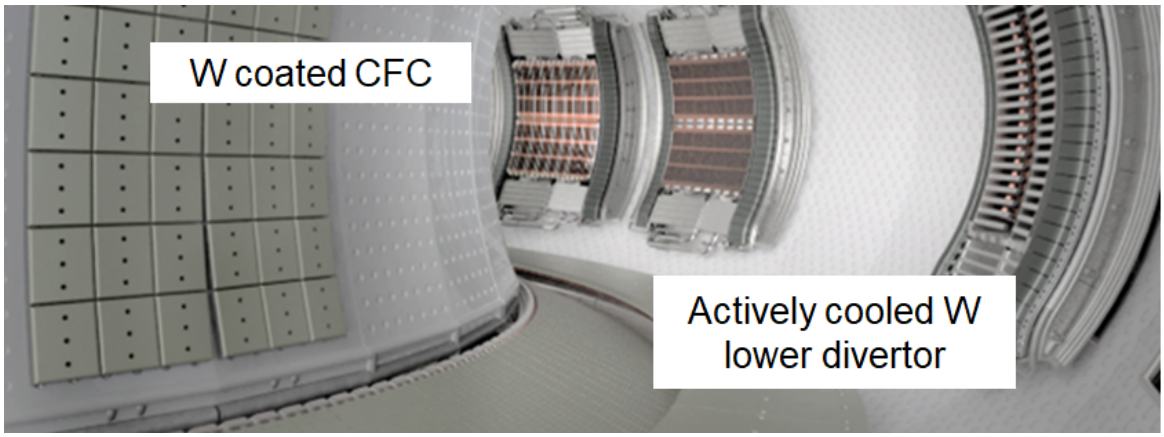

Figure 2.8: Internal view of the Tokamak WEST. Image adapted from [57]

coatings [49] (see figure 2.5). With Div-III, the full W AUG machine is finally able to prepare the physics of erosion and fuel retention with solid bulk tungsten under ITER-relevant scenarios.

Bulk and coated W PFCs have been widely investigated also within the framework of the **JET-ILW** project, started in 2011 [44]. In this experimental campaign at the large size tokamak JET, the initial CFC FW, was completely replaced by a full W divertor and a Be blanket, with the aim of investigating the PWIs effects on a W-Be mix similar to the one of ITER (figure 2.6). For the divertor, both bulk W (i.e. Load Bearing Spetum Replacement Plate) and W-coated CFC tiles, exploited also for other FW regions (e.g. limiters), were adopted. Taking advantage of the results obtained by AUG, W coatings on CFC tiles were deposited by VPS and *combined magnetron sputtering and ion implantation* (CMSII) methods, which, in particular, resulted in better coatings adhesion to substrates with respect to VPS, becoming the reference deposition technique for CFC coverage [53].

The results obtained during the JET-ILW and AUG campaigns, gave crucial insights for the final design and optimization of the **ITER** FW. In particular, the ITER divertor will be made by 54 cassettes assemblies, remotely handled, where each cassette includes one cassette body, and three PFCs, namely the inner and outer vertical targets and the divertor dome. The inner and vertical targets consist in actively cooled W monoblocks and they are exposed to the highest thermal loads, while the dome, made by W tiles, is subjected to lower heat fluxes [54, 55]. The schematic representation of the ITER divertor is shown in figure 2.7.

However, both AUG and JET-ILW show evident differences if compared to ITER operating conditions. As already mentioned in section 1.4.4, the quasi-steady state regime of ITER will deliver extremely high heat fluxes to the PFCs that can not be obtained in current tokamak experiments, such as AUG or JET-ILW, due to their conventional magnets exploited for plasma confinement. To support ITER divertor tests under ITER-relevant high heat fluxes, the superconducting tokamak **Tore Supra**, that started the **WEST** project in 2014,

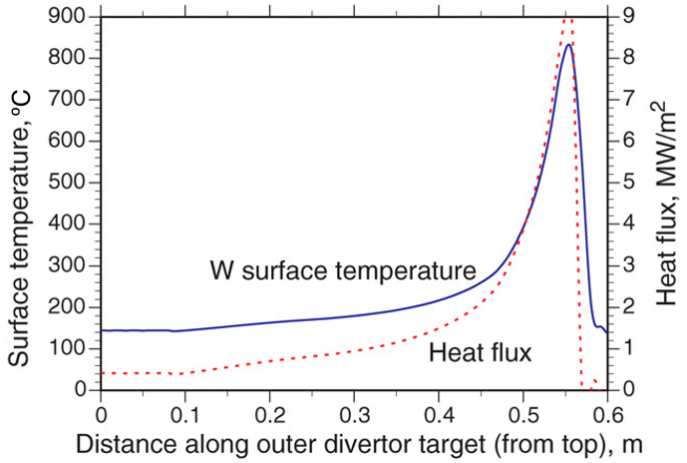

Figure 2.9: Temperature profile at the lower divertor as function of heat flux. Image taken from [59]

upgraded the original FW with an actively cooled ITER-like divertor and W coated CFC tiles [57] (see figure 2.8). First tests of the behavior of PFCs under ITER-like divertor relevant conditions have started in 2016. Finally, it must be mentioned the Divertor Tokamak Test Facility (DTT) machine, a medium size tokamak that will be realized in Italy within 2024 with the specific aim of testing, as in the case of WEST, ITER divertor and PFCs under ITER divertor-relevant conditions.

2.4 Plasma-Wall Interactions effects on W divertor

The W divertor described in the previous section is expected to work in ITER from day 1, from the non nuclear phase operation to the DT nuclear phase, when the milestone of $Q = 10$ will be achieved. However, W surface can be damaged by PWIs even in the non nuclear phase, so that its impact on power handling capability and lifetime of the divertor must be investigated. In particular, thermal and atomistic effects on W based PFCs at ITER-relevant conditions must be still completely understood. In this section, the main findings about PWIs effects on W based PFCs obtained in recent tokamak experiments are briefly summarized.

For what is concerning thermal effects, in steady state conditions, peaks power of 8 MW m^{-2} and 10 MW $^{-2}$ are expected at the divertor during the non-nuclear and nuclear phases respectively [39]. In the former case, surface temperature can reach $\approx$ 800 °C, while, for the latter case, it can increase up to $\approx$ 1100 °C [39] (see figure 2.9). In any case, the temperature remains below W recrystallization temperature (i.e. 1200 - 1400 °C), and no appreciable consequences on materials properties are expected. During slow-transient events (i.e. plasma reattachment), however, the peak power loads can reach even 20 MW m^{-2}, with a corresponding peak extimated temperature of $\approx$ 2000 °C, which obviously can have a non negligible impact on W properties [58]. Under these loading conditions, also taking into account multiple plasma discharges, **recrystallization**, progressive deformation,

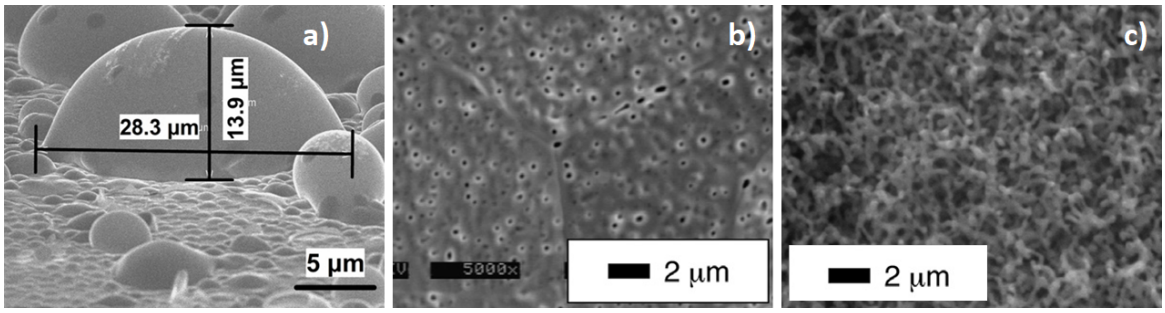

Figure 2.10: a) Blistering formation on W surface. Image taken from [73]. b) He bubbles. Image taken from [71]. c) Fuzzy W nanostructure. Image taken from [72]

creep damage and thermal fatigue can severely alter W surface, leading to the **formation of cracks** networks that affect the performance of PFCs [56].

During ELM-like cyclic pulsed loads, instead, thermal fatigue effects (i.e. surface roughening and cracking) and melting are likely found between 0.45 GW m^{-2} and 2 GW m^{-2} [60]. These effects result in an **enhanced surface erosion** and **dust** formation. This situation gets worst as the power load of plasma instabilities increases, when, for example, MD events take place. In this critical scenario, tens of GW m^{-2} are delivered, and W surface is completely **melted** or **vaporized** [39].

On the other hand, atomistic effects induced by particles bombardment can cause severe damage to W PFCs. For example, H, D, T and He bombardment results in surface **blistering** (see figure 2.10a). Blistering occurs under supersaturation conditions of H or He beneath the surface, as a net result of pressure increase. This induces micrometric swelling and surface deformation. As a consequence, cracks and protrusions with several shapes form [60]. Blistering on W happens when H or He atoms have a kinetic energy of tens of keV or more. In edge plasma condition, the energy of the impinging species is relatively low, and blistering is not usually directly induced by H bombardment, but it is indirectly associated to H implantation and diffusion when high temperatures are reached [62]. Conditions for W blistering are well known, being for temperatures between 25 - 600 °C and particles fluences $> 10^{24}$ m^{-2} [62, 63]. Several aspects can obviously affect blistering formation, enhancing (e.g. use of N or C plasma seeding) or suppressing it (e.g. use of He of Be plasma seeding). For more detailed information see [60].

Since the trapping energy of a single He atom in a W single vacancy is of the order of 4 eV [64], also He atoms can be implanted in W and strongly trapped at lattice defects. The progressive accumulation of He atoms at vacancies or grain boundaries results in the formation of nanometric **bubbles**. As W temperature increases, the bubbles can dffuse, can interconnect, forming pores, that travel up to the surface, exploding and releasing He gas atoms (figure 2.10b). Above 700 °C, He bubbles form large size clusters that diffuse and alter the surface, eventually forming **fuzzy W** nanostructure [65] (figure 2.10c). The threshold energy of He particles for fuzz formation has been assessed to $\approx$ 20 eV [65]. For

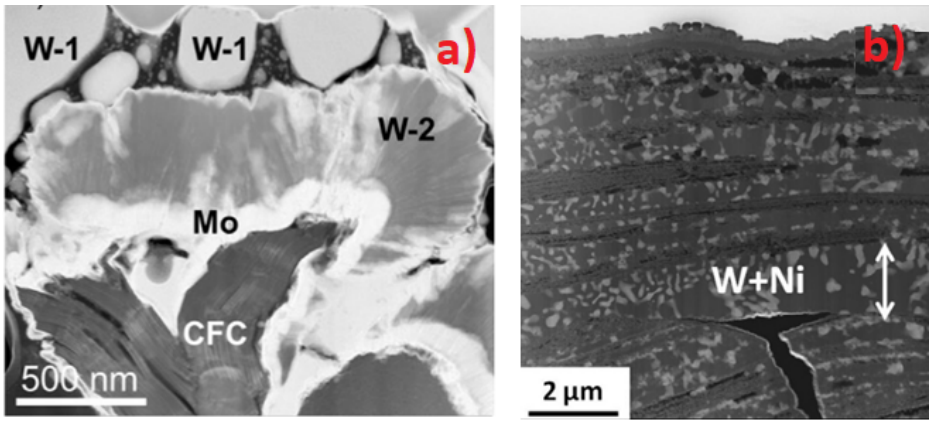

Figure 2.11: a) Structure and composition of W redeposit found in JET-ILW. W-1 and W-2 stand for amorphous and crystalline phases of W. Image taken from [66]. b) Thick multielemental porous coredeposit on tile 1 of JET-ILW. Image taken from [68].

detached plasma the ion bombardment energy is roughly 8 eV, so in the nuclear phase fuzzy W can be formed only in the plasma attached regions of the divertor, where peak paricle loads are expected [65]. When W recrystallization temperature is overcome, He holes start to appear at the W surface. In general, all these He nanostructures have a severe impact on W properties, usually inducing embrittlement and enhancing erosion and dust formation [60, 65].

W and FW PFMs erosion leads to the formation of **W based co/re-deposits** above PFCs. This process can be analyzed thanks to post-mortem surface analysis of present-day tokamaks PFMs surfaces. After the first JET-ILW experimental campaign distinct types of W based redeposits were found in the divertor region: (i) agglomerates of W and W-Be, (ii) multi-layered and multielemental deposits (i.e. W with C, Ni, Al, Si, B, N and O), and (iii) Be flakes, small spherical ball-like objects and thick Be-O-C layers at the top horizontal corner of the inner divertor [66]. All these layers can be very rich of nuclear fuel atoms. Generally, co/re-deposits in JET-ILW differ each other as function of the position they are found inside the machine and the operating condition exploited during the experiments. The presence of different elements is thus strictly correlated to the operation history. Moreover, it can be severely affected by the presence of plasma instabilities that, as already mentioned, enhances W erosion and redeposition [68]. The structure and the morphology of co-redeposits can be thus really complex. In particular, as shown in figure 2.11a, a coexistence of different W phases can be found in the redeposited layers (i.e. crystalline and amorphous phases). Figure 2.11b, instead, shows a highly porous mixed deposit found on divertor tiles during the second JET-ILW campaign [68]. In general, Be has been found with the highest concentration, highlighting its higher affinity to sputtering phenomena with respect to W. The collected layers on divertor tiles resulted in a good adhesion to the substrate. However, it is expected that when exposed to plasma, in particular to plasma instabilities, they eventually can delaminate, drastically increasing dust formation.

Similar JET-ILW redeposits were also found in AUG [67]. Here, W based coatings with different thicknesses (i.e. from few to hundreds of nm) were found containing B, C, Fe and O. The presence of B is explained by the pre-operation tokamak wall conditioning [69, 70]. Moreover, the presence of conglomerate materials, irregular dust particles, flakes and W droplets highlights the fact that the surface of the divertor tile suffers *arcing* activity. The arcs burn from the coating into the graphite substrates, splashing away W particles. This arcing activity is critical for W based PFMs and it must be taken into account also for ITER. Finally, it has to be mentioned that, during accident scenario, the formation of radioactive and volatile W oxide compounds can be achieved [30, 74]. In case of loss of coolant or air ingress W can be suddenly oxidated, and WO_3 compounds can form above the FW. W-oxide layers usually show a thermal conductivity several times lower than the one of pure W, so their presence can deeply affect the performances of W PFCs [74].

2.5 Laboratory scale investigation of fusion relevant W materials

The tokamak approach allows to investigate all thermal and atomistic effects at the same time in a fusion environment. However, it demands long experimental times (i.e. due to post mortem analysis of components), and the operating machines are hardly accessible. In addition, all the observed effects can severely differ from the ones that will be seen in ITER, since ITER operating conditions have never been achieved. These aspects consistently justify a laboratory scale approach, that, being complementa to the tokamak one, can help in the investigation of all the PWIs effects on PFCs. Following this approach, it is possible to mimic some ITER conditions and, eventually, to decouple the various atomistic and thermal effects. In addition, with respect to tokamak machines, lab-scale devices are more affordable in terms of machine time, they are more easily accessible and less expensive. The guideline of the lab-scale research activity is thus based on: (i) the study of the synergetic effects of heat and particle loads, or (ii) the study of decoupled heat or particles loads effects.

This thesis focuses on nanostructured coatings and their thermomechanical behavior under fusion-relevant thermal loads. For this reason, in section 2.5.1, the main experimental devices exploited for mimicking at the lab-scale ITER-relevant thermal loads, and the main results obtained on W are briefly summarized. Suitable deposition techniques can be opportunely exploited to obtain coatings that can mimic co-redeposits in tokamaks. In this framework, in section 2.5.2 the production of nanostructured coatings by Pulsed Laser Deposition (PLD) is thus briefly presented. Thanks to the versatility of this lab-scale deposition technique, the coating properties (i.e. structure, morphology and composition) can be finely tuned during deposition in order to opportunely mimic different tokamak coating scenarios.

2.5.1 Lab-scale devices for fusion-relevant high heat fluxes tests on W materials

Generally, lab-scale facilities can be distinguished in function of the induced effects on target materials. In this sense, it is possible to classify different machines in terms of: (i) neutron irradiation effects, (ii) particles (i.e. ions and neutrals) loads effects, (iii) thermal loads effects and (iv) combined particles and thermal loads effects.
Focusing only on aspect (iii), at the present state of the art, two are the main strategies to investigate the thermal effects alone on PFMs, namely **electron beams** and **lasers**. These techniques do not induce any radiation damage to the material (no dpa), favouring only a heat transfer process. Heat loads can be induced also by **plasma generators**, **neutral particles** or **ion beams** (e.g. QSPA, PSI-2 and GLADIS [75,76]). However, these facilities, relying on energetic massive particles, can not completely decouple thermal and atomistic effects.
An useful parameter, particularly suitable at the laboratory scale to describe the thermal effects thresholds of various PFMs is the *heat flux factor* (HFF) [40], defined as:

$$HFF = P_{absorbed}\sqrt{\Delta t} \tag{2.1}$$

where $P_{absorbed}$ is the power density absorbed by the material and Δt is the characteristic time of the excitation. Thanks to the definition of HFF, different sources with different characteristic times can be exploited for mimicking the high thermal loads expected on PFCs during quasi stationary and transient conditions. Various thresholds for thermal effects can be then compared in terms of HFF. This is a crucial aspect for this thesis work and it will remembered in chapter 3 and chapter 5. It is fundamental to highlight that the HFF emerges from the energy balance equation of an irradiated surface. In particular, if the classical heat diffusion equation is valid to describe the heat transfer process, the HFF is a consistent parameter to compare different thermal effects induced by different irradiation sources, forgetting about the type of irradiation (i.e. heavy ions, electrons, photons). Classical HFF for different transient events can go from few to several tens of MW m^{-2} $s^{0.5}$ [41]. The most extreme scenario estimated for ITER regards the thermal quench of a 350 MJ thermal energy burning plasma during an unmitigated major disruption (MD) on the inner divertor region, which can deliver an energy between 87.5 and 175 MJ, with a corresponding HFF in the range 105 - 1984 MW m^{-2} $s^{0.5}$ [39].

Electron beams suited best to simulate thermal loads in the sub-millisecond regime with ITER relevant energy densities [41]. In this framework, the JUDITH 1 and JUDITH 2 facilities at FZJ have been widely exploited in the recent years to test W PFCs behavior under GW m^{-2} thermal loads. The schematic representation of the JUDITH 2 machine is presented in figure 2.12. With this electron beam test facility, power densities up to 10 GW m^{-2} can be reached, with the possibility to span a wide range of HFFs (from few to hundreds of MW m^{-2} $s^{0.5}$) [78]. In addition to JUDITH 1 and 2, several other electron beams

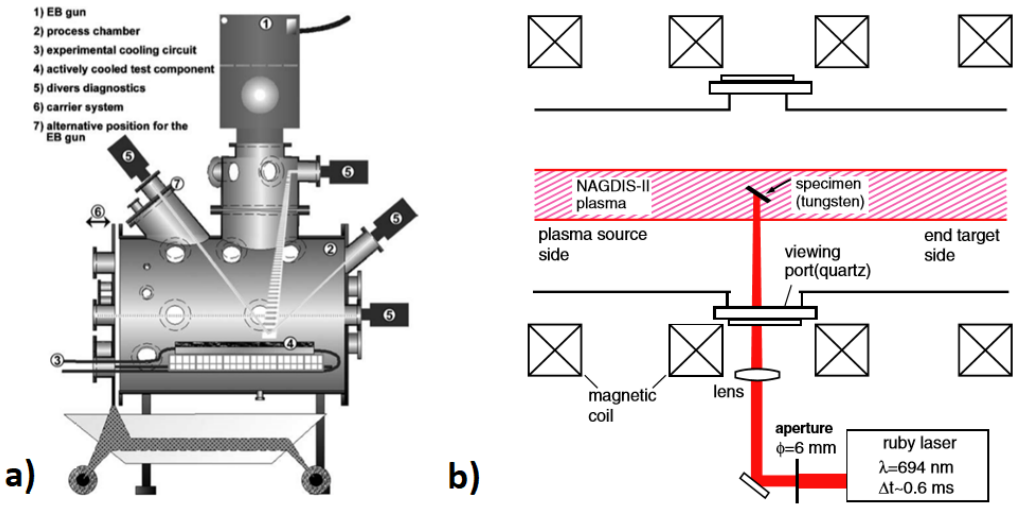

Figure 2.12: a) Schematic of the JUDITH 2 electron beam test facility. Image taken from [77]. b) Schematic of NAGDIS-II divertor simulator equipped with a sub-millisecond laser. Image taken from [81].

facilities are exploited to this purpose: *FE 200* (CEA, EU) with 60 GW m^{-2}, *JEBIS* (JAEA, Japan) with 2 GW m^{-2} and *EB 1200* (SNLA, USA) with 10 GW m^{-2}.
Electron beams are advantageous with respect to other high heat fluxes testing machines (e.g. ion beams) since they deliver very defined thermal loads without inducing any dpa, with high power densities and high number of cycles. However, high voltage electrons can deeply penetrate inside the material, promoting bulk heating effects, that usually do not correspond to the radiation heating effects of the hot plasma of fusion devices. To better confine to the surface the energy deposition, usually **long pulse lasers** are adopted [81, 83]. To this purpose standalone, or implemeneted in plasma generators (e.g. PSI-2, NAGDIS-II), millisecond and sub-millisecond lasers (e.g. Nd:YAG, Ruby lasers) are exploited. For example, the schematic of the linear plasma machine NAGDIS-II, equipped with a sub-millisecond Ruby laser is reported in figure 2.12b. Also with millisecond lasers, the span of a wide range of HFFs is guaranteed. The main drawback associated with the use of lasers is the eventual laser enhanced materials damaging that, in the case of metals, for which the laser energy is commonly absorbed in few tens of nanometers, can induce high surface roughening, with a consequent decrease of damage thresholds with respect to e-beams.
Thanks to these facilities, several W materials, both in the bulk and the coating form, have been tested in order to detect the damage thresholds for the various thermal effects (i.e. melting, recrystallization, cracking and delamination). In particular, *Pintsuk* et al. in [42], irradiating different W grades target materials at JUDITH by 5 ms e-beam under single shot at room temperature, found a threshold for cracking of 23 MW m^{-2} $s^{0.5}$ for coarse-grained samples, and 39 MW m^{-2} $s^{0.5}$ for fine-grained W. *Linke* et al. [41, 78], investigating the thermomechanical response of different bulk W samples, as well as of 25 μm thick CMSII W coated CFC targets to a high number of e-beam pulses (up to 1000) at different baseline temperatures, found that the damage thresholds for W coatings, being severely affected by

the substrate material, were always lower than the ones of bulk W. In particular, at HFF = 7.5 MW m^{-2} $s^{0.5}$ the coatings were already melted and almost completely delaminated, while bulk W could easily withstand e-beam pulses with no irreversible surface damage until 20 MW m^{-2} $s^{0.5}$. Moreover, baseline temperature of 500 °C of ITER-grade W resulted in no damage for HFF < 10 MW m^{-2} $s^{0.5}$, melting of edges between 20 and 40 MW m^{-2} $s^{0.5}$, complete surface melting from 45 to 60 MW m^{-2} $s^{0.5}$ and for HFF > 60 MW m^{-2} $s^{0.5}$ droplets ejection and tile bridging. Finally, *Suslova et al.* [83], irradiating by a 1 ms Nd:YAG laser (λ = 1064 nm, f = 1 Hz, 500 shots) two different microstructured W samples, namely ultrafine-grained (i.e. grain size between 100 and 500 nm) and nanocrystalline (grain size below 100 nm), found that ultrafine-grained samples recrystallize at 24.7 MW m^{-2} $s^{0.5}$, in contrast to 15.4 MW m^{-2} $s^{0.5}$ for nanocrystalline ones. In both cases, melting occured above 36.3 MW m^{-2} $s^{0.5}$.

As it can be seen, even if similar thresholds are found for W under electron beams and millisecond lasers, unique damage thresholds do not exhist, being strictly correlated to the irradiation conditions (e.g. baseline temperature, single or multishots) and on materials properties (e.g. composition, micro/nanostructure). However, all these results are mandatory to assess limits to the behavior of W under high heat fluxes.

In this thesis, alternatively to millisecond lasers and electron beams, a more compact, costless and more easily accessible at the lab-scale **nanosecond laser** is exploited for the investigation of bulk W and W coatings behaviors under fusion-relevant thermal loads. This type of study is the first of its kind, so the use and the validation of nanosecond laser for high heat fluxes tests in ITER-relevant conditions are carefully described in chapter 3. It has to be mentioned that nanosecond lasers have been gaining much more interest through recent years for fusion relevant applications. In particular, they have been already adopted for *Laser Induced Breakdown Spectroscopy*, T desorption of the first wall and laser cleaning of diagnostic mirrors [79, 80], and for investigating the behavior of He bubbles in plasma exposed W [130]. Recently, they have been also exploited for testing bulk W materials under extreme thermal loads [84]. However, the experimental investigation reported by *Farid et al.* in [84] is performed in the ablation regime and it does not explicitly consider the effect of different HFFs on W, making it difficult to compare with thermal effects induced by other irradiation techniques. It must be remembered that, in this case, the pulse duration is several times lower than the characteristic times of plasma instabilities. For this reason, trying to irradiate samples with the same energy fluence of classic ITER relevant thermal loads, as it happens in the cases of e-beams and millisecond lasers, results in extremely high power densities, with obviously non representative consequent thermal effects on the materials.

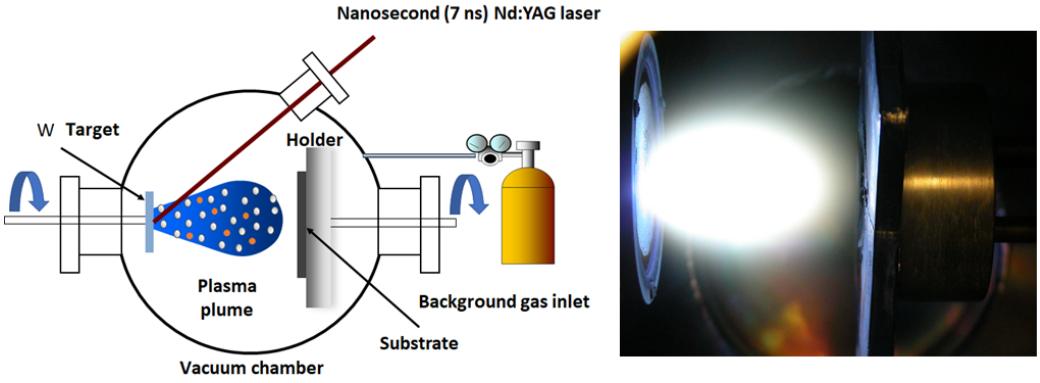

Figure 2.13: a) Schematic representation of the PLD system at NanoLab. b) Photography of a plasma plume expanding to the substrate.

2.5.2 Mimicking at the lab scale of different coating scenarios in tokamaks: Pulsed Laser Deposition

As discussed in section 2.4, the co/re-deposition process of W in a tokamak is a really complex phenomenon, since different types of co/re-deposits, with different morphologies, structures and compositions can be found in different machines, or in the same machine but in different regions. In addition, the study of these layers is not trivial, since only at the end of each experimental campaign the tokamak chamber can be opened and the layers can be collected and studied. For these reasons the lab-scale investigation of possible W co/re-deposits is crucial to support tokamaks data, but also to mimic the possible co/re-deposited layers expected for ITER. To this purpose suitable deposition techniques can be exploited to deposit coatings with different morphologies, structures and elemental composition that can mimic the ones of W co/re-deposits. In this framework, **PVD** deposition techniques are usually adopted [85–87].

Among the various PVD techniques, **Pulsed Laser Deposition** (PLD) has proven to be highly versatile in tailoring the structure and the morphology of single element or compounds coatings down to the nanoscale [88]. In this thesis work, fusion relevant nanostructured coatings deposited by PLD are characterized. All the analyzed coatings were deposited during a previous Ph.D activity [89]. For this reason, only a brief description of the PLD system and the production of the analyzed coatings is presented here and summarized in chapter 4. For further details about the deposition parameters see [88, 89]. The experimental setup is also reported in Appendix B.

In a PLD device, the materials that have to be deposited are vaporised by means of an intense pulsed laser. The laser induced ablation of the target materials produces a weakly ionized plasma plume, which contains the ablated particles, that expands inside a chamber. Through the plasma plume expansion dynamic, the particles can be collected onto a proper substrate, finally forming the coating. A schematic representation of the PLD system present at the NanoLab (Politecnico di Milano) is shown in figure 2.13. As it can be seen,

a Q-switched Nd:YAG laser (Neodymium-doped Yttrium Aluminum Garnet) Continuum Powerlite II 8010, with a pulse duration (FWHM) (τ_P) of 7 ns, maximum repetition rate of 10 Hz, maximum energy per pulse of 1.8 J at its fundamental harmonic (i.e. λ = 1064 nm), enters in a vacuum chamber and strikes at 45° the target surface. The deposition process can be performed in vacuum, i.e. 10^{-4} Pa guaranteed by a pumping system made by a primary scroll and a turbo-molecular pumps, or either in presence of a background gas, whose pressure is tuned by a PID controller that regulates the gas mass flow. The background gas can be both chemically inert, such as He or Ar, or reactive, like H_2, N_2 and O_2. Both the target and the substrate holder are remotely controlled by an ad-hoc dedicated software, and combining the holder shift and rotation it is possible to guarantee deposits planarity over areas of cm^2.

The presence of a background gas during deposition strongly affects the shape and the expansion dynamic of the plasma plume. Basically, through collision processes, the ablated particles transfer part of their energy to the atoms of the gas, slowing down, and reaching the substrate with a lower energy. The higher the background gas pressure, the lower will be the energy of the particles impinging on the substrate. As a consequence, the coating growth process is severely affected by the plasma plume behavior. In this sense, till the background pressure is sufficiently low, so that no plume confinement is obtained, the ablated particles are sufficiently energetic to favour an *atom-by-atom* growth mechanism, which in turn results in **compact films**. On the contrary, as the background pressure increases, the plume is more confined, and the species less energetic, enhancing *clusters formation*, so the growth of hierarchical or **porous coatings**. In addition, multielemental targets can be exploited to deposit compounds coatings, while reactive gases, in particular N and O, to promote chemical reactions and form nitrides or oxide layers. Finally, it is fundamental to remember that coating properties depend also on laser parameters, such as laser wavelength or laser fluence on target (i.e. the higher the fluence, the higher the ablation rate and the kinetic energy, but also the emission of particulate), as well as they are strictly correlated to other process parameters, e.g. target-to-substrate distance, substrate temperature and chemical composition.

From the main results coming from the various experimental campaigns at JET-ILW and AUG, which are summarized in section 2.4, the co/re-deposited layers show different morphologies, from compact to porous, different structures, from nanocrystalline to amorphous, and various elemental compositions, being rich of FW materials, with the addition of fuel atoms and gas impurities (e.g. O, N and B). By taking advantage of the high PLD versatility, various coatings can be deposited, mimicking these various co/re-deposits properties. In particular, the samples analyzed in this thesis divide into four classes:

Metallic W samples, obtained by the ablation of W targets in vacuum condition or in presence of an inert background gas (i.e. Ar and He) with various pressures.

W-oxide coatings, deposited in an oxygen atmosphere with various pressures, with a net

result of different oxygen concentrations.
W-nitrides coatings, deposited with nitrogen as background gas with various pressures, with a net result of different nitrogen concentrations.
Metallic B samples, obtained by the ablation of a B target in vacuum conditions.
As already proposed in past works [87,89,90], these coatings have been qualified as suitable to mimic W based coatings in tokamaks, they have been already tested in terms of D retention and electrical properties, and exposed to linear plasmas (i.e. PSI-2, MAGNUM-PSI and PILOT-PSI). In particular, these different coatings can represent different W coatings scenarios in tokamaks:
Metallic nanocrystalline columnar (c-W) coatings as proxy of W coatings on CFC tiles, as the ones deposited by VPS or CMSII for JET-ILW [91].
Metallic compact amorphous-like (a-W) and porous (p-W) coatings as proxy of promptly redeposited W layers onto PFCs.
Amorphous W-oxide (a-WO) and amorphous W-nitride (a-WN) coatings for mimicking the codeposition of W with gas impurities present in tokamaks as a consequence of gas puffing (i.e. N_2) or accident scenarios (i.e. O_2).
Metallic amorphous B coatings of particular interest for FW conditioning of tokamaks.

This thesis work focuses on the thermomechanical characterization of this wide set of coatings. In the next section, the specific goals of the thesis are highlighted.

2.6 Specific goals of the thesis

As highlighted in the previous sections, the complexity of a nuclear fusion system constantly requires a substantial laboratory scale investigation in order to provide supporting information about the possible behaviors of PFMs in ITER. In particular, one of the most crucial aspects is the assessment of the properties of co/re-deposited layers in tokamaks and their behavior under extreme thermal loads. Following an advanced materials science approach, the main aim of this doctoral thesis is to investigate the thermomechanical properties of fusion relevant nanostructured coatings, that, in particular, mimic different coating scenarios in tokamaks. This investigation is performed both experimentally and numerically. This macro-objective can be divided, in turn, into three main tasks:
1) Development of thermomechanical investigation methods for nanostructured coatings. This first task consists of two main aspects. Firtly, since the thermomechanical properties of coatings are strictly correlated to its specific structure, morphology and composition it is mandatory to have suitable characterization techniques sensitive to these features. A crucial part of this thesis is thus devoted to the realization and optimization of a new experimental setup for the thermomechanical characterization of nanostructured coatings, which relies on the combined use of Brillouin spectroscopy and a new ad-hoc setup for substrate curvature measurements. Thanks to this system, a non-destructive thermomechanical

characterization of elastic moduli, coefficient of thermal expansion, residual and thermal stresses can be achieved. Secondly, the coatings must be tested under ITER-relevant thermal loads. To this purpose, nanosecond laser irradiation is adopted, for the first time, to mimic thermal effects on various nanostructured coatings under fusion-relevant scenarios. In addition, a numerical code for nanosecond laser-matter interaction is developed for the prediction of the thermomechanical behavior of nanostructured coatings under these pulsed loads and for relevant tokamak scenarios. This first task is presented in chapter 3.

2) Characterization of the thermomechanical properties of as-deposited nanostructured coatings: thanks to the developed method, various nanostructured coatings are characterized. As described in the previous section, the target samples are fusion relevant coatings, deposited by PLD, that mimic different coating scenarios in tokamaks. The characterization is performed exploiting the new experimental setup, as well as other morphological and structural characterization techniques (e.g. SEM, Raman spectroscopy, AFM, XRD), with the aim of deeply investigating the correlation between structure, morphology, composition and the thermomechanical properties of the coatings. All the thermomechanical properties derived for as-deposited coatings are discussed in chapter 4.

3) Exposure of the as-deposited coatings to fusion relevant thermal loads: this last stage consists in the investigation of the thermomechanical response of the coatings to ITER-relevant thermal loads conditions. The coatings are thus subjected to standard thermal annealing processes at ITER-relevant steady operating temperatures and to nanosecond laser irradiation. In the first case, the crystallization behavior and the total stress evolution are monitored during *slow* thermal treatments (i.e. the temperature is kept fixed for 2 hours) and *fast* thermal treatments (i.e. temperature ramps of 50 K min^{-1}). In the latter caser, instead, the aim is devoted to the determination of the damage thresholds of different thermal effects (i.e. melting, cracking, recrystallization and delamination) as function of the specific coating properties and nanosecond irradiation conditions (i.e. single and multishots irradiation), in order to assess the unknown behavior of coatings under extreme thermal loads, mimicking the effects induced by plasma transient heat fluxes in ITER-relevant scenarios. The developed numerical code is thus applied to predict these thresholds and preliminarly extended to realistic tokamak scenarios. All these results are contained in chapter 5.

These tasks have been done entirely at the Micro-and Nanostructured Materials Lab (NanoLab) of the Politecnico di Milano. I directly developed all the numerical codes, the experimental setup and performed all the samples characterizations (except for XRD analysis). Part of the results obtained in sections 3.1 and 3.2 are syntetically published in peer reviewed papers, namely on *Besozzi et al. 2016* [92] and on *Besozzi et al. 2018* [93]. The results of chapter 4 are published in [92, 93] and in *Dellasega et al. 2017* [94], for which I directly contributed to the Brillouin measurements of B coatings. Laser irradiation results, instead, are published in *Besozzi et al.* [95].

CHAPTER 3

Development of the thermomechanical investigation method for nanostructured coatings

As already discussed in chapter 2, the thermomechanical properties of coatings can substantially differ from the ones of the corresponding bulk form, being deeply affected by the specific structure, morphology and composition. For this reason, suitable characterization techniques, sensitive to these properties variation must be exploited. The developed investigation scheme is based on the combined use of Brillouin spectroscopy and the substrate curvature method, whose data are supported by other characterization techniques (e.g. SEM, XRD, Raman). While Brillouin spectroscopy is a well established technique at NanoLab, a completely new experimental apparatus for the substrate curvature measurements is built. Moreover, when dealing with metallic coatings, it is likely that the information coming from Brillouin spectroscopy are very limited, and suitable procedures should be applied to opportunely treat the experimental data. Therefore, in section 3.1, an optimized procedure that has been developed in this thesis for deriving the elastic moduli from Brillouin spectroscopy measurements of metallic coatings is presented. In section 3.2, instead, the design, realization, validation and optimization of the experimental setup based on the optical implementation of the substrate curvature method are carefully described. Moreover, nanosecond laser irradiation is exploited for the investigation of the thermal effects thresholds of the various nanostructured coatings under fusion-relevant transient thermal loads conditions. Since this study is the first of its kind, in section 3.3, the use of nanosecond laser for mimicking ITER-relevant thermal effects is described and opportunely validated. Finally, in section 3.3, a 2D numerical code developed for the computation of the temperature and the stress profiles during nanosecond irradiations, as well as for the predictions of the various thresholds for nanostrcutured coatings is presented and validated.

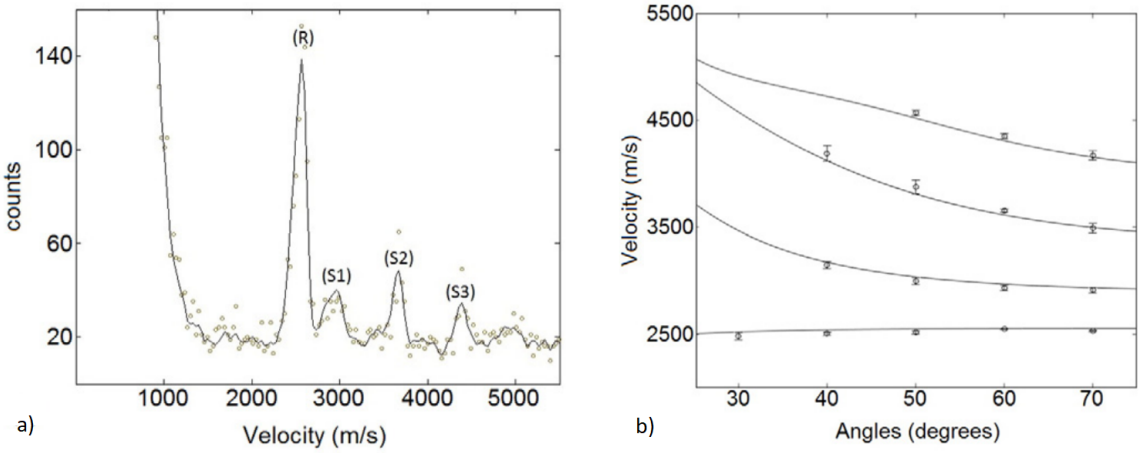

Figure 3.1: a) Typical Brillouin spectrum of opaque metallic W film on Si(100) substrate. Different SAWs are visible (R and S modes). b) Experimental and computed dispersion relation for a W coating. The dots represent the experimental phase velocities while the lines are the theoretical dispersion relations.

3.1 Elastic properties derivation from Brillouin spectroscopy

Brillouin spectroscopy (BS) is a powerful versatile technique to measure non destructively the elastic properties of films. To this purpose, it has been extensively exploited in the last years for both opaque and transparent media [97–100]. BS relies on the inelastic scattering (i.e. *Brillouin scattering*) between an incident laser photon and low frequency phonons of the material (i.e. acoustic phonons). In the case of transparent systems bulk acoustic waves can also be measured, but in the case of metallic films only surface acoustic waves (SAWs) are detectable. It thus measures the dispersion relations of the acoustic waves of the film-substrate system; from them, for known substrate properties, it is possible to derive the elastic constants of the film. More details about the physics that governs Brillouin scattering can be found in appendix B.

When bulk waves can not be detected, such as in the case of metallic films, a suitable procedure for extracting information about the elastic properties of the coating from the observed SAWs have to be implemented. To this purpose, an optimized procedure is developed in this work. This procedure is based on a numerical computation, which, in turn, relies on statistical considerations. For its description, let us consider, for instance, a typical Brillouin spectrum obtained for a metallic W coating on Si(100) substrate, as the one reported in figure 3.1a. The spectrum is plotted as a function of the measured acoustic waves velocity $v_m = \omega/k_{\|}$, where $k_{\|}$ is the exchanged wavevector determined by the incidence angle of the laser onto the sample. ω is the circular frequency measured by the spectrometer. Several branches of the dispersion relation can be measured (i.e. the peaks present in the spectrum). Due to the metallic opaque nature of the film, all the observed modes are surface acoustic waves. In particular, the lowest velocity branch is the Rayleigh wave (R), modified by the film itself, and the other branches are due to Sezawa waves (S). These modes are associated

to elastic waves that travel parallel to the surface, with an associated displacement field that can be considered exponentially decreasing with depth, such that it can be treated as completely confined to a penetration depth of the order of the probed mode wavelength. In the case of isotropic solids, R waves can cause the surface particles to move with elliptical trajectories in planes normal to the surface and parallel to the direction of propagation. The associated speed is slightly lower than the shear speed (v_T) of the material, being approximated by [96]:

$$\frac{v_R}{v_T} \approx \frac{0.862 + 1.14\nu}{1 + \nu} \tag{3.1}$$

where ν is the Poisson's ratio (v_R for metals is $\approx 90\%\ v_T$). When dealing with supported film, the displacement field associated to acoustic waves can eventually interact with the substrate. This is much more evident for coatings with thicknesses of the order of waves wavelenght. As a result of this coupling process, S modes can be detected. These guided modes are generally faster than R and shear waves. For film thicknesses higher than μm, these modes mix up with the continuum of bulk modes and can be no more detected. Both R and S waves can be differently affected by the choice of the substrate material (that, in turn, define a certain acoustic impedance). The case of W coatings on Si substrate, for instance, is classical example of *slow films on fast substrates*, where the R mode is always slower than the shear mode of the substrate. On the contrary, for *fast films on slow substrates* (e.g. Boron films on Si) this is not true, and the R mode can radiate its energy into the substrate. Both in the case of fast films on slow substrates and viceversa, the velocity of SAWs are strictly correlated to the elastic properties of the material (i.e. the elastic constants C_{ij} of the stiffness tensor C_{ijkl}). For this reason, the dispersion relations of these waves can be opportunely investigated in order to derive these properties. In this thesis, by collecting Brillouin spectra at different laser incidence angles, so at different $k_\parallel$, experimental dispersion relations $v_m(k_\parallel, j)$ of different SAWs, where j is the branch index, are obtained. At the same time, also numerical dispersion relations for the coating-substrate system can be computed, by solving the Christoffel's saecular equations, which governs modes propagation, as a function of different materials parameters, such as the mass densities of the film and the substrate (ρ^f and ρ^s), the elastic constants of the film and the substrate (C^f_{ij} and C^s_{ij}), the film thickness t and the exchanged wavevector $k_\parallel$: $v_c = v_c(\rho_s, C^s_{ij}, \rho^f, C^f_{ij}, t|k_\parallel, j)$ (see figure 3.1b). The coating properties can be thus identified by minimizing the least square estimator between the experimental and the computed numerical dispersion relations:

$$LS(C^f_{ij}, \rho^f) = \sum_{j,k_\parallel} \frac{[v_c(C^f_{ij}, \rho^f|j, k_\parallel) - v_m(j, k_\parallel)]^2}{\sigma^2(j, k_\parallel)} \tag{3.2}$$

where $\sigma^2(j, k_\parallel)$ is the uncertainty associated to each value of v_m. This minimization is performed by a MATLAB code. The number of independent free parameters depends on the symmetry of the elastic continuum which represents the film and that is taken into account

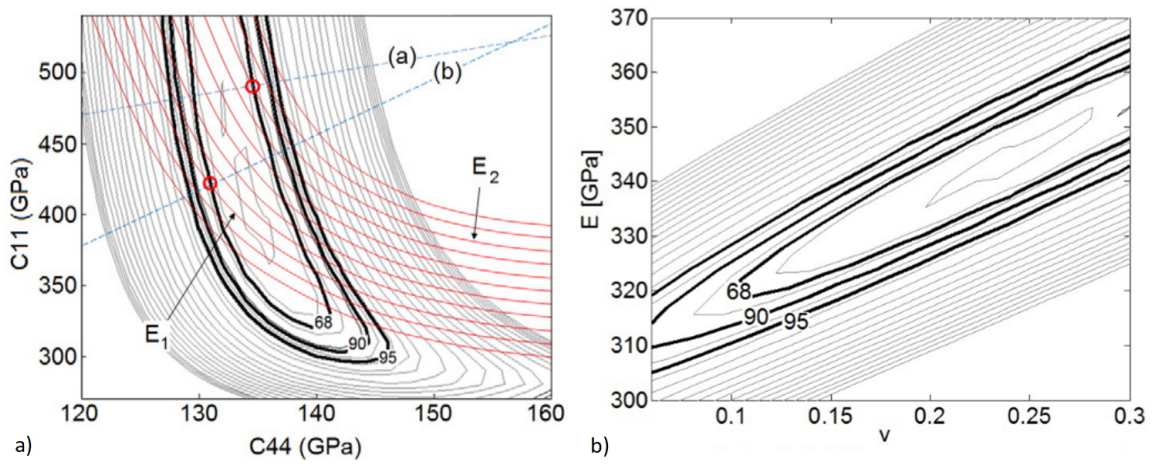

Figure 3.2: a) Isolevel curves for the LS estimator; the curves corresponding to the 68%, 90% and 95% confidence regions are highlighted by the bold black lines. The lines (a) and (b) refer respectively to (K_{bulk}) and (G/K_{bulk}). In red: isolevel curves for E. b) Conversion map of the isolevel curves of (C_{11}^f, C_{44}^f) plane into the (E, ν) plane.

for the computation of v_c. The simplest model is the isotropic one, which is fully characterized by two independent elastic constants, taken as C_{11}^f and C_{44}^f. If the mass density ρ^f is kept fixed (i.e. it is previously known), the minimization of equation 3.2 returns the map of the isolevel curves of the estimator LS (figure 3.2a). The minimum of the LS estimator identifies the most probable value of the (C_{11}^f ,C_{44}^f) couple. Alternatively, if also ρ is considered as a free parameter, this procedure returns a set of isolevel curves for each value of ρ. It is now evident that the mass density is one of the most critical parameter for Brillouin data analysis. As it will be discussed in the next chapters, ρ is not always known for all the coatings investigated in this thesis. In some cases, when Brillouin signal is particularly vivid (i.e. multiple SAWs are detected), this numerical procedure can be exploited to opportunely estimate ρ directly from the detection of acoustic modes. In other cases, however, in particular for thick coatings where only one SAW is detectable, if the value of ρ is not *a priori* known, only guess values can be considered.

The outcomes of the LS minimization must be, in turn, opportunely treated. To this purpose, the method developed in this thesis considers the fact that the isolevel curves (or surfaces) of the estimator, at levels determined by estimation theory, supply the confidence regions at any predetermined confidence level. The confidence region at any confidence level α is determined following the Fisher-Snedecor statistics as the isolevel curve of the normalized estimator at a value which is identified as function of (i) the number of independent parameters to be estimated (in this case two), (ii) the number of available points of the dispersion relations (the number of measured spectral peaks), and (iii) the confidence level [101]. The confidence regions turn out to be the most robust result of the minimization, the minimum being more sensitive to experimental and discretization errors. In both the Rayleigh and the Sezawa waves the shear component prevails; consequently, the confidence region supplies

a good estimate (a narrow interval) for the shear modulus $G = C_{44}^f$, and a poor estimate (an unreasonably wide interval) of the C_{11}. The indication coming from the confidence region is therefore supplemented by two physical bounds, set by the stiffness of the bulk crystalline corresponding material (in this case W). It is assumed that the bulk modulus K cannot exceed the relative crystalline value, and that also the ratio of the shape stiffness to the volume stiffness, G/K, cannot exceed the corresponding crystalline limit. The ratio G/K is directly related to the Poisson's ratio ν, such that the upper bound for G/K is a lower bound for ν [102]. It must be remembered that the (G/K) ratio can be seen as an index of the ductility of the material. The 68% confidence region is considered; its parts which exceed one of the two limits are discarded, and the remaining part has a quadrilateral shape. The center of this quadrilateral is taken as the best estimate, and the half amplitudes of the encompassed intervals are taken as estimates of the uncertainties for C_{11} and C_{44}. In the same way, as shown in figure 3.2a, by plotting the isolevel curves of the Young Modulus E, its mean value and uncertainty can be taken from the values of E (i.e. E_1 and E_2) which circumscribe the confidence region. The obtained result is equivalent to mapping the (C_{11}, C_{44}) isolevel curves into other constants planes (e.g. (E, ν) plane), and applying the same physical boundaries restrictions (figure 3.2b). This is a simple and clearly defined algorithm to identify the measured value and its uncertainty, for each of the parameters adopted to represent the stiffness.

The estimates obtained by the isotropic model for the coatings can be improved by a better consideration of their nanostructure. This is the case, for example of columnar nanostructures, for which the film modeling by an equivalent homogeneous continuum of average properties remains appropriate, because the probed wavelength is higher than the columns width, but the isotropic continuum is not fully adequate. Irrespective of the specific crystalline anisotropy of each column, the columnar films are statistically isotropic in plane, and aniso-tropic in the normal direction. In this case, the overall symmetry is considered as hexagonal. Full characterization of the elastic properties in the hexagonal symmetry requires five independent parameters, which can be taken as (C_{11}^f ,C_{13}^f ,C_{33}^f ,C_{44}^f ,C_{12}^f). Since the velocities of the Rayleigh and Sezawa modes are slightly influenced by C_{12}, the independent parameters can be reduced to four. A full minimization of the LS estimator in a 4-D space would be too expensive, and would require more information than available from the measured spectra. Therefore, in this case, a refinement of the results is obtained starting from the isotropic values of the (C_{11}^f ,C_{44}^f) couple, keeping them fixed, and allowing C_{13}^f to C_{33}^f to differ from their values in the isotropic case, which are respectively C_{12}^f and C_{11}^f. In the hexagonal symmetry, the elastic moduli become direction dependent. Their values are thus computed exploiting the functional dependence on the C_{ij}^f and the direction [103].

The presented procedure is validated by the analysis of a bulk polycrystalline pure W sample. BS is performed exploiting an Ar^+ laser (subsequently substitued by a Nd:YAG laser), operating at 200 mW at a wavelength λ_0 = 514.5 / 532 nm. The laser is focused on the cen-

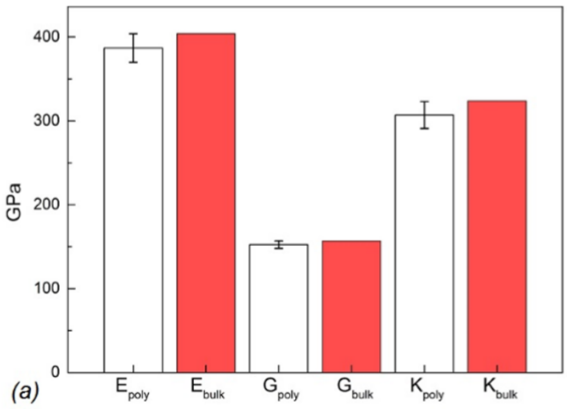

Measured elastic moduli of bulk polycrystalline W.

	E (GPa)	G (GPa)	K (GPa)	ν
W_{poly}	404	157	323.8	0.282
Measured	387 ± 17	152.5 ± 4.5	307 ± 16	0.288 ± 0.001

Figure 3.3: Elastic moduli of bulk polycrystalline W. Comparison between measured and litterature data.

tral region of the sample. The focusing spot size is of the order of tens of micrometers. The measurement is thus sensitive to the properties of the material in this area. The backscattering geometry is adopted, with incident light polarized in the sagittal plane. Scattered light is collected without polarization analysis and analyzed by a tandem multipass Fabry-Perot interferometer of the Sandercock type, typically with a free spectral range (FSR) of 16 GHz. More details on the experimental setup can be found in appendix B. Since polycrystalline W is elastically globally isotropic, the isotropic symmetry model can be appropriate to describe the real elastic behavior of the sample. With the mass density fixed at the bulk value of 19.25 g cm^{-3}, the values of the elastic moduli shown in figure 3.3 are obtained. As it can be seen, these values are in excellent agreement with those proposed in literature [104].
This method will be applied to all the metallic samples analyzed in this thesis (see chapter 4). In the case of transparent coatings (e.g. W-oxides), the derivation of the elastic constants of the films can be eventually more direct, being the information of C_{11} and C_{44} directly derivable for the velocities of bulk waves (see appendix B). From them, the elastic moduli are obtained exploiting common correlations:

$$E = \frac{C_{44} \cdot (3C_{12} + 2C_{44})}{C_{12} + C_{44}} \tag{3.3a}$$

$$\nu = \frac{C_{12}}{C_{12} + C_{11}} \tag{3.3b}$$

$$K = \frac{C_{11} + 2C_{12}}{3} \tag{3.3c}$$

$$G = C_{44} \tag{3.3d}$$

In this case, the uncertainties related to the elastic moduli are computed by means of the standard error propagation, starting from the uncertainties of C_{11} and C_{44}, which, in turn, are related to bulk acoustic waves peaks widths.

3.2 Thermal properties: development of an optimized experimental setup for substrate curvature measurements

It is well known that coatings are subjected to *residual stresses*, already present at the end of the deposition process. These stresses have two main origins. *Intrinsic stresses*, which are due to the deposition process itself, depending on the deposition conditions and by the mismatch of the properties between the coating and the substrate materials (e.g. lattice parameter) [105]. *Thermal stresses*, due to a thermal expansion mismatch between the coating and the substrate, they depend on the elastic properties of the deposited and the base material, usually rising when the sample is cooled down to room temperature after deposition. When the coated components operate at variable temperatures, additional thermal stresses generate. These stresses, typically intensifying at the coating-substrate interface, can lead to coating failure, by either cracking or delamination. Predicting and monitoring these stresses is crucial to assess the operational stability of the coated devices. This requires, beside the knowledge of the elastic moduli, the CTE of the materials. In the case of coatings, its direct measurement can be a challenging task.
In this thesis, the CTE characterization and the monitoring of residual and thermal stresses are obtained by the development of a new ad-hoc experimental setup based on the optical implementation of the substrate curvature method (SC). Even if the SC method is quite old and widely exploited in literature [106, 107, 109–111, 151], it remains a powerful non destructive and versatile technique, which can be adopted for both opaque and transparent coatings. It basically relies on the fact that, when the coating is attached to a substrate, the adhesion constraint results in a bending of the whole system induced by a mismatch of the properties between the coating and the substrate materials. These properties can be the elastic properties, the CTEs and the lattice parameter. Laser beams can thus be exploited to detect the curvature radius of the film-substrate system at room temperature, and, from the curvature measurement, the coating state of stress (i.e. residual stress (σ_{res})) [112]. If the samples are heated, the different thermal expansion behaviors between the coating and the substrate induce an additional bending to the system, that can be detected, as briefly discussed below, to obtain the CTE or to monitor the thermal stress evolution of the coating. In the simpler case of a bilayer formed by a film much thinner than the substrate, such that the stress within the film can be taken as approximately uniform, the stress within the coating can be expressed in terms of the bending curvature radius R by the well known *Stoney's equation* [113, 114]:

$$\sigma_f(T) = \frac{E_s}{1-\nu_s}\frac{t_f}{t_s^2}\frac{1}{6}\left(\frac{1}{R(T)} - \frac{1}{R_0}\right) \tag{3.4}$$

where the sub-indexes f and s stand for film and substrate respectively, $R(T)$ and R_0 are the curvature radii at a certain temperature T and at a reference temperature T_0, while t is

the coating or substrate thickness. If, instead of $R(T)$ and R_0, the curvature radii after and before deposition are considered in eq. 3.4, the residual stress can be determined. When thermal stresses arise upon heating or cooling due to a CTE mismatch between the coating and the substrate, the CTE of the coating can be deduced by the following equation:

$$CTE_f = CTE_s + \frac{d\sigma_f}{dT}\frac{1-\nu_f}{E_f} \tag{3.5}$$

As it can be seen from this equation, the elastic properties of the films must be known to obtian the CTEs. Here comes the coupling with BS, which consistently provides all the information about E_f and ν_f. Equations 3.4-3.5 are written under the assumption of temperature independent elastic moduli, and allow to find a single value of CTE. It is well known that the above properties show some temperature dependence. A more detailed approach would therefore consider the temperature dependence of the elastic moduli of both the substrate and the film and of the CTE of the substrate, and would allow to find the temperature dependence of CTE of the film. However, the measurement of the temperature dependence of the elastic moduli of the coatings is a challenging task. This type of approach would be unavoidable if the explored temperature interval approach the melting temperatures of either the substrate or the film, where phase transitions likely occur. In all the thermal treatments adopted in this work case, the maximum temperature remains far from both the melting and the recrystallization temperatures, at which more significant variations of the elastic moduli could be expected. Therefore, neglecting the temperature dependence of the elastic moduli introduces only small inaccuracies. It must be remembered that the measured CTE refers to the $in-plane$ component of the liner expansion thermal coefficient. In anisotropic sample the in-plane component can significantly differ from the out-of plane CTE, that must be determined by other techniques.

The curvature radius measurement is performed exploiting an array of parallel laser beams. The procedure is briefly analyzed in the simplest case of two parallel laser beams, with an initial spacing D_0, that impinge on a sufficiently reflective surface at two points A e B, at a nominal incidence angle θ with respect to the normal to the surface (see figure 3.4a). If the surface is flat ($R = \infty$), reflection occurs at an angle 2θ and the two beams are again parallel, at distance D_0. If the surface has a convex shape with a finite radius R, the two reflected beams are no longer parallel. Simple reflection implies that the angle α between the normals to the surface at the reflection points A and B is related to the nominal incidence angle θ as:

$$\sin\alpha = \frac{D_0}{2R\cos\theta} \tag{3.6}$$

and that the angle between the two reflected laser beams is 4α. The beams are finally detected by a CMOS sensor, supported by a measurement arm of length A. The beams produce on the CMOS screen two spots, at distance d = d(R); for a perfectly flat surface d = d($R = \infty$) = $d_\infty = D_0$. It is intuitive, and it is detailed in the Appendix A, that

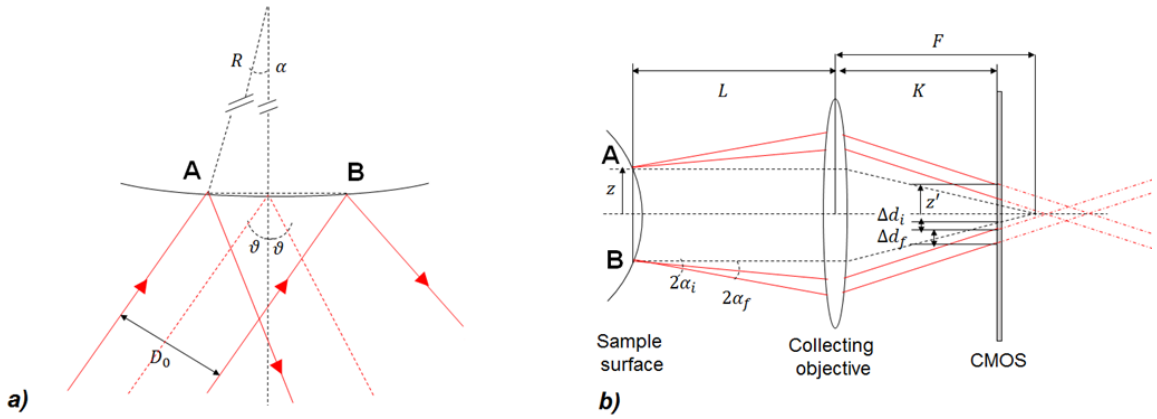

Figure 3.4: a) Schematic principle of two initially parallel laser beams that are reflected by a curved surface. b) the reflected beams are collected by the collecting objective and recorded by the CMOS.

the absolute sensitivity $d\mathrm{d}/d(1/R)$ increases with the arm length A. However, a larger arm length also implies a stronger sensitivity to vibrations and the need of a larger sensor (although d_∞ does not increase). With respect to commonly adopted setups that can be found in literature [107, 112], the insertion of a converging lens, of focal length F, in the measurement arm has been considered, with the objectives of reducing the spot distances, to allow a smaller CMOS sensor, and to limit the arm length A, without losing sensitivity. However, the presence of this lens severely alters beams propagation. This effect of the lens is considered as it follows. The lens is at distance L from the sample, and the sensor is at a further distance K : $A = L + K$ (see figure 3.4b). In a typical experiment the sample has an initial radius of curvature R_i, due to the residual stresses, which makes the beams to be reflected with an angle α_i; the distance between the spots is shifted by $\Delta\mathrm{d}_i$ from d_∞. Imposing a temperature variation, the curvature changes to the final value R_f, the angle changes to α_f, and the distance between the spots undergoes a further shift $\Delta\mathrm{d}_f$. The change of the curvature radius can be derived from the final displacement $\Delta\mathrm{d}_f$ exploiting the classical matrix optics used in ray tracing algorithms. This method adopts two approximations: the paraxial one, i.e. the smallness of the deviation angle of the beam with respect to the optical axis of the system, and the thin lens one. Both approximations are fully appropriate: firstly, since (see eq. 3.6) $D_0 \sim 1$ cm and R is at least several meters, $\sin\alpha \precsim 10^{-3}$; secondly, the radius of curvature of the adopted collecting lens is much larger than its thickness. The beams on the sample surface and on the CMOS screen are related by a transfer matrix as follows:

$$\begin{bmatrix} z' \\ \alpha' \end{bmatrix} = \begin{bmatrix} 1 - K/F & L(1-K/F)+K \\ -1/F & 1 - L/F \end{bmatrix} \begin{bmatrix} z \\ 2\alpha \end{bmatrix} \tag{3.7}$$

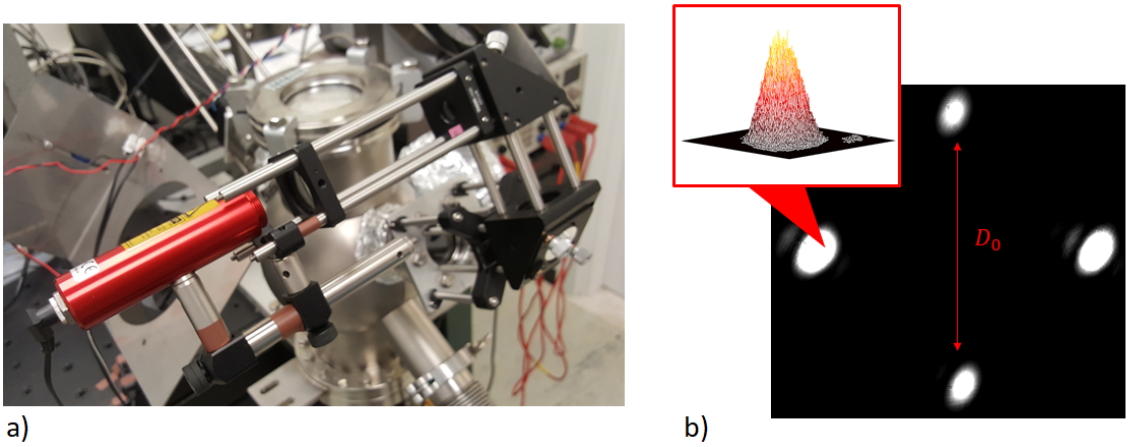

Figure 3.5: a) Laser beam array generation provided by a pair of etalons mutually oriented at 45°. b) CMOS image analysis performed on MATLAB.

where z, α, $z\prime$ and $\alpha\prime$ are the distance of the beam and its deviation angle, from the optical axis, respectively on the sample and on the CMOS. Eq. 3.7 gives

$$z' = (1 - K/F)z + 2\alpha[L(1 - K/F) + K] \tag{3.8}$$

and Δd_f is given by (see Fig. 3.4b)

$$\Delta d_f = 2 \cdot (z'(2\alpha_f) - z'(2\alpha_i)) \quad . \tag{3.9}$$

that, combined with eq. 3.6, results

$$\frac{\Delta d_f}{D_0} B = (\frac{1}{R_f} - \frac{1}{R_i}) \tag{3.10}$$

where $B = (\cos(\theta))/(2[L(1-K/F)+K])$ is a pure geometrical factor that depends on the angle of incidence of the beams, on the arm length and on the presence of the focusing lens. If the lens is removed, eq. 3.10 becomes the standard equation for measuring the curvature change of a sample by a 2D array of parallel laser beams $\frac{\Delta d_f}{D_0}\frac{\cos\theta}{2A} = (\frac{1}{R_f} - \frac{1}{R_i})$ [107, 112]. In the experimental setup, K,L and F can be varied; the relative lens position K can drastically affect the measurement sensitivity. For this reason, it has been optimized. The optimization process is reported in Appendix A.

Operationally, a small array of laser beams is adopted (i.e. 2 x 2 beams, with spacing D_0 = 1 cm). The laser beam array is generated by coupling a laser diode ($\sim$ 5 mW output, 630 nm wavelength) and a pair of etalons. The first etalon multiplies the input laser beam in a direction, while the second etalon, oriented at 45° with respect to the first one, duplicates the 1D array in the other direction, obtaining a 2D parallel laser beams array (see figure 3.5a). A total coverage of 1 x 1 cm^2 measurement area is achieved. The array strikes with an angle of incidence of 60° at the center of the samples. In principles, both uncoated polished

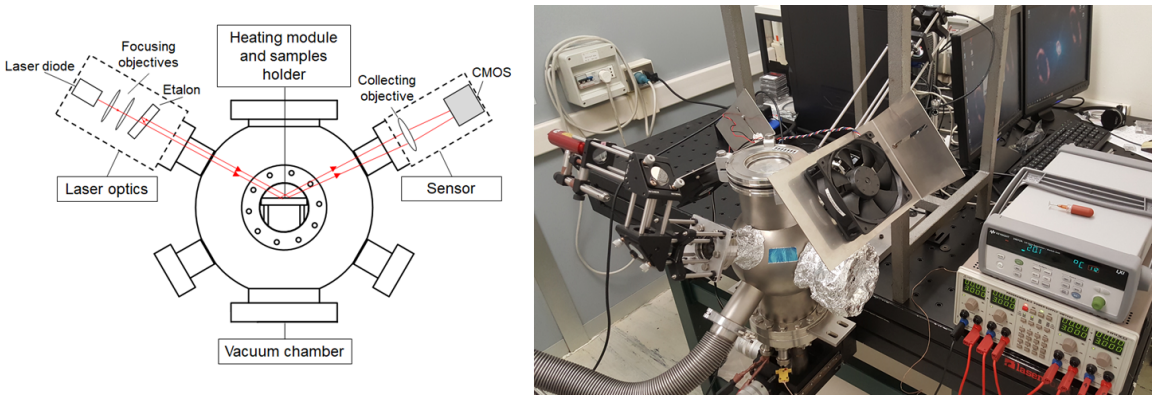

Figure 3.6: Experimental setup for substrate curvature measurement.

substrate surface and coating surface can be probed for metallic coatings. In the case of transparent coatings, instead, due to multiple laser scattering interferences that unavoidably deform the spot shape, only the substrate surface is investigated. The measurement position is kept constant during the entire analysis process. The reflected beams are recorded by the CMOS camera. The adopted camera is characterized by a 4/3, 1.3 Megapixel sensor with a 1024 x 1248 digitized image. The acquisition rate of the sensor is 10 fps in the full format, but it can be further increased up to 200 fps if only certain regions of interest are selected. In this way, multiple measurements for a certain temperature step can be acquired, so that the signal can be averaged on successive frames in order to reduce the overall noise. The position of the beams on the CMOS is followed by the determination of the centroid of each laser spot. The centroids are determined by a classical centroid of intensity algorithm, which weights the intensity of each pixel in the irradiation area over the total irradiated pixels (see figure 3.5b). This procedure is numerically implemented in MATLAB. It has to be noted that the accuracy of the method is deeply affected by noise sources (see Appendix A), such as vibrations from the vacuum system or gas flow and fluctuations of pixels intensity. The use of multiple laser beams array is thus crucial to guarantee high measurement accuracy. The laser beams strike all at the same time on the sample surface and the differential beam spacing between adjacent spots, which is less sensitive to the sample vibrations than the absolute position of the beam, is adopted to measure the change of sample curvature. With this setup, an accuracy of the beam spacing measurement of 0.09 pixels, that with a sensor of 6.66 x 6.66 μm/pixel stands for $\pm$0.5 μm maximum deviation, is obtained. This, in turn, is related to curvature radii of the order of kilometers.

The optical generation and collection modules are mounted on a vacuum chamber, which accommodates the heating module for controlled thermal annealing processes (figure 3.6). This chamber is equipped with various flanges, that provide connections with the vacuum system and the gas inlet for controlled atmosphere treatments, as well as suitable mount for the heating module manipulator and samples handling. A coupled rotary and turbomolecular pumps are exploited to guarantee a base pressure of 5 x 10^{-6} mbar during each thermal

treatments. The heating module is completely handmade. It consists in ceramic plates (i.e. MACOR and Shapal-M ceramics) heated by alumina tubes filled with high purity tantalum wires. To reduce radiative heating to the vacuum chamber walls, the heating stage is partially screened by a molybdenum shield. An external power supply provides heating up to 1200 °C. The temperature is measured by a thermocouple (type K) place under the sample in the middle of the holding Shapal-M plate (5 mm thick). Temperature is measured every 0.5 s by an external acquisition system triggered with the CMOS data acquisition by an ad-hoc developed Labview interface. In this way, the centroid positions of each spot are automatically synchronized with temperature data.

This setup has been tested by investigating the CTE and the residual stresses of various coating materials. The residual stresses measurement accuracy has been examined at room temperature by a direct comparision with the results obtained on the same samples by optical profilometry. The measured coatings were PLD alumina coatings, deposited on double side polished Si(100) and steel substrates. The residual stresses have been determined for Al_2O_3 coatings with different thicknesses. As shown in figure 3.7, the results obtained by this SC setup and by optical profilometry are in excellent agreement.

Moreover, the accuracy of the setup for the determination of the CTE and the monitoring of thermal stresses have also been tested. In particular, the CTE measurement accuracy is evaluated on thermally evaporated silver (Ag) films, whose CTE was measured by the same SC technique with a similar setup [151]. The coatings are deposited in very similar deposition conditions as the ones exploited in [151], so that the reported biaxial modulus of 50 $\pm$ 10 GPa can be chosen for the CTE computation. This value, however, has been verified by BS analysis, showing a good agreement with the one reported in [151]. The CTE of Ag films are thus investigated in the same temperature range of [151] (i.e. 25 - 150 °C) (see

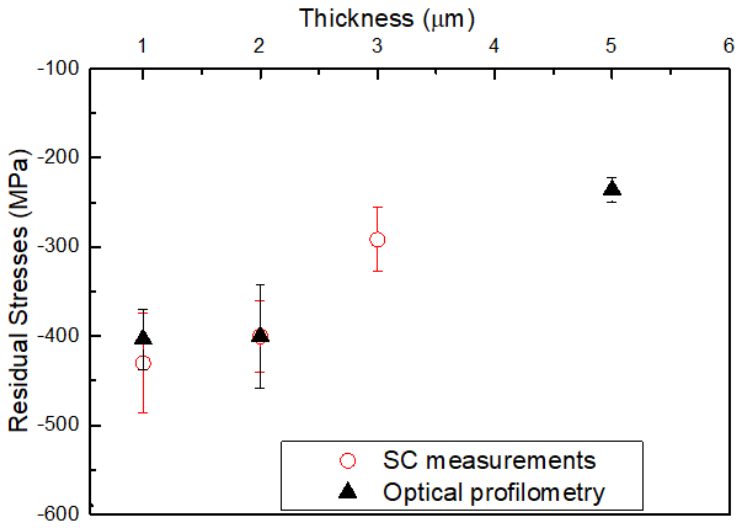

Figure 3.7: Comparison between the residual stresses measured by the SC setup developed in this work and by optical profilometry.

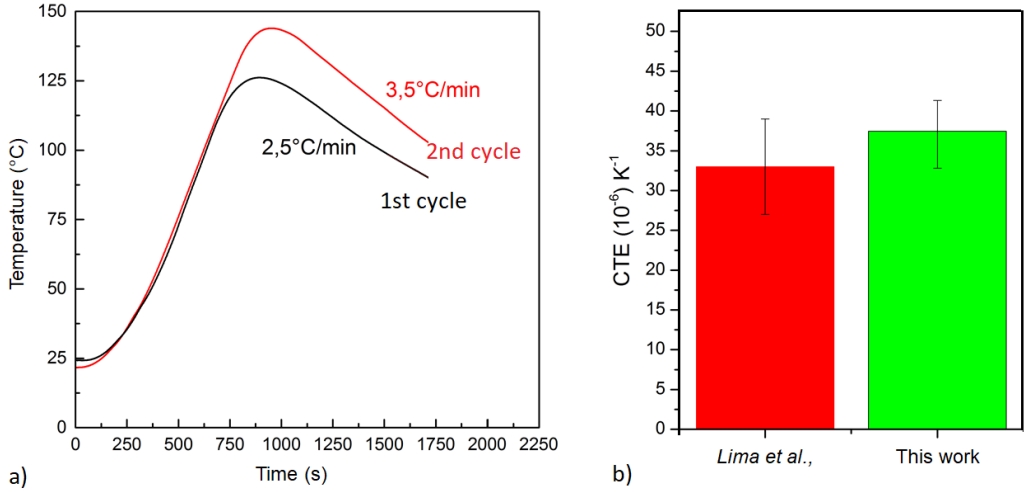

Figure 3.8: a) Temperature ramps exploited for Ag coatings. b) Comparison between the CTE of Ag coating obtained in [151] and in this work.

figure 3.8a). The CTE results to be 38 $\pm$ 4 10^{-6} K^{-1}, that well fits the reported value of 33 $\pm$ 4 10^{-6} K^{-1} (figure 3.8b).

Finally, the reproducibility of thermal stresses measurements is evaluated by investigating the thermal stress on the same coating for a high number of thermal cycles. This procedure is shown, for instance, for rhodium coatings in figure 3.9. As already mentioned, the temperature is measured by a thermocouple placed in the middle of the samples holding plate. The reliability of the temperature value is confirmed by the temperature of the sample surface measured by a pyrometer (see point B in figure 3.9). In general, an accuracy of $\approx$ 0.1 °C is obtained. As it can be seen, the sample is heated from room temperature to about 620 °C and then cooled down to a certain temperature before being heated again. This cycle is performed three times. The measured thermal stress is thus plotted versus temperature. The

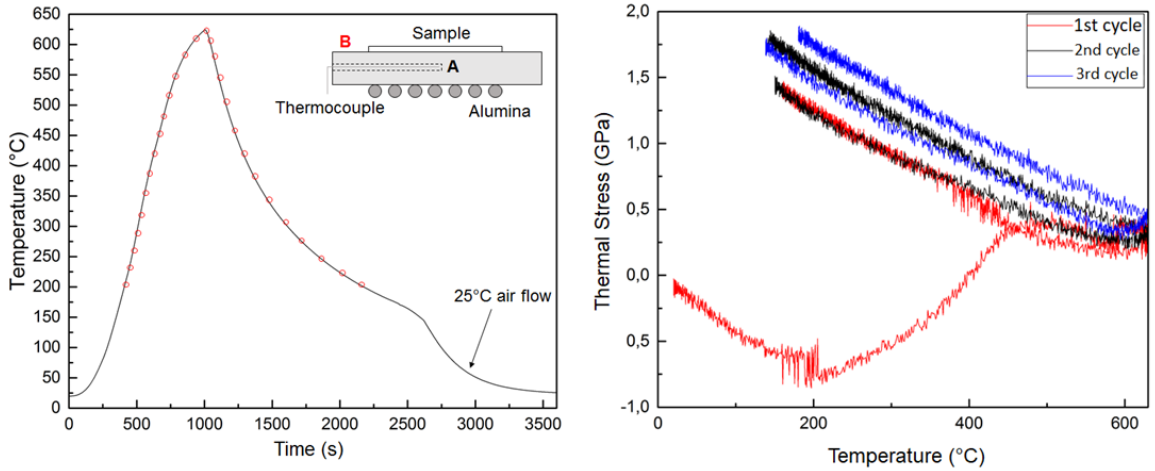

Figure 3.9: a) Temperature ramp adopted for measurements; b) Measured thermal stress during multiple thermal cycles performed on the same coating.

negative intensity of the thermal stress stands for a compressive state of stress in the coating. This is always the case when the film shows a higher CTE than the one of the substrate material (this is exactly the case of Rh films on Si substrate). This means that the coating tries to dilatate but it is constrained by the substrate, developing a compressive stress which grows as the annealing temperature increases. Accordingly, the stress decreases during cooling. A clear difference can be found between the first and the following cycles. During the first heating cycle the compressive thermal stress grows, as expected, linearly with temperature till around 200 °C. Over 200 °C up to the maximum temperature, a clear non-linear behavior is observed. This trend is exhausted during cooling, when the tensile state of stress starts to grow again linearly with decreasing temperature. This characteristic feature can be explained by the beginning of stress relaxation processes, which lead to material yield and to plastic deformation. The relaxation process is driven by an enhanced surface and bulk atoms diffusion, which continues till the atoms reach their equilibrium positions. The consequent volume shrinkage associated with the developed plastic flow results in the growth of a tensile state of stress which is highlighted in the stress-temperature curve by the deviation from linearity during heating. After plastic deformation behavior takes place, the sample is not able to recover the same state of stress during cooling. On the contrary, the second and the third cycles are almost identical and almost free of the enhanced stress non linearity that characterizes the first heating ramp. Operationally, the CTE is determined by linearly fitting the σ(T) curve of figure 3.9 in order to derive the dσ/dT contribution of equation 3.5. Due to the development of relaxation irreversible changes of the layer structure, the non linear part of the stress curve can not be used to derive the CTE of the material. Basing on these observations, the operational procedure adopted for all the measurements that will be presented in chapters 4 and 5 is: a) for residual stresses, measurements are repeated multiple times (i.e. $n \approx 10$), by changing the scanned area on the sample each time. Mean value and uncertainties related to σ_{res} are thus computed accordingly to the independent values obtained for each measurement. b) the CTE is, instead, determined after a first *preparatory* annealing cycle between the same temperatures exploited for the final measurement. This allows some stress relaxation in order to take into account all the stress-temperature curve for the determination of the CTE. Even in this case the measurements are repeated multiple times (i.e. n =3), so that mean value and uncertainties can be determined. In addition, the uncertainty also depends on the uncertainties related to the elastic moduli and the thicknesses which are independently measured. c) Thermal stresses and relaxation processes are monitored during each temperature ramp as described above. From these measurements, yield stresses can be eventually derived.

3.3 Nanosecond laser irradiation: modeling of nanosecond laser induced thermal effects and validation for mimicking ITER-relevant transient thermal loads effects

3.3.1 Modeling of laser-matter interaction

In this thesis a nanosecond laser source is exploited for mimicking the thermal effects related to high heat fluxes proper of ITER-relevant conditions on nanostructured coatings. Due to the really short characteristic time of the source, the direct effects of laser irradiation on the material, i.e. temperature and stress fields, can not be measured easily by conventional experimental devices (e.g. pyrometers, thermocouples). To this purpose, for example, pump-probe techniques could be exploited (e.g. reflectivity change measurements, X-ray diffraction) [115]. For this reason, numerical simulations must be performed to opportunely help the analysis of the experimental data. Moreover, the development of a reliable numerical code can provide a useful tool for predicting the thermomechanical behavior of materials under different irradiation conditions.
In this work, the development of a completely new thermomechanical code has been preferred to the use of standard commercial softwares (e.g. ANSYS, COMSOL). This is basically due to the need of a completely customizable tool, that can be more easily applied to sub-micrometric length scales, as well to very short timescale dynamics, and is possible because a computational tool for general geometries is not needed. It is thus sufficient to develop a numerical code specific for the very simple geometry of a layered medium with plane parallel interfaces. The 2-dimensional code is implemented in MATLAB, and it is based on the finite difference discretization of the thermomechanical equations. In particular, it consists in the resolution of the heat and dynamic displacements equations: the heat equation is firstly solved following the laser excitation and, from the resulting temperature field, the displacements, so the stresses in the material, can be obtained. The thermoelastic effect is neglected, since only a very small increase of the temperature due to material deformation is expected even at high temperatures. The main governing equations for a 2D cartesian isotropic model can be written as:

$$\rho_i c_i \frac{\partial T(x,z,t)}{\partial t} = \nabla \cdot (k_i \nabla T(x,z,t)) + Q(x,z,t) \tag{3.11a}$$

$$\rho_i \frac{\partial^2 \vec{U}(x,z,t)}{\partial^2 t} = \nabla \cdot \sigma \tag{3.11b}$$

where the x-axis and the z-axis are taken along the surface and the thickness respectively, T is the temperature, k the thermal conductivity, c the specific heat, Q the laser power density, $\vec{U}$ the total displacement field and σ the stress tensor. The subindex i refers to the i-layer for which the two equations are solved (i.e. coating and substrate). Equation 3.11a is the classical heat equation, which can be consistently applied to nanosecond scales, since

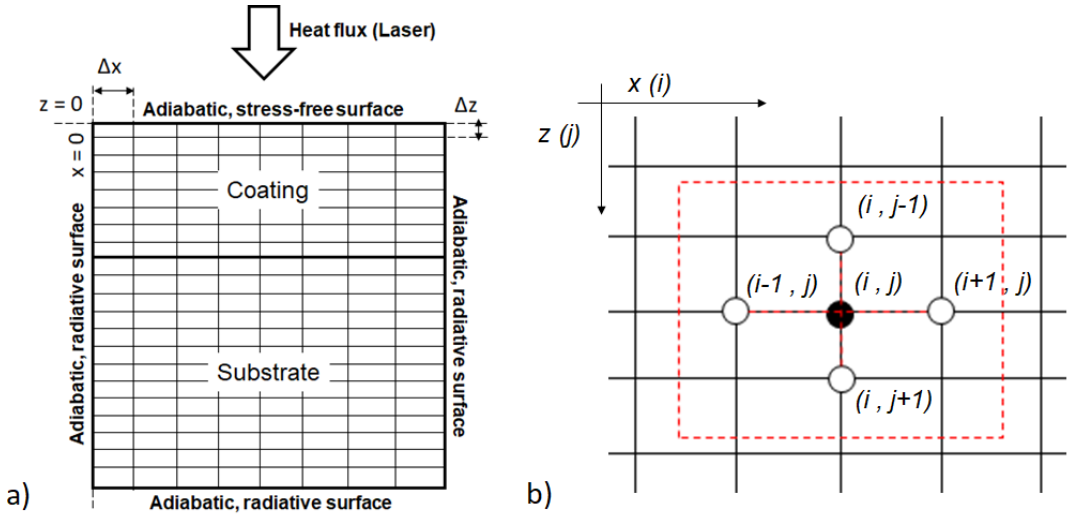

Figure 3.10: a) Schematic representation of the numerical domain adopted for the simulations for a sample of lateral dimension L and thickness d. b) finite difference discretization stencil.

the characteristic time of the excitation is higher than the photon-phonon relaxation time (i.e. picoseconds). The laser energy can be thus considered as directly delivered to the lattice atoms and converted into heat (disregarding the generated electron cloud motion characteristic of a two temperature model for shorter timescales). The heat equation is an elliptic PDE, which does not intrinsically contain any characteristic propagation velocity of the penomenon (i.e. thermal wave velocity), as, differently, it happens for the hyperbolic wave equation 3.11b. This means that, if the physical boundaries become very small (i.e. few nm), such as few atoms are contained in the domain, the concept of heat equilibrium and diffusion could no more be valid. In this case, equation 3.11a must be rewritten as an hyperbolic equation as proposed by many authors [116]. In the model developed in this thesis, the numerical domain is however sufficiently larger (i.e. μm) to contain an high amount of atoms, which guarantees the validity of the standard elliptic heat equation.
The laser source is considered with a gaussian temporal profile with a rectangular spatial distribution, which is exponentially damped along thickness. This description well fits the real laser source, which is a Nd:YAG Q-switched laser with a pulse duration (τ_p) of 7 ns (i.e. $\tau_p = \tau_{FWHM}$), and with an almost top-hat intensity spatial distribution. The term Q for this kind of laser can be written, as proposed by [117, 118], as:

$$Q(x,z,t) = \sqrt{\frac{\beta}{\pi}} \frac{F_0(1-R)}{\tau_{FWHM}} \mu_a (e^{-\mu_a z})(e^{-\beta \frac{(t-2\tau_{FWHM})^2}{\tau^2_{FWHM}}}) K(x) \tag{3.12}$$

where F_0 is the incident laser fluence (J cm^{-2}), μ_a (cm^{-1}) the absorption coefficient and $\beta = 4ln(2)$ a laser constant. The rectangular spatial distribution $K(x)$ has a characteristic dimension fixed to the elliptic beam spot major axis. The laser, strikes at $z = 0$ on the sample surface (see figure 3.10a), its energy is then converted into heat, which propagates along the x and z directions following equation 3.11a.

The resulting temperature gradient gives rise to a dynamic stress field described by equation 3.11b. Here, an isotropic, linear elastic material, is cosidered. Under these assumptions, the stress tensor σ can be written as:

$$\sigma = \begin{bmatrix} \sigma_{xx} & \sigma_{xz} \\ \sigma_{xz} & \sigma_{zz} \end{bmatrix} \tag{3.13}$$

where σ_{xx} and σ_{zz} are the stress components parallel to the two axis directions, while the σ_{xz} refers to the shear stress part. By taking into account the stress-displacements relationships and the force equilibrium conditions, these stress components can be written in terms of the displacement field as [120]:

$$\sigma_{xx} = A\frac{\partial u}{\partial x} + B\frac{\partial w}{\partial z} - C(T - T_0) \tag{3.14a}$$

$$\sigma_{zz} = A\frac{\partial w}{\partial z} + B\frac{\partial u}{\partial x} - C(T - T_0) \tag{3.14b}$$

$$\sigma_{xz} = G\frac{\partial w}{\partial x} + G\frac{\partial u}{\partial z} \tag{3.14c}$$

where $A = \frac{E(1-\nu)}{(1+\nu)(1-2\nu)}$, $B = \frac{E\nu}{(1+\nu)(1-2\nu)}$ and $C = \frac{\alpha E}{1-2\nu}$ are materials constants that depend on the Young modulus, the Poisson's ratio and the α (i.e. CTE), T_0 the baseline temperature and G the shear modulus. u and w stand for the displacement along the x and z directions respectively. In this model no temperature dependence of the elastic properties is considered.

Equations 3.11 and equations 3.14, are finally solved together with suitable boundary conditions. In particular, for the heat problem, all the boundaries are treated as *adiabatic surfaces*, so that:

$$-k\nabla T_{boundaries} = 0 \tag{3.15}$$

For the mechanical problem, instead, a *stress-free* surface condition (i.e. $\sigma_{zz} = \sigma_{xz} = 0$) is applied at $z = 0$, while the remaining boundaries are considered as fictitious numerical boundaries, to which Sommerfeld radiation conditions are inserted (i.e. *one-way* wave equations) as:

$$\rho\frac{\partial \vec{u}}{\partial t}|_{x=0,L} = \pm A\frac{\partial \vec{u}}{\partial x}|_{x=0,L} \tag{3.16a}$$

$$\rho\frac{\partial \vec{u}}{\partial t}|_{z=d} = -G\frac{\partial \vec{u}}{\partial z}|_{z=d} \tag{3.16b}$$

$$\rho\frac{\partial \vec{w}}{\partial t}|_{x=0,L} = \pm G\frac{\partial \vec{w}}{\partial x}|_{x=0,L} \tag{3.16c}$$

$$\rho\frac{\partial \vec{w}}{\partial t}|_{z=d} = -A\frac{\partial \vec{w}}{\partial z}|_{z=d} \tag{3.16d}$$

For both termal and mechanical equations, a perfect matching condition between two following layers is assumed. This, in turn, consists in zero contact resistance, which guarantees

the continuity of the heat flux and temperature, and the continuity of displacements field at the layers interface. In addition, no material modifications after each pulse are considered. The thermomechanical problem is thus solved numerically by a classic Eulerian explicit finite difference method for a fixed mesh of equally spaced Δx and Δz nodes (see figure 3.10a). The node spacing Δz is fixed at 3 nm, such as a suitable large number of nodes can be exploited to describe the penetration depth of the source along the z-direction, while Δx is about 0.1 mm. To satisfy the *Courant* stability criterion, each time step corresponds to a Δt of $\approx$ 10 ps [119]. The description by the time evolution of a temperature field is still meaningful, because a time step of 10 ps is two order of magnitude longer than the period of phonons at the Debye frequency (the Debye temperature of W is slightly above room temperature). This timestep is imposed by the mechanical problem which requires a finer time discretization, imposed by the sound speed, than the heat equation which, with this kind of Δt is clearly oversampled. Choosing a higher Δz would thus result in higher Δt, however loosing accurcay for the discretization of the laser exctintion length. The finite difference discretization, following the stencil shown in figure 3.10b, leads to the following algebraic set of equations:

$$\begin{aligned} T_{ij}^{n+1} &= T_{ij}^{n} + \frac{\Delta t}{\rho_{ij} c_{ij}^{n} \Delta x^2}[(k_{i+1,j}^{n} - k_{i,j}^{n})(T_{i+1,j}^{n} - T_{i,j}^{n}) + \\ &+ k_{ij}^{n}(T_{i+1,j}^{n} - 2T_{i,j}^{n} + T_{i-1,j}^{n})] + \\ &+ \frac{\Delta t}{\rho_{ij} c_{ij}^{n} \Delta z^2}[(k_{i,j+1}^{n} - k_{i,j}^{n})(T_{i,j+1}^{n} - T_{i,j}^{n}) + \\ &+ k_{ij}^{n}(T_{i,j+1}^{n} - 2T_{i,j}^{n} + T_{i,j-1}^{n}] + \\ &+ \frac{\Delta t}{\rho_{ij} c_{ij}^{n}} Q_{ij}^{n} \end{aligned} \tag{3.17a}$$

$$\sigma_{xx|i,j}^{n} = A\frac{u_{i+1,j}^{n} - u_{i,j}^{n}}{\Delta x} + B\frac{w_{i,j+1}^{n} - w_{i,j}^{n}}{\Delta z} - C(T_{i,j}^{n} - T_{i,j}^{0}) \tag{3.17b}$$

$$\sigma_{zz|i,j}^{n} = B\frac{u_{i+1,j}^{n} - u_{i,j}^{n}}{\Delta x} + A\frac{w_{i,j+1}^{n} - w_{i,j}^{n}}{\Delta z} - C(T_{i,j}^{n} - T_{i,j}^{0}) \tag{3.17c}$$

$$\sigma_{xz|i,j}^{n} = G\frac{w_{i+1,j}^{n} - w_{i,j}^{n}}{\Delta x} + G\frac{u_{i,j+1}^{n} - u_{i,j}^{n}}{\Delta z} \tag{3.17d}$$

$$\begin{aligned} u_{i,j}^{n+1} &= 2u_{i,j}^{n} - u_{i,j}^{n-1} + \frac{\Delta t^2}{\rho_{i,j}\Delta x}(\sigma_{xx|i+1,j}^{n} - \sigma_{xx|i,j}^{n}) + \\ &+ \frac{\Delta t^2}{\rho_{i,j}\Delta z}(\sigma_{xz|i,j+1}^{n} - \sigma_{xz|i,j}^{n}) \end{aligned} \tag{3.17e}$$

$$\begin{aligned} w_{i,j}^{n+1} &= 2w_{i,j}^{n} - w_{i,j}^{n-1} + \frac{\Delta t^2}{\rho_{i,j}\Delta x}(\sigma_{xz|i+1,j}^{n} - \sigma_{xz|i,j}^{n}) + \\ &+ \frac{\Delta t^2}{\rho_{i,j}\Delta z}(\sigma_{zz|i,j+1}^{n} - \sigma_{zz|i,j}^{n}) \end{aligned} \tag{3.17f}$$

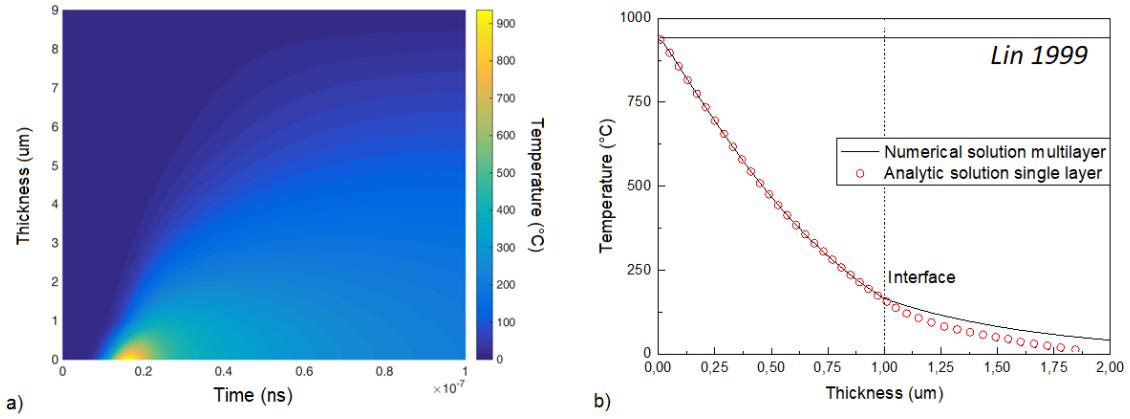

Figure 3.11: a) Numerical solution of 1D heat equation for a multilayer sample composed by a first bulk W layer and a silicon substrate. The temperature distribution along thickness is plotted for each time step. b) Comparison of the numerical hot spot maximum temperature and temperature distribution with analytical solutions [121, 122].

where the sub-indexes i and j stand for the x and z nodes and n is the time index. Equations from 3.17a to 3.17f are consecutively solved. Once the displacements u^{n+1} and w^{n+1} are determined, equations 3.17b to 3.17d are exploited to derive the σ^{n+1} stress components.
The code has been tested by comparing analytical and numerical solutions for the thermal and mechanical problem that can be found in many literature works. For example, the reliability of the numerical resolution of the heat equation can be easily assessed by a direct comparison with the analytical solution of the 1D heat equation for a semi-infinite medium. In the case of a laser gaussian excitation, the maximum surface temperature can be determined as [121]:

$$T_{max} = T_0 + 0.783 \cdot \frac{F_0(1-R)}{\tau_{FWHM}} 2\sqrt{\frac{\tau_{FWHM}}{\pi k \rho c}} \tag{3.18}$$

The comparison with numerical simulations has been performed taking temperature independent bulk W properties (i.e. ρ = 19.25 g cm^{-3}, k = 1.74 W m^{-1} K^{-1}, c = 0.13 J g^{-1} K^{-1}), for a τ_{FWHM} = 7 ns gaussian pulse which delivers a total energy fluence F_0 = 0.1 J cm^{-2}. The temperature distribution along thickness, instead, is obtained by [122]:

$$\Delta T(z,t) = \frac{F(1-R)}{k}\sqrt{Dt}\left[ierfc\left(\frac{z}{2\sqrt{Dt}}\right) - ierfc\left(\frac{\sqrt{z^2+r^2}}{2\sqrt{Dt}}\right)\right] \tag{3.19}$$

where r is the beam radius and D is the thermal diffusivity (i.e. $D = k/(\rho c)$). The comparisons are shown in figure 3.11. As it can be seen the numerical and analytical solutions are in excellent agreement. Moreover, the numerical solution for multilayer well satisfies the imposed perfect matching condition between the coating and the substrate (i.e. temperature continuity at the interface, figure 3.11b).
The mechanical part of the code, instead, is validate firstly by considering an impulsive

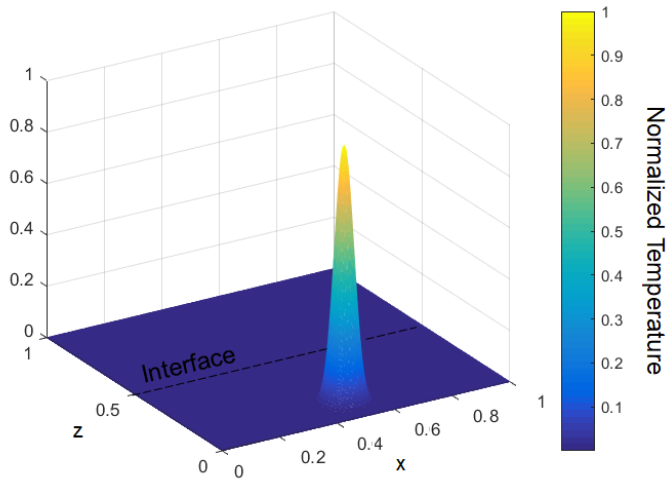

Figure 3.12: Normalized impulsive temperature source for the thermomechanical problem.

temperature source with a gaussian symmetrical spatial distribution (see figure 3.12) (i.e. thermal shock source). As it can be seen in figure 3.13, the impulsive excitation gives rise to spherical mechanical waves in the stress components, which preserve the pristine source symmetry. The continuity condition of stresses at the interface is also satisfied, as well as the stress-free boundary condition at $z = 0$. However, reflection of low intensity mechanical waves is always observed when crossing the interface between two materials with different thermomechanical properties. This results in the growth of small oscillations, that are composed by a physical part, related to the reflection of the wave at the interface, and a numerical part, which is produced by the explicit finite difference method exploited for the discretization of the thermomechanical problem. These numerical oscillations always rise in the tail of the physical pulse and they are particularly enhanced at radiation boundaries (in this case non-physical reflection is observed when the ”real” wave crosses the boundary). Their intensity, however, is smaller than the one of the physical solution and does not severely affect the overall quality of the results. Better performances can be achieved switching to other discretization schemes (e.g. Lax-Wendroff or implicit time domain schemes). Moreover, the stability of the method can be further increased by consid-

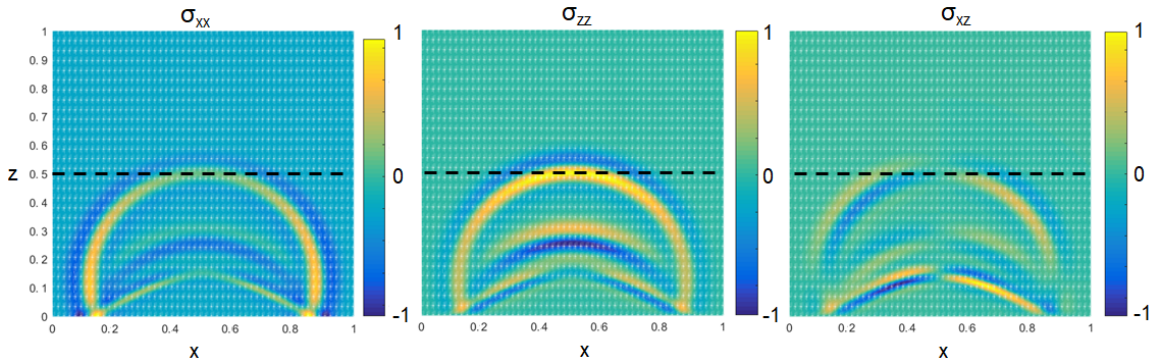

Figure 3.13: Normalized stress profiles following the excitation of figure 3.12.

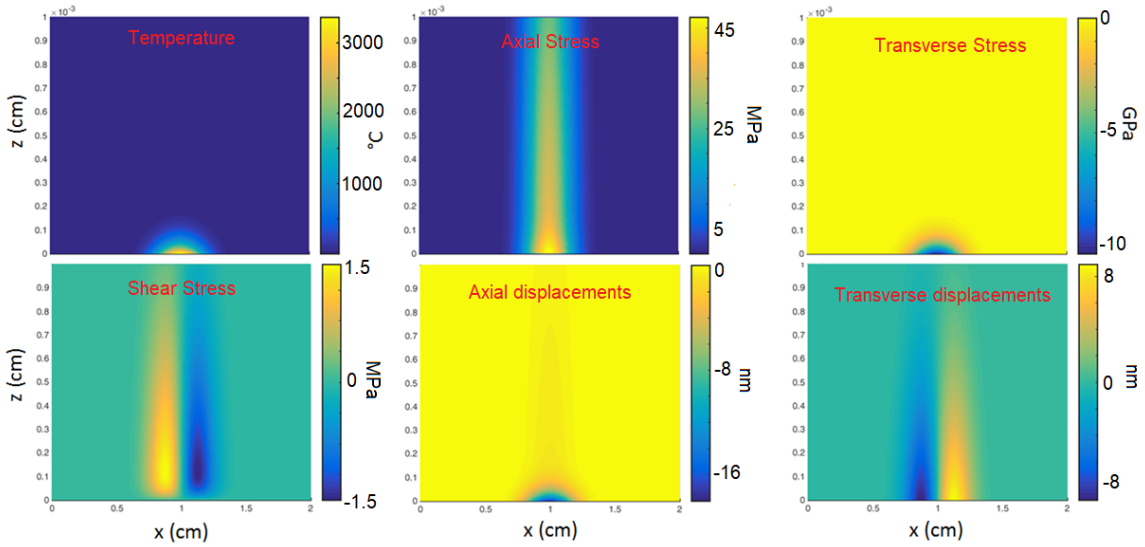

Figure 3.14: Temperature, stresses and displacements fields associated to 7 ns pulse excitation computed at t = 12 ns.

ering, for example, staggered grids for the finite difference discretization of the governing equations.

A further validation of the code is proposed by considering a total thermomechanical simulation performed with realistic irradiation conditions and sample geometry, as shown in figure 3.14. In this case, a sample of lateral dimension L = 2 cm and thickness d = 500 μm is irradiated by a 7 ns laser pulse with a total energy of E = 1.4 J and spot diameter D = 0.9 cm. The sample is considered as a bilayer, composed by a 1 μm thick W coating, to which bulk W properties are applied, and a 500 μm thick Si substrate, with corresponding bulk Si properties. The total thickness considered in the computation is set to 10 μm. For the adopted laser input parameters, the temperature reaches the melting temperature of W (i.e. 3690 K). As it can be seen, the intensity of the axial stress (i.e. σ_{zz}) and the shear stress (i.e. σ_{xz}) is two order of magnitude lower than the intensity of the transverse stress (i.e. σ_{xx}), being $\sigma_{zz} \approx \sigma_{xz}$ of the order of MPa and σ_{xx} of the order of GPa. This means that the total equivalent stress, which can be computed as the Von Mises equivalent stress (σ_{VM}), can be approximated as [123]:

$$\sigma_{VM} = \sqrt{3(\frac{(\sigma_{xx} - \sigma_{zz})^2}{4} + \sigma_{xz}^2} \approx \sigma_{xx} \tag{3.20}$$

This is an expected result, since the thickness of the sample is several times smaller than its lateral dimension and the beam spot diameter. Therefore, for this particular geometry, the thermomechanical problem can be considered as a quasi 1D problem, to which the plane stress assumption can be applied. Under this approximation, there is an exact solution of

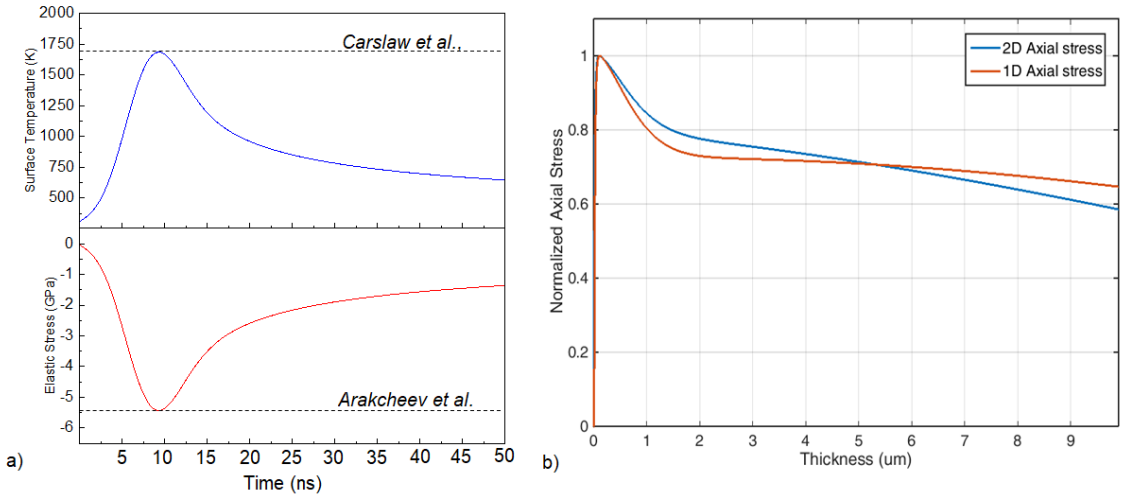

Figure 3.15: a) Numerical temperature and total elastic stress (i.e. σ_{VM}) profiles compared with the analytical solutions by [122, 124]. b) Comparison between 1D and 2D axial stress.

the thermomechanical problem at the surface, which can be written as [124]:

$$\sigma_{xx} = -\frac{\alpha E}{1-\nu}\Delta T \tag{3.21a}$$

$$\sigma_{zz} = \sigma_{xz} = 0 \tag{3.21b}$$

In figure 3.15a, the numerical transverse stress computed at the sample surface (i.e. z = 0) is compared to the analytical solution of equation 3.21a, showing perfect agreement.
In figure 3.15b, instead, a comparison between the axial stresses computed by 1D and 2D (i.e. the axial stress of the centerline) simulations is also porposed. Even if the maximum stress occurs at the same position and at the same time for both the models, the stress distribution along thickness is quite dissimilar. For this reason, even if a simpler 1D problem could be enough accurate to describe the thermomechanical problem of nanosecond laser irradiation of micrometric thick coatings, for a higher versatility of the model, the bi-dimensionality of the problem is always considered.
This code is thus exploited to predict the thermal effects thresholds for various nanostructured coatings. These thresholds are computed in terms of the HFF. In particular, the numerical HFF thresholds for melting and recrystallization are determined by equation 3.17a, when the maximum temperature (i.e. the hot spot temperature) overcomes the melting temperature (i.e. 3690 K) and the recrystallization temperature (i.e. 1400 K - 1600 K) of bulk W. The numerical cracking threshold, instead, is found by applying to the model theoretical results proposed by *Arakcheev et al*, derived under the plane stress assumption for an ideal elasto-plastic material (i.e. no hardening). Following this approach, it is possible to consider a total stress composed by an elastic part, computed from the mechanical problem of equations 3.17b-f, and a plastic one, determined as reported in [124]. The process applied for the computation of the cracking threshold is highlighted in figure 3.16a. A com-

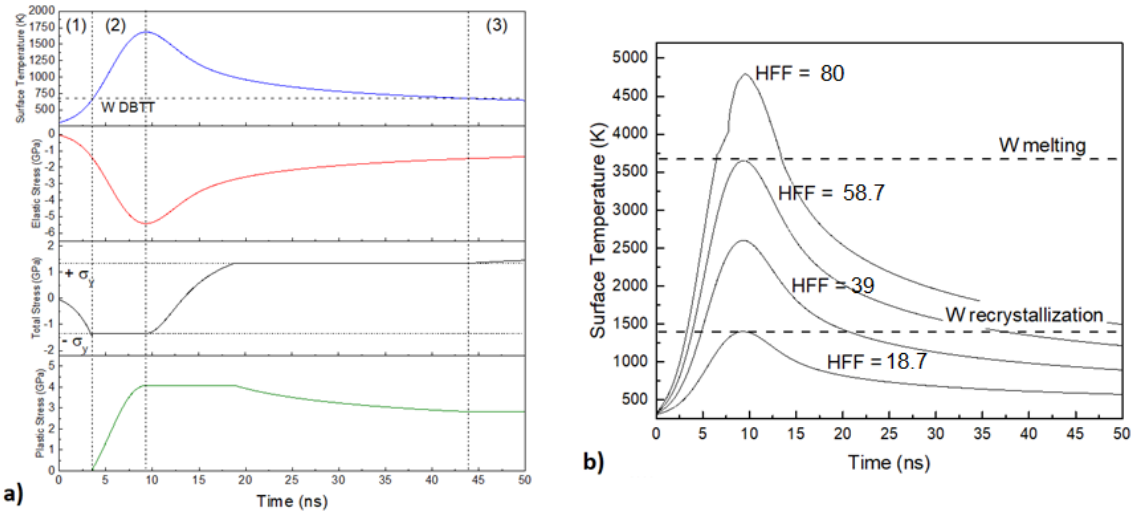

Figure 3.16: a) temperature, elastic stress, total stress and plastic stress computed for bulk W. The three regions (1), (2) and (3) for cracks formation are highlighted. b) temperature profiles computed for bulk W with different HFFs.

pressive state of elastic stress rises upon heating. For $T < DBTT$ (i.e. ductile-to-brittle transition temperature), W shows a brittle behavior, so no plastic deformation can occur, thus the total stress can be made only of the elastic part. When $T > DBTT$, W begins to behave like a ductile material, so the total stress can not exceed the yield strength. As a consequence of yielding, plastic deformation takes place and the plastic stress increases until the maximum temperature is reached. In the cooling phase, the elastic stress decreases and the total stress reverses its sign. No additional plastic deformation is observed until the total stress overcomes again the yield strength. At this point, opposite plastic deformation occurs until the temperature reaches again the DBTT. Finally, below DBTT, W is again brittle, and yield could induce cracking rather than plastic deformation. Following these steps, at least three different conditions for cracks formation can be distinguished: (i) if the temperature exceeds the ductile-to-brittle transition temperature (DBTT) (region 1), (ii) if, when $T > DBTT$ (region 2), the maximum thermal stress exceeds the ultimate stress of the material and (iii) if, when cooling down at $T < DBTT$ (region 3), the maximum thermal stress is higher than the yield strength. In this numerical model, both the yield and the ultimate stress are considered temperature independent. A more rigorous approach should comprehend their temperature dependence, as well as more general plastic flow correlations for the plastic stress component (e.g. Drucker-Prager, Mohr-Coulomb).

3.3.2 Comparing the thermal effects induced by thermal loads between different irradiation sources: extension of the heat flux factor concept to non constant temporal source profiles in the nanosecond regime

As already mentioned in section 2.5, the various thermal effects induced by different irradiation sources can be compared in terms of the heat flux factor (HFF), generally defined as:

$HFF = P_{abs}\sqrt{\tau_p}$. This formulation derives directly from the energy balance equation of an irradiated surface of thickness equal to the thermal diffusion length (i.e. $\approx \sqrt{4D_k\tau_p}$) [40]:

$$\frac{F_0(1-R)}{\tau_p} = \rho c \Delta T \sqrt{4D_k\tau_p} \tag{3.22}$$

Equation 3.22, which was derived by *Benz et al. 1989*, intrinsically considers a source with a constant temporal power profile (i.e. a square or rectangular temporal pulses). This type of temporal profile is usually exploited in almost all the high heat fluxes testing machines based on electron beams or long pulsed lasers irradiation. Moreover, all these sources operate with characteristic times of the order of ms. Since the irradiation source exploited in this thesis is a nanosecond temporal gaussian laser, an extension of the definition of HFF to non-constant temporal sources in the nanosecond regime is proposed.
For a rectangular pulse, the maximum reached temperature can be determined directly from the analytical solution of the 1D heat equation as [121]:

$$T_{max} = T_0 + \frac{F_0(1-R)}{\tau_p}\frac{2\sqrt{\tau_p}}{\sqrt{\pi k \rho c}} \tag{3.23}$$

where $\frac{F_0(1-R)\sqrt{\tau_p}}{\tau_p}$ is the HFF (i.e. $P_{abs}\sqrt{\tau_p}$). Considering bulk W properties, from equation 3.23, an HHF $\approx$ 62 MW m^{-2} s$^{0.5}$ is needed to reach the melting condition. Now, if the same HFF is delivered by a gaussian pulse with $\tau_p = \tau_{FWHM}$, this results in a lower maximum temperature. This is basically due to a higher spread of energy of the gaussian profile with respect to the square one. In this case, indeed, melting occurs at 80 MW m^{-2} s$^{0.5}$ (see equation 3.18). This discrepancy is strictly correlated to the fact that, for temporal profiles different from the rectangular one, the choice of τ_p for the computation of HFF is not unique, but it has some freedom, with an interval of reasonable choices. Consequently, in this work, the pulse duration of the gaussian laser needed for the computation of HFF is chosen in order to have, for fixed laser energy fluence F_0, the same maximum surface temperature rise (T_{max}), i.e. the temperature of the hot-spot, of the one obtained by a rectangular profile. Therefore, by comparing equations 3.23 for rectangular excitations and 3.18 for gaussian profiles, it is clear that, in order to have the same temperature rise, $\sqrt{\tau_p^{gauss}} = 0.783\sqrt{\tau_{FWHM}}$, so that $\tau_p = 0.613\tau_{FWHM}$. This result can be better demonstrated by considering again equation 3.22. F_0 is the total incidence energy fluence, so it is defined as $F_0 = \int I_0(t)dt$. If $I_0(t)$ is constant over time, the integral returns the product between $I_0 \cdot \tau_p$, where I_0 is the peak power, and everything reduces to equation 3.23. However, if $I_0(t)$ shows a temporal gaussian dependence as the one described in equation 3.12, the integral results again in the product $I_0 \cdot \tau_{FWHM}$, but, this time, multiplied by the constant 0.783, which derives from the gaussian integration.

Following this new HFF formulation, numerical simulations are performed on bulk W materials in order to derive the HFF thresholds for melting, recrystallization and cracking.

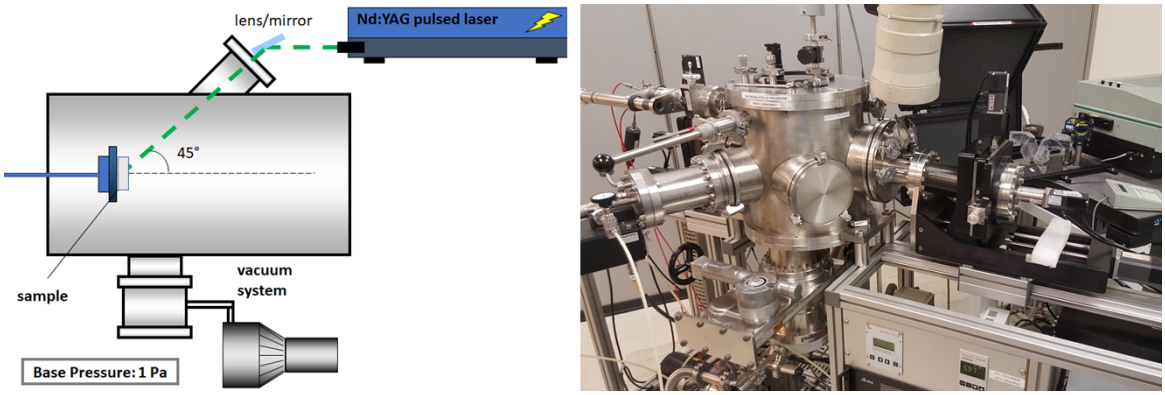

Figure 3.17: Experimental setup for laser irradiation.

For this type of material, bulk W mechanical and thermal properties (i.e. ρ = 19.25 g cm^{-3}, E = 411 GPa, G = 160 GPa, ν = 0.28 and α = 4.2 10^{-6} K^{-1}) are considered. The surface reflectivity is 55%. A tensile yield strength (σ_y) of 1350 MPa (i.e. at room temperature) and an ultimate stress (σ_u) of 1500 MPa are chosen as reference values for all the computations [125]. Simulations are performed considering a temperature dependence of k and c as the one reported in [126], and with an absorption coefficient of 1.46 10^6 cm^{-1} at λ = 1064 nm [128]. Over the melting temperature, a constant thermal conductivity of 0.7 W cm^{-1} K^{-1} and a constant specific heat of 0.23 J g^{-1} K^{-1} are considered for liquid W [127]. HFF thresholds of 58.72 MW m^{-2} s$^{0.5}$ and 18.8 - 22 MW m^{-2} s$^{0.5}$ are found for melting and recrystallization respectively (see figure 3.16a). The HFF threshold for cracking, instead, turns out to be $\approx$ 12.9 MW m^{-2} s$^{0.5}$, which corresponds to a critical temperature value of $\approx$ 1073 K. All these values well fit numerical and analytical data that can be found in various literature works (see table 3.1) [42, 60, 129].

3.3.3 Validation of nanosecond laser irradiation for mimicking thermal effects under fusion relevant transient heat loads conditions

The validation of nanosecond laser irradiation as a fusion relevant high heat fluxes testing method is performed by irradiating bulk W samples, and by comparing the obtained experimental HFF thresholds for the different thermal effects (i.e. melting, cracking and recrystallization) with the ones reported in literature by millisecond lasers and electron beams. Finally, also a direct comparison with the predicted numerical thresholds is proposed.
Laser irradiation is performed exploiting the fundamental harmonic (λ = 1064 nm) of a Q-

	Melting (MW m^{-2} s$^{0.5}$)	Recryst. (MW m^{-2} s$^{0.5}$)	Cracking (MW m^{-2} s$^{0.5}$)
This study	58.72	18.8 - 22	12.9
Literature	50 - 62 [42, 121]	-	12.01 - 13.8 [125, 129]

Table 3.1: Numerical HFFs thresholds for the different thermal effects for bulk W determined by the developed numerical model and compared with common analytical and numerical results reported in literature.

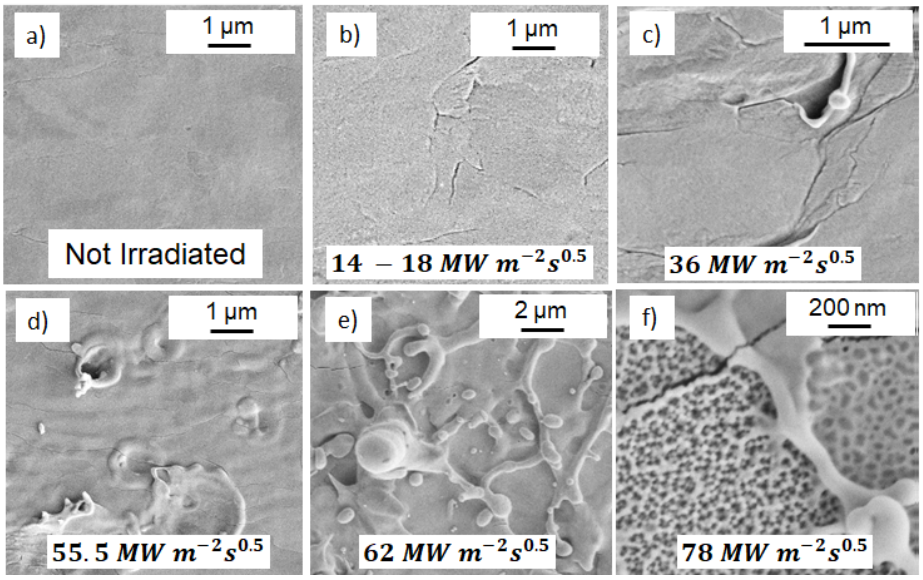

Figure 3.18: SEM images of bulk W_{ML} before and after nanosecond one shot laser exposure at different HFFs. a) Not irradiated surface, b) cracking threshold, c) localized melting, d) melting threshold, e) droplets formation and f) surface nanostructuring.

switch Nd:YAG laser. The laser enters in a vacuum chamber and strikes the sample surface with an angle of incidence of 45° (see figure 3.17). Bulk W samples are irradiated with different HFFs, from 1 to 100 MW m^{-2} $s^{0.5}$ (the laser energy fluence varies from 25 mJ cm^{-2} to $\approx$ 2.4 J cm^{-2}), with both single shots and high number of pulses (i.e. up to 18000). The irradiation is performed at room temperature and under vacuum conditions (i.e. 1 Pa base pressure). The morphology evolution after irradiation is investigated by a Zeiss Supra 40 field emission Scanning Electron Microscope (SEM) with an accelerating voltage of 3 - 7 kV, and by optical miscroscopy.

The investigation is performed on Plansee bulk W sheets 100 μm thick with a mirror-like surface finish (W_{ML}).

The surface of unirradiated W_{ML} is shown in figure 3.18a. After a single shot, surface cracking is observed between 14 and 18 MW m^{-2} $s^{0.5}$ (figure 3.18b). Below this cracking threshold, no surface modification is detected. Even if localized surface melting evidence is found at 36 MW m^{-2} $s^{0.5}$ at the edges of surface imperfections and cracks (figure 3.18c), the HFF melting threshold is considered at 55.5 MW m^{-2} $s^{0.5}$, where W surface is more widely melted (figure 3.18d). The spot area is completely melted above 62 MW m^{-2} $s^{0.5}$, where also droplets formation occurs (figure 3.18e). At 78 MW m^{-2} $s^{0.5}$, surface nanostructuring is found inside the melted regions (figure 3.18f). Probably due to the pristine large grains (i.e. micrometric grains) of W or not sufficient time (i.e. pulses) at the disposal of the material, no recrystallization is found.

Bulk W behavior under a high number of thermal cycles is then investigated. The irradiation is performed with the laser striking always in the same sample position with a repetition rate of 10 Hz. If irradiation is performed at 10 MW m^{-2} $s^{0.5}$, which is well below the single

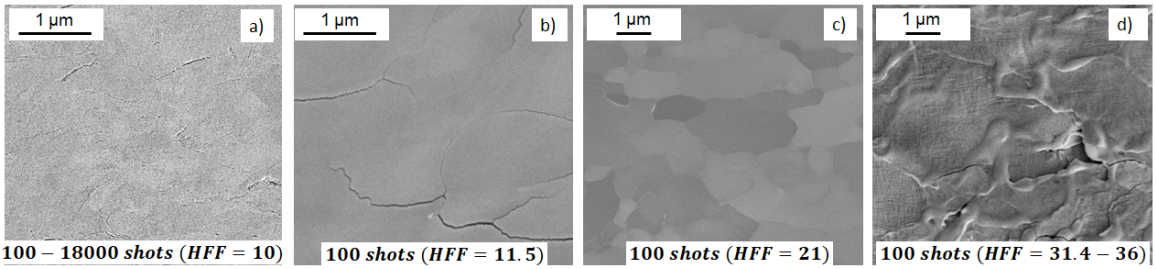

Figure 3.19: HFF thresholds after multishot irradiation: a) no damage threshold, b) cracking threshold, c) recrystallization threshold and d) melting threshold.

shot cracking threshold (i.e. 14 MW m^{-2} $s^{0.5}$), no surface damage is observed neither after 18000 pulses (figure 3.19a). At this irradiation condition, indeed, the maximum numerically estimated temperature is ≈ 650 - 700 K, which is very close to the DBTT value of W. Therefore, only elastic deformation takes place, such that total stress can not exceed the yield stress, and cracks can not initiate or propagate. Cracking is firstly found starting from 11.5 MW m^{-2} $s^{0.5}$ after 100 shots (figure 3.19b). After 100 pulses at 21 MW m^{-2} $s^{0.5}$ a clear recrystallization occurs (figure 3.19c). Surface melting, instead, is observed after 100 pulses between 31.4 and 36 MW m^{-2} $s^{0.5}$ (figure 3.19d). In general, as HFF increases, less pulses are needed to induce cracking, recrystallization or melting. The observed surface damages as function of the number of shots and HFF are shown schematically in figure 3.20. In general, melting occurs at very lower HFF with respect to the single shot irradiation. It is well known that the threshold damage for laser irradiation is drastically lowered by an increasing number of performed shots. This is mostly due to the laser driven material surface modification after each shot, that, altering the morphology (e.g. surface roughness), induces local centres of absorption that significantly increase the local absorbed laser energy.

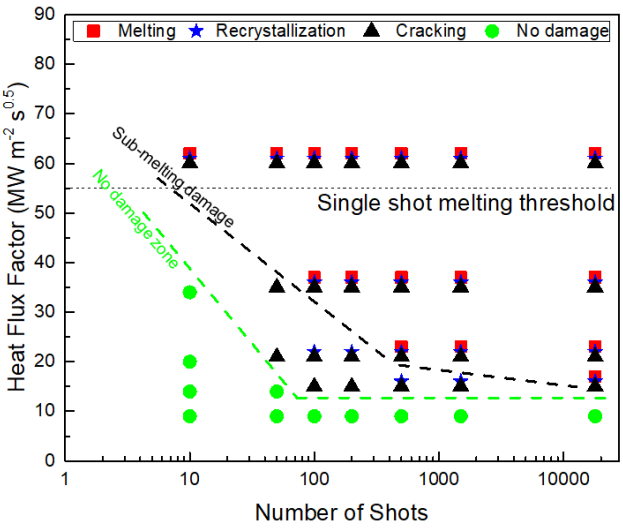

Figure 3.20: Thermal effects observed after different number of laser shots and different HFF.

Number of shots	Melting	Recrystallization	Cracking
Single-shot	>50 ([42], e-beam)	23 - 39 ([42], e-beam)	12 - 18 ([129],e-beam)
Single-shot (This work)	55.5	-	14 - 18
Single-shot (This work, model)	58.7	18.8 - 22	12.9
Multi-shots	30 ([131],e-beam, 100)	15 - 24 ([83],ms laser, 500)	12 ([131], e-beam, 100)
Multi-shots (This work)	31.4 - 36 (100)	15 (500)	11.5 (100)

Table 3.2: Experimental HFF (MW m^{-2} $s^{0.5}$) thresholds reported for different bulk W samples under single shot and multishots irradiation by electron beams and millisecond lasers at room temperature. The various HFF thresholds are compared with the ones obtained in this work by nanosecond laser irradiation for both single and mulstishots conditions and by numerical simulations.

In table 3.2, the HFF thresholds reported in literature for various bulk W materials, under both single and multishots irradiation by millisecond laser and electron beams, are reported. These thresholds are compared to the ones obtained in this thesis by nanosecond laser irradiation and by the numerical model. The specific microstructure of W and its composition, as well as the environmental conditions, can deeply affect the thermomechanical response of the material. For this reason, unique threshold values for the different thermal effects can not be found. However, the results are in good agreement, confirming the effectiveness of the HFF parameter in determining the material behavior under thermal loads, regardless the type of source exploited, and consolidating its definition proposed in section 3.3.2. Moreover, the experimental values found in this work for the single shot irradiation well fit the numerical ones. This confirms the validity of the simplified hypothesis that are taken into account in the model. The little discrepancy can be attributed to surface imperfections or intensity spikes in the laser profile, as well as to other enviromental factors (e.g. radiative thermal losses from the heated surface) that are not taken into account in the model definition.

CHAPTER 4

Thermomechanical characterization of nanostructured coatings

This chapter focuses on the thermomechanical characterization of nanostructured W and B coatings deposited by PLD, with the aim of finding a relationship between the specific nanostructure, morphology, composition and the thermomechanical properties of the samples. The characterization is performed by exploiting the experimental method developed in this thesis and presented in chapter 3, which must be supported by other common characterization techniques, whose details are reminded in Appendix B. Elemental composition is assessed using Energy Dispersive X-ray Spectroscopy (EDXS). The films structure and morphology are analyzed by Scanning Electron Microscopy (SEM), by X-ray Diffraction spectroscopy (XRD) and by Raman spectroscopy analysis.

As mentioned in section 2.5, PLD allows a fine control of the material properties. Thanks to its versatility, mono or multi-elemental coatings can be deposited, and, by varying various deposition parameters, their structure and morphology can be tailored down to the nanoscale. The obtained thermomechanical properties are mandatory for the further investigation of the coatings behavior under thermal loads, that will be presented in chapter 5. In this chapter, the thermomechanical properties of nanostructure metallic W coatings are analyzed in section 4.1. In this case, the nanostructure is tailored during deposition by opportunely varying the backgorund gas pressure or by adding tantalum (Ta) atoms to the W lattice as solid solution. In section 4.2, the role of O_2 and N_2 on the thermomechanical properties of W coatings is elucidated. Here, W-O and W-N coatings are chosen with an increasing O_2 and N_2 content, mimicking codeposited W in tokamaks in presence of gas impurities. Finally, section 4.3 is devoted to the discussion of the elastic properties of B coatings.

4.1 Metallic W coatings

Metallic W coatings are produced by PLD, exploiting the second and the fourth harmonic of a Nd:YAG laser with wavelengths λ = 532 nm and λ = 266 nm, repetition rate of 10 Hz, pulse width of 7 ns and energy per pulse between 150 - 815 mJ. The laser strikes with an angle of incidence of 45° on a 2 in. diameter W target. The laser fluence on target is 1.6 - 9.3 J cm^{-2}. The species ablated from the W target expand in the deposition chamber in presence of He (purity 99.999%) as background gas. Since expansion features of the ablated particles are related to the atomic mass and the pressure of the background gas (heavy gas is very efficient in quenching kinetic energy), the first solution adopted for tailoring the nanostructure of the coating is by opportunely change the background gas pressure during deposition. He pressure ranges between 10^{-3} Pa base pressure (vacuum) and 200 Pa. Given the higher mass number, also argon (Ar) is exploited as background gas. In this case, only a backgorund pressure of 50 Pa is considered. The expanding species are collected on a substrate, Si(100), positioned 60 mm away from the target. More details about the deposition process are reported in [88]. As already mentioned in section 2.5, these coatings are particularly interesting for fusion-relevant applications, since c-W coatings can be considered as proxy of W coatings on CFC in tokamaks, while a-W and p-W coatings mimic promptly redeposited W above the first wall. These samples are investigated in section 4.1.1.
Alternatively, the nanostructure is also tailored by the addition of Ta atoms in W lattice (section 4.1.2). In this way, the properties of binary W-Ta systems are investigated. In this case, W-Ta coatings are deposited at fixed background pressure (i.e. vacuum condition), exploiting a heterogeneus target similar to those described in [132]. The target consists of a W disk (purity 99.9%), with a superposed grid obtained from a Ta wire (purity > 99.95%) of 0.25 mm diameter. The amount of Ta in the deposited film is varied tuning the pitch of the Ta grid. Thanks to this setup, W-Ta films with various Ta concentration can be deposited.
Film thicknesses, determined by cross sections using a Zeiss Supra 40 field emission SEM with an accelerating voltage of 3 - 5 kV, range from 200 nm to 2 μm depending mainly on deposition time. Coating thickness distribution is gaussian centered in the middle of the sample where a homogeneous area of about 1 cm^2 is present.

4.1.1 Metallic nanostructured W coatings: proxy of coated Plasma Facing Components and W redeposits

During the PLD process an adiabatic expansion takes place due to the high pressure and temperature of the ablated material (e.g. 10^6 Pa, 5 10^3 K). The expanding species push away the He and Ar gas present in the vacuum chamber. The gas becomes increasingly compressed, (snow-plough effect) eventually forming a shock wave [133]. In this regime interactions between ablated species and background gas molecules are very weak. During

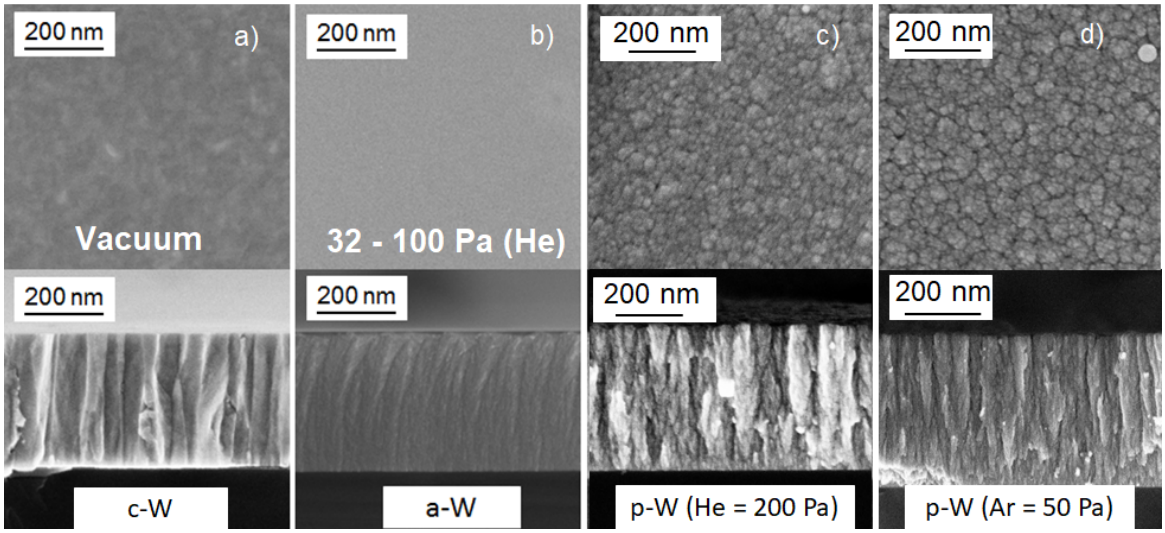

Figure 4.1: Top view and cross-section SEM images of metallic W coatings: a) columnar nanocrystalline W, b) amorphous W, c) porous W deposited at 200 Pa of He and d) porous W deposited at 50 Pa of Ar.

the expansion the internal pressure drops down and diffusion and mixing processes of the ablated species with the gas atoms take place. The kinetic energy distribution of the expanding species can substantially vary between the shock wave and the diffusion regimes. The film properties, morphology and structure, are strictly related to the energy of the impinging species. At high energy the growth of nanocrystalline compact columnar films (i.e. c-W) is favoured, while at low energy the deposited film can exhibit a disordered amorphous structure (i.e. a-W) or can be porous (i.e. p-W) [134]. This effect, depending on the mass number of the backgound gas, is completely different between He and Ar.

This is remarked by SEM analysis shown in figure 4.1. As it can be seen, at vacuum condition, the ablated particles are sufficiently energetic to promote compact columnar growth (figure 4.1a). Increasing He pressure between 32 and 100 Pa results in the disappearing of the columnar grains in favour of an isotropic amorphous structure (figure 4.1b). Finally, when He pressure is between 100 and 200 Pa, porous *cauliflower* growth can occur (figure 4.1c). The same porous morphology is obtained at 50 Pa of Ar (see figure 4.1d).

From EDXS analysis, it is found that the different nanostructures are characterized by W rich of gas impurities. In particular, coatings show severely different oxygen content. c-W samples are characterized by an O_2 concentration below 5%. This is basically due to the really compact structure obtained in vacuum conditions. In the case of a-W amd p-W coatings, instead, O_2 concentration between 10 - 20% and up to 55 - 60% is respectively observed. This is obviously related to the more open morphologies, that result in a higher number of available sites for O_2 trapping.

XRD spectra of the samples deposited with pressures ranging from vacuum to 60 Pa of He are summarized in figure 4.2a. The spectrum related to c-W clearly shows a strong reflection around 40° (2θ), which is assigned to the (110) reflection of α-W. The absence of other reflections (e.g. (200) reflection) is related to the crystallographic oriented growth

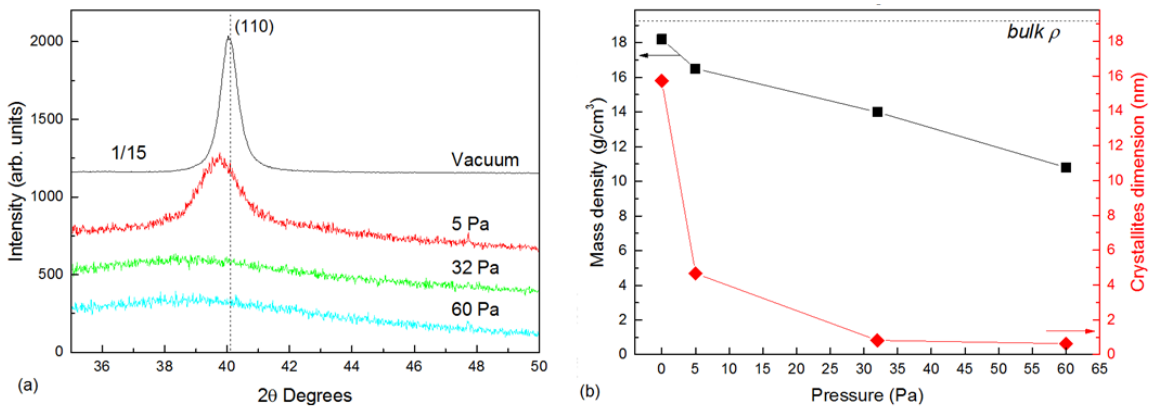

Figure 4.2: a) XRD spectra of metallic nanostructured W coatings deposited at different He pressures. b) Trends of the mean crystallites size $\bar{D}$ and of the measured mass density ρ of W coatings.

that is found for columnar coatings. The deposition by PLD of metallic films with an oriented crystallographic growth is found in literature in the case of fcc metals like Au [135], Pt [137] and Rh [138] where the main crystallographic growth direction is the (111). For fcc crystals, the (111) is the direction of minimum configurational energy [139]. In the case of W, which is a bcc crystal, the atomic planes perpendicular to the (110) direction exhibit the highest planar density, in agreement with the observed direction of growth. The film deposited at 5 Pa exhibits a broader peak, still close to the (110) reflection, but shifted towards lower angles. At 32 Pa and 60 Pa the spectra are different from the previous ones: a broad band classic of amorphous metals becomes visible. The same feature is observed for all the coatings deposited at He pressures higher than 60 Pa (not reported in the graph), clearly indicating the same amorphous nature. By means of the Scherrer equation it is possible to obtain the mean crystallites size $\bar{D}$ as:

$$\bar{D} = \frac{K\lambda}{\beta cos\theta} \tag{4.1}$$

where K is a dimensionless shape factor, that varies with the actual shape of the crystallite, λ is the X-ray wavelength, β is the line broadening (FWHM) and θ is the Bragg angle. In figure 4.2b the trends of $\bar{D}$ and the film mass density ρ versus He pressure are thus summarized. The values of ρ are determined by crystal quartz microbalance measurements during deposition and confirmed by the numerical procedure exploited for Brillouin spectroscopy, which is described in section 3.1, by considering ρ as a free parameter for the minimization of the least square estimator of equation 3.2. c-W coatings are characterized by a mean global density of 18.2 g cm^{-3}, that is 5% lower than the polycrystalline value of 19.25 g cm^{-3}, and by crystallites size of about 16 nm. Increasing He pressure to 5 Pa leads to the decrease of the crystallites size to around 4 nm, without significantly affecting mass density (17 g cm^{-3}). This intermediate growth regime, where crystallites ranges between 4 nm and 10 nm, has been called *ultra-nanocrystalline* ($u-nano$) regime. Higher He pressures result

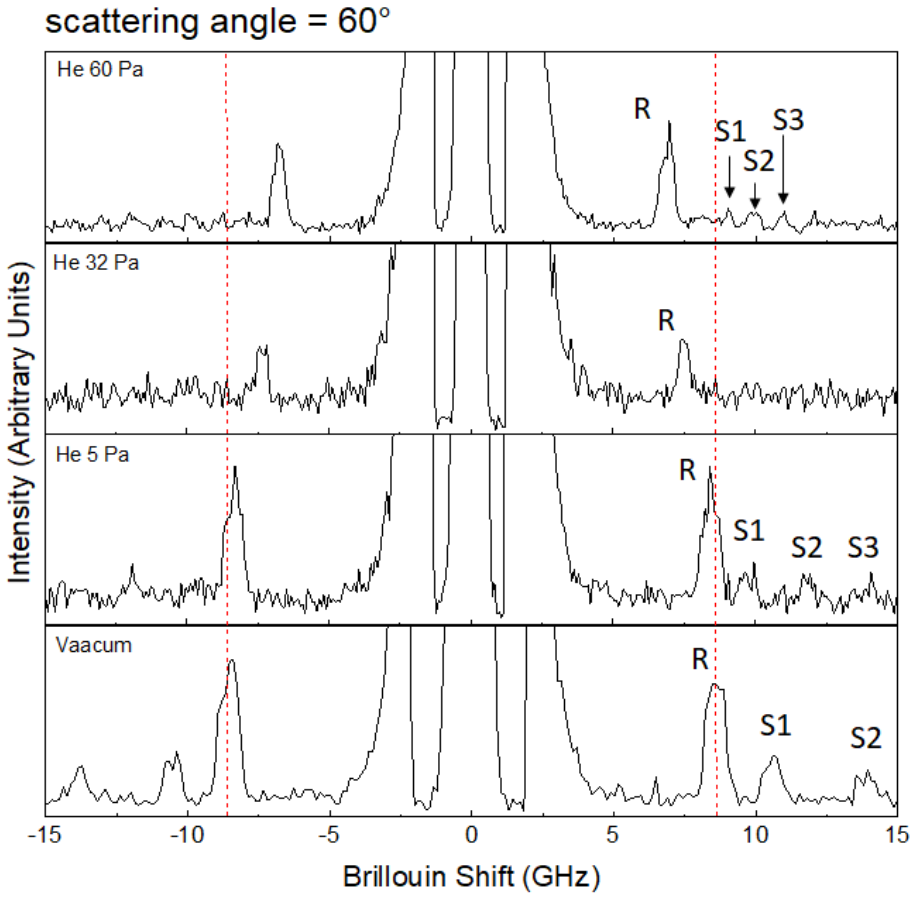

Figure 4.3: Brillouin spectra recorded at 60° of laser incidence for the different nanostructured W coatings. R, Rayleigh mode, S, Sezawa modes. p-W coatings do not show any Brillouin activity.

in the growth of a-W coatings, with a further drop of ρ to 14 g cm^{-3} at 32 Pa and to 11.5 g cm^{-3} at 60 Pa. At the same time, $\bar{D}$ goes from 4 nm to below 2 nm respectively. It is fundamental to remember that the use of the Scherrer equation to derive the mean crystallites size is reliable for crystallites dimension of several nanometers. Therefore, for $\bar{D} < 2$ nm, only qualitative extimation can be performed (alternative quantitative methods require for example Rietveld analysis). At 100 Pa of He (not shown in the graph) a further drop of ρ to 9 g cm^{-3} is observed, while $\bar{D}$ remains below 2 nm. No information of ρ is available for p-W deposited at 200 Pa of He or 50 Pa of Ar. In these cases, a linear dependance of ρ by He pressure is considered as a guess. This results in a mass density of ≈ 7 g cm^{-3}. Due to the very similar morphology, the same value is then considered also for p-W samples deposited at 50 Pa of Ar.

The drops of ρ and $\bar{D}$ are related to a higher free volume fraction within the film, meaning a higher mean interatomic distance and a lower mean interatomic binding energy. This unavoidably affects the thermomechanical properties of the samples that are in some way related to the interatomic potential. This is the case of the elastic moduli and the thermal expansion coefficient. These properties are determined by the new experimental setup de-

veloped in this thesis work based on the combined use of Brillouin spectroscopy and the substrate curvature method. In this case, due to the metallic nature of the samples, BS is limited to the surface investigation (see chapter 3 and appendix B). The Brillouin spectra of the various metallic W coatings are shown in figure 4.3. For simplicity, only the spectra recorded at 60° of laser incidence are reported. As it can be seen, for the majority of the coatings several surface acoustic waves are detected. As already mentioned in section 3.1, these surface acoustic waves are the Rayleigh and the Sezawa modes. They are mainly shear modes, that are modified by the presence of the film itself, with velocities below, in the case of the R mode, and above, in the case of S modes, the Rayleigh and the shear velocities of W (i.e. $\approx$ 2680 and 2800 m s^{-1}). The number and the presence of S modes are strictly correlated to the thickness of the film; in particular, they are likely detectable for film thickness of the order of the laser wavelength (i.e. 532 nm), while they are not found in micrometric thick coatings, where only the R mode is present. This latter condition results in the confinement of the displacement field, associated to acoustic modes, within the film, which, in turn, acts a semi-infinite medium (as a consequence, the R mode velocity does not depend on the probing angle). The presence of multiple S modes provides a remarkable quantity of experimental data that make the numerical computation of the elastic properties of the coatings very reliable. In addition, as noted above, the rich Brillouin signal allows also a quantitative estimation of the film mass densities. As it can be seen in figure 4.3, the spectra related to porous W coatings are not present. This is due to the fact that porous metallic films show no surface Brillouin activity. This is related to the cauliflower morphology, which, being really open, does not support acoustic waves propagation along the surface. For this reason, only a qualitative estimation of the elastic moduli can be proposed for these coatings (see below).

From figure 4.3, it is evident that c-W shows the highest Rayleigh velocity (v_R) (i.e. $\approx$ 2500 m s^{-1}). v_R clearly decreases with increasing background He pressure. In the case of a-W coatings, the Rayleigh velocity is $\approx$ 2150 m s^{-1} at 60 Pa, while it drops to $\approx$ 2080 m s^{-1} at 100 Pa (not shown in the figure). This trend suggests a consequent variation of the elastic moduli of the samples when going from c-W to a-W. As described in section 3.1, from Brillouin spectra recorded at various angles, the elastic properties can be derived. Trends of the elastic moduli versus He pressure are shown in figure 4.4. E drops from 381 to 145 GPa and G similarly drops from 148 to 53 GPa when going from c-W to a-W. Accordingly, G/K varies from 0.48 (c-W) to 0.24 (a-W). Inside the amorphous region, at 100 Pa of He, the moduli successively further decrease to E = 119 GPa, G = 43 GPa and G/K = 0.2. Lower stiffness is consistent with the lower values of ρ and $\bar{D}$ proper of the structures discussed above. For the same reasons, also c-W is characterized by E, G and G/K values slightly below the bulk ones (i.e. E = 411 GPa, G = 160 GPa and G/K = 0.52). The significant variation of the elastic properties induced by the transition from nano-crystalline to amorphous nanostructure has been widely studied through recent years. *Alcala et al.* [140]

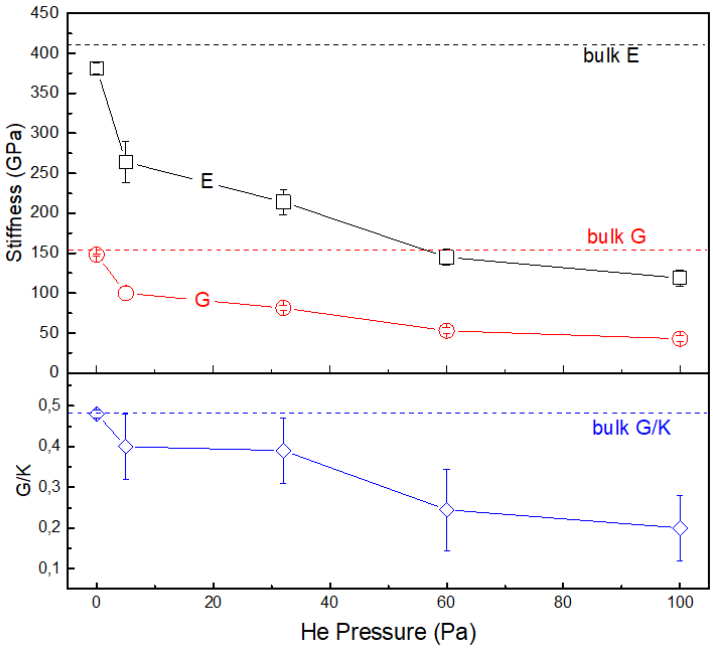

Figure 4.4: Elastic moduli computed by BS analysis for W coatings deposited at different He pressures.

found a drop in E of about 70% when going from $\gamma - Al_2O_3$ to amorphous alumina. *Jiang et al.* [141] found, for amorphous metals, G/K values 30% lower than those of the polycrystalline forms. The decrease of G/K can be interpreted qualitatively as an index of an increased ductility. In the case of amorphous metals, plasticity is attributed to the ability of the material to form shear bands analogous to the slip systems of their crystalline counterparts. The short-range atomic order of amorphous metals can determine the elastic moduli in a way different from that of the crystalline phase, where a long range order is also present [142]. In this way amorphous metals can be macroscopically brittle but microscopically capable of sustaining plastic shear flow [143]; in these terms, the observed decrease of G/K can be interpreted as an index of increased ductility with the growth of the amorphous phase. The results found in this work are in qualitative agreement with the observed decrease of the G/K ratio going from nanocrystalline to amorphous phases that can be found in other literature works [140, 141].

Since no information from BS analysis is detectable for p-W coatings, the elastic moduli of these coatings are derived by considering a linear dependance of E, G and G/K by the film mass density. This means that, if ρ, going from 9 g cm^{-3} for a-W to 7 g cm^{-3} for p-W, decreases by $\approx 22\%$, the same drop is considered for the elastic moduli with respect to the a-W ones. This results in E = 93 GPa, G = 34 GPa and G/K = 0.15. These values are considered for both of p-W coatings deposited at 200 Pa of He and 50 Pa of Ar. Since these values are not directly measured, they are not summarized in figure 4.4. The elastic constants of porous media can be properly estimated by considering recent relevant literature results proposed by *Braeckman et al.* [136] about Brillouin scattering in porous

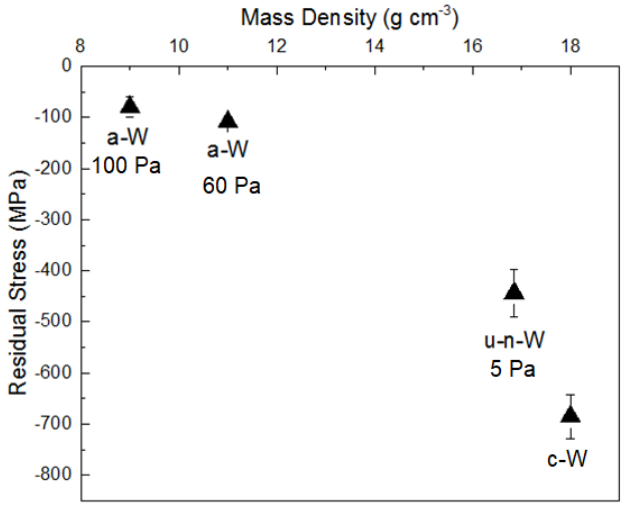

Figure 4.5: Residual stress measured for c-W, u-n-W and a-W coatings with approximately the same thickness (i.e. 400 nm).

metallic films. These properties can be derived as reduced elastic constants of a-W by a factor which is the porosity degree of the material, which, in turn, is estimated as function of the film mass density as $D_p = (\rho_{a-W} - \rho_{p-W})/(\rho_{a-W})$ (see chapter 5).
Exploiting the substrate curvature apparatus, residual stresses of the coatings are obtained by measuring the curvature change between the uncoated and coated Si wafer at room temperature. The results are reported in figure 4.5. Since the stress is strictly related to the coating thickness, only the residual stresses of the coatings with aproximately the same thickness (i.e. 400 nm) are reported. They are plotted versus film mass density. In the case of c-W an initial state of compressive residual stress of 684 $\pm$ 42 MPa is found. The compressive stress is in agreement with the residual stresses found for other compact coatings deposited by PLD. As pointed out in different works [144–148], the higher the energy of the ablated particles, the higher the compressive residual stresses. For this reason, columnar nanocrystalline W samples that, being deposited in vacuum conditions are formed by more energetic particles, are characterized by a higher compressive residual stress than amorphous ones, which, on the contrary, are not as closely packed as columnar film. The residual stress, indeed, drops from 684 MPa for c-W, where the highest mass density is observed, to around 80 MPa for the a-W structure obtained at 100 Pa of He, when the mass density becomes the 50% the c-W one. In the case of cauliflower morphologies (i.e. at 200 Pa of He and 50 Pa of Ar), the residual stress is, instead, slightly tensile (i.e. $\approx$ 50 MPa). This could be associated to the increasing porosity degree as remarked by *Portinha et al.* in [149]. It is fundamental to remember that σ_{res} depends only on the thicknesses of the film and the substrate (which are accurately measured by SEM), and on the elastic properties of the substrate, that are usually known. For this reason, quantitative information about σ_{res} can be acquired also in the case of p-W coatings even if no Brillouin data are available.

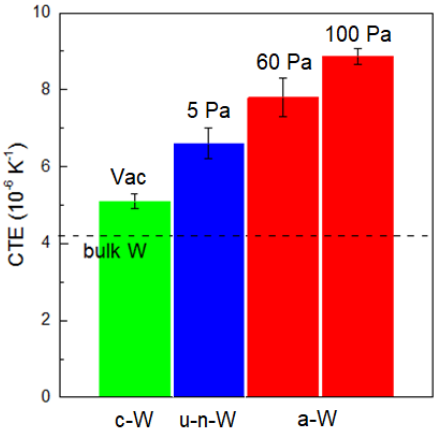

Figure 4.6: Residual stress measured for c-W, u-n-W and a-W coatings with approximately the same thickness (i.e. 400 nm).

Finally, by measuring the curvature change upon temperature variation, the CTEs of the films are obtained. For their computation, the elastic moduli (i.e. E and ν) derived by BS are considered. The obtained CTEs of metallic W coatings are shown in figure 4.6. As it can be seen, all the CTEs lie above the bulk value of 4.2 x 10^{-6} K^{-1} reported in literature for polycrystalline W [150]. A clear dependence of this parameter by the nanostructure is found. c-W has a mean CTE of 5.1 x 10^{-6} K^{-1}, which is close to the bulk one. For a-W samples, the CTE is around 8.1 - 8.9 x 10^{-6} K^{-1}, which is almost twice the bulk one. Due to their very low adhesion to the substrate, which resulted in early delamination from the substrate during heating, no information about p-W coatings is available.
The measured values are in good agreement with commonly reported literature results. Generally, nanocrystalline metals are used to show a higher CTE with respect to the one of the crystalline counterpart [151–153]. With respect to a crystalline bulk W, the presence of a higher fraction of interfaces between the small grains deeply affect the properties of the

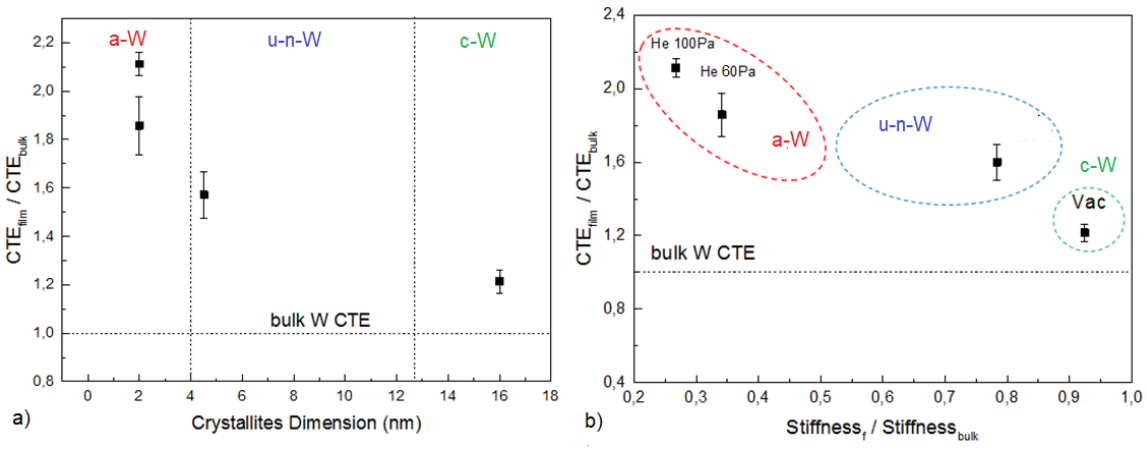

Figure 4.7: Residual stress measured for c-W, u-n-W and a-W coatings with approximately the same thickness (i.e. 400 nm).

material [154]. The weaker bonding of grain boundaries atoms modify the interatomic potential, lowering it and making it more asymmetrical. The net result is a favoured movement of the atoms around their lattice positions upon heating. This means an enhancement of the CTE, which is thus strictly related to the volume fraction of grain boundaries. It has been shown that, in the case of nanocrystalline metallic films, the CTE at grain boundaries can even increase 2 - 5 times the crystalline value [155, 156]. This dependence of the CTE with the crystallites dimension is shown in figure 4.7a. As it can be seen, the overall observed behavior is that as $\bar{D}$ decreses the CTE increases. c-W sample shows a CTE 1.2 times the bulk one, which increases up to 2.1 times the bulk one for a-W samples. As shown by *Lu et al.,* in [152], copper films with 8 nm grains show a CTE 1.8 times higher than the one of the corresponding crystalline structure. The monotonically increasing behaviour of the CTE in the a-W region is not worthy, since the investigation of the CTE of amorphous materials still leads to controversial results in literature. In some cases [151, 157, 158], starting from the coarse grained structure, an increase of the CTE is observed as $\bar{D}$ decreases until the amorphous region is reached. The disappearing of a crystalline order finally results in a consistent drop of the CTE. This has been observed, for example, in the case of gold films [157] and Fe alloys [158]. On the other hand, other works [152, 154, 159, 160], in accordance with the trend observed in this work, report a CTE of the amorphous phase still higher wih respect to the nanocrystalline one. This is consistent with higher mean interatomic distance, which means a lower binding energy. Moreover, the mean interatomic potential can be affected by the density of defects, that in turn are related to the tensile or compressive residual state of stress [161, 162]. For this reason, the porosity of the film can be a key parameter in driving the thermal expansion of the coating, inducing preferred dilatation directions, with a net result of an increase of material CTE as the porosity of the material increases [160]. This is fully consistent with the decrease of the film mass density observed when going from c-W to a-W coatings. It has been previously shown that the drop of ρ drastically affects the stiffness of coatings. In the same way, as reported in figure 4.7b, the softer the material, the higher the CTE. This well known stiffness-CTE behaviour is reported in several literature works [151, 153, 161]. However, this relationship is not linear as it could be expected from the Stoney equation. The deviation from linearity can be attributed to an interplay between the crystallites dimension and the mass density of the material in affecting the overall thermal expansion behavior.

4.1.2 W-Tantalum coatings

W-Ta films with Ta concentrations ranging from 4 to 23% are now considered. Cross section SEM images are shown in figure 4.8. As it can be seen, all the samples show the same columnar structure of metallic W deposited in vacuum. In the XRD spectra in figure 4.9a it is evident that when Ta concentration increases, no new reflections appear, and the main peak, corresponding to the (110) reflection of crystalline α-W, gradually shifts from 40.416

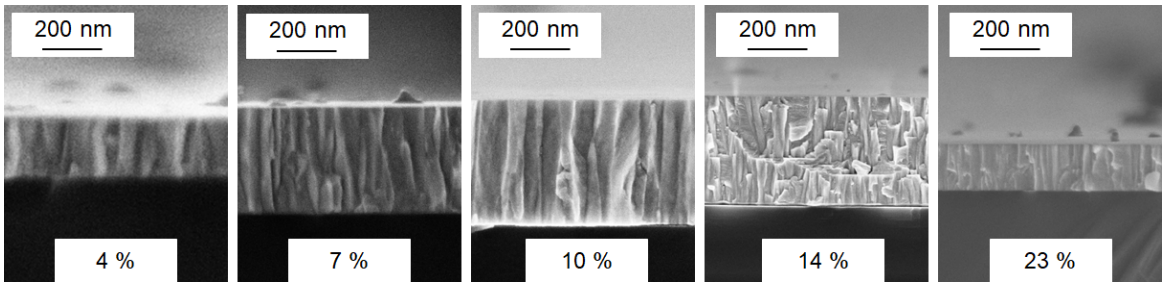

Figure 4.8: SEM images of W-Ta coatings deposited by PLD with increasing Ta concentration.

- 2θ degrees, the angle corresponding to α-W, towards 38.473 - 2θ degrees, the angle corresponding to α-Ta. As already reported in [163–165], this shows that the addition of Ta to a W matrix leads to solid solution regime in which the Ta atoms are substitutional. However, boosting the Ta amount leads to a decrease in the crystallinity of the film. Ta atoms interfere with the W lattice hindering the growth of the crystallites. As a result, $\bar{D}$ goes from 16 to 7 nm when the Ta content goes from zero to 23%. Therefore, Ta alloying does not promote any amorphization of the material. For Ta concentration below 23% the coatings are all characterized by the c-W structure, while at 23% the films are ultra-nanocrystalline. The variation of $\bar{D}$ is clearly more appreciable than the mass density one. Dealing with solid solution regimes, the mass density can be computed by the lever rule:

$$\rho_{W-Ta} = [W]\rho_W + [Ta]\rho_{Ta} \tag{4.2}$$

This leads to values of ρ ranging from 18.2 g cm^{-3} (pure c-W) to 17.4 g cm^{-3} (23% Ta) (see figure 4.9b).

Brillouin spectra are shown in figure 4.10. As it is found for metallic W coatings, even for W-Ta coatings the presence of R and S modes is clearly visible. Focusing on the R mode, it is evident that with increasing Ta concentration, the peak shifts towards lower frequencies, so towards lower velocities. In particular, the Rayleigh velocity goes from $\approx$ 2450 m s^{-1}

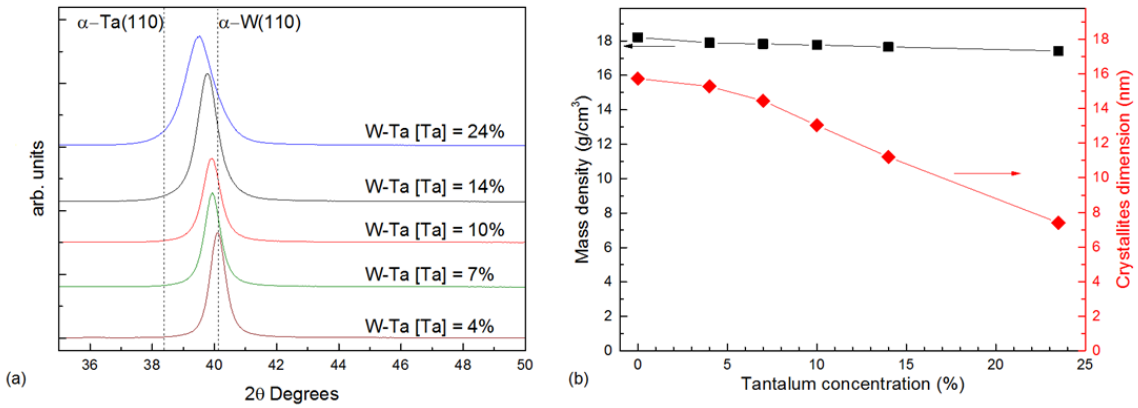

Figure 4.9: a) XRD spectra of W-Ta coatings, b) Mean crystallites size and mass density of W-Ta films

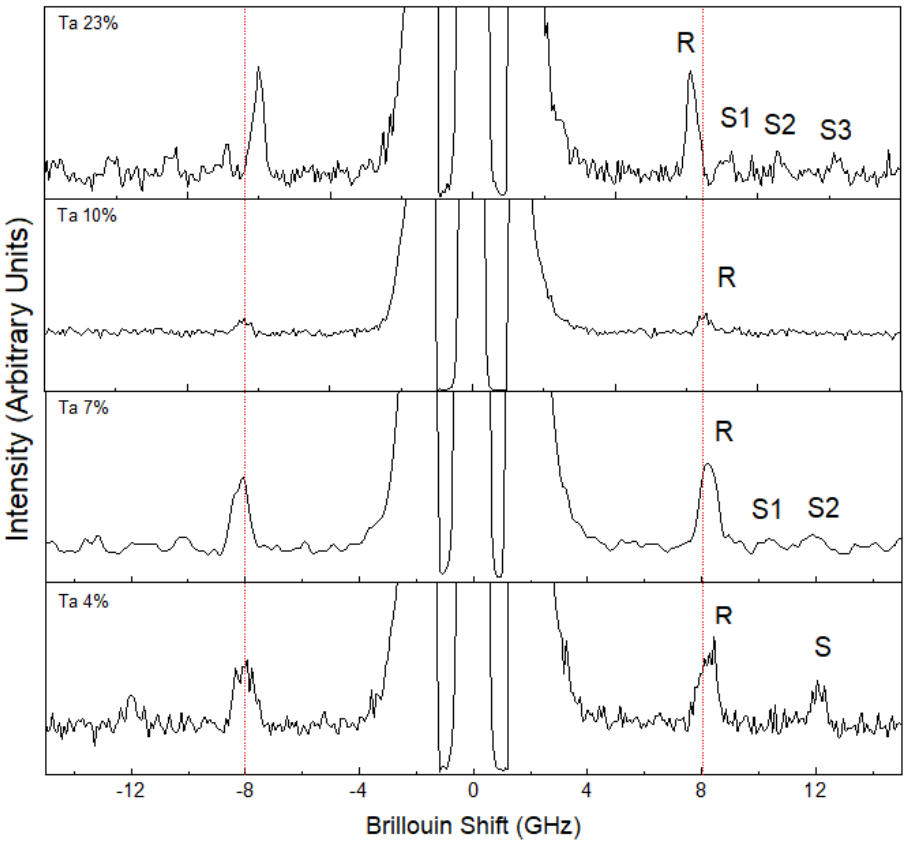

Figure 4.10: Brillouin spectra recorded at 60° for W-Ta coatings.

in the case of 4% of Ta concentration, to $\approx$ 2250 m s^{-1} for the 23% W-Ta sample, progressively approaching the bulk Ta value of 1900 m s^{-1}. The presence of multiple S modes allows the estimation of ρ by Brillouin data. The obtained results well confirm the predictions made by the lever rule of equation 4.2. As shown in figure 4.11, the trends of E and G are almost linearly decreasing with increasing Ta concentration. In particular, the material is softened by about 28%: E falls from 381 GPa to 271 GPa and similarly G from 148 GPa to 101 GPa. The most probable value of the G/K ratio does not substantially change between zero and 14%, while decreasing by 30% in the alloy with 24% of Ta. Figure 4.11 shows that the gap between the experimental values of E, G and G/K and those computed by the lever rule (the dotted lines) becomes remarkable for Ta concentrations above 10%. This discrepancy can be attributed to the above mentioned reduction of the crystallites size, which leads to a variation of the mechanical behaviour beyond the one foreseen by the solid solution regime alone when the concentration of Ta atoms becomes relevant. Accordingly to the above discussion, the decrease of the G/K ratio can be interpreted as indicating the increasing material ability to support local plastic flow. When the Ta fraction increases, the higher elastic moduli of W are gradually shifted towards the lower values proper of Ta, leading to a global softening and local ductilization of the material. This is a quite surprising result, since in previous studies no appreciable ductilization of microcrystalline W has been

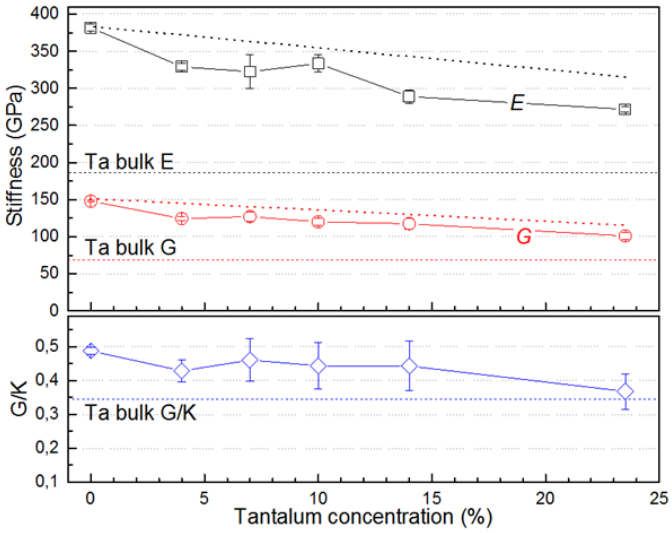

Figure 4.11: Elastic moduli computed by BS analysis for W-Ta coatings deposited with different Ta concentration.

reported upon alloying with Ta [166]. However, different materials production methods, in addition to specific microstructures, can diversely affect the overall mechanical properties of the materials. Therefore, further investigations are mandatory in order to clearly assess the effect of Ta alloying on the ductilization of W in the coating form.

The residual stress and the thermal expansion coeffcient of W-Ta coatings are summarized in table 4.1. The residual stress is compressive, reflecting the columnar structure of the coatings, very similar for all the samples (i.e. $\approx$ 300 MPa), but lower than the ones observed in the case of pure c-W and u-n-W. This could probably be related to a worse crystalline quality induced by the presence of Ta substitutional atoms (σ_{res} decreases as Ta% increases) [145]. On the contrary, the CTE is found to be severely affected by the concentration of Ta atoms. As it can be seen, at 4% the CTE is $5.23 \cdot 10^{-6}$ K^{-1}, which is really close to the c-W value (i.e. $5.1 \cdot 10^{-6}$ K^{-1}), while it approaches the bulk value of Ta (i.e. $6.2 \cdot 10^{-6}$ K^{-1}) even at 10% (i.e. $6.34 \cdot 10^{-6}$ K^{-1}). At 23%, the CTE is $\approx 7.26 \cdot 10^{-6}$ K^{-1}, which is almost twice the CTE value of bulk W and 1.2 times the bulk Ta one (i.e. $6.3 \cdot 10^{-6}$ K^{-1}). Since this value is even higher the CTE of bulk Ta and the variation of ρ is really small between the various samples, the shrinkage of the crystallites down to 7 nm predominately governs the thermal expansion behavior of W-Ta. This tunable increase of the CTE with respect to pure W has been already observed in past works, and it has

Ta concentration	Residual Stress (MPa)	CTE (10^{-6} K^{-1})
4%	-330	5.23
10%	-350	6.34
23%	-280	7.26

Table 4.1: Residual Stress and thermal expansion coefficient of W-Ta coatings.

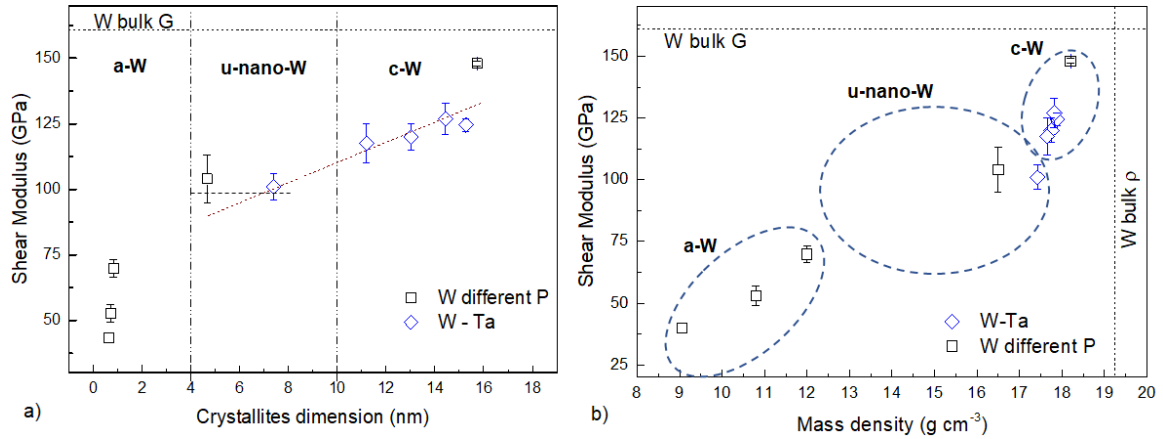

Figure 4.12: a) Trend of the shear modulus G vs crystallites size $\bar{D}$, b) trend of the shear modulus G vs film mass density ρ.

made W-Ta coatings interesting for many applications even in the nuclear fusion research field (e.g. joining with Cu heat sink in the W divertor) [167]. However, the observed high irradiation embrittlement proper of this type of alloy is the cause of the abandonment of this solution, at the moment, for any kind of application in nuclear fusion reactors.

4.1.3 Relationship between the nanostructure and the thermomechanical properties of metallic W coatings

It is shown above that the elastic moduli, the coefficient of thermal expansion and the residual stress of a coating can be tuned varying the mass density and the crystallites dimension, simultaneously or independently. This is best shown by the trend of shear modulus G which, as noted in section 3.1, is the most reliable outcome of Brillouin spectroscopy. Figure 4.12 summarizes the trends of G of the all analyzed samples versus $\bar{D}$ (4.12a) and ρ (4.12b). The amorphous region ($\bar{D} < 4$ nm) is characterized by markedly lower values of G. In this re-

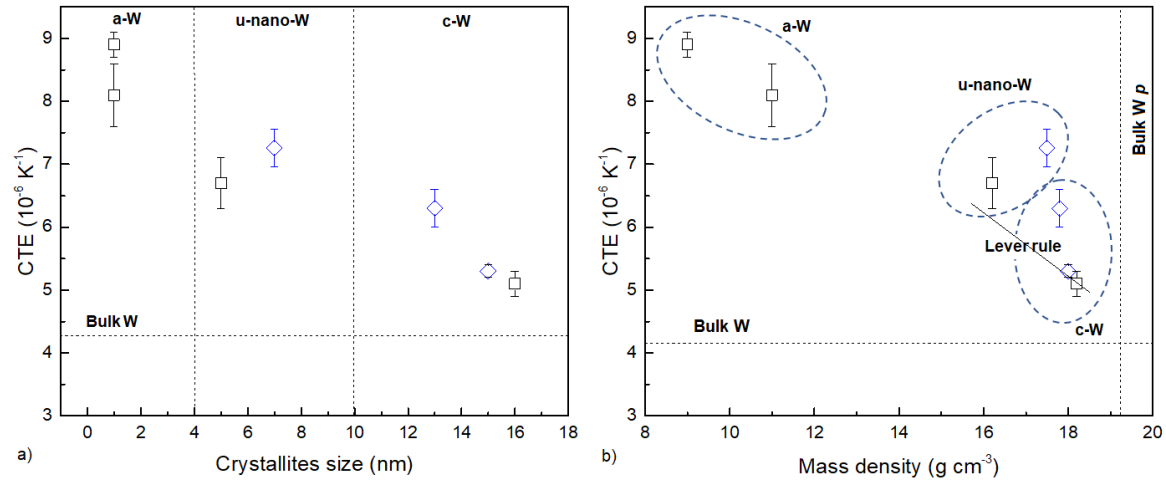

Figure 4.13: a) Trend of the CTE vs crystallites size $\bar{D}$, b) trend of the CTE vs film mass density.

gion the samples behave as metals in the amorphous regime, and the shear stiffness changes appreciably even for a very small variation of $\bar{D}$. The transition to the ultra-nanocrystalline region is characterized by crystallites size becoming of at least few nanometers ($\approx$ 4 nm). This crystallites remain embedded in an amorphous matrix of different elastic properties; the overall shear stiffness is thus determined by both the properties of the crystallites and those of the matrix. For $\bar{D}$ above 10 nm, the nanocrystalline domain is achieved, in which G is almost linear with the crystallites dimension. Extrapolating this linear trend, the mean crystallites size necessary to confer the bulk elastic properties to c-W turns out to be $\approx$ 25 nm. From figure 4.12b, it is evident that in the amorphous region the different stiffnesses are mainly related to the different mass densities. In the ultra-nanocrystalline region, a low sensitivity of G to the mass density is found, the crystallite size becoming also relevant. This region includes samples obtained by the two different preparation processes described above. The interplay between crystallites and matrix properties is such that the overall stiffness remains, fortuitously, almost constant, for mass densities going from 16 to 17 g cm^{-3}, while the crystallite sizes go from 8 to 4 nm. For the samples analyzed in this study, the growth of the crystallites balances the decrease of ρ. Finally, in the columnar nanocrystalline region, where $\bar{D}$ goes from 10 to 16 nm and ρ from 17.6 to 18.2 g cm^{-3}, G turns out to be linearly increasing with ρ as confirmed by the lever rule, but more influenced by a variation of $\bar{D}$. A similar trend is clearly visible also in figure 4.13, where the CTE of W and W-Ta coatings is shown as function of the crystallites size and mass density. In this case, the amorphous region is characterized by markedly higher values of the CTE. As it happens for the stiffness, in this region, the variation of the mass density (so the porosity degree of the material) governs the thermal expansion behavior of the coatings. In the ultra-nano-crystalline region, instead, the CTE between the two samples analyzed in this work changes more than the stiffness does. This means that in the ultra-nano-crystalline region the CTE is more governed by a variation of $\bar{D}$. Finally, in the columnar nanocrystalline region, the CTE turns out to be linearly decreasing with increasing $\bar{D}$ and ρ, but it does not correspond to the values computed by the lever rule.

4.2 Influence of Oxygen and Nitrogen: W co-deposits

4.2.1 W-oxide coatings

W-oxide coatings are investigated as proxy of co-deposited W in tokamaks in presence of oxygen as gas impurity. Since very little is known about the redeposition process and the effective amount of retained oxygen in redeposited W layers, it is fundamental to investigate a wide range of samples. Moreover, beside the mere nuclear fusion interest, W-oxide coatings are exploited in many different applications, such as electrochromic devices, photocatalysis and gas sensing, solar-cell research, smart windows, superhydrophobic surfaces and photoelectrochemical water splitting. The understanding of their properties, in partic-

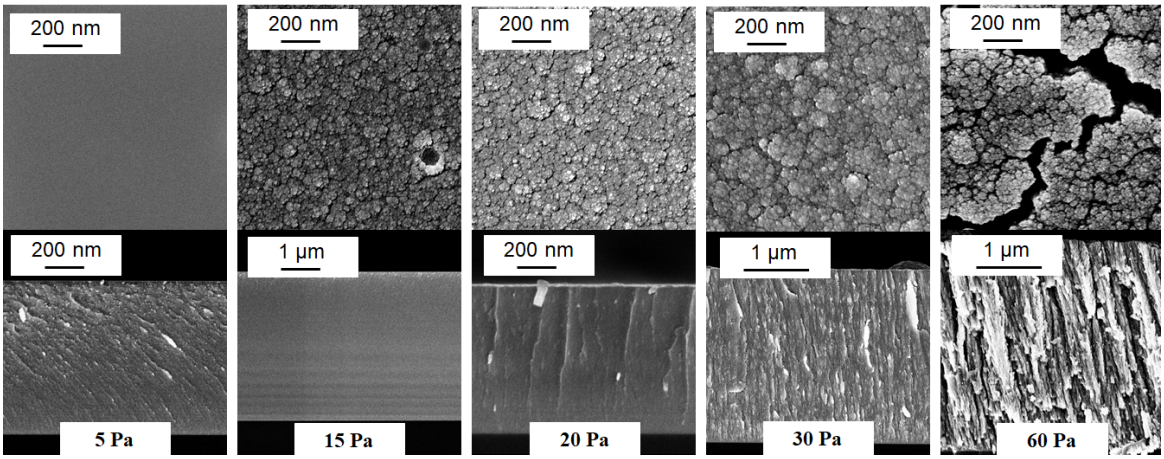

Figure 4.14: SEM top view and cross-section images of W-oxide coatings deposited at various O_2 pressures.

ular when dealing with nanostructured W-oxide coatings, is thus of peculiar relevance for materials science.

W oxide coatings are produced by PLD by exploiting a 99.9% pure W target, ablated by the same Nd:YAG laser adopted for the previous depositions, with λ = 532 nm and laser fluence $\approx$ 15 J cm^{-2}. The ablated W particles expand in the vacuum chamber in presence of O_2 atmosphere, and deposit above a Si(100) substrate. Being a reactive gas, that chemically react with W, O_2 can promote, under some conditions, the formation of W-oxide films. In this section, the effect of different O_2 pressures on the thermomechanical properties of the coatings is investigated.

The variation of O_2 pressure leads, as already explained, to different plasma expansion dynamics, affecting, in particular, the energy loss of ablated species before the deposition on the substrate. As the pressure increases, plasma plume confinement is such that the ablated species likely interact between each other before reaching the substrate. This favors clustering and the formation of porous coatings. At low O_2 pressures, instead, the plume is less confined and the species start compacting once deposited onto the substrate, leading to more compact morphologies. This is well highlighted by SEM images of figure 4.14: samples produced with at O_2 pressure below 30 Pa are characterized by a compact morphology, while, for higher pressures, an open porous morphology prevails. At 60 Pa the pressure is sufficiently high to start promoting cauliflower growth. In addition, probably due to the high state of residual stress which develops during the growth, an extended crack network is clearly visible. From EDS analysis (see figure 4.15) it is clear that the O/W stoichiometric ratio is severely affected by the deposition pressure. It is $\approx$ 2.1 at 5 Pa, increasing to $\approx$ 2.6 at 15 Pa. Those values are well below the WO_3 stoichiometry. At 30 Pa, instead, the film is almost stoichiometric WO_3, while slightly sub-stoichiometric (i.e. O/W $\approx$ 2.9) at 20 and 60 Pa. It is fundamental to remember that EDS analysis alone are not sufficient to assess the real material stoichiometry. The detected oxygen content, indeed, could be the total amount of bonded and unbounded O_2 which is present in the film, thus resulting in possible

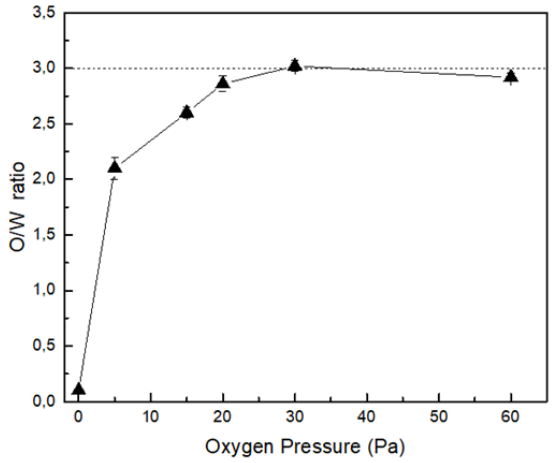

Figure 4.15: EDS measurements of W/O composition.

interpretation errors of the real film stoichiometry. The strong evidence of WO_3 formation is, however, provided by Raman analysis of figure 4.16. In all the acquired spectra two broad bands are visible: a low frequency band in the range of 100 - 500 cm^{-1}, which is associated to the O-W-O bending modes, and a high frequency band in the range of 600 - 900 cm^{-1}, that is attributed to the W-O stretching modes [169]. The small band at about 960 cm^{-1}, instead, can be attributed to the W = O stretching modes at grain boundaries, and it is related the nanocrystallinity of the material [169]. All these Raman features are well described in literature and clearly underline that the samples are amorphous WO_3 [169–171]. The different band shapes between the samples can be attributed, instead, to stoichiometric defects. This is much more evident at 5 and 15 Pa, where higher differences in the O/W ratio are observed. Moreover, in contrast to the spectra obtained for coatings deposited above 20 Pa, in these cases the peak at 521 cm^{-1} associated to the first order scattering of the Si substrate is not present. This is a strong evidence that these coatings are not completely

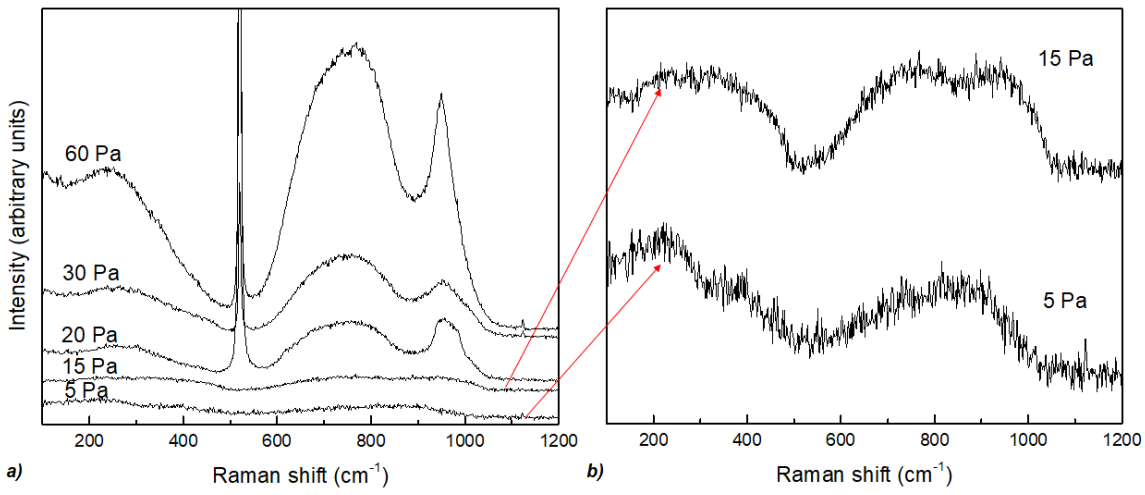

Figure 4.16: Raman spectra of W-oxide coatings deposited at various O_2 pressures.

O_2 Pressure (Pa)	n	ρ (g cm^{-3})	R^c	R
5	-	11	-	47
15	-	8.5	-	-
20	1.7 ± 0.1	5	17 ± 1	18
30	1.65 ± 0.08	4.7	16 ± 0.5	17
60	1.5 ± 0.1	4	12 ± 2	13

Table 4.2: Refractive index (at 532 nm), mass density, computed optical reflectance R^c, and measured optical reflectance R of a-WO_{3-x} coatings. The error bars associated to R^c are related to thickness inhomogeneities.

optically transparent, such that the oxide formation regards only a part of the sample (reasonably the surface), while the rest of the film still behave like metals (i.e. due to the low laser extinction length of metals the probing laser is rapidly absorbed within few nanometers). For this reason these samples will be called **a-W(O)**, to better stress the amorphous metallic nature of the material with high oxygen content. Coherently, samples deposited at 20, 30 and 60 Pa will be **a-WO_{3-x}**, in order to highlight the small stoichiometric defect with respect to WO_3.

EDS analysis are also exploited to obtain the mass density of the coatings. The mass density (ρ) of a-WO_{3-x} coatings turns out to be $\approx$ 5 g cm^{-3} at 20 Pa, 4.7 g cm^{-3} at 30 Pa and $\approx$ 4 g cm^{-3} at 60 Pa. All the obtained values are below the bulk value of 7.1 g cm^{-3} of crystalline WO_3. This is in agreement with the high porosity degree that characterizes our samples. No direct measurements of ρ of a-W(O) coatings are performed. Due to their amorphous structure and compact morphology that clearly remind the one observed for a-W coatings (see above), the mass density is computed starting from 11.5 g cm^{-3} (i.e. ρ of a-W) and considering the different O/W ratios. All ρ values are summarized in table 4.2. Experimental values of the optical reflectivity R of the coatings are obtained by a UV-Vis-NIR PerkinElmer Lambda 1050 spectrophotometer with a 150 mm diameter integrating sphere. R is evaluated for successive BS analysis at λ = 532 nm (i.e. the wavelength of the probing lasers). It goes from 47% for a-W(O) coatings to 18% at 20 Pa, 17% at 30 Pa and 13% at 60 Pa. This clearly underlines the bivalent metallic - oxide nature of the deposited samples below and above 20 Pa.

This bivalent nature is well highlighted also by BS analysis. Brillouin spectra recorded for a-W(O) and a-WO_{3-x} samples are shown in figure 4.17. All the spectra are recorded at a laser angle of incidence θ = 60°. As it can be seen, in the case of metallic W(O) coatings, only a low frequency mode can be detected. It is associated to the surface Rayleigh wave of the film. The micrometric thickness of the probed films is such that the Rayleigh wave is the only detectable surface wave. This obviously results in a low amount of experimental data for the numerical computation of the elastic moduli (so in higher uncertainties). The Rayleigh mode, then, shifts towards lower frequencies, so towards lower velocities, as the O_2 pressure increases from 5 Pa to 15 Pa. In the case of optically transparent WO_{3-x} sam-

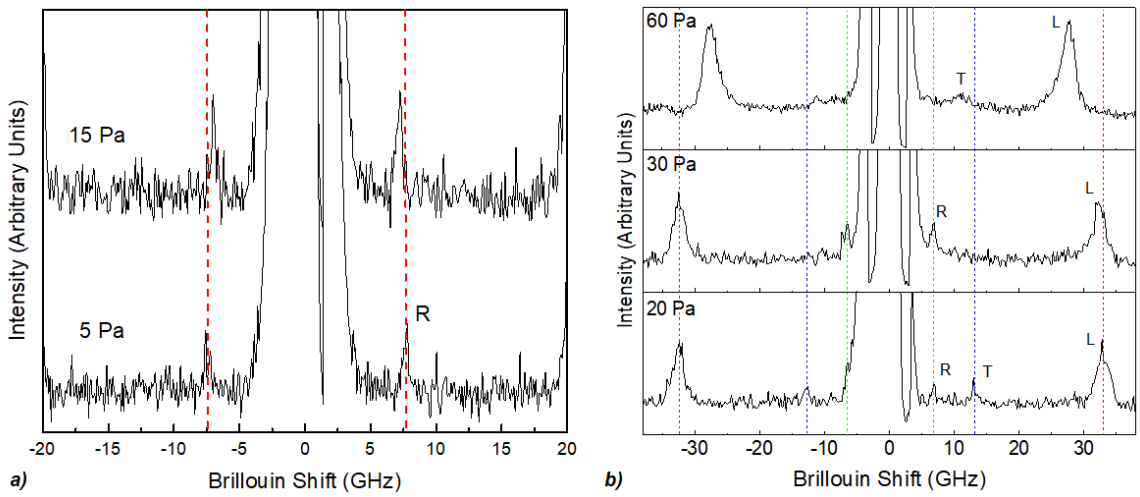

Figure 4.17: a) Brillouin spectra obtained for W(O) coatings, b) Brillouin spectra of a-WO_{3-x} coatings. R = Rayleigh mode, T = bulk transverse mode and L = bulk longitudinal mode.

ples, in addition to the low frequency R mode, two additional peaks associated to scattering events of the probing laser within the bulk are clearly visible: the mid frequency transverse bulk acoustic wave (T) and the high frequency longitudinal bulk acoustic wave (L). The scattering cross-sections of these two modes are evidently different, as it is remarked by the much higher intensity of L peaks with respect to T ones. As it can be seen, while the spectra obtained at 20 and 30 Pa are quite similar, at 60 Pa an evident shift of the modes towards lower frequencies is detected. In addition, the R mode disappears. In this case, due to the really open porous morphology, surface wave propagation is no more supported. From the positions of the bulk waves in the spectra, so their velocities v_L and v_T, the C_{11} and the C_{44} constants can be directly determined from the following relations:

$$v_L = \sqrt{\frac{C_{11}}{\rho}} \quad v_T = \sqrt{\frac{C_{44}}{\rho}} \tag{4.3}$$

without exploiting, in principle, the numerical procedure adopted for surface acoustic waves. On the opposite of what happens for surface modes, in the case of bulk waves there is no dependence of the peak position in the spectrum by the incidence angle θ (see Appendix B). Therefore, when bulk waves are detected, only one angle can, in principle, be explored to derive all the information about C_{11} and C_{44}. v_L and v_T can be, in turn, directly computed from the frequency shifts ($\Delta\omega$) of the L and T peaks in the spectra as:

$$v_{L,T} = \frac{\Delta\omega_{L,T}\lambda_0}{4\pi n} \tag{4.4}$$

In equation 4.4, λ_0 is the laser wavelength and n the refractive index of the material [168]. Therefore, in order to obtain information coming from bulk waves, the refractive index of the material must be known. Here, no direct measurements of n are available (e.g.

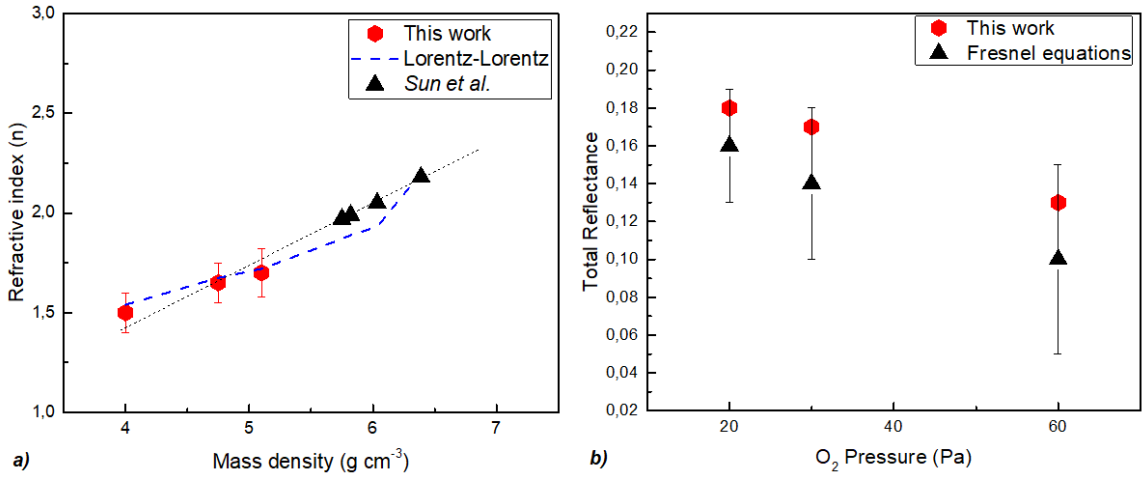

Figure 4.18: a) Refractive index computed for the different a-WO_3 coatings plotted as function of the film mass density (red marks). The experimental data are compared with the ones reported in literature [172] and the ones computed by equation 4.5. b) Comparison between the total reflectance obtained by experimental results and by theoretical solution.

by ellipsometry). On the other hand, the simultaneous presence of the R and T waves, observed at 20 Pa and 30 Pa, can be exploited to indirectly derive a consistent estimation of n. Due to its predominantly shear nature, the Rayleigh velocity can be approximated in terms of v_T as function of the Poisson ratio (see chapter 3). Since the computation of v_R from the corresponding frequency shift does not require the knowledge of n, v_T is guessed to be $\approx v_R$. The Poisson's ratio is usually between 0 and 0.5, therefore $v_T \approx v_R$ does not introduce a significant error in this approximation. The obtained value is thus inserted in equation 4.4, such that n can be extracted. At 60 Pa, due to the absence of the R wave, n is estimated by means of the well known *Lorentz-Lorentz* correlation:

$$\rho_{60} = \rho_{20} \frac{n_{20}^2 - 1}{n_{20}^2 + 2} \frac{n_{60}^2 + 1}{n_{60}^2 - 1} \tag{4.5}$$

where ρ_{20} and ρ_{60} are the mass densities of the amorphous coatings at 20 and 60 Pa respectively, while n_{20} and n_{60} the corresponding refractive indexes. The obtained values of n at 532 nm are summarized in table 4.2. These values are quite lower than the commonly reported ones of crystalline and nanocrystalline WO_3 that can be found in literature (i.e. n between 1.9 and 2.2) [172]. However, they agree with the low measured mass density, that is well known that affects the refractive index of the material [172]. These results are verified by computing, from the obtained n values, the theoretical optical reflectivity R^c of the coatings by means of the complex matrix form of the Fresnel equations that can be easily found in many books [173, 174]. Theoretical and measured R values are summarized in table 4.2. As it can be seen, the results are in good agreement. The associated error bars are computed from the uncertainty related to thickness inhomogeneity. As it can be seen, the results are in good agreement. Therefore the obtained values of n can be consistently

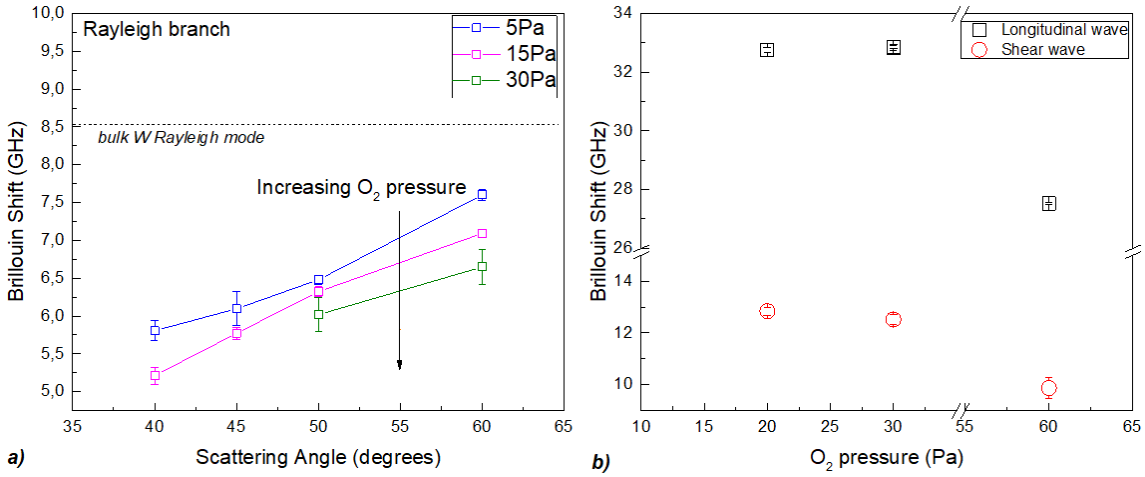

Figure 4.19: a) Rayleigh disperion relations for the W-oxide coatings; b) Bulk waves Brillouin shifts for a-WO_3 samples.

applied for the derivation of the bulk waves velocities.

As it can be seen from figure 4.19, the frequencies of each peak in the spectra are strongly affected by the deposition condition. This obviously results in a severe variation of the elastic properties. In figure 4.20 the values obtained for E, G and G/K are reported. E goes from $\approx$ 160 GPa to $\approx$ 67 GPa when the pressure is increased from 5 to 20 Pa. Coherently, G drops from $\approx$ 65 GPa to $\approx$ 30 GPa. The W(O) sample obtained at 5 Pa of O_2 shows a similar structure and morphology of metallic a-W samples analyzed in section 4.1.1. The values of E, G and G/K, indeed, are very close to the ones reported for a-W in figure 4.4.

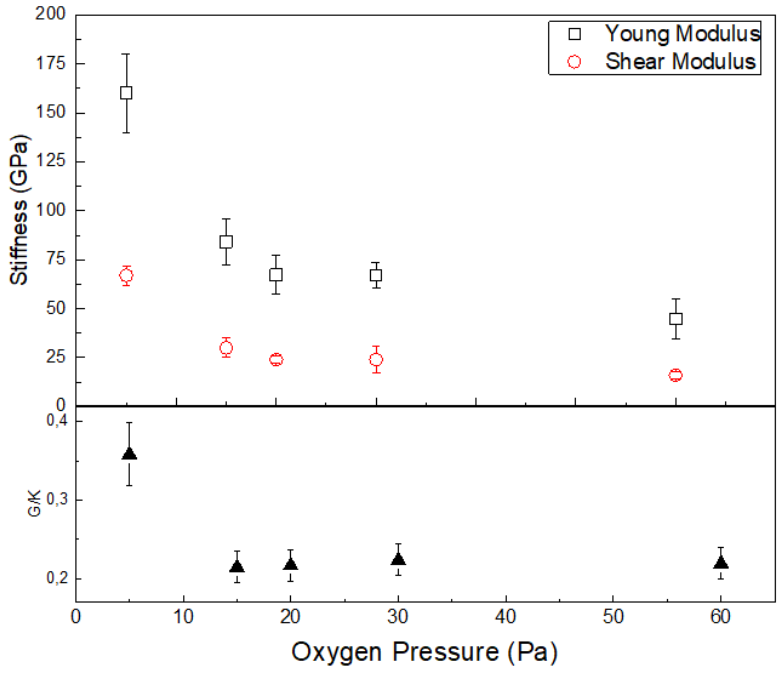

Figure 4.20: Elastic properties of W-oxide coatings.

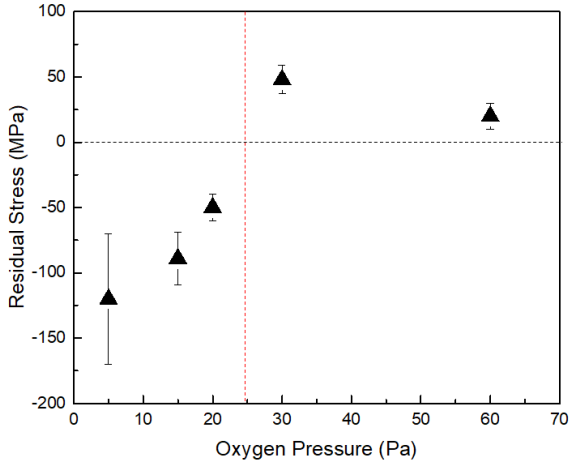

Figure 4.21: Residual stresses of W oxide coatings.

In general, the formation of the a-WO_3 phase is associated to a lower stiffnes with respect to W(O). Indeed, a drop by about 54% of the stiffness is observed when going from 5 Pa to 20 Pa. These results can be compared to the ones reported in some literature works [175–177] for sputtered WO_3 coatings. *Parreira et al.* [175] found a Young modulus of amorphous WO_3 samples of $\approx$ 100 GPa, which is slightly higher than the values found in this thesis. For lower oxygen contents this discrepancy is, instead, evidently less pronounced: E varies between 170 and 100 GPa for O_2 concentrations between 67% and 72%, which correspond to the E values measured for W(O) coatings of 160 GPa and 80 GPa. *Polcar et al.* [176] and *Carrejo et al.* [177], instead, report higher Young modulus (i.e. between 110 and 164 GPa) for compact amorphous-WO_3 coatings. Nevertheless, the correlation between all these results is difficult since there is no information about the material mass density, that severely affects the elastic properties of the material. Moreover, the morphology of the samples is completely different (i.e. compact vs porous) and in this thesis there is no information about the amorphous degree of the samples (e.g. from XRD analysis), in order to perform quantitative comparison between the structures of the coatings. However, the authors show an evident softening of the coatings with O_2 enrichment in the sputtering atmosphere. This trend is qualitative in accordance with the proposed results. Quantitative deviation from the two observed trends can be thus attributed to differences in film structure and morphology, that can be directly related also to different samples preparation techniques (i.e. magnetro-sputtering vs PLD).

A low compressive residual stress state is found for compact samples deposited up to 20 Pa (see figure 4.21). Within this pressure range, a decreasing trend of σ_{res} is clearly appreciable: σ_{res} goes from -120 MPa at 5 Pa to -50 MPa at 20 Pa. This is strictly correlated to the above mentioned decreasing of the ablated particles energy as O_2 pressure increases, and almost linearly dependent by films mass density decrease. Moreover, the compressive state of stress is in accordance with the ones proper of metallic a-W films reported in section 4.1. When the coatings become porous, instead, σ_{res} switches to tensile. Tensile residual

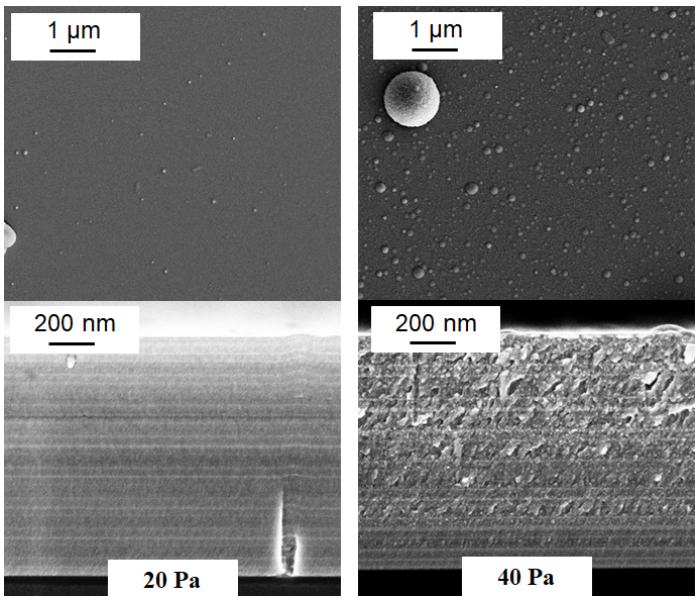

Figure 4.22: Top view and cross-section images of W-nitride coatings deposited at 20 and 40 Pa of N_2.

stresses are usually proper of coatings full of defects [178]. The high porosity degree can thus explain the tensile state of stress. In particular, $\sigma_{res} \approx 50$ MPa at 30 Pa which decreases down to 20 MPa at 60 Pa. The almost vanishing σ_{res} value at 60 Pa can be attributed to the detected high density of cracks, which can lead to stress relaxation.
Due to the high thickness inhomogeneity of the coatings, that unavoidably results in a non uniform bending curvature in particular upon heating, a reliable measurements of the CTE could not be obtained. Only for the W(O) deposited at 5 Pa a CTE of $6.7 \pm 0.3 \cdot 10^{-6}$ K^{-1} is measured. This values is in accordance with the ones proper of metallic a-W films reported in section 4.1.

4.2.2 W-nitride coatings

W nitrides are investigated because they eventually mimic W redeposits rich of N_2, which is usually puffed in the divertor region for obtaining plasma detachment. This usually results in the mixing of eroded W particles with N_2, and, consequently, to the growth of composit redeposits. These films are obtained in this thesis exploiting the same metallic W target and the same laser energy fluence adopted for the deposition of W-oxide coatings. In this case, N_2 is added as a background gas during deposition, promoting chemical reactions between the ablated W particles and N_2 molecules. This results in the formation of W-N composits, whose stoichiometric ratio depends on the N_2 pressure. In this work, only W-N coatings deposited at 20 and 40 Pa of N_2 are investigated. In these cases, EDXS and XRD analysis assess the formation of amorphous W_2N [89]. In particular, the samples show a N atomic concentration of about 33%. The SEM cross section and top view images are reported in figure 4.22. As it can be seen, the films are both compact, even if at 40 Pa a slightly more irregular surface appears. No experimental information of the film mass density is available.

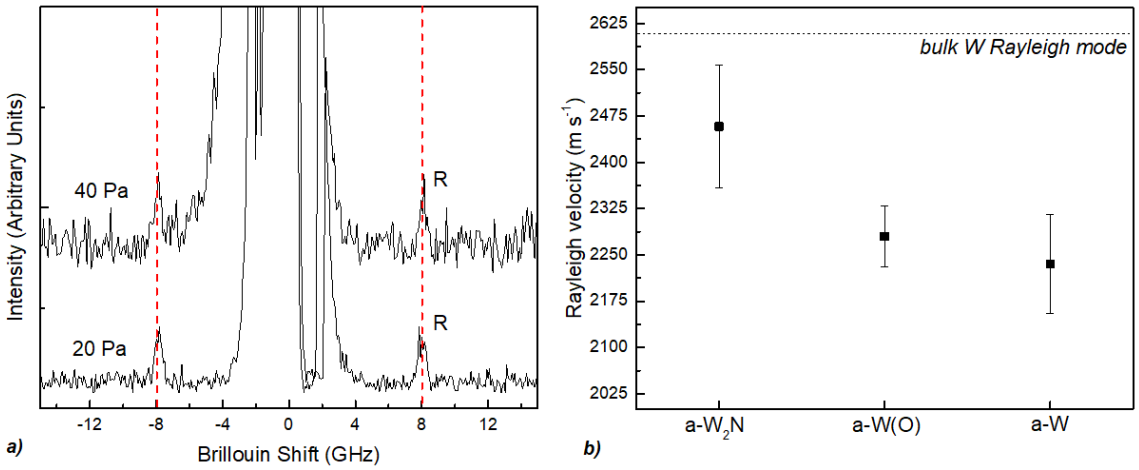

Figure 4.23: a) Brillouin spectra of amorphous W_2N coatings; b) Comparison of the Rayleigh velocities between different amorphous W coatings.

As a guess value, since the coatings are amorphous, ρ is considered starting from the bulk value of crystalline β-W_2N (i.e. 18 g cm^{-3} [179]) and by reducing it in the same way ρ changes for metallic W when going from c-W to a-W (i.e. $\rho_{a-W} = 0.37\rho_{c-W}$). Under this approximation, a lower bound density value of $\approx$ 11.3 g cm^{-3} is obtained. An upper bound value for ρ, instead, is chosen as 16 g cm^{-3}, which is the mass density of nanocrystalline W-N coatings deposited by PLD under similar deposition conditions [179].

Brillouin spectra recorded for these two samples are summarized in figure 4.23. Due to the metallic nature of the coatings, only surface acoustic waves are detectable. Here the R mode is present in both the samples. Its frequency shift is very similar for both the 20 Pa and the 40 Pa samples. Moreover, the high thickness of the coatings (i.e. $>$ 1.5 μm) makes the R mode, the only detectable SAW, and its velocity regardless of the scattering angle. In this case, v_R is very similar for the two coatings (i.e. $\approx$ 2470 m s^{-1}), thus suggesting similar values of the elastic moduli between the samples. In figure 4.23b, the velocities of the R mode found in this work for different amorphous W based coatings are presented. As it can be seen, while v_R is almost constant in metallic a-W and amorphous W(O) coatings, the formation of W_2N compounds clearly results in an increase of v_R by about 200 m s^{-1}. Therefore, also the elastic moduli of amorphous W_2N coatings consequently increase with respect to the ones found for the other amorphous W coatings. This observation, even if it is only qualitative, is completely general, and does not take into account the estimations made for the mass density.

The thermomechanical properties computed for ρ = 11.3 g cm^{-3} and ρ = 16 g cm^{-3} are shown in table 4.3. For the first mass density value, E is found to be 226 $\pm$ 25 GPa, G 85 $\pm$ 5 GPa and G/K 0.38 $\pm$ 0.1. These values, if compared to the ones reported for W(O) and a-W samples, which are characterized by very similar mass density, clearly underline the fact that the addition of N induces a high stiffening of the material. The obtained values are in good agreement with the ones reported in literature for other amorphous W_2N coatings (i.e.

Sample	E (GPa)	G (GPa)	G/K	CTE (10^{-6} K^{-1})
a-W_2N (ρ = 11.3 g cm^{-3})	226 ± 25	85 ± 5	0.38 ± 0.1	5.8 ± 0.2
a-W_2N (ρ = 16 g cm^{-3})	312 ± 25	120 ± 5	0.4 ± 0.1	5.1 ± 0.2
a-W (ρ = 11.5 g cm^{-3})	145 ± 7	53 ± 3	0.24 ± 0.7	8.1 ± 0.3
a-W(O) (ρ = 11.5 g cm^{-3})	160 ± 15	65 ± 3	0.37 ± 0.3	6.7 ± 0.3

Table 4.3: Thermomechanical properties of amorphous W_2N coatings. The properties are compared with the ones obtained for metallic a-W and a-W(O) samples.

$E > 190$ GPa) [179, 180]. Moreover, since W-N compounds behave like ceramics, the high value of E even if the material is in the amorphous phase, could indicate an appreciable hardening of the material with respect to pure a-W and W(O), which is characteristic of this type of compound [180]. Ceramics usually show a low value of the thermal expansion coefficient. Accordingly, the corresponding CTE of amorphous W_2N coatings is found to be 5.8 ± 0.2·10^{-6} K^{-1}, which is about 65% the CTE of metallic a-W. Moreover, this value is in very good agreement with the one reported in literature for similar W-N coatings (i.e. 5.66 - 5.8 ·10^{-6} K^{-1}) [181]. For ρ = 16 g cm^{-3}, even higher elastic moduli are found. In particular E = 312 ± 25 GPa, G = 120 ± 5 GPa and G/K = 0.4 ± 0.1. The CTE, accordingly, decreases to 5.1 ± 0.2·10^{-6} K^{-1}. It is fundamental to remember that, due to the unknown value of ρ, the values found for the elastic moduli and the CTE have to be considered as boundary values. The real properties lie between these boundary values. In any case, the stiffening of the material driven by the formation of the a-W_2N phase is clearly remarkable. Finally, the residual stress is found to be, in accordance to the other measured a-W samples ≈ - 80 ± 40 MPa, so compressive and very similar for the two analyzed samples.

4.3 Boron coatings

In this last section, the elastic moduli of B coatings are investigated. As already mentioned in section 2.5, B is widely exploited in fusion reactors for first wall conditioning. In this case, B coatings are deposited by PLD exploiting a metallic B target, which is ablated by

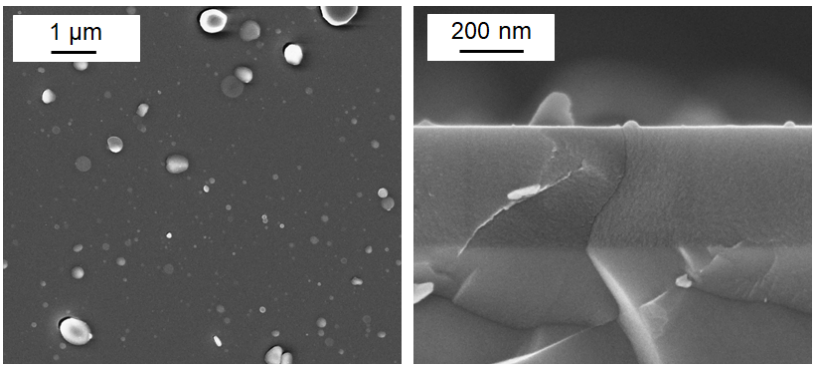

Figure 4.24: SEM images of amorphous B coating.

the same laser system adopted for all the previous depositions (i.e. $\lambda = 532$ nm), with a laser fluence of 9 J cm^{-2}. The ablated B atoms expand in vacuum conditions (i.e. background pressure $\approx 4 \cdot 10^{-4}$ Pa) and deposit onto Si(100) substrate. Under these conditions, the coatings grow with a compact amorphous structure (i.e. **a-B**). SEM images are shown in figure 4.24. Film density is assessed by quartz crystal microbalance measurements during deposition, and turns out to be 2.51 $\pm$ 0.35 g cm^{-3}. The mean value of ρ is close to the mass density of bulk β-rhombohedral boron (i.e. 2.35 g cm^{-3}).
Due to the very small dimension of the samples (i.e. < 1 cm^2), that could not allow the exploitation of the substrate curvature method, the investigation of the thermomechanical properties is limited only to the elastic moduli.
Under the acoustic point of view, B coatings deposited on Si substrates show some peculiar features. As far as the acoustic wave propagation is concerned, B-Si samples, on the contrary of W-Si, are fast films on slow substrates (i.e. stiffening layers), so that the velocity of the surface acoustic waves are higher than the v_R of the substrate. For this reason, surface waves can be more appropriately classified as pseudo- Surface Acoustc Waves (PSAW), because, being faster than the R mode of the substrate, they radiate energy into the substrate [182]. When a high mismatch of the elastic properties between the film and the substrate is observed, the PSAWs can eventually split, evolving into strong attenuated interfacial modes and the R at the free surface of the layer [182, 183].
The Brillouin spectra of the a-B film, recorded at different incidence angles, are shown in figure 4.25. Only one acoustic mode is detected. This mode is attributed to the PSAW mentioned above. Due to the rough morphology of the film, the peaks are quite broad. The elastic constats of the films are computed by considering two different values of the film mass density: 2.51 g cm^{-3}, estimated from the quartz microbalance, and the bulk β-boron value of 2.35 g cm^{-3}. The results are summarized in table 4.4. A comparison with the

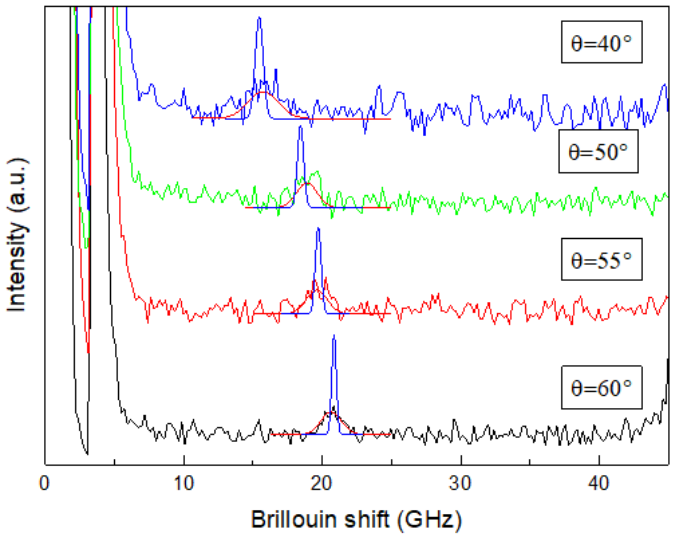

Figure 4.25: Brillouin spectra recorded at different scattering angles for a-B coating.

Sample	E (GPa)	G (GPa)	K (GPa)	ν	ρ (g cm^{-3})
β - B [185]	396	168	206	0.178	2.35
a-B [184]	280	-	-	-	-
a-B [186]	273 ± 7	-	-	-	2.48
Present study	296 ± 16	124 ± 8	159 ± 25	0.19 ± 0.04	2.51
Present study	272 ± 25	114 ± 7	152 ± 32	0.19 ± 0.04	2.35

Table 4.4: Elastic moduli of a-B coating compared with various litterature data.

bulk values of E, G, K and ν of β-rhombohedral crystalline boron as well as the E values coming from nano-indentation measurements performed on a-B coatings deposited by cathodic arc and magnetron sputtering of B powders is reported [184–186]. The obtained results are in fair agreement with the results obtained on amorphous boron coatings. In comparison to crystalline β-rhombohedral boron the values of elastic constant are slightly lower as expected for an amorphous coating.

4.4 Summary

Thanks to the results proposed in this chapter, the effects of the film mass density and the crystallites size on the thermomechanical properties of metallic nanostructured coatings has been elucidated. It has been found that, in the amorphous region, the loss of stiffness and the increase of the CTE are mainly attributed to the decrease of the mass density, so, coherently, to an increase of the porosity degree. In the intermediate ultra-nanocrystalline region, instead, the mass density drop is accompained by a consistent shrinkage of the crystallites, resulting in a non-obvious interplay, which, in turn, is related to constant stiffness, but not a constant CTE. In the nanocrystalline region, finally, both the stiffness and CTE linearly depend by $\bar{D}$ and ρ. Moreover, the less dense the coatings, the lower the residual stress, which has found to be compressive for all compact coatings, accordingly to many measured PLD coatings found in literature. As the porosity degree increses and coatings become porous, the residual stress is tensile. This is in agreement with theory because coatings with lower porosity have higher elastic modulus and also higher stiffness which induces higher levels in compressive residual stresses.

The effects of various chemical compositions on these properties have been also highlighted. The addition of Ta atoms results in the formation of a solid solution regime, where the measured stiffness can be well approximated by the lever rule inside the nanocrystalline domain. However, the CTE is more strictly affected by the presence of substitional atoms in the native lattice than the elastic moduli. When W is deposited in presence of an O_2 atmosphere, instead, the formation of a-WO_3 phase is eventually achieved. In this case, the coatings are characterized by very low stiffness (i.e. $\approx 20\%$ the bulk one), that depends on both the O/W stoichiometric ratio and the structure of the films. The addition of N_2, instead, besides leading to the formation of amorphous W_2N coatings with a structure and morphology close to the one observed for a-W, enhances material stiffness (i.e. increase by

about 70%) with respect to the other measured amorphous W coatings, with a consequent decrease of the CTE.
The last part of the thesis, focusing on the investigation of the behvaior of the various nanostructured W coatings under fusion relevant thermal loads, obviously requires the knowledge of all these thermomechanical properties of the as-deposited coatings. In the following chapter, the coatings will be subjected to thermal annealing treatments at steady ITER-relevant temperatures and to high heat fluxes induced by nanosecond laser irradiation. The evolution of the structure and the morphology will be consequently investigated after all the thermal treatments and compared with numerical predictions, that are obtained by taking as input parameters all the measured films properties. The selected samples for these tests are summarized in table 4.5.

Sample	E (GPa)	G (GPa)	G/K	CTE (10^{-6} K^{-1})	σ_{res} (MPa)	ρ (g cm^{-3})	$\bar{D}$ (nm)	Morphology	O_2 content (%)
c-W	381	148	0.48	5.1	- 684	18.2	16	Compact	< 5
a-W	145	53	0.24	8.1	-100	11.5	<2	Compact	≈ 20
p-W	93	34	0.15	-	+50	7	<2	Porous	55 - 60
W(O)	160	65	0.37	6.7	-120	11.5	<2	Compact	55 - 66
a-WO_{3-x}	67	30	0.22	-	-	5	<2	Compact	67
a-W_2N	226	85	0.38	5.8	- 80	11.3	<2	Compact	20 + N_2 37%

Table 4.5: Measured thermomechanical properties of fusion relevant coatings that are investigated under thermal loads.

CHAPTER 5

Thermomechanical behavior of tungsten coatings under fusion relevant thermal loads

The last chapter of the thesis focuses on the behavior of nanostructured W coatings under high thermal loads. As already mentioned in chapter 2, all the plasma facing materials must withstand high thermal loads delivered by the edge plasma. As a consequence, the material temperature can substantially increase and different thermal effects can take place. In particular, during steady heat load conditions, the surface of bulk W plasma facing components is not expected to overcome 1200 °C; the behavior of these components under such heat load conditions has been deeply investigated through the recent years, reporting no irreversible damage to the materials. During transient events, instead, the temperature can easily overcome the recrystallization and the melting temperatures of W, such that the surface of the components can be drastically altered, mining to the overall performances of the device. Even if a lot of work on bulk W behavior under plasma steady and transient heat loads can be found in literature, no studies report on the behavior of co-redeposited coatings under such operating conditions. To obtain a deeper understanding of the behavior of co-redeposits in ITER and future fusion reactors environments, in section 5.1 nanostructured W coatings, namely amorphous W and W-oxide coatings, are subjected to thermal annealing treatments at ITER-relevant steady operating temperatures. The effects of such temperatures on the morphology, the structure and the thermomechanical properties is investigated ex-situ by the same experimental setup exploited for all the characterizations of chapter 4. In section 5.2, finally, the coatings of table 4.5 are subjected to nanosecond laser irradiation, in order to mimic the thermal effects induced by plasma transient events on tokamak materials. Damage thresholds for the different thermal effects are thus investigated under a wide range of irradiation conditions as function of the specific morphology

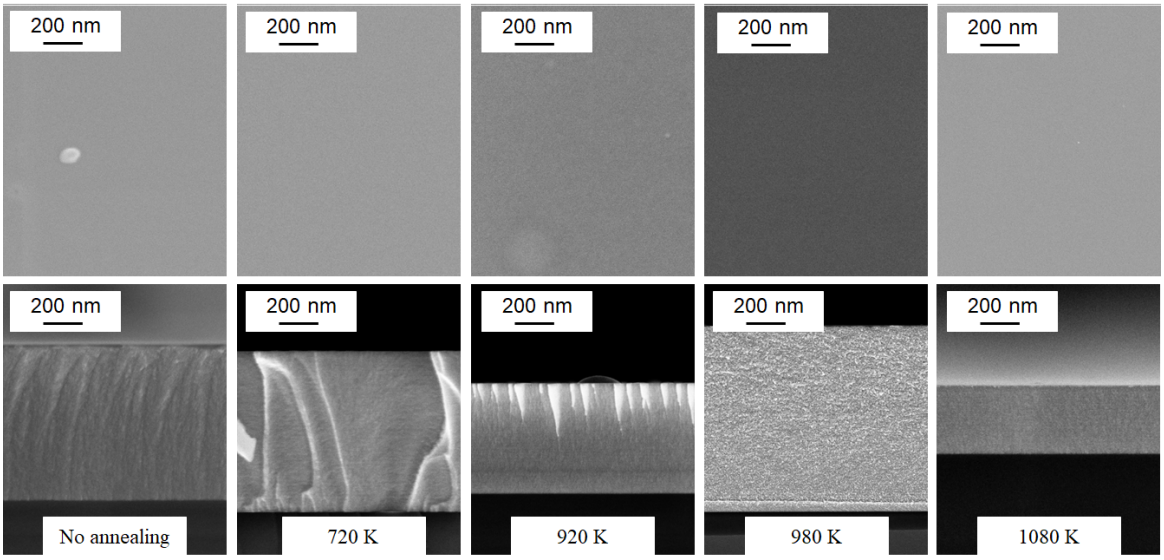

Figure 5.1: Top view and cross-section SEM images of a-W coatings annealed at various temperatures.

and structure of the coatings. The numerical code developed in chapter 3 is thus exploited for the prediction of these effects following nanosecond pulses, and finally preliminarly extended to realistic tokamak scenarios.

5.1 Effects of high temperatures on the thermomechanical properties of nanostructured W coatings

In this first section, the behavior of a-W and a-WO_3 coatings under thermal annealing treatments at ITER-relevant steady operating temperatures is investigated. The effect of thermal annealing temperature on the properties reported in table 4.5 is investigated performing "*steady*" annealing treatments in vacuum for 2 hours, at temperatures between 570 K and 1080 K. Moreover, the evolution of the thermal stresses under high temperatures is studied by "*fast*" annealing treatments, where temperatures up to 770 K are reached by $\approx$ 50 K min^{-1}.

5.1.1 Amorphous metallic W coatings for mimicking redeposited W layers behavior under steady operating temperatures

Metallic a-W coatings deposited on Si substrate are firstly annealed at temperatures between 720 K and 1080 K. SEM images of annealed a-W samples are shown in figure 5.1. As it can be seen, all the coatings remain compact with no surface nanostructuring at all annealing temperatures. Moreover, they do not delaminate from Si substrate at any annealing temperature. Appreciable differences in the coatings structure are not detectable from SEM analysis. To support these data, XRD is performed. The XRD spectra are shown in figure 5.2a. At 720 K the spectrum remains almost identical to that of the as-dep a-W, except for a small peak appearing in correspondence of the α-W (110) reflection. This feature indicates

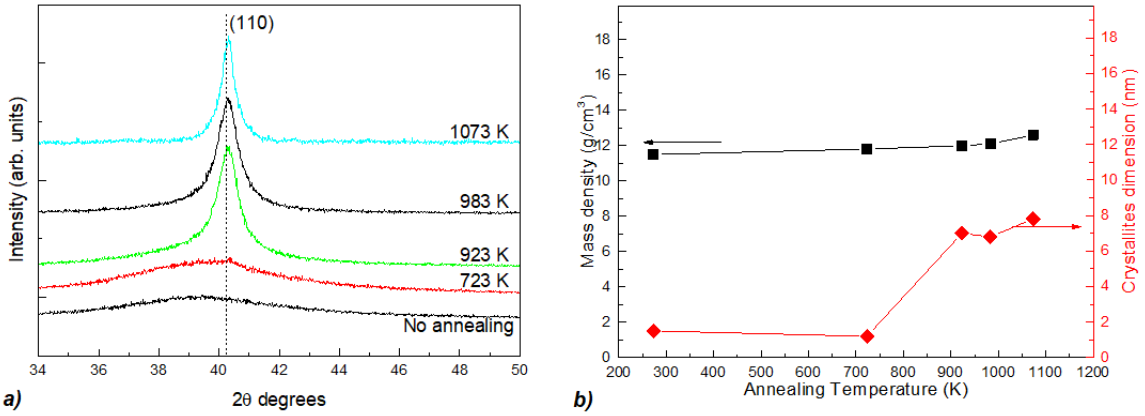

Figure 5.2: a) XRD spectra of annealed a-W coatings. b) Crystallites size and mass density plotted vs annealing temperature.

that the defects diffusion process is already active at a temperature below one half of the recrystallization temperature of bulk W ($\approx$ 1400 - 1600 K), although it is not yet able to radically change the structure of the film. Instead, for annealing temperatures at or above 920 K the amorphous band essentially disappears in favour of the peak associated to the crystalline α-W phase, which becomes better defined. This feature clearly underlines that, at 920 K, the crystallization process is already active. The mean crystallites dimension, reported in figure 5.2b, remains below 2 nm till 720 K and then suddenly changes over 920 K, remaining approximately constant around 8 nm until 1080 K. This shows that a-W films, as a consequence of the crystallization process, become u-nano-W.

No experimental information about the film mass density after annealing treatment is available. For this reason, ρ is estimated by combining the computational procedure adopted for Brillouin analysis and SEM cross-section images taken before and after annealing. SEM cross section images taken before and after annealing are compared in order to detect possible changes of the films thickness. In this way, ρ can be estimated as function of the coating volume variation with respect to the as-dep condition. No appreciable film thickness variation is observed. The information coming from Brillouin analysis is also considered. However, due to the presence of only one acoustic mode (see below), the estimation of ρ can be subjected to high uncertainties. For what concerns the mean values, as it can be seen in figure 5.2b, ρ undergoes only a limited variation, going from the as-dep value of 11.5 g cm^{-3} to 12.8 g cm^{-3} at 1080 K. This results confirms the fact that film thickness does not substantially change. Since the nanocrystals have higher mass density than the pristine a-W, this small variation of ρ suggests that nanocrystals remain embedded in a more amorphous matrix which retains a significant average void fraction. In parallel to the nucleation of crystalline seeds, the void fraction of the amorphous phase might coalesce, nucleating ultra nano voids, which however remain too small to be detected by SEM. This small density increase is consistent with the annealing temperature still well below the recrystallization temperature of bulk W, not yet allowing phenomena like e.g. a massive flow of vacancies

to the outer surface. The features of such nanostructure could be further elucidated by Grazing-Incidence Small-Angle X-ray Scattering, which clearly distinguishes between the regions with different electron density, or by Positron Annihilation Lifetime Spectroscopy, sensitive to the void dimension and distribution.

The observed crystallization, in turn, is expected to affect the thermomechanical properties of the coatings. It is known from experimental observations that can be found in various literature works that crystallization of amorphous materials can be related to a progressive stiffening and embrittlement of the material [187]. The stiffening process can be attributed to different competitive processes, such as structural relaxation, free volume annihilation, chemical decomposition and short-range ordering. These processes, in turn, depend on the specific annealing temperature, on the characteristic size of the pristine annealed material (e.g. completely amorphous, nanocrystalline) and on the initial residual stress state. In particular, annealing kinetics depends on temperature: in some literature cases [187] it is shown that below the glass transition temperature T_g the stiffening process is governed by structural relaxation, while for $T > T_g$ crystallization prevails. Furthermore, if thermal annealing is performed above the recrystallization temperature threshold, amorphous recrystallized materials can eventually recover bulk properties [188–190]. In general, when dealing with nanostructured materials, the stiffening process is very complex and not completely understood. Many other factors can affect the overall behavior of the material under high temperatures. For example, it is well known that the surface energy is one of the most important physical quantities of nanoscaled materials in determining their elastic behavior. Annealing treatments can eventually alter the nanometric size of the material, thus varying the surface/volume ratio and, therefore, the surface energy [191]. In addition, with respect to bulk materials, the interatomic potential of nanostructured materials can be substantially different. The elastic properties of a solid are inherently related to the atomic interaction energy and the atomic distance, so on the bond length and the bond energy of crystals [192]. In the case of nanomaterials, these two quantities are size-dependent, being affected by the coordination number and long/short range ordering of atoms, that, in turn, can be deeply affected by the annealing induced structural reorganization. To detect the possible material stiffening, Brillouin analysis are perfomed, ex situ, on each annealed a-W coating. The obtained spectra, recorded at a scattering angle of 60°, are shown in figure 5.3. As it can be seen, only the R mode is detectable (coherently to the micrometric thickness of the films). Moreover, the R mode significantly shifts to higher frequencies, so to higher velocities, if annealing is performed above 720 K. In particular, v_R goes from $\approx$ 2200 m s^{-1} for the samples below 720 K to $\approx$ 2400 m s^{-1} at 1080 K. This clearly highlights the progressive stiffening of the films.

The computed values of E, G and G/K are shown in figure 5.4. An increase in E, G and G/K with respect to the as-dep coating is found for temperatures either above or below 720 K. In particular, a trend similar to the one of $\bar{D}$ is observed: at low annealing temperatures

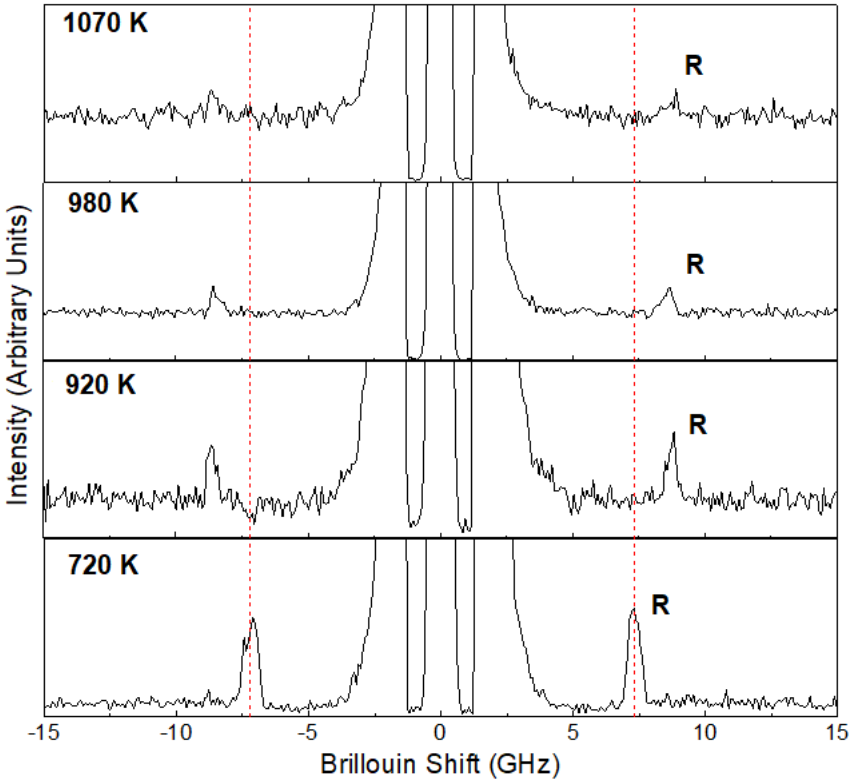

Figure 5.3: Brillouin spectra of annealed a-W coatings recorded at $\theta = 60°$.

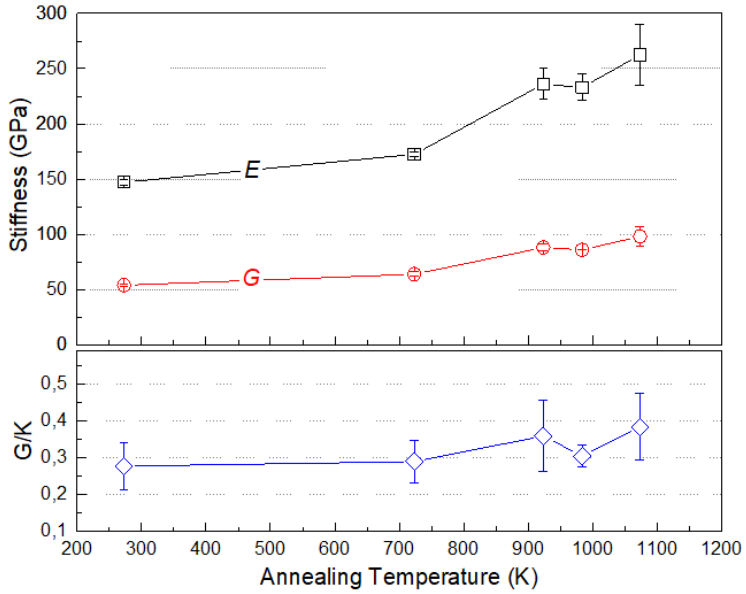

Figure 5.4: Elastic moduli of annealed a-W coatings plotted vs annealing temperature.

the elastic moduli are not significantly modified, while at 920 K, E and G increase by about 60% (E goes from around 150 GPa to around 230 GPa), with a corresponding rise of G/K by 33% (G/K from 0.27 to 0.36). Finally, it can be seen that the a-W sample annealed at 1080 K (u-nano-W) is characterized by $E = 262$ GPa, $G = 98$ GPa and $G/K = 0.38$. The observed progressive stiffening of the material is thus in accordance with what is usually

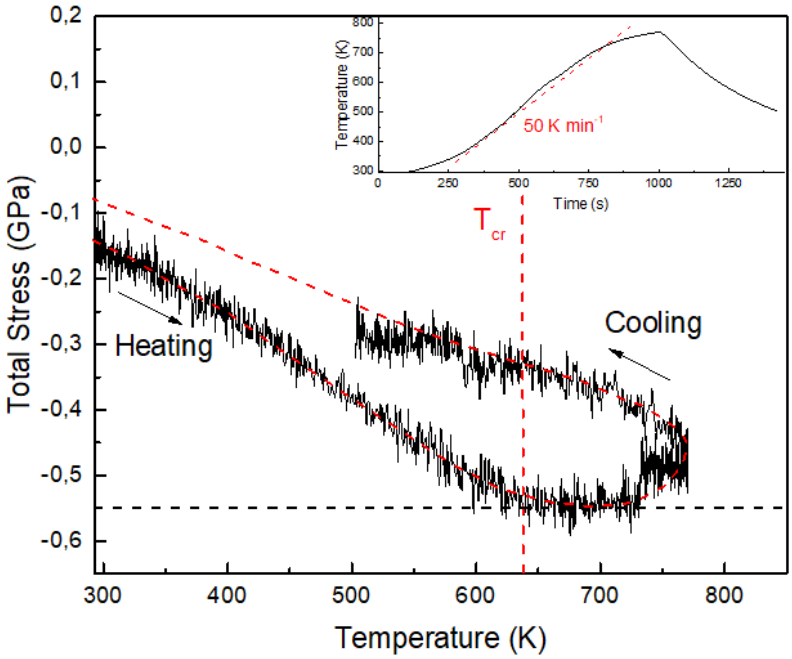

Figure 5.5: Total stress evolution of a-W during fast annealing treatments. The black line represents the experimental data, while the dotted red line the mean value of the total stress. The temperature ramp is highlighted in the inset.

observed upon annealing of amorphous materials. The formation of a new crystalline phase results in the modification of the surface energy of the material and, at the atomic level, it changes the interatomic potential by varying the mean atomic coordination number. As already mentioned, the crystalline phase is characterized by a long range order where the atoms occupy a specific position in the lattice, and these atoms are forced to bond at fixed angles. This obviously confers a higher stiffness to the material with respect to the amorphous phase, where, instead, a high structural disorder is present. As it can be seen, these values remain well below the bulk values. This is consistent with the lower mass density that characterize the coatings: the more dense nanocrystals, so with a higher atom packaging, remain embedded in a softer less dense amorphous matrix. A complete recovery, till the microcrystalline state, would require higher annealing temperatures and/or longer annealing times, that would allow the growth of crystallites.

The remarked stiffening of the material consequently affects the thermal expansion coefficient of the coatings. In particular, the CTE remains almost constant and equal to $8.1 \pm 0.3 \cdot 10^{-6}$ K^{-1} for annealing below 920 K. When crystallization occurs, the CTE drops to $6.2 \pm 0.4 \cdot 10^{-6}$ K^{-1}, approaching the value proper of nanocrystalline c-W (i.e. $5.1 \cdot 10^{-6}$ K^{-1}).

Finally, the evolution of the total stress of the coating under high temperatures is investigated. The trend of σ_f vs annealing temperature is shown in figure 5.5. In the inset, the temperature ramp is hihlighted. The stress starts from the initial residual stress value of - 100 MPa, and linearly increases (i.e. the compressive stress increases) during heating.

When it reaches ≈ 550 MPa, which corresponds to a relaxation temperature (T_{cr}) of ≈ 640 K, the material yields: σ_f does not substantially changes for temperatures up to ≈ 720 K. At 720 K, a small step in σ_f is observed, probably related to the beginning of the crystallization process. Upon cooling, the compressive stress starts to decrease linearly with temperature (i.e. tensile stress rises), but with a different slope with respect to the heating phase. This suggests that the film undergoes to some structural modifications during the heating process. Thanks to these measurements the yield stress of the coatings can be estimated as the total stress value corresponding to T_{cr}. In this case, as reported in figure 5.5, it is ≈ 550 MPa. This value is well below the bulk W one (i.e. 1350 MPa [125]). It is well known that σ_y can be severely affected by the porosity degree of the samples. As reported by *Li et al.* [193], power law or expontential law equations can be adopted to correlate the yield stress of a material by its porosity degree. Here, the porosity degree (D_P) is estimated by the variation of the coating mass density with respect to the bulk one as:

$$D_P = \frac{\rho_{bulk} - \rho_{coating}}{\rho_{bulk}} \tag{5.1}$$

The reduction of the yield stress is thus evaluated by the following linear approximation:

$$\sigma_y^{coating} = \sigma_y^{bulk} \cdot (1 - D_P) = \sigma_y^{bulk} \cdot \frac{\rho_{coating}}{\rho_{bulk}} \tag{5.2}$$

Equation 5.2 returns, in the case of $\rho_{coating}$ = 11.5 g cm^{-3}, ρ_{bulk} = 19.25 g cm^{-3} and σ_y^{bulk} = 1350 MPa, a reduced value of σ_y = 770 MPa, that is not so far from the obtained experimental value.

5.1.2 Amorphous W-oxide coatings for mimicking codeposited W-O layers behavior under steady operating conditions

Amorphous WO_3 coatings deposited on Si substrates (at 30 Pa of O_2) are firstly annealed at temperatures between 570 K and 870 K. This upper temperature limit is set by the fact that above 870 K coatings likely delaminate from the substrate. The annealing treatment

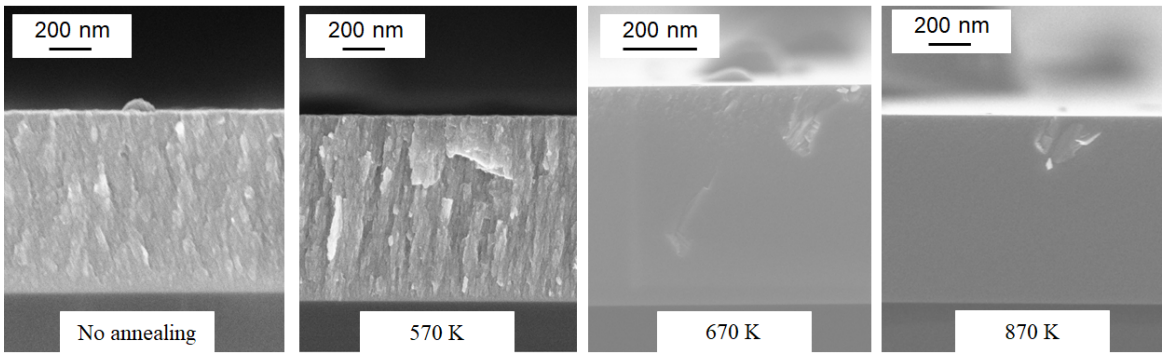

Figure 5.6: SEM cross section images of annealed a-WO_3 coatings.

is performed, as in the case of a-W, in vacuum for 2 hours. SEM cross section images of annealed a-WO_3 coatings, summarized in figure 5.6, clearly show a structural evolution when the films are annealed at, and above, 670 K, the coatings being more compact. This suggests that crystallization has occurred. Raman analysis are thus performed to assess the crystallization process of the a-WO_3 phase. The Raman spectra are shown in figure 5.7. As already described in chapter 4, the spectrum related to the as-deposited coating shows the classic broad bends characteristic of the amorphous phase, which are related to the O-W-O bending and W-O stretching modes, and the nanocrystallinity peak at about 960 cm^{-1}. Coherently to SEM analysis, no differences in the spectrum of the coating annealed at 570 K are found. Over 570 K, instead, several peaks become visible. The phonon activity (i.e. the presence of the peaks in the spectrum) can be grouped into a first set of peaks at low Raman shifts between 100 and 400 cm^{-1}, and a second one at higher wavenumbers between 600 and 900 cm^{-1}, that are related to the O-W-O bending modes and the W-O stretching modes respectively [195]. Moreover, the detected peaks almost coincide with the reported dotted red lines at 133 cm^{-1}, 273 cm^{-1}, 715 cm^{-1} and 805 cm^{-1}. These lines correspond to the peaks of the crystalline monoclinic (I) phase (i.e. γ-phase) of WO_3 [196]. This result clearly underlines that, from 670 K, the initial amorphous WO_3 evolves into a crystalline monoclinic WO_3 phase. However, the peaks broadening observed at 670 K suggests that, at this temperature, the crystallization process is not completed. At 870 K, instead, definetly sharper peaks are found. These results are in good agreement with what observed by *Pezzoli et al.* [90] on very similar a-WO_3 samples.

The annealing induced phase change consequently modifies the properties of the coatings. In particular, mass density is strongly affected. This is confirmed by SEM cross section images, that highlight a high variation of film thickness when crystallization occurs. For

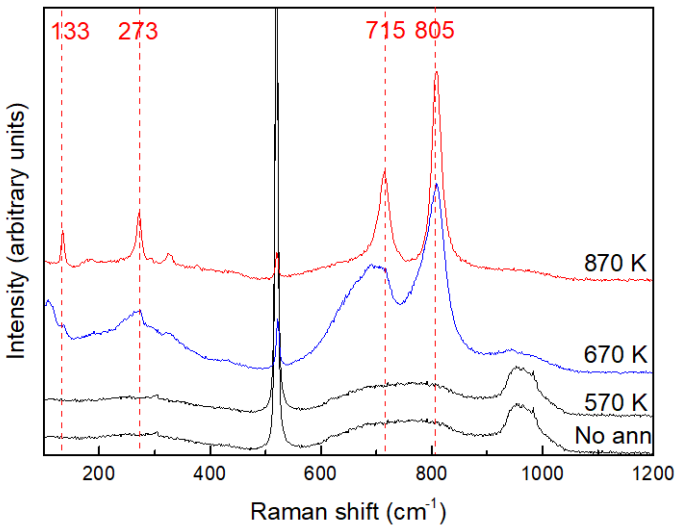

Figure 5.7: Raman spectra of annealed a-WO_3 coatings. The red dotted lines refer to the main peaks of monoclinic WO_3.

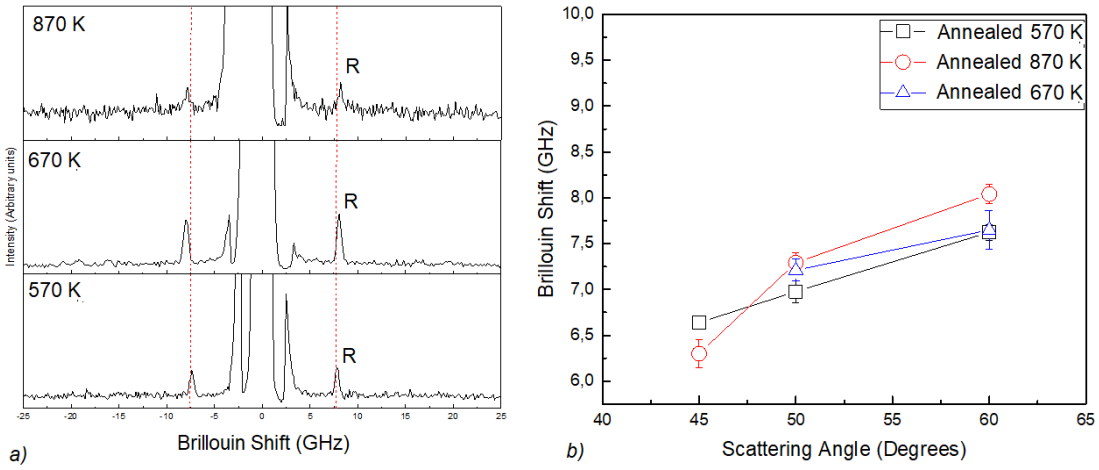

Figure 5.8: a) Brillouin spectra, recorded at 60° of scattering angle, of annealed a-WO_3 coatings. b) Dispersion relations of the Rayleigh mode at the different annealing temperatures.

temperatures above 670 K the WO_3 bulk value of ρ (i.e. 7.1 g cm^{-3}) is considered for successive computations. The recorded Brillouin spectra are shown in figure 5.8a. As a consequence of phase change, also the refractive index of the coating must vary. However, no optical reflectivity measurements after annealing, needed to validate the estimates of n (see chapter 4), are performed. For this reason, in order to uncouple the determination of E, G and G/K from the knowledge of n, the analysis is limited only to the surface acoustic waves. As expected from the micrometric thickness of the coatings, only the R mode can be detected. Its dispersion relations are highlighted in figure 5.8b. A clear increase of the Brillouin shift of the mode is found with increasing annealing temperature. The R wave is thus faster for higher annealing temperatures (i.e. from $\approx$ 2290 m s^{-1} at 570 K to $\approx$ 2390 m s^{-1} at 870 K). From the dispersion relations of the R mode, the elastic moduli are computed. The results are summarized in table 5.1. If annealing is performed at 570 K, i.e. below the observed crystallization temperature, no substantial increase of material stiffness is observed, being the coating very similar to the as-deposited one. At 670 K, instead, when crystallization begins, E = 101 GPa, G = 36 GPa and G/K = 0.24, with a consequent increase by about 50% of E with respect to the as-deposited condition. Finally, when the monoclinic WO_3 phase is completely formed at 870 K, E = 127 GPa, which is about twice the as-dep value, G = 47 GPa and G/K = 0.38. In this case, the value obtained of E is in well agreement with the ones derived by *Polcar et al.* for sputtered WO_3 (i.e. 110

Annealing Temperature (K)	E (GPa)	G (GPa)	G/K	ρ (g cm^{-3})	Phase
No annealing	67	30	0.22	5	a-WO_3
570	70	31	0.22	5	a-WO_3
670	101	36	0.24	7.1	Monoclinic-γ WO_3
870	127	47	0.38	7.1	Monoclinic-γ WO_3

Table 5.1: Mechanical properties of annealed a-WO_3 coatings.

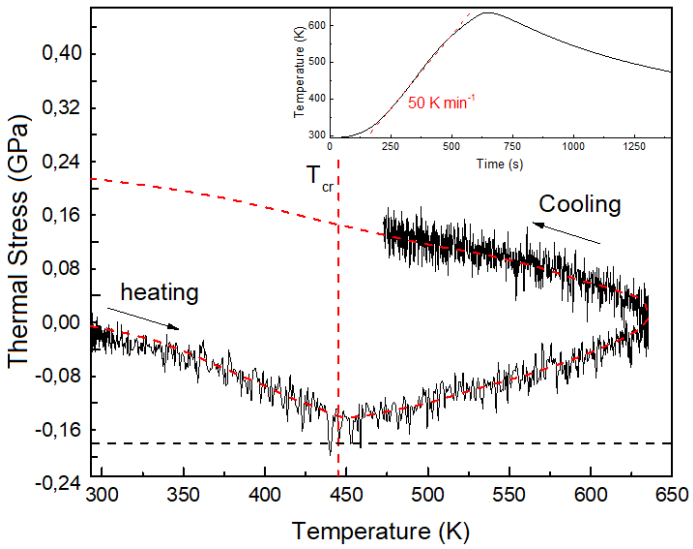

Figure 5.9: Thermal stress evolution of a-WO_3 during fast annealing treatments. The black line represents the experimental data, while the dotted red line the mean value of the stress. The temperature ramp is highlighted in the inset.

GPa) [197] and by *Parreira et al.* (i.e. 110 - 160 GPa) [175].

The thermal stress evolution is finally investigated under fast thermal ramps. The maximum reached temperature, in this case, is set below the observed crystallization temperature (i.e. 670 K). The trend of σ_{th} vs temperature is shown in figure 5.9. In the inset, the adopted thermal ramp is highlighted (i.e. 50 K min^{-1}). The stress increases linearly with temperature up to $\approx$ -180 MPa. This stress corresponds to a relaxation temperature T_{cr} of $\approx$ 445 K. Above this temperature, stress relaxation processes begin, with a consequent rise of a tensile stress. This trends continues up to the maximum temperature of the cycle. Upon cooling, the tensile stress proceeds increasing again linearly with temperature. Since no information on σ_{res} is available, the absolute value of σ_{yield} can not be determined.

5.2 Thermomechanical behavior of nanostructured W coatings under pulsed heat loads

The previous section has shown that the exposure of nanostructured W coatings to high temperatures, that mimic steady operating conditions in tokamaks, results in severe changes of the materials properties, likely inducing crystallization, stiffening and decrease of CTE. In this last section of the thesis, the behavior of nanostructured W coatings under ITER-relevant transient conditions is finally investigated. To this purpose, nanosecond laser irradiation is exploited to simulate the thermal effects induced by extreme thermal loads delivered by plasma instabilities. Thanks to their highly localized energy absorption around the surface (i.e. laser extinction length for metals $\approx$ 20 nm), lasers can be consistently exploited for the irradiation of coatings, without promoting, as it happens in the case of electron beams, bulk heating effects that directly involve the heating of substrate materi-

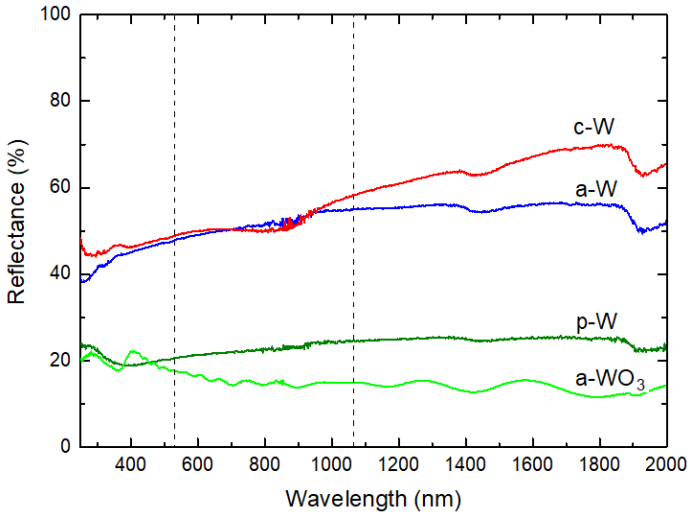

Figure 5.10: Total optical reflectance of the various nanostructured W coatings evaluated before irradiation.

als. The samples are thus irradiated under single and multishots conditions, such that the damage thresholds of the various thermal effects (i.e. melting, cracking, crystallization and delamination) can be determined. Being representative of W coatings and co/re-deposited layers in tokamaks, their investigation under high thermal loads is crucial to assess their not completely understood thermomechanical response to critical transient heat loads that can be found in fusion reactors. To better mimic real tokamak conditions, some of the coatings are also deposited on bulk W substrates. In section 5.2.1 the thresholds obtained under single shot irradiation are presented. In section 5.2.2, instead, the thresholds for multishots irradiation are investigated. Finally, in section 5.2.3, the numerical model developed in chapter 3 is exploited to predict the various thermal effects thresholds under single shot irradiation, so that numerical and experimental data can be compared. This model is conclusively applied to a representative condition of a tokamak environment.

Laser irradiation of metallic W coatings is performed exploiting the fundamental harmonic (λ = 1064 nm) of the Q-switch Nd:YAG laser presented in chapter 3. In the case of a-WO_3 coatings, instead, due to their optical transparency in the IR region, the samples are irradiated by the second harmonic (λ = 532 nm) of the same laser system. The temporal gaussian profile of the laser is characterized by a τ_{FWHM} of 7 ns. The laser beam enters in a vacuum chamber and strikes the coating surface with an angle of incidence of 45°. The beam spot has an elliptical shape with a total area of 0.81 cm^2. The total beam trasmittance along the optical path is $\approx$ 80%. The samples are irradiated with different laser energy fluences, that vary between 50 mJ cm^{-2} and 3.5 J cm^{-2}. In this way, a broad range of HFFs is spanned (i.e. from 1 up to 100 MW m^{-2} $s^{0.5}$). The irradiation is performed at room temperature and under vacuum conditions (i.e. 1 Pa base pressure).

The morphology evolution after irradiation is investigated by SEM analysis (accelerating voltage of 3 - 5 kV), and by optical miscroscopy. EDXS measurements are performed to

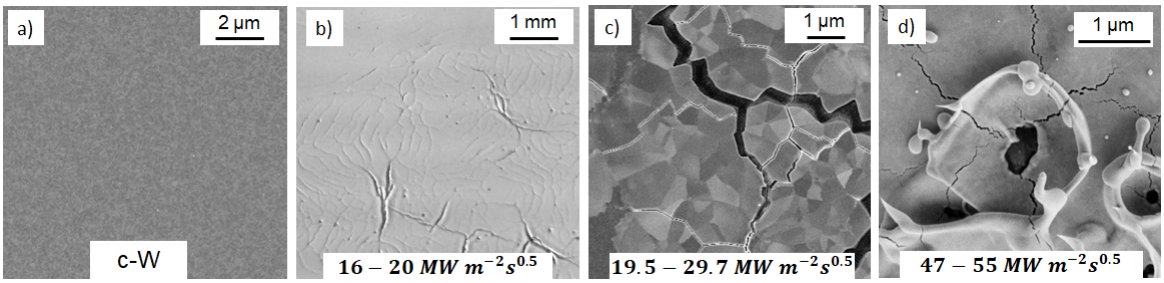

Figure 5.11: Microscopy images of unirradiated (a) and irradiated (b-d) surface of c-W coatings. The thresholds of cracking (b), crystallization (c) and melting (d) are highlighted.

obtain information about the laser induced modification of the elemental composition of the samples. A Thermoscope Atomic Force Microscope (AFM), operating in the non-contact mode, is also exploited to assess surface roughness evolution after irradiation. Finally, W oxidation is monitored by Raman analysis. The total optical reflectance R of the as-deposited samples, needed for the computation of P_{abs} (i.e. $P_{abs} = P_0(1 - R)$) is evaluated by a UV-Vis-NIR PerkinElmer Lambda 1050 spectrophotometer with a 150 mm diameter integrating sphere. The obtained reflectance spectra are shown in figure 5.10. R at λ = 1064 nm is 58% for c-W coatings, 52% for a-W and 22% for p-W. Metallic W(O) coatings and a-W_2N coatings, not shown in the graph, show a total reflectivity at λ = 1064 nm very similar to the one of a-W (i.e. $\approx$ 50%). At λ = 532 nm the total reflectance of a-WO_3 coatings is $\approx$ 18%. To directly compare the thresholds obtained in this thesis with other results that can be found in literature, all the damage thresholds are expressed in terms of the heat flux factor (HFF = $P_{abs}\sqrt{\tau_p}$).

5.2.1 Damage thresholds under single shot irradiation

Columnar W coatings

Columnar W coatings, deposited on both Si and W substrates, are firstly investigated under single shot irradiation. Being proxy of W coatings on CFC tiles in tokamaks, they are expected to withstand the high plasma heat flux, with consequently high damage thresholds proxy to the ones of bulk W. SEM and optical microscopy images of as-deposited and irradiated c-W coatings are shown in figure 5.11. The as-deposited surface is shown in figure 5.11a. The sample is flat and its surface roughness well replicates the ones of the substrates, being $\approx$ 0.7 nm in the case of Si and $\approx$ 40 nm in the case of bulk W (i.e. Si wafer roughness $\approx$ 0.6 nm, bulk W plate roughness $\approx$ 35 nm). Cracking occurs between 16 and 20 MW m^{-2} $s^{0.5}$ (i.e. incident laser fluence F between 0.4 and 0.5 J cm^{-2}) (figure 5.11b). This threshold is slightly higher than the one obtained for bulk W in chapter 3 (i.e. 14 - 18 MW m^{-2} $s^{0.5}$). However, it is very close to the ones reported in literature for different columnar W coatings (i.e irradiation by e-beams at room temperature, between 20 and 23 MW m^{-2} $s^{0.5}$) [129, 198, 199]. The higher cracking threshold with respect to bulk W samples can be

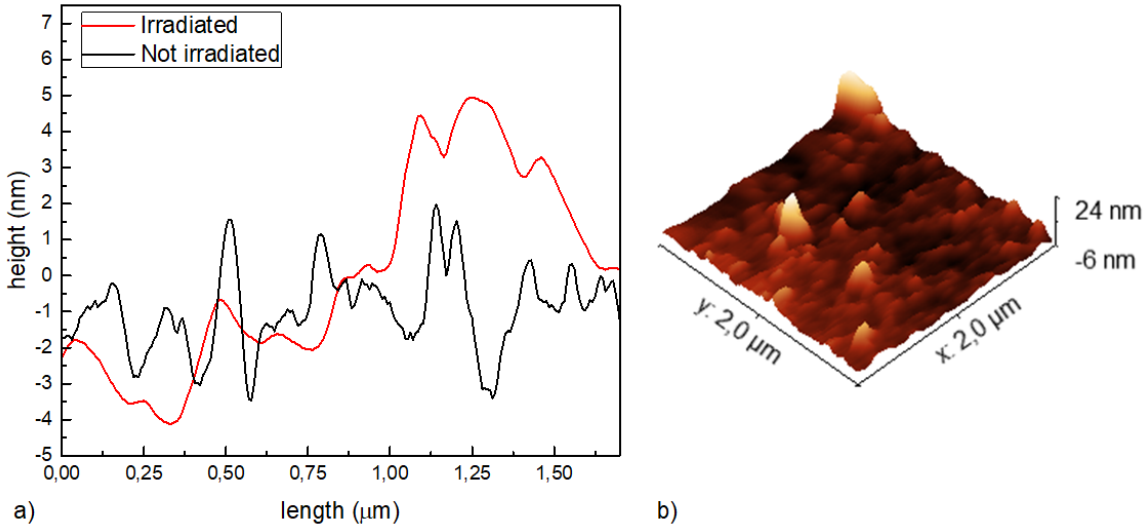

Figure 5.12: a) AFM profilometry images for as-deposited and irradiated c-W surface. The irradiation is performed at the melting threshold. b) 3-D AFM image reconstruction of melted c-W surface.

attributed to the columnar grains and their preferential orientations that help in mitigating cracking, improving the thermomechanical resistance of the material [129, 198, 199]. No differences in the cracking threshold between c-W deposited on Si or on W are found.
Crystallization is clearly detected at 29.7 MW m^{-2} $s^{0.5}$, when micrometric grains are uniformly visible inside the irradiation area. However, even at around 19.5 MW m^{-2} $s^{0.5}$ localized micrometric grains start to appear (see figure 5.11c) (i.e. F values between 0.5 and 0.75 J cm^{-2}). At 29.7 MW m^{-2} $s^{0.5}$, the temperature of the silicon substrate exceeds its melting temperature (i.e. 1600 K), and wide cracks full of melted substrate material appear on the surface (black regions in the figure 5.11c). This obviously, due to the higher melting point, does not happen in the case of bulk W substrate. Surface melting is found between 47 - 54 MW m^{-2} $s^{0.5}$ (figure 5.11d) (i.e. F between 1.2 and 1.4 J cm^{-2}). These values are really close to the melting threshold of bulk W (i.e. 55.5 MW m^{-2} $s^{0.5}$). On the contrary of what is observed for cracking, crystallization and melting, the delamination behavior of the coating is strictly correlated to the type of substrate material. In the case of Si substrates, delamination starts at 29.7 MW m^{-2} $s^{0.5}$, while, in the case of bulk W substrates, the fraction of the delaminated coating is really small even at the melting threshold. This difference can be explained by two main factors; firstly, as already mentioned, the melting temperature of Si is much lower than the W one, promoting molten layer movement that enhances cracking and delamination at lower HFFs. Secondly, a decrease of thermal expansion mismatch between the coating (CTE $\approx$ 5.1 10^{-6} K^{-1}) and the substrate, when silicon (CTE $\approx$ 2.6 10^{-6} K^{-1}) or W (CTE $\approx$ 4.2 10^{-6} K^{-1}) are exploited, limits the thermal stress at the coating substrate interface, so the delamination probability.
No substantial increase of surface roughness is observed for irradiation below the melting threshold. Figure 5.12a shows the AFM profiles of unirradiated and irradiated (i.e. at 54

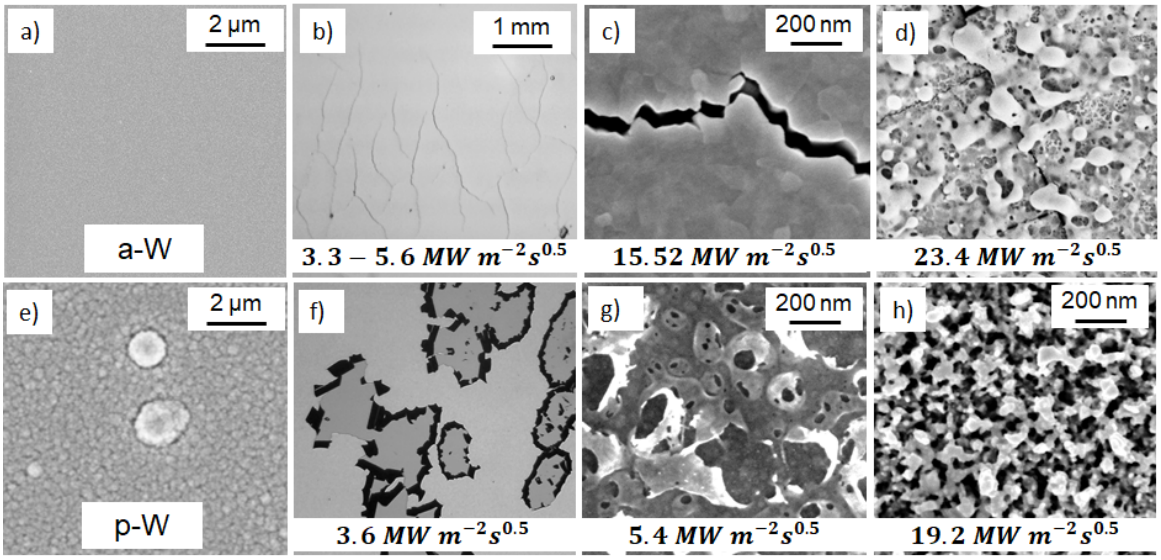

Figure 5.13: Microscopy images of unirradiated (a, e) and irradiated (b-d, f-h) a-W and p-W coatings.

MW m^{-2} $s^{0.5}$, melting threshold) c-W surface in the case of Si substrate. Figure 5.12b, instead, represents the 3-D AFM image of irradiated c-W surface. The roughness (R_q) slightly increases from the as-deposited value of 0.7 nm to 1.1 nm. In the case of bulk W, instead, the roughness goes from 40 nm to ≈ 70 - 90 nm.
Raman analysis performed after irradiation does not detect any laser-induced oxidation, even after surface melting and resolidification (the Raman spectrum remains flat as expected for metallic W). This is clearly strictly correlated to the low retained oxygen concentration in the coating (i.e. $< 10\%$).

Re-deposited tungsten: a-W and p-W coatings

In order to mimic W redeposits behavior under ITER-relevant conditions, a-W and p-W are irradiated. As for c-W coatings, the samples are deposited on both Si and bulk W substrates. Microscopy images of the various HFF thresholds are shown in figure 5.13. The as-deposited surface of a-W (figure 5.13a) is flat and well reproduces the roughness of the substrates, being ≈ 1 nm in the case of Si and ≈ 42 nm in the case of bulk W. p-W coatings, instead, are characterized by a slightly higher surface roughness with respect to a-W, i.e. ≈ 2.2 nm for p-W on Si and ≈ 50 nm for p-W on bulk W. After single shot irradiation, cracking of a-W coatings occurs between ≈ 3.3 MW m^{-2} $s^{0.5}$ and 5.6 MW m^{-2} $s^{0.5}$ (figure 5.13b). Due to their porous morphology, it is not easy to detect surface cracking in the case of porous W coatings. In this case delamination is usually observed in extended areas starting from ≈ 3.6 MW m^{-2} $s^{0.5}$ (figure 5.13f). a-W coatings crystallize at ≈ 15.5 MW m^{-2} $s^{0.5}$ (figure 5.13c). No evidence of crystallization can be observed, instead, for p-W at any HFF. On the contrary, starting from 5.4 MW m^{-2} $s^{0.5}$, features similar to sub-micrometric bubbles, with around 80 - 100 nm size, appear on the surface of the coatings

(figure 5.13g). Similar bubbles are also found on a-W at 10 MW m^{-2} $s^{0.5}$. Since they are not observed in the case of c-W, which is the most compact morphology and with the lowest O_2 content, their formation could be enhanced by the oxygen content retained in the material, being $\approx$ 20% for a-W and up to 55% - 60% for p-W.
Melting starts at very lower HFFs with respect to c-W, namely at $\approx$ 23.4 MW m^{-2} $s^{0.5}$ for a-W (figure 5.13d) and above 15 MW m^{-2} $s^{0.5}$ for p-W. This consistent melting threshold drop can be evidently mainly attributed to the drop of the thermal diffusivity of the coatings, that is, in some way, affected by the increaing porosity degree of the material. In the case of p-W, over the melting threshold, peculiar nanostructures, with a shape that remember *fuzzy-like* W, form on the surface (figure 5.13e). Their formation is better highlighted in figure 5.14. As it can be seen, comparing the native and the irradiated structures at 19.2 MW m^{-2} $s^{0.5}$, the fuzzy-W like layer extends to $\approx$ 200 nm thickness. Its formation, which is not observed in the case of c-W and a-W coatings, is thus strictly related to the native surface morphology of p-W coatings and to its roughness enhanced by the coupling with the laser. The presence of fuzzy-like W nanostructures induces a high surface roughening: AFM measurements, shown in figure 5.15, confirms that R_q goes from 2.2 nm to 12 nm, for samples deposited on Si.
Raman analysis are also performed after irradiation above the melting thresholds on a-W and p-W coatings, in order to detect possible laser induced oxidation of the material. The spectra are summarized in figure 5.16. The as-deposited metallic W coatings show a flat spectrum. After irradiation over the corresponding melting thresholds (i.e. 23.4 and 19.2 MW m^{-2} $s^{0.5}$ (red and blue spectra)), two broad bands becomes visible for both a-W and p-W coatings. These two broad bands highlight the formation, even if in small quantity, of an amorphous sub-stoichiometric W-oxide layer on the surface of the sample. The different stoichiometric ratio, with respect to a-WO_3, is highlighted by the different spectra shapes observed for a-WO_3, for p-W and a-W coatings. The absence of the Si peak, instead, confirms the surface nature of the oxide layer, since the probing laser can pass through the transparent oxide coating, while it is completely absorbed in the first few nanometers

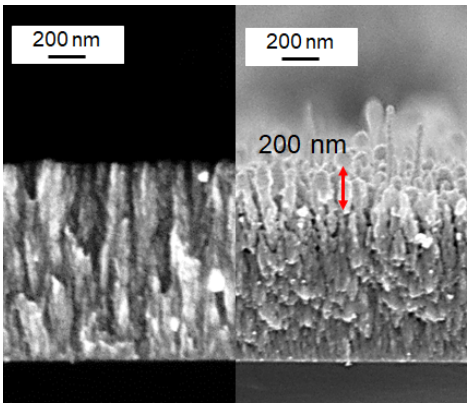

Figure 5.14: a) As-deposited structure of p-W, b) formation of fuzzy-like W nanostructures.

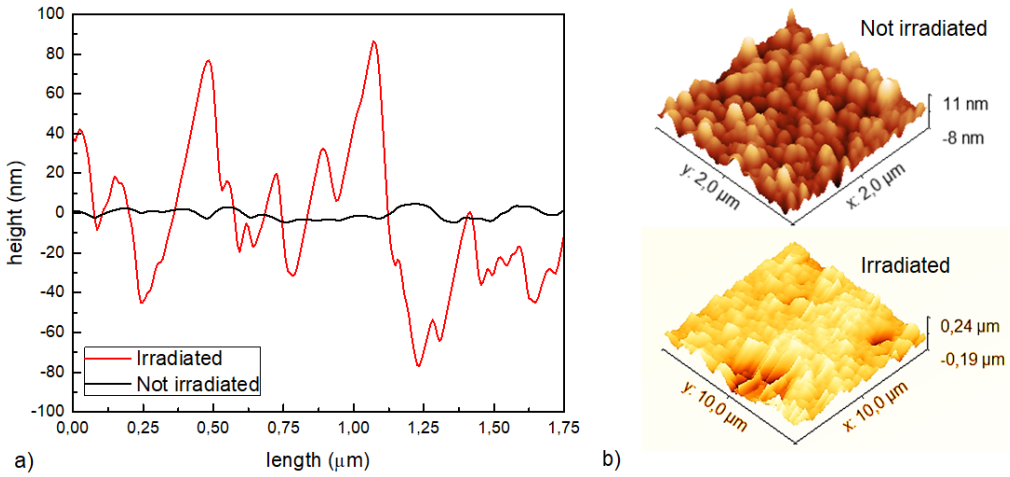

Figure 5.15: a) AFM profiles of unirradiate and irradiated p-W surface. b) 3-D AFM image reconstruction of unirradiated and irradiated p-W.

of the underlying metallic material. Since the irradiation is always performed in vacuum conditions, it is the high oxygen content initally present in the coating that can lead to the formation of W-O bonds when the temperature of the material is sufficiently high to trigger dffusion processes and recombination within the melted layer.

The delamination behavior of a-W and p-W coatings, in accordance to what is observed for c-W coatings, depends on the type of substrate material. In particular, delamination starts at very low HFFs, mamely at $\approx$ 5.6 MW m^{-2} s$^{0.5}$ for a-W and 3.6 MW m^{-2} s$^{0.5}$ for p-W in the case of Si substrate, while at $\approx$ 8 MW m^{-2} s$^{0.5}$ for a-W and at $\approx$ 4 MW m^{-2} s$^{0.5}$ for p-W in the case of bulk W substrate. The decrease of these thresholds with respect to c-W can be mainly attributed to two reasons; firstly, both a-W and p-W are characterized

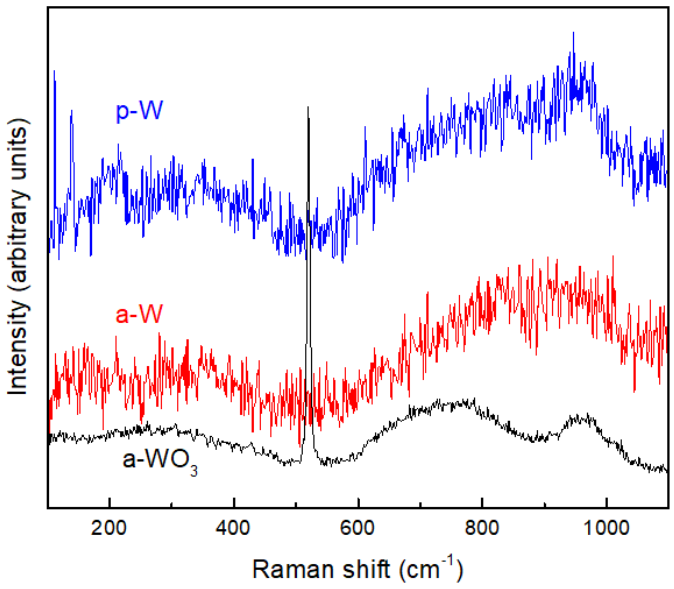

Figure 5.16: Raman spectra of irradiated a-W and irradiated p-W over the melting threshold. The two spectra are compared to the spectrum of a-WO_3.

by a higher CTE with respect to c-W. This, in turn, results in higher thermal stresses at the coating-substrate interface due to higher thermal expansion mismatch between the two materials. Secondly, in general, the more porous the coating, the lower the adhesion to the substrate.

Co-deposited tungsten with oxygen and nitrogen: a-WO_3 and a-W_2N coatings

Finally, a-WO_3 and a-W_2N coatings are irradiated. These coatings are chosen for their high oxygen and nitrogen contents (i.e. $O_2 \approx 67\%$, $N_2 \approx 37\%$) that satisfy the requirements of the EUROfusion workplan (WP PFC). For these coatings, surface damaging is always present for the entire spanned HFF range (i.e. from 1 to 25 MW m^{-2} $s^{0.5}$). In this case, only Si substrates are exploited.

Microscopy images of the irradiated samples are summarized in figure 5.17. As it can be seen, cracking occurs at very low HFFs, i.e. 2.7 MW m^{-2} $s^{0.5}$ for a-WO_3 and 1.6 MW m^{-2} $s^{0.5}$ for a-W_2N (figure 5.17c,d). Thanks to Raman analysis, crystallization of a-WO_3 can be assessed. In figure 5.18, the Raman spectra recorded for the as-deposited a-WO_3 coating and after the single shot irradiation at various HFFs are shown. When a-WO_3 is irradiated, at 7.5 MW m^{-2} $s^{0.5}$ the peaks corresponding to the monoclinic γ-WO_3 phase rise. However, the broadening of the peaks observed in the spectrum highlights that this crystallization process is not completed. Higher energies or time (i.e. number of pulses) are probably needed to completely crystallize the sample. If irradiation is performed over 7.8 MW m^{-2} $s^{0.5}$, melting is always found in the irradiated areas. In these regions, nanocrystals form after resolidification (figure 5.17g). Raman spectra of the resolidified regions clearly show an increase of the total observed peaks. In general, all the peaks related to the γ phase are sharper than the ones observed for HFF = 7.5 MW m^{-2} $s^{0.5}$. This clearly underlines a

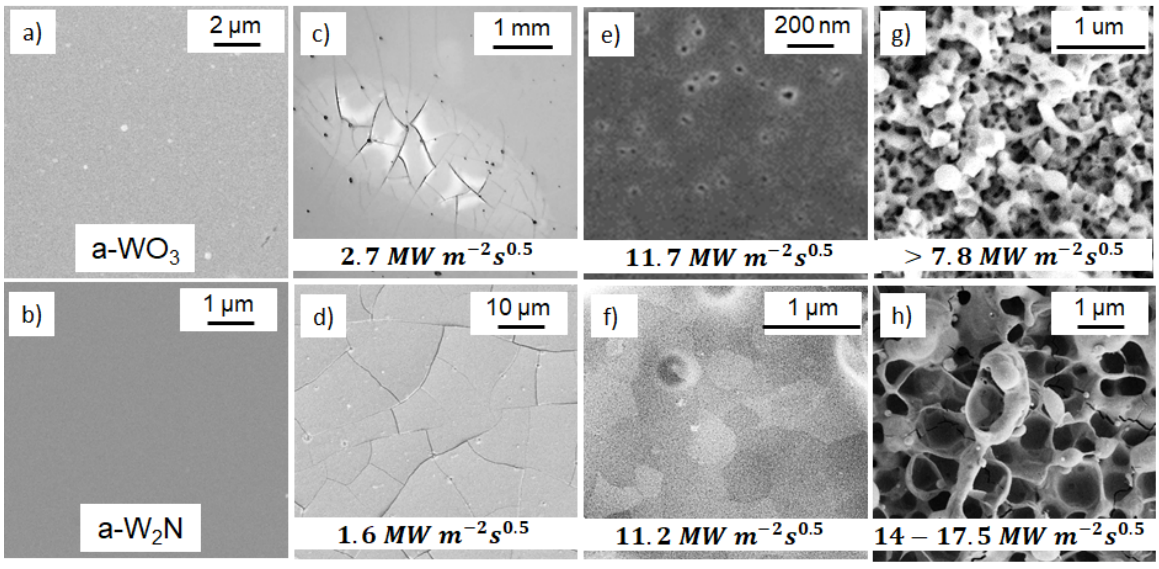

Figure 5.17: Microscopy images of irradiated a-WO_3 and a-W_2N coatings.

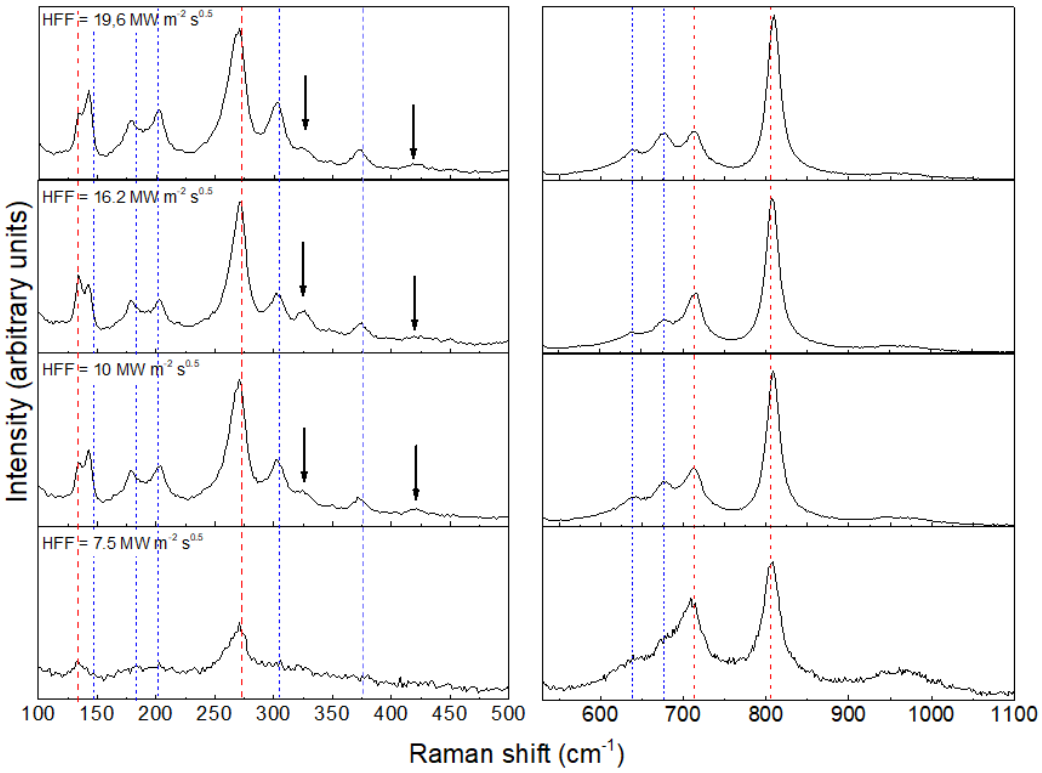

Figure 5.18: Raman spectra acquired for a-WO_3 irradiated with various HFFs. The red dotted lines refer to the peaks of the crystalline monoclinic γ-WO_3 phase, while the blue ones to the ϵ-WO_3 phase.

higher crystalline degree with respect to the one observed in the previous case. The new peaks, instead, which grow in correspondence of the blue dotted lines, are associated to the peaks found at 147 cm^{-1}, 183 cm^{-1}, 202 cm^{-1}, 305 cm^{-1}, 376 cm^{-1}, 636 cm^{-1} and 675 cm^{-1} in the case of the monoclinic (II) phase (i.e. ϵ-phase) of WO_3, which, in particular, form at high pressure and temperature conditions [200, 201]. The peak at 318 cm^{-1} and the small peak at 422 cm^{-1} indicated by the black arrows, instead, are classic features of micro-crystalline WO_3 [201]. The coexistence of both the γ-phase and the ϵ-phase of WO_3 suggests that during resolidification a high state of pressure (i.e. stress) is present in the irradiated area. Finally, in the peripheral regions of the melted area, nano-bubbles similar to the ones of a-W and p-W coatings are found starting from HFF = 11.7 MW m^{-2} $s^{0.5}$ (figure 5.17e).

In the case of a-W_2N coatings, crystallization is evidently found at 11.2 MW m^{-2} $s^{0.5}$ (see figure 5.17f). Surface melting, instead, occurs between 13 and 17.5 MW m^{-2} $s^{0.5}$ (figure 5.17h). The most interesting thermal effect found for this type of coatings is the formation of surface bubbles, several times bigger than the ones found for all the other coatings. This effect is better highlighted in figure 5.19. As it can be seen, bubbles uniformly extend over all the irradiated area. They are found at any exploited HFF, and their size increases with increasing HFF (i.e. from $\approx$ 1 μm at 1.6 MW m^{-2} $s^{0.5}$ to $\approx$ 4 μm at 17.5 MW m^{-2} $s^{0.5}$). Their formation is thus a peculiar characteristic of W_2N coatings, probably related

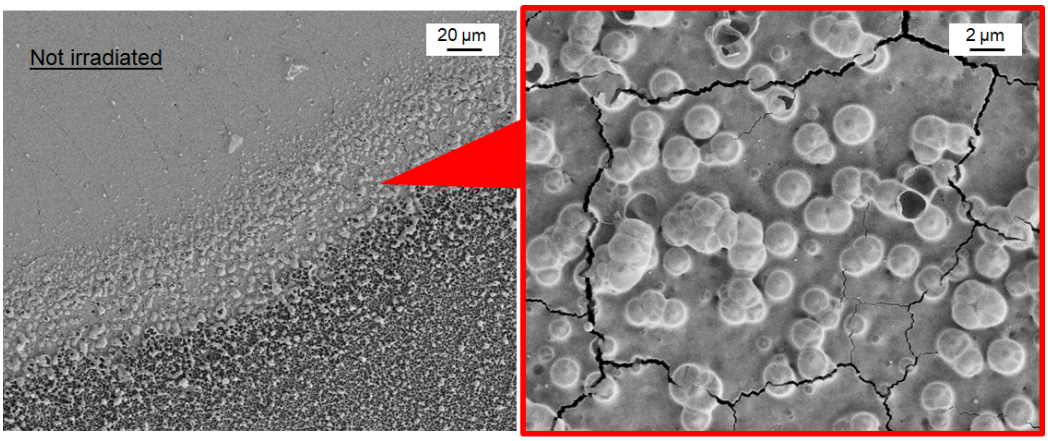

Figure 5.19: SEM images of irradiated a-W_2N where surface bubbles are highlighted.

to the high gas content (i.e. $\approx$ 20% O_2 and $\approx$ 37% N_2), and, since a-W_2N shows the lowest cracking threshold, can be indicated as the possible cause of material embrittlement. Raman spectra of the irradiated a-W_2N samples are summarized in figure 5.20. Crystalline W_2N is not raman active, so a flat spectrum is expected for the as-deposited coating. Upon irradiation, a sub-stoichiometric oxide layer forms at the surface (i.e. the spectrum obtained at 2.7 MW m^{-2} $s^{0.5}$, with no evidence of the substrate Si peak at 521 nm). The spectrum changes when melting occurs (i.e. at 17.5 MW m^{-2} $s^{0.5}$). In this last case, the two broad bands characteristic of W-oxide evolve into a broader band at high wavenumbers, between 400 and 1000 cm^{-1}, and a band at low wavenumbers, around 200 cm^{-1}, which can be related to the presence of N_2 that induces several lattice defects in the material.
For both a-WO_3 and a-W_2N coatings delamination is observed at very low HFFs, namely starting from 2.7 and 1.6 MW m^{-2} $s^{0.5}$, when first cracks are detected.

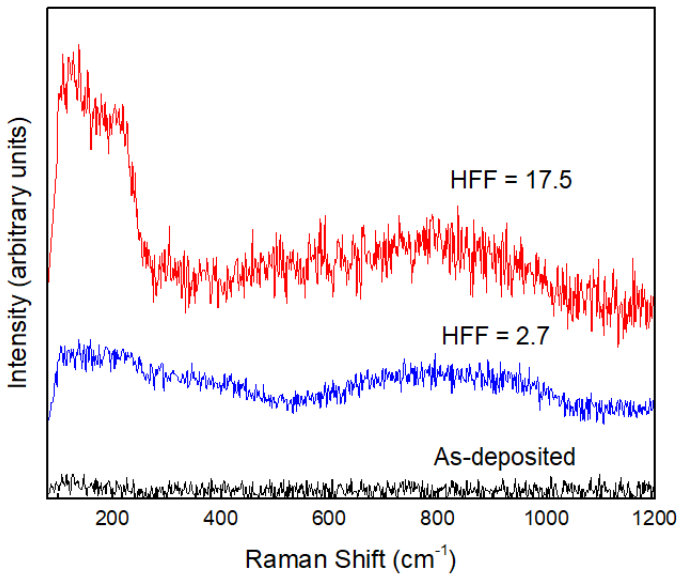

Figure 5.20: Raman spectra of irradiated a-W_2N samples.

5.2.2 Damage thresholds under multishots irradiation

Since all the coatings must withstand several thermal cycles during a single plasma discharge, they are tested up to 500 shots (with a repetition rate of 10 Hz) with HFFs ranging from 1 to 12 MW m^{-2} $s^{0.5}$. This HFF interval, if rescaled to power densities proper of plasma instabilities in a tokamak environment, corresponds to P_{abs} between 0.1 and 1.2 GW m^{-2} for a 0.1 ms ELM event. Since this part of the work is preliminar, all the irradiated coatings are deposited only on Si substrate. Bulk W will be adopted as substrate in future experimental campaigns to better mimic ITER-relevant conditions.
As it was observed for bulk W in chapter 3, a critical drop of the different damage thresholds is found as the number of pulses increases. Only for c-W coatings a lower damage threshold can be obtained. In particualr, after 500 shots at 6.2 MW m^{-2} $s^{0.5}$ no damage is observed. The various multishots thresholds are shown in figure 5.21. As it can be seen, increasing the HFF to 7.8 MW m^{-2} $s^{0.5}$, c-W start cracking after 200 pulses. After 500 shots, at the same irradiation condition, a clear surface roughening is detected. Melting and delamination occur, instead, at 12 MW m^{-2} $s^{0.5}$ starting already after 100 pulses. After 500 pulses at 12 MW m^{-2} $s^{0.5}$, a major fraction of the coating is delaminated. Nanometric bubbles are also observed on the back surface of the coating when it starts delaminating from the substrate (see figure 5.21). Their formation can be due to the high temperature of Si substrate that promotes the formation of tungsten carbides. However, further investigations must be performed to completely assess this bubbles formation mechanism.
In the case of a-W, p-W, a-WO_3 and a-W_2N coatings, irreversible surface damage is always found after 500 shots at any HFF value between 1 and 12 MW m^{-2} $s^{0.5}$. In the case of a-W coatings (see figure 5.22), at $\approx$ 4.3 MW m^{-2} $s^{0.5}$, cracking occurs between 1 and 10 shots, while melting after 50 - 100 shots. After 200 shots at this irradiation condition, the majority of the coating is already delaminated. Particularly interesting is the evolution of the fuzzy-like nanostructures formed on p-W under multishots irradiation (figure 5.23). Their formation, in contrast to the single shot threshold of $\approx$ 19 MW m^{-2} $s^{0.5}$, occurs in localized areas after only 10 shots at 3.1 MW m^{-2} $s^{0.5}$ (see figure 5.23). Increasing the shots number to 50, results in a complete melting of the surface, and fuzzy-like nanostructures are uniformly found above all the surface. After 200 shots, these nanostructures start to evaporate,

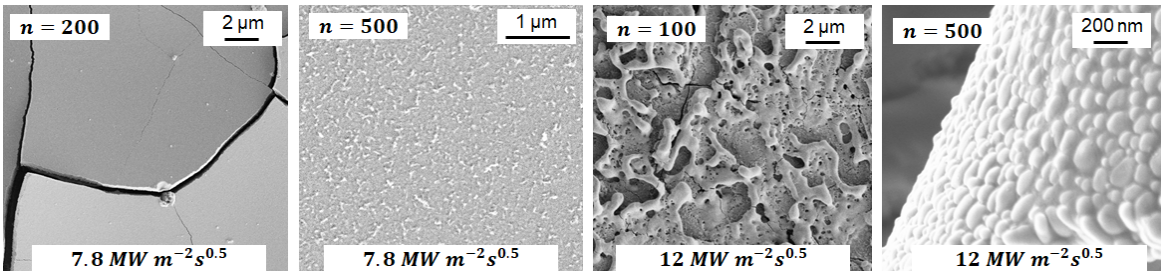

Figure 5.21: Multishots damage thresholds of c-W coatings.

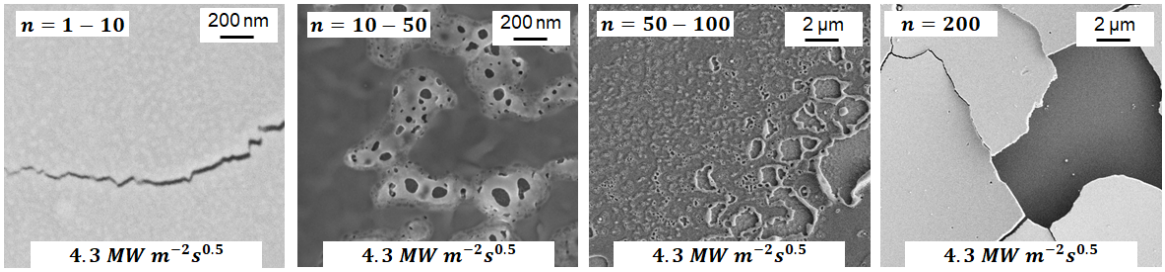

Figure 5.22: Multishots damage thresholds of a-W coatings.

such that, after 500 pulses, in the few remaining non delaminated regions, a compact melted W layer is observed.

Generally, both a-WO_3 and a-W_2N coatings do not withstand a high number of pulses without delaminating from substrates. In the case of a-W_2N samples, after only 10 shots at 1.6 MW m^{-2} $s^{0.5}$ coatings are already almost completely delaminated. For a-WO_3, instead, delamination occurs after 200 shots at 2.1 MW m^{-2} $s^{0.5}$. For this reason, thermal effects thresholds for the other effects can not be accurately determined.

As a general observed trend, if amorphous and porous coatings are irradiated multiple times, they easily delaminate from their substrates. After 100 pulses, all these coatings delaminate between 1 and 3.1 MW m^{-2} $s^{0.5}$. This HFF range, if translated into power loads of plasma transient events, corresponds to power densities between 0.1 - 0.31 GW m^{-2} for ELMs with characteristic time duration of 0.1 ms. These power densities are below the ones estimated for ELMs instabilities under ELMy H-mode during the non-nuclear phase of ITER (i.e. above 0.45 GW m^{-2}) [39]. In addition, one has to remember that thousands transient events are expected during a single plasma discharge. This unavoidably suggests that, if few plasma transient events deliver their energy onto redeposited layers, the coatings are suddenly easily removed from their substrate, they can enter the plasma, migrate and add to the dust formation inventory, which is a critical issue for both machine and PFCs operations. This is a crucial aspect that should require further analysis, considering, for example, the delamination behavior of coatings with different thicknesses and compositions from different substrates, as well as the migration of delaminated particles inside the tokamak.

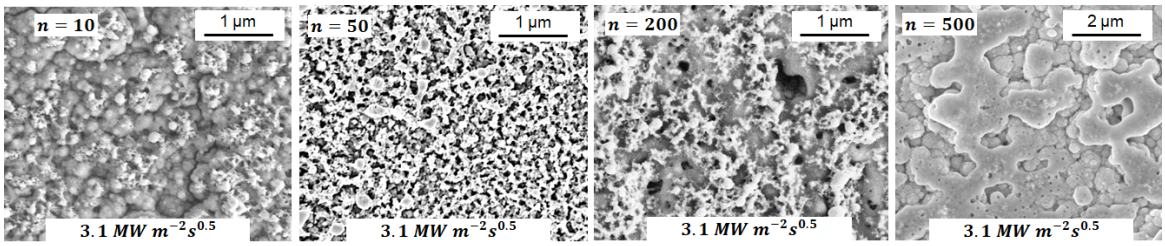

Figure 5.23: Multishots damage thresholds of p-W coatings.

5.2.3 Numerical predictions of coatings behavior under pulsed thermal loads

In section 5.2.1, single shot experimental damage thresholds are obtained for the various nanostructured W coatings. In this last section, the numerical model of laser-matter interaction developed in chapter 3 is exploited to predict these thresholds for various nanostructured coatings, by taking as input parameters all the measured properties of the coatings reported in chapter 4. The investigation is limited to metallic W coatings (i.e. c-W, a-W and p-W). Since the model does not take into account materials modifications after each shot, only the single shot thresholds can be quantitatively determined. Finally, a preliminary application of the code to a tokamak environment is presented.

From the experimental observation it is evident that the porosity degree of the material is one of the main parameters that affects the thermomechanical behavior of the coatings under thermal loads. When it increases, lower damage thresholds are found. The porosity degree (D_P) is thus considered in the model by its effect on the thermal diffusivity D_k and the yield stress σ_y. In particular, it is observed in literature that the higher the D_P, the lower the D_k [202, 203]. In the case of coatings, no direct experimental measurements about D_k are available. For this reason, a simple approximation of a reduced thermal diffusivity for the various morphologies is determined, as already done for σ_y in section 5.1, as:

$$D_k^{coating} = D_k^{bulk} \cdot (1 - D_P) = D_k^{bulk} \cdot \frac{\rho_{coating}}{\rho_{bulk}} \tag{5.3}$$

From this equation, the various D_k values of the coatings are calculated, being $D_k \approx 0.642$ cm^2 s^{-1} for c-W, 0.397 cm^2 s^{-1} for a-W and 0.25 cm^2 s^{-1} for p-W coatings. From these values, the thermal conductivities of the samples are estimated by considering the measured mass densities and by fixing the specific heat to the bulk W value (i.e. supposing that the non-void fraction of the material shows the same heat capacity of the bulk form). In this way, k is found to be $\approx$ 150 W m^{-1} K^{-1} for c-W coatings, while it drops down to $\approx$ 57 W

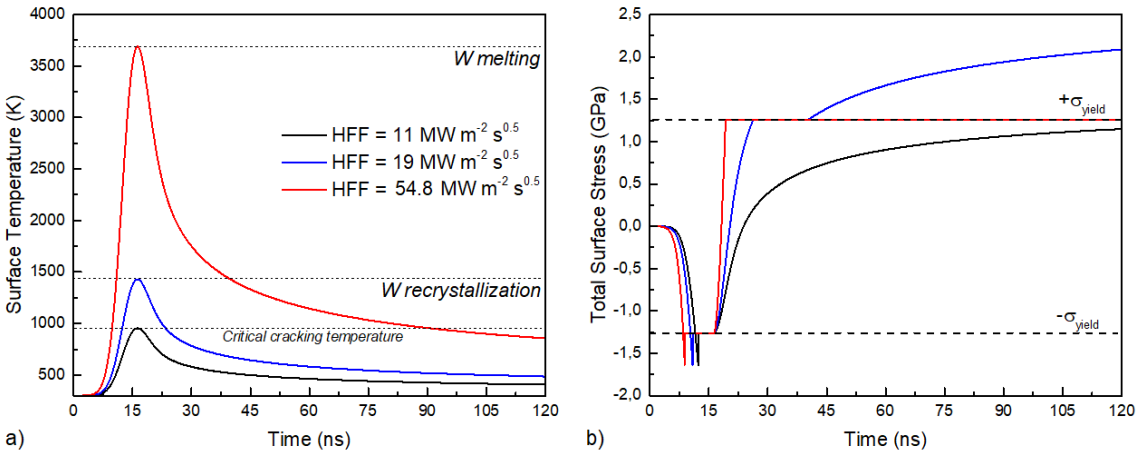

Figure 5.24: Numerical maximum surface temperature (a) and total stress (b) computed for the various HFF thresholds for c-W coatings.

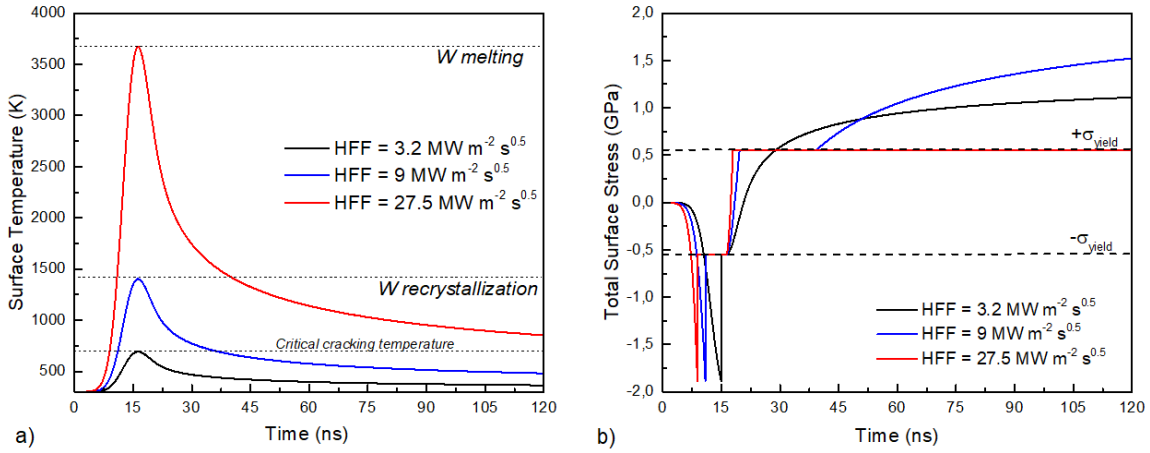

Figure 5.25: Numerical maximum surface temperature (a) and total stress (b) computed for the various HFF thresholds for a-W coatings.

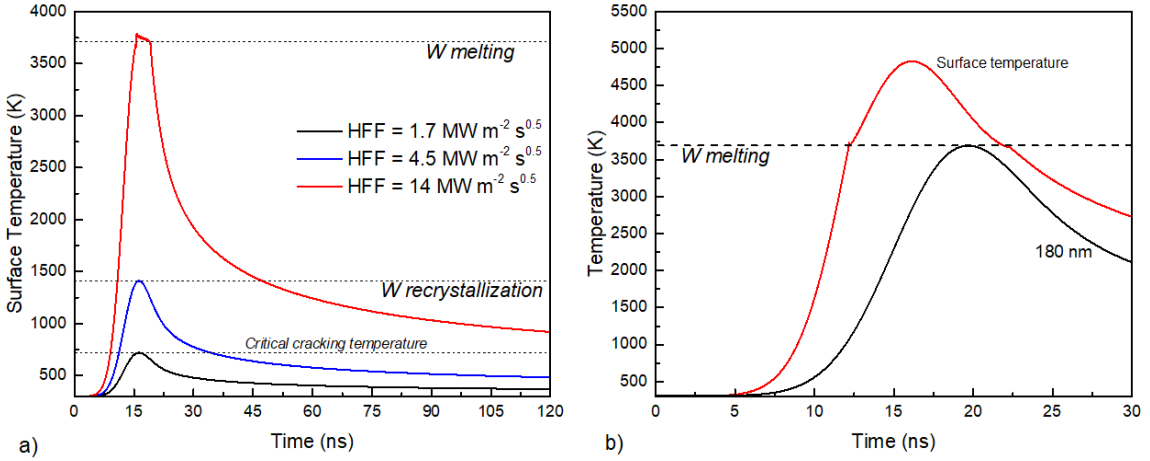

Figure 5.26: Numerical maximum surface temperature (a) computed for the various HFF thresholds for p-W coatings; (b) Numerical estimation of the melted thickness of p-W coatings for HFF = 19.2 MW m^{-2} $s^{0.5}$.

m^{-1} K^{-1} and $\approx$ 25 W m^{-1} K^{-1} in the case of a-W and p-W coatings respectively.
These values, together with the measured values of ρ and the bulk W value of the specific heat c (i.e. 130 J kg^{-1} K^{-1}) are thus considered as the inputs of the heat problem. The inputs for the mechanical problem, instead, are the measured Young Modulus E, the shear modulus G, the Poisson's ratio ν (i.e. $G/K = (3/2 - G/K)/(3 + G/K)$), the CTE and the bulk W ultimate stress. The yield stress is estimated as proposed in section 5.2 by equation 5.2. The absorbed laser power density is finally evaluated from the measured incident power density, considering the measured optical reflectance R of each coating. The value of R takes also, indirectly, into account surface roughness of the samples. It is fundamental to remember that the model considers all the coatings as homogeneous and isotropic materials. Therefore, the different morphologies and structures are taken into account only by considering the different values of the above mentioned properties. In all the simulations, silicon is considered as the substrate material. The numerical thresholds of melting, crys-

Sample	Melting Exper. - Num.	Crystallization Exper. - Num	Cracking Exper. - Num
c-W	47 - 55 / 54.8	19.5-29.7 / 19 - 23.5	16-20 / 11
a-W	23.4 / 27.5	15.5 / 9 - 11	3.3-5.6 / 3.2
p-W	15 / 14	- / 4.5 - 6	- / 1.7

Table 5.2: Comparison between the experimental and numerical HHF thresholds (MW m^{-2} $s^{0.5}$) for the single shot irradiation of nanostructured W coatings.

tallization and cracking are determined, as function of the heat flux factor, accordingly to section 3.1, when the maximum temperature exceeds the W melting temperature (i.e. 3690 K), the recrystallization temperature (i.e. 1400 - 1600 K), the DBTT (i.e. 673 K) and the total stress is higher than the yield and/or the ultimate stress during heating and cooling respectively. The computed maximum temperature and maximum total stress profiles obtained for the numerical HFF thresholds for c-W, a-W and p-W are shown in figures 5.24, 5.25, and 5.26. As it can be expected, the HFF thresholds are strongly correlated to the specific type of coating. In particular, melting occurs at 54.8 MW m^{-2} $s^{0.5}$ for c-W, at 27.5 MW m^{-2} $s^{0.5}$ for a-W and at 14 MW m^{-2} $s^{0.5}$ in the case of p-W. Crystallization, instead, is found between 19 and 23.5 MW m^{-2} $s^{0.5}$ for c-W samples, between 9 and 11 MW m^{-2} $s^{0.5}$ for a-W and between 4.5 and 6 MW m^{-2} $s^{0.5}$ for p-W. Finally, the cracking thresholds drops from 11 MW m^{-2} $s^{0.5}$ to 1.7 MW m^{-2} $s^{0.5}$ when going from c-W to p-W coatings. These thresholds correspond to critical temperatures that go from $\approx$ 980 K for c-W to $\approx$ 670 K for a-W and p-W.

The derived numerical thresholds are summarized and compared with the experimental ones in table 5.2. As it can be seen, the melting thresholds are quite in good agreement. In the model, this threshold is directly correlated to the thermal diffusivity of the coatings. Therefore, the estimation of D_k based on the porosity degree, beside being a simplified approximation, turns out to be suitable to describe the melting behavior of the analyzed complex nanostructures. As described in section 5.2.1, if p-W is irradiated over the melting threshold, fuzzy-like W nanostructures forms in the resolidified layer. In figure 5.26b, simulations are performed to investigate the thickness of the molten p-W layer if irradiation is performed, in accordance with the experiments, at HFF = 19.2 MW m^{-2} $s^{0.5}$. On the surface (i.e. red line) W melts and the temperature reaches $\approx$ 5000 K. The molten layer, consequently, extends to 180 nm (black line), where the temperature approaches the W melting temperature. This result is in very good agreement with the experimental evidence reported in figure 5.14, where the fuzzy-like layer thickness is $\approx$ 200 nm.

For c-W and a-W coatings, numerical and experimental recrystallization thresholds are also quite in good agreement. Crystallization is a much more complex process than melting, depending on the specific nanostructure, on the annealing time and the concentration of defects. The numerical thresholds, by considering only crystallization temperature, do not take into account all these parameters. For this reason, the obtained thresholds are a

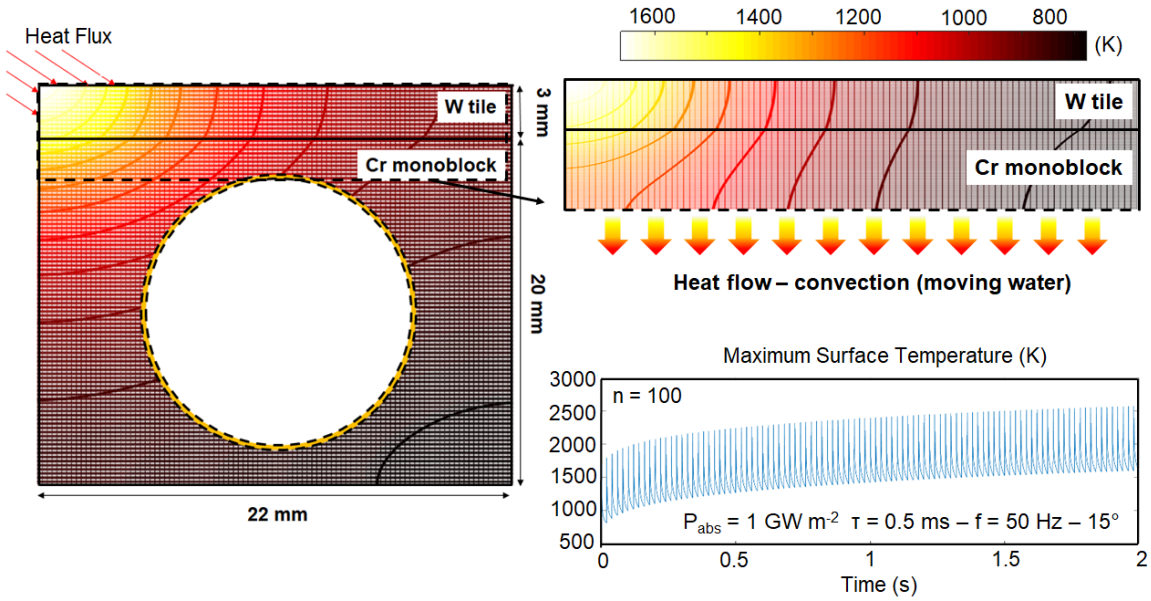

Figure 5.27: a) Numerical model of a W-Cr divertor monoblock ([129]. b) Preliminar numerical model and simulation performed in this thesis.

little lower than the observed experimental ones. In the case of p-W, crystallization is not observed experimentally, so this comparison can not be performed.

The porosity degree allows also the estimation of the yield stress of the coatings, which is required for obtaining the cracking thresholds. As it can be seen for a-W, the experimental and numerical values are in very good agreement. In this case, the material is mechanically isotropic, so the hypothesis made for the model well represent the real mechanical behavior of the sample. In the case of c-W, instead, a higher discrepancy between the two thresholds is observed. This is basically related to the mechanical anisotropy of c-W coatings, which is observed along the growth direction (i.e. along the columns), that, on the contrary, is not taken into account in the simulations. In addition, it is noteworthy that also the residual stresses and their relaxation processes, that unavoidably affect the thermomechanical behavior of coatings under thermal loads, are not considered.

From the obtained results it is evident that the thermomechanical behavior of coatings with complex structure and morphology under nanosecond laser irradiation can be well predicted by the numerical code developed in this thesis. For this reason, the model is being improved in order to extend the thermomechanical analysis also to a tokamak environment, by considering, for instance, plasma transient thermal loads (i.e. pulse duration of the order of ms), multi-shots irradiation and peculiar geometrical and materials configurations. For example, first thermal simulations are performed on ITER divertor-like W monoblocks as the one reported in figure 5.27. In this case, a 3 mm thick W tile is placed on top of a chromium (Cr) monoblock 23 mm thick, which is actively cooled by flowing water. The plasma (i.e. only the heat flux) strikes with an angle of 15° on the edge of the element (see figure 5.27a), as a classic scenario of PWIs [78]. Preliminary simulations are performed by considering

the numerical domain of figure 5.27b, where a *Robin* mixed boundary condition is applied to the lower face of the Cr layer in order to take into account the convective heat flow from the solid to the coolant. In this case, the component is at a baseline temperature of 770 K, and it is irradiated by 100 ELMs with P_{abs} = 1 GW m^{-2}, with pulse duration of 0.5 ms and frequency 50 Hz. A global convection coefficient $h = 1 \cdot 10^4$ W m^{-2} K^{-1} is considered for heat exchange with moving water in turbulent regime. As a result of the multiple irradiation, the surface temperature increases to $\approx$ 2000 K. These are only preliminary investigations that are shown here only to present the potentiality of the developed model. Future improvements will allow to take into account the real geometry of the component, the presence of redeposited layers on the top of the W tile and the complete thermal stress problem at the various interfaces.

CHAPTER 6

Conclusions and perspectives

The main aim of this thesis was to provide a thermomechanical characterization of nanostructured coatings in order to better clarify the role on such properties of the specific nanostructure, morphology and composition of the samples. In fact, it is well known that the thermomechanical properties of coatings can substantially differ from the ones of the corresponding bulk form, being deeply affected by their structure, morphology and chemical composition, but this correlation is not clarified such as these properties are hardly predictable. In this thesis, the target samples were chosen in the framework of nuclear fusion engineering, by considering coatings that mimic different coating scenarios found in operating tokamaks and expected for the future fusion reactor ITER. In particular, W coatings with different morphologies, from compact to porous, different structures, from nanocrystalline to amorphous, and different chemical compositions (i.e. W-tantalum, W-oxide and W-nitrides), and amorphous B coatings were deeply investigated. The coatings were deposited, by Pulsed Laser Deposition, by other researchers of the Micro and nano Structured Materials laboratory. In particular, nanocrystalline W coatings (c-W) were chosen as proxy of W coated plasma facing components of tokamaks (e.g. JET-ILW, ASDEX-UG, WEST). As described in chapter 2, as a result of plasma-wall interactions, plasma facing materials can be eroded and the eroded particles can enter the plasma, migrate and give rise to co/redeposition processes above the first wall materials. Co-redeposited layers properties are hardly predictable, usually showing different structures, morphologies and compositions as function of the specific machine where they are found and operating conditions history. In this thesis, amorphous and porous metallic W are thus considered as proxy of promptly redeposited W coatings, while W-oxide and W-nitride coatings as proxy of the results of co-deposition processes between W and gas impurities that can be found in the reactor.

Finally, B coatings are also investigated for their relevance for the first wall conditioning of tokamaks. The analysis of these coatings was divided into three main tasks, that were completely accomplished during this three year Ph.D period.
In order to derive the thermomechanical properties of the coatings, the first task of the thesis was the development of a novel experimental investigation method at the laboratory scale suitable for the characterization of nanostructured coatings. As described in chapter 3, this method relies on the combined use of Brillouin spectroscopy, whose data analysis procedure was optimized to derive the elastic moduli of metallic coatings, and the substrate curvature method, exploited for the detection of thermal and residual stresses and the thermal expansion coefficient of various samples. An ad hoc experimental apparatus for the substrate curvature measurements was completely developed, tested and optimized during the three year Ph.D period. This project required a multi-disciplinary approach, regarding engineering aspects for the design and the realization of the whole system, as well as computer science skills for the development of the software for the data analysis. The coupling of this system with Brillouin spectroscopy turns out to be a powerful non destructive and very versatile thermomechanical characterization method that was succesfully exploited for all the above mentioned nanostructured coatings. All the obtained data were supported by other more conventional characterization techniques, such as Scanning Electron Microscopy, X-ray Diffraction, Raman spectroscopy and Atomic Force Microscopy, adopted for the derivation of structural and morphological information. It is fundamental to stress that the exploited method, besides being applied to fusion-relevant coatings, could be adopted for a variety of samples for different types of applications (e.g. thermal barrier coatings and protective coatings). Nanosecond laser irradiation was adopted for mimicking thermal effects, such as melting, cracking and crystallization, induced by ITER-relevant transient thermal loads. The use of nanosecond lasers for this type of fusion-relevant investigation was the first of its kind, therefore it was carefully validated. As reported in chapter 3, the validation was performed by a direct comparison between the thermal effects induced on bulk W by the nanosecond laser apparatus and by more conventional fusion-relevant high heat fluxes irradiation techniques (i.e. millisecond lasers and electron beams). It was demonstrated that, by considering the heat flux factor as the irradiation comparison term between the various irradiation sources, similar thermal effects thresholds are obtained under similar heat flux factors. This required, for the first time in literature, the extension of the definition of HFF to non constant temporal sources (i.e. gaussian profiles) in the nanosecond regime. A numerical code was also completely developed and validated for predicting the thermomechanical response of nanostructured coatings during nanosecond laser irradiation. This code, basing on the finite-difference discretization, solves the heat and dynamic displcements equation for a supported coating, which, in particular, is considered homogeneous, isotropic and linear elastic.
Exploiting the above techniques, the second task of the thesis was the characterization of

the thermomechanical properties of as-deposited nanostructured coatings. These properties, presented in chapter 4, were determined and deeply discussed in terms of their relation to the specific nanostructure, morphology and chemical composition of the samples. The developed method resulted really sensitive to nanostructure changes, and could provide quantitative information about various thermomechanical properties, like the stiffness, the thermal expansion coefficient and residual and thermal stresses. In particular, it was observed that the differences of these properties between various samples were strictly related to mass density (ρ), crystallites size ($\bar{D}$) variations and to material composition. This explained why amorphous metallic W coatings, being characterized by a mass density about 60% the bulk W one and negligible crystallites dimension, showed a loss of stiffness by about 40% with respect to the nanocrystalline counterpart. The softening of the coatings, in turns, resulted in an increase of the thermal expansion coefficient (i.e. the CTE of amorphous W is about twice the one of bulk W), that, as oberved for the elastic moduli, was found to be strictly correlated to ρ and $\bar{D}$. A peculiar nanostructure was found for crystallites size between 4 and 10 nm. This structure was called ultra-nano-crystalline structure, and its related thermomechanical properties resulted from a non obvious interplay between the crystalline fraction and the averaged size of the crystalline seeds and void fraction. The addition of Ta atoms, within the explored concentrations, resulted in the formation of a solid solution regime, where both the measured stiffness and CTE, within the nanocrystalline domain, well agree with the prediction made by the lever rule of mixtures. Moreover, the properties of amorphous W coatings resulted to be strongly affected by the chemical composition of the samples. In particular, the formation of amorphous W-oxide phase drastically lowers the stiffness to about 20% the nanocrystalline W one, as the O/W stoichiometric ratio increases. The addition of N_2, instead, gave the amorphous phase a higher stiffness, being increased by about 70% when W_2N compounds form, with, consequently, a coherent reduction of the thermal expansion coefficient.

The last task of the thesis was devoted to the investigation of the behavior of these coatings under thermal loads. In particular, in chapter 5, the coatings were tested under two different fusion-relevant scenarios that mimic both steady and transient thermal loads. For the former case, standard annealing treatments were exploited to investigate the behavior of amorphous W and W-oxide coatings at ITER-relevant steady operating temperatures. Two different annealing treatments were performed, namely "steady" annealing at temperatures up to 1080 K (i.e. the temperature is kept fixed for 2 hours) and "fast" annealing (i.e. temperature ramps ≈ 50 K min^{-1}). In the former case, the crystallization behavior was investigated. It turned out that amorphous W crystallizes at temperatures well below the bulk W recrystallization temperature (i.e. between 670 K and 920 K). This induced a substantial stiffening of the material and a reduction of the thermal expansion coefficient. During fast annealing treatments, instead, the total stress of the coatings was monitored during heating and cooling processes, so that material yield and relaxation processes could be detected. It

was found that also the yield stress of the coatings was strictly affected by the specific material nanostructure, being in the case of amorphous W $\approx 40\%$ the bulk value. In general, all these tests have demonstrated that the exposure to high temperatures, which, however, are far from the recrystallization temperature of bulk W, drastically changes the properties of the coatings. This could represent a crucial aspect also for tokamak environments, where PFCs will be eventually coated by layers with unknown pristine properties, that could also change during machine operation. Finally, the behavior of W nanostructured coatings was investigated under pulsed thermal loads mimicked by nanosecond laser irradiation. To this purpose, the coatings were tested under both single and multishots laser irradiation, and the heat flux factor thresholds for the different thermal effects were obtained for the various structures and morphologies. Damage thresholds were found to be strongly affected by the porosity degree of the coatings, being lower as the coatings become more porous. This was observed for the melting and the cracking threshold, which, in turn, strictly depend on the thermal diffusivity and the yield stress of the material. For this reason, the role of the porosity degree was considered in the numerical model by estimating reduced values of these two properties. Reduced thermal diffusivities and yield stresses were thus obtained simply starting from the bulk values and by applying a reduction factor given by the variation of the coating mass density with respect to the bulk one. The obtained values, together with all the measured thermomechanical properties of the coatings, were thus taken as inputs for the numerical code, in order to predict the experimentally observed damage thresholds. The computed numerical thresholds were finally compared to the experimental ones obtained under single shot irradiation, showing a very good agreement. This clearly underlined the possibility to predict the thermomechanical behavior of nanostructured coatings without considering the real complex coating structure and morphology.

All the thresholds observed for nanostructured coatings could have a significant impact in better understanding the thermal effects induced by plasma-wall interactions in tokamak environments. In particular, it was demonstrated that amorphous and porous coatings could eventually delaminate from W substrates after few hundreds of shots performed at HFF between 1 MW m^{-2} $s^{0.5}$ and $\approx$ 4 MW m^{-2} $s^{0.5}$. These values can be easily rescaled to power densities proper of a plasma instability. For instance, considering a 0.1 ms ELM, this stands for P_{abs} between $\approx$ 100 and 400 MW m^{-2}, which are well below the power densities expected on divertor PFCs during ELMs in ITER. This unavoidably suggests that, if few plasma transient events deliver their energy onto redeposited layers, the coatings can be suddenly easily removed from their substrate, they can enter the plasma, migrate and add to the dust formation inventory, which is a critical issue for both machine and PFCs operations.

In conclusion, this Ph.D thesis has brought tangible and fruitful results that can allow a deeper understanding of the thermomechanical properties of nanostructured coatings, even under extreme fusion-relevant conditions. Basing on these results, further investigations

could be:

- To study the thermomechanical properties of W based coatings with different elemental composition (e.g. H, D) that better mimic co-deposited tokamak layers in presence of nuclear fuel.
- To apply the thermomechanical characterization method to other critical fusion-relevant coatings, such as the W graded micrometric joints for the CuCrZr heat sink of divertor monoblocks.
- To investigate synergistically the effects of the exposure to particles and heat fluxes on the thermomechanical properties of the coatings. This can be performed, for example, by exposing the coatings to linear plasmas and then to nanosecond laser irradiation, or directly into fusion-relevant dedicated facilities (e.g. GLADIS).
- To extend the numerical model also to multishots irradiation, by considering material modification after each shots (e.g. through the variation of the optical reflectivity after each pulse).
- To apply the numerical code to ITER-relevant scenarios, considering, for instance, repetitive ELM loads, actively cooled divertor W monoblock configurations, edge heating.

APPENDIX A

Optimization of the Substrate Curvature apparatus

A.1 Optimization of the experimental setup

In our experimental setup, K, L and F can be varied; an optimization process has been performed. Both cases $K < F$ and $K > F$ have been considered. The image on the CMOS sensor can be shrinked, such that the spot distance for a flat specimen, $\mathrm{d}(R = \infty) = \mathrm{d}_\infty$, becomes smaller than D_0. The absolute sensitivity $d\left(\Delta d_f\right)/d(1/R)$ has to be assessed against the physical pixel size of the sensor; however, the performance of the experimental configuration is better characterized by the relative sensitivity $d(\Delta d_f/\mathrm{d}_\infty)/d(1/R)$, which

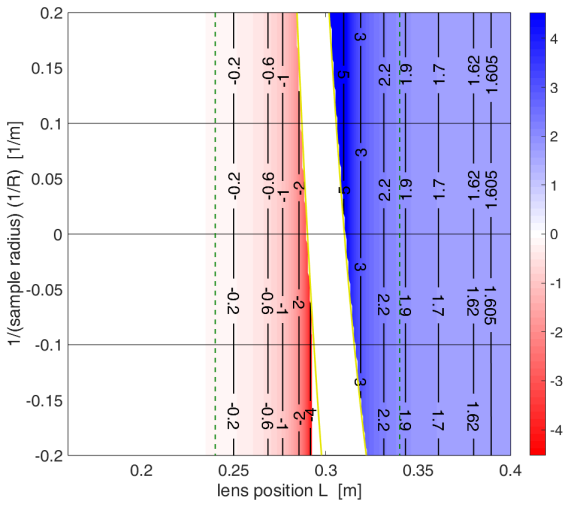

Figure A.1: Relative sensitivity $d(\Delta d_f/\mathrm{d}_\infty)/d(1/R)$ [m] map for different lens positions L, sample curvature radii R, and for fixed arm length $A = 0.4$ m and focal length $F = 0.1$ m. Continuous yellow lines delimit the white region where the measurements are not possible (see Appendix). Dashed green lines indicate the positions $L = 0.24$ m and $L = 0.34$ m of Fig. A.2c and Fig. A.2b respectively. The right border ($L = 0.4$ m) is the lens-less case of Fig. A.2a.

has to be assessed against the sensor resolution, in terms of the number of sensor pixels. Fig. A.1 presents the relative sensitivity obtained for a fixed $A = 0.4$ m and a fixed $F = 0.1$ m, varying L between 0.16 m and 0.4 m (the latter distance is the lens-less case). The distance $L = 0.34$ m has been identified, which allows an image shrinkage by a factor of more than 2, therefore a significantly smaller sensor, with a relative sensitivity which is larger, by over 20%, than that of the lens-less case with the same A (as shown by Fig. A.1). This configuration ($A = 0.4$ m, $F = 0.1$ m and $L = 0.34$ m) is adopted in our measurements; it is suitable up to strong curvatures (R down to 5 m or even less). As it can be seen from Fig. A.1, if the curvature is not very strong (e.g. R above 10 m) the lens can be shifted to slightly smaller values of L, obtaining a further boost of the relative sensitivity.

The analysis of the measurement configuration, under the paraxial approximation discussed in the text, is simple in the case in which the measurement arm, of length A, does not include a lens. With reference to figure 3.4, in this case the distance of the two spots, on the light sensor, is

$$\mathrm{d} = D_0 + 2A \sin 2\alpha \tag{A.1}$$

i.e., exploiting equation 3.4

$$\mathrm{d} = D_0 + 4A \frac{D_0}{2R \cos\theta} \quad . \tag{A.2}$$

Therefore

$$\frac{\mathrm{d}}{D_0} = \left(1 + \frac{4A}{2R\cos\theta}\right) \tag{A.3}$$

and the relative sensitivity is

$$\frac{d\,(\mathrm{d}/D_0)}{d\,(1/R)} = \frac{4A}{2\cos\theta} \quad . \tag{A.4}$$

Since in the lens-less case $\mathrm{d}_\infty = D_0$, the relative sensitivity of equation A.4 coincides with the more general definition $d\,(\mathrm{d}/\mathrm{d}_\infty)\,/d\,(1/R)$. Eq. A.4 shows that in the lens-less case the relative sensitivity is simply proportional to the arm length A, and increases when the incidence angle increases. However, for incidence angles approaching 90° (grazing incidence) the measurement becomes very delicate, and more sensitive to various causes of error. In our set up $\theta = 60^\circ$, a good compromise between sensitivity and robustness of the measurement. The relative sensitivity is thus simply $4A$, i.e. 1.6 m for $A = 0.4$ m and 3.2 m for $A = 0.8$ m.

It can be noted that the relative sensitivity does not depend on D_0. The resolution of the light sensor is measured by its number of pixels; the relative sensitivity can be translated into a resolution in terms of $1/R$ (see below). The sensor size must obviously be larger than D_0, but not too much larger. A full exploitation of the sensor area is achieved when the sensor size is, say, $1.5\,D_0$ to $2\,D_0$. The independence of the relative sensitivity from D_0 might suggest that the value of D_0 be irrelevant. If sensors of different sizes were available, with the same number of pixels, measurements with different values of D_0 would have the

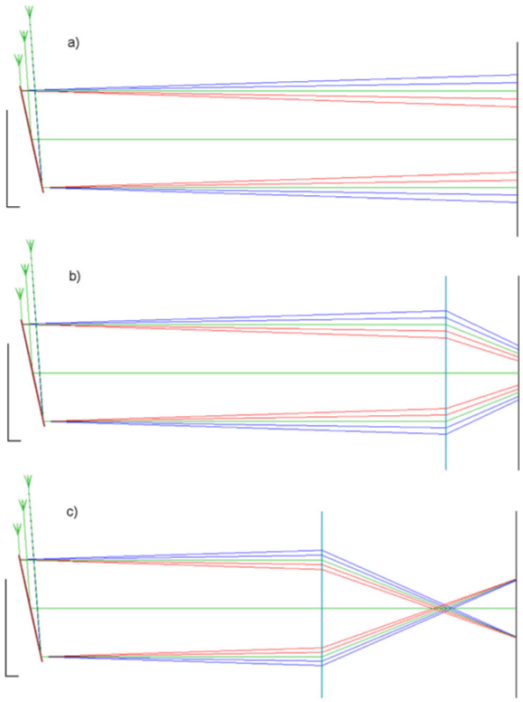

Figure A.2: Rays trajectories for fixed arm length $A = 0.4$ m, focal length $F = 0.1$ m and beams distance D_0 = 10 mm, for the lens-less case (a), ad the lens at $L = 0.34$ m (b) and $L = 0.24$ m (c). of Fig. A.2c and Fig. A.2b respectively. In order to improve the readability, the representations are stretched in the vertical direciton (the unit lengths of the two directions are indicated by the black segments).

same relative sensitivity, i.e. would be of the same quality, provided the appropriate sensor size was always selected. The only consequence of a larger, or smaller, D_0 would be the need, or not, of a larger sample. This is not completely true. The beams have a finite lateral size, which is independent from D_0, and if their distance becomes too small they cannot any longer be resolved, and the measurement becomes impossible. The beams become too close when D_0 is small and/or the sample has a strong concavity. If the minimum distance at which the beams can be resolved is, say, 2 mm, when D_0 is 5 mm the threshold is reached when $\mathrm{d}/\mathrm{d}_\infty$ is reduced to 0.4, while when D_0 is 10 mm measurements are possible until $\mathrm{d}/\mathrm{d}_\infty$ is reduced to 0.2. The size D_0=10 mm is adopted in our set up and in the following analyses.

The configuration with the lens is analyzed by an in-house developed Matlab code which implements the ray tracing technique, under the same paraxial and thin lens approximations, already mentioned. The results are presented here in detail for fixed $A = 0.4$ m, $F = 0.1$ m and D_0=10 mm, and varying L between 0.16 m and 0.4 m (the latter distance is the lens-less case). The direct outcomes of the ray tracing analysis are presented in Fig. A.2, for the representative cases of $L = 0.4$ m (the lens-less case), $L = 0.34$ m ($K < F$) and $L = 0.24$ m ($K > F$). Some qualitative considerations are already possible from these figures. A quantitative analysis is presented in Figs. A.3 and A.1, which have the same scales, for all the L values between 0.16 m and 0.4 m and for all the R values between ∞

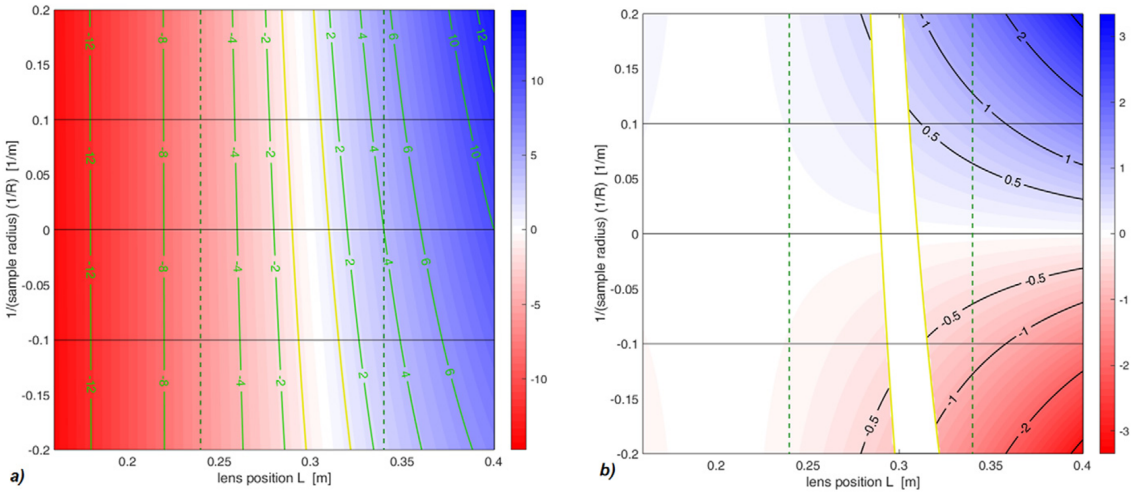

Figure A.3: Maps of spot distance d ([mm], a)) and spot displacement d - d_∞ ([mm], b)) on the light sensor, for different lens positions L, sample curvature radii R, and for fixed arm length $A = 0.4$ m and focal length $F = 0.1$ m. Continuous yellow lines delimit the white region where the measurements are not possible because the spots are too close to be resolved. Dashed green lines indicate the positions $L = 0.24$ m and $L = 0.34$ m of Fig. A.2c and Fig. A.2b respectively. The right border ($L = 0.4$ m) is the lens-less case of Fig. A.2a.

(perfectly flat sample) and $R = +5$ m (convex sample) and $R = -5$ m (concave sample). The lens-less case of Fig. A.2a corresponds to the right border of these figures, while the two cases of Figs. A.2b and c are indicated by dashed lines. Fig. A.3a maps the distance among the spots on the light sensor. It shows that that the lens at $L = 0.34$m shrinks the image by a factor of more than 2. A band exists around $L = 0.3$ m ($K \simeq F$) in which the measurement is not possible because the spots on screen cannot be resolved: although the beams are partially focalized, they still have a finite size. In Fig. A.3a, this band is delimited by the yellow lines, drawn for d $= 1$ mm, and the same band is indicated in Figs. A.3b, and A.1. The limit at 1 mm is not conservative, but the maps are drawn for d down to 1 mm to appreciate the trends when approaching the measurability limit. In Fig. A.3a the right part of the map presents positive values, meaning that for $K < F$ the beams impinge on the sensor in the same order they have in the lens-less case (see Fig. A.2b), while the negative values in the left part indicate that that for $K > F$ they impinge in the reversed order (see Fig. A.2c). Fig. A.3b maps the distance variation d $-$ d_∞ (the spot displacements); positive and negative values indicate the expansion and the shrinkage of the image. From these two maps the map of the relative sensitivity, Fig. A.1, is derived. It shows that, perhaps unexpectedly, the behaviours for $K < F$ and for $K > F$ are very different. For $K < F$, the relative sensitivity is always larger than its value in the lens-less case. Starting with the lens very close to the sensor, and shifting it towards larger distances, the sensitivy starts from the lens-less values and increases, at first very slowly, then more and more steeply approaching the region at $K \simeq F$, in which the measurement becomes impossible because the image is too shrinked. Conversely, when K exceeds F, a small interval of L exists, in

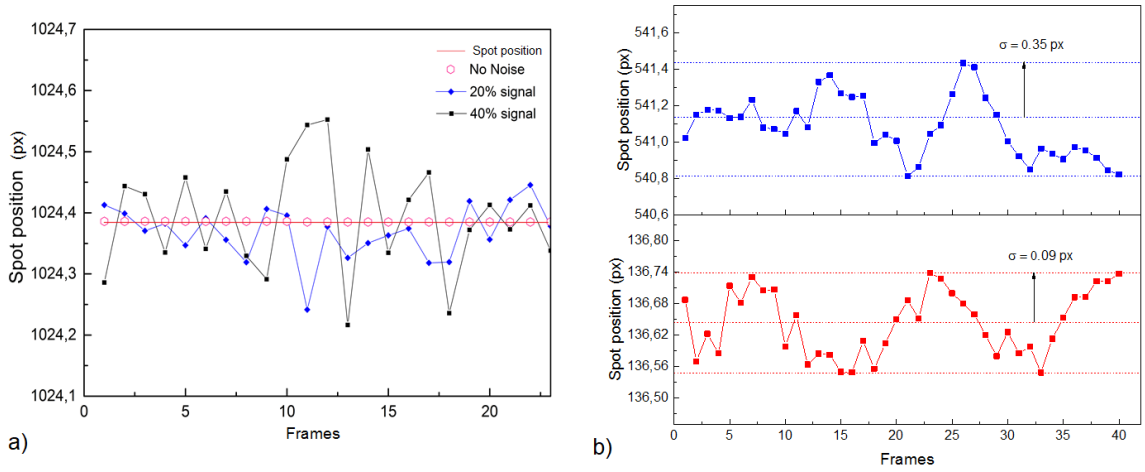

Figure A.4: a) Single spot centroid determination testing by synthetic code with increasing background noise. b) the blue line refers to a single spot centroid determination in the real apparatus subjected to vacuum system vibration. The red line is the differential spacing between two adjacent spots under the same operating conditions.

which the image is very shrinked and the sensitivity is high, but then the sensitivity rapidly drops to values much smaller that those of the lens-less case. Figs. A.2b and c allow to appreciate these different behaviours. The optimal lens position is thus found for $K < F$. In particular, the distance $L = 0.34$ m has been selected, in which the image is shrinked by a factor of more than 2 (see Fig. A.3a), but remains well readable up to strong curvatures (R down to 5 m or even less), either convex or concave. For this value of L the relative sensitivity is larger, by over 20%, than that of the lens-less case with the same A (as shown by Fig. A.1).

A.2 Centroid determination algorithm

The centroid determination algorithm is a classic centroid of intensity algorithm which weights the intensity of each pixel in the spot with respect to the overall pixel intensity in the selected region. This procedure is developed in MATLAB. The first step is the identification of a certain number of region of interests (ROI) which contain the laser spot. These regions are firstly determined by hand. Intensity cutoff thresholds are then applied independently for each ROI. This step is necessary to *clean* the spot from irregolarities or interference fringes that can eventually distort the shape of the spot, inducing large errors in the centroid determination. Once this starting routine is completed, the software computes the centroids by applying the image proccessing toolbox routine of MATLAB (i.e. *regionprops* command). Automatically, the software updated the ROIS and follows the centroids for each frame, eventually stopping if some conditions are not satisfied (e.g. the spot is no more contained totally in the ROI).

The algorithm has been synthetically tested to determine the accuracy of the method. The tests are shown in Fig. A.4a in the case of (a) a fixed laser spot, (b) a fixed laser spot

with an artificial random background noise of 20% signal intensity and (c) a laser spot with artificial random background noise of 40% signal intensity. As it can be expected, the accuracy of the centroid determination is strictly related to the quantity of background noise contained in the image, going from 0.04 pixels to 0.12 pixels in the case of 20% and 40% noise respectively. Fig. A.4b shows the repeatability of the determination of the centroids of a fixed laser beam in the real experimental apparatus when the vacuum system is operating (blue line). Here, the accuracy is about 0.3 pixel. If the relative beam spacing (red line) is evaluated instead of the absolute spot position, the accuracy increases up to 0.09 px. With our sensor of 1280 x 1024 pixels, in which the spots are usually at a distance of around 800 pixels, the relative uncertainty $\delta \mathrm{d}/\mathrm{d}_\infty$ is of the order of 10^{-4}. With a relative sensitivity ($d\left(\mathrm{d}/\mathrm{d}_\infty\right)/d\left(1/R\right)$) of 1.6 m in the lens-less case and around 2 m in our setup, this corresponds to an uncertainty $\delta(1/R)$ around 5×10^{-5} m^{-1}. With a typical curvature radius of 100 m, this means a relative uncertainty $\delta(1/R)/(1/R)$ of 5×10^{-3}, down to 5×10^{-4} when the curvature radius decreases to 10 m.

APPENDIX B

Experimental Details

B.1 Pulsed Laser Deposition

The PLD system exploited for the deposition of the coatings analyzed in this thesis work consists of a solid state laser, optics for laser focusing onto the target, a high vacuum chamber, a pumping system and a set of manipulators, remotely controlled, for both the target and the substrate motions. This setup is better highlighted in figure B.1. The laser is a Nd:YAG Continuum Powerlite II 8010 laser, operating in the Q-switched mode, which generates nanosecond pulses (FWHM = 7 ns) at the fundamental wavelength of λ = 1064 nm. The maximum repetition rate is 10 Hz. The maximum energy per pulse is tunable by an external amplification module, and depends on the specific selected wavelength, ranging from 160 mJ for λ = 266 nm (i.e. UV), to 800 mJ at λ = 532 nm (i.e. Vis), to 1800 mJ at the fundamental harmonic (i.e. IR). The laser beam has a circular shape with a diamater of $\approx$ 9 mm. Then, it strikes with an angle of 45° on the target surface (the laser spot on target

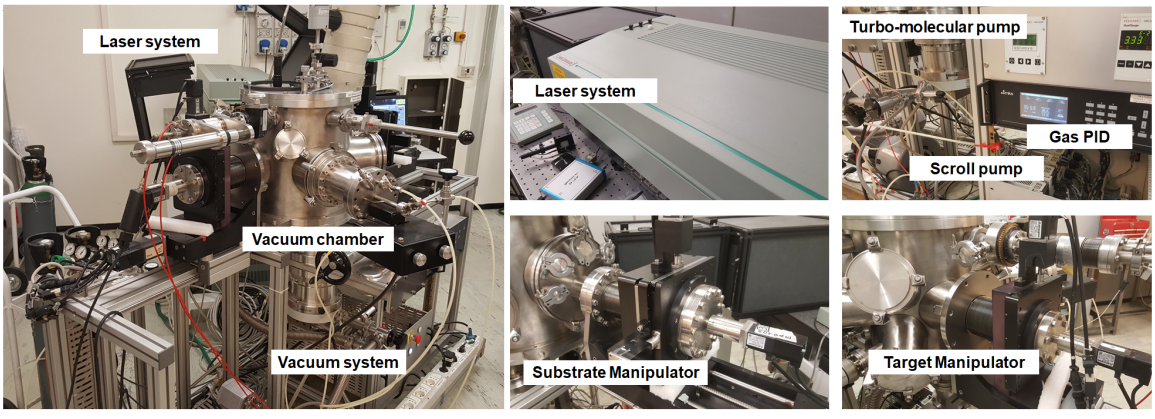

Figure B.1: PLD apparatus present at the NanoLab of Politecnico di Milano.

thus shows an elliptical shape).
The vacuum chamber is a stainless steel cylinder. The pumping system (i.e. scroll pump + turbo-molecular pump) provides nominal vacuum conditions of 10^{-4} Pa. The pressure is measured by a capacitance gauge and by a full range gauge. The gas inlet is controlled by a mass-flow meters system, which is regulated by a PID controller. The target and the substrate holders are mounted onto remotely controlled manipulators, that can provide translational and rotational motions. These motions are commanded by software-controlled (i.e. Labview) stepper motors. The combined translation and rotation motions of the substrate holder make possible to obtain films with high planarity over areas of few cm^2. The chamber is also equipped with various flanges, that can allocate crystal quartz microbalance and an ion gun for substrate pre-treatments.

B.2 Brillouin Spectroscopy

B.2.1 Principles of Brillouin Scattering

The Brillouin spectroscopy relies on the inelastic scattering between an incident laser photon and an acoustic phonon which propagates in the probed sample. This interaction does not involve the excitation of the acoustic waves, but relies only on their thermal fluctuations. These thermal fluctuations are governed by the equipartition principle of thermodynamics, which associates to each degree of freedom, which for a continuum body corresponds to an acoustic mode with a certain wavevector k, a mean energy of:

$$< E >= k_B T \tag{B.1}$$

where k_B is the Boltzmann constant (i.e. $1.38 \cdot 10^{-23}$ J K^{-1}) and T the temperature of the medium. The specific scattering geometry expoloited for the experimental measurements selects a specific value of k, in order to investigate the thermal fluctuations at this particular wavevector and to determine the dispersion relations of the acoustic modes.
The laser exploited in this thesis is characterized by a wavelength λ = 532 nm, such that $\lambda >> a$, where a is the interatomic distance. The medium, in this case the coating, can be thus assumed as an elastic continuum which is characterized by different parameters, such as the elastic constants C_{ij}, the mass density ρ and the thickness t. Most of the incident light is absorbed, refracted or specularly reflected by the probed surface. However, due to the thermal fluctuations, part of the laser light is diffusively scattered undergoing a frequency change that can be opportunely determined in order to detect the acoustic modes. This scattering process is very similar to the Raman one, even if in the case of Raman spectroscopy it entails molecular vibrations (or optical modes).
In the case of metallic opaque solids the laser can penetrate few nanometers beneath the surface, thus probing the acoustic modes that propagates at the surface of the coating (these modes are the surface acoustic modes (SAWs)). In this case, Brillouin spectroscopy is com-

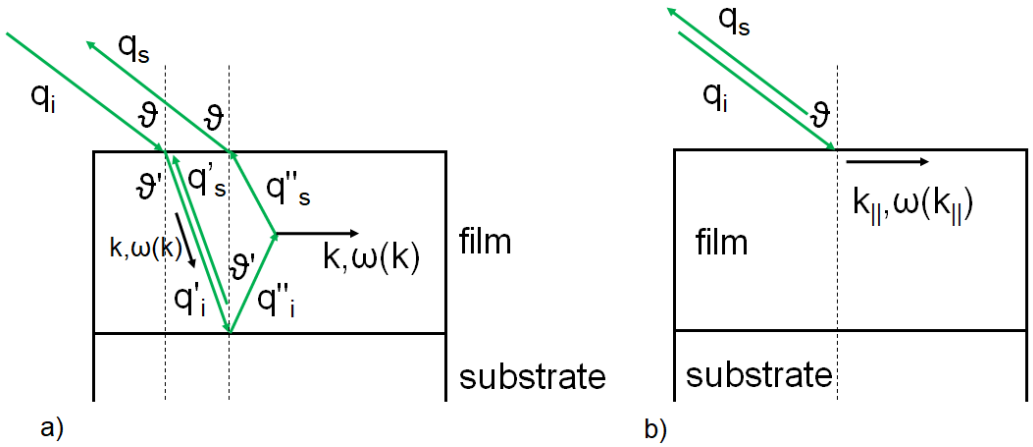

Figure B.2: a) Case of transparent supported coating with a refractive index n. b) Surface Brillouin scattering in the case of opaque coating. The probed wavevector of the SAW is determined by $k_{||} = (q_i - q_s)_{||} \approx 2q_i sin\theta$.

monly referred to as Surface Brillouin Spectroscopy (SBS). For transparent media, instead, the light can deeply penetrate in the coating, reaches the substate, and it can probe a higher amount of acoustic modes from within the bulk (these are the bulk waves (BW)), and BS can be referred to as Bulk Brillouin Spectroscopy. These two different scattering configurations are better highlighted in figure B.2a and b. Here, a laser beam characterized by an incidence angular frequency Ω_i and a wave vector q_i strikes on the coating surface with an angle of incidence θ. In the case of transparent coatings, the incident linght can be refracted and scattered from the bulk. In this case, the scattering is mediated by the so-called *elasto-optic scattering mechanism*, which is basically due to the fluctuations in the refractive index n mediated by the dynamic fluctuations in the strain field. The strain field in the bulk, in turn, can be expressed in terms of a superposition of the displacement fields associated to all the bulk acoustic modes of the solid. In the case of anisotropic media, these modes are the bulk *primary* or *longitudinal* mode (L) and the *fast-transverse* (FT) and the *slow-transverse* (ST) modes. In the case of an isotropic continuum, the two transverse modes degenerate into a single bulk transverse acoustic wave (T). For a particular backscattering scattering geometry, only the bulk waves having $k = q_i' - q_s'$ can be detected. In this way, the collected spectrum contains the contributions of these three/two bulk modes at frequency shifts (ω) determined as:

$$\omega = \pm 2 q_i' c_{bulk} \tag{B.2}$$

where c_{bulk} is the phase velocity associated to the L, FT and ST modes in the direction highlighted by k. Remembering the Snell's law, then, equation B.2 can be rewritten in terms of the incident wave vector q_i as:

$$\omega = \pm 2 n q_i c_{bulk} \tag{B.3}$$

In addition to the Brillouin spectra coming from the refracted beam, in some cases scattering can occur also from the wave vector q_i'' reflected by the substrate surface. In this case, only scattering with bulk waves having k parallel to the surface and of magnitude $k = 2q_i'' sin\theta'$ can be detected. By means of Snell's law, the detected bulk waves parallel to the surface are characterized by a frequency shift

$$\omega = \pm 2 q_i c_{bulk} sin\theta \tag{B.4}$$

yielding one or more bulk wave velocities parallel to the surface.
When scattering by opaque solids is considered, the scattering mechanism is mediated by the *surface ripple scattering mechanism*, which is basically due to the scattering by dynamic corrugations in the surface profile related to the wave displacement. In this case the probed wave vector is limited only to the component $k_{||}$, which is parallel to the surface. This component can be described as:

$$k_{||} = 2 q_i sin\theta \tag{B.5}$$

This, in turn, allows a coupling with a continuous spectrum of bulk modes having this wavevector parallel to the surface and any value of k along the thickness (i.e. *Lamb shoulder*), and with SAWs having exactly $k_{||}$. These modes are thus characterized by a frequency shift

$$\omega = \pm q_i c_{SAW} sin\theta \tag{B.6}$$

In the collected spectra, peculiar features are present. First of all a very intense broader central peak, unshifted in frequency, which is due to the elastic scattering from static inhomogeneities and surface roughness of the sample. The peaks related to acoustic waves, usually are present in the form of doublets, related to the *Stokes* (i.e. formation of an acoustic phonon) and *anti-Stokes* (i.e. annihilation of an acoustic phonon) events. Their frequency shifts with respect to the central elastic peak is of the order of $c_{acousticwaves}/c_{laser} \approx 10^{-5}$, while their intensity proportional to $k_B T$. Due to the very low values of ω a suitable system able to resolve frequency shifts from few GHz to hundreds of GHz, which correspond to very small wave vector (i.e. from fraction to few cm^{-1}), is required. A **Fabry-Perot interferometer** is usually exploited to this purpose. This instrument is composed by a couple of plane mirrors, spaced by a quantity D, that form a sort of resonant cavity that acts as a very selective band-pass filter for the components of the collected light that satisfy the following relation:

$$2D = m\lambda \tag{B.7}$$

where m is an integer positive index. This maximum transmittivity condition is achieved by an infinite range of possible frequencies. By means of the so-called *Airy function*, a strict correlation between the transmittivity and the selected frequency can be obtained. For more details concerning the Airy function see [204]. The interferometer is then character-

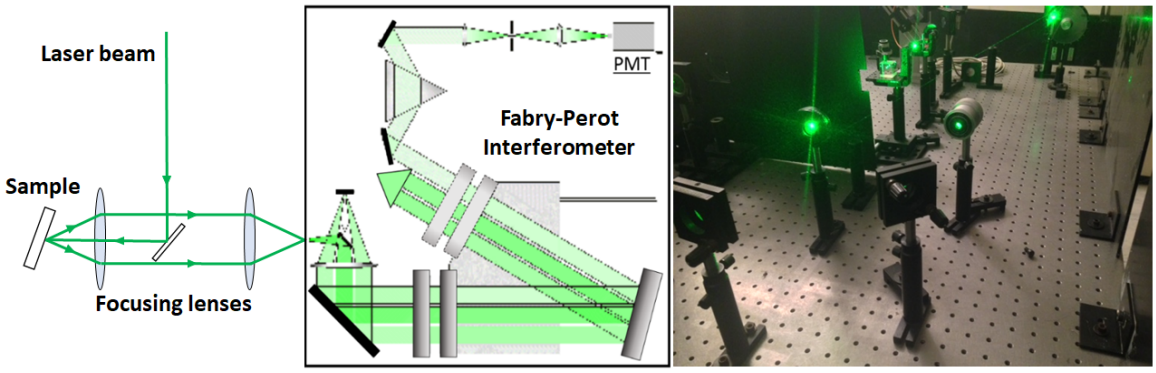

Figure B.3: Experimental setup adopted for Brillouin measurements.

ized by three main parameters, namely the **free spectral range** (FSR), which indicates the difference in frequencies in order to obtain following maxima in the transmittivity, the **finesse** (F), which describes the resolution power of the interferometer, and the **contrast** (C), defined as the ratio between the maximum and the minimum of the Airy function. High filtering efficiencies are thus achieved with interferometers with the highest contrast and finesse.

B.2.2 Experimental setup

The setup exploited in this thesis work is highlighted in figure B.3. A continuum Nd:YAG laser operating at λ = 532 nm, with a maximum output power of 800 mW, operating at 200 mW in order to avoid damaging of the sample, is exploited. The laser beam, before impinging on the coating surface, passes through a series of optical components. Initially, it is splitted into two beams, namely a *principal* beam, which is the probing beam, and an *auxiliary* one, exploited for interferometer alignement. The principal beam encounters a $\lambda/2$ lens, which modifies the polarization of the beam, making it sagittal for maximizing the cross-section for the Brillouin scattering. A pair of focusing objectives are then adopted for focusing the beam onto the sample surface (beam spot of the order of microns), for collecting the diffused light and driving it into the interferometer pinhole. The sample is mounted onto a specific holder which can be properly remotely rotated with high accuracy (0.006°). The adopted scattering geometry is the backscattering geometry.
A Fabry-Perot of the Sandercock type (see [205]), operating in the *tandem multi-pass* mode, is adopted for the analysis of the collected diffused light. This multi-pass configuration results in a substantial higher contrast with respect to the single-pass one, increasing the filtering power of the interferometer, therefore decreasing the collected photons which contribute to the background noise and allowing the detection of very small frequency shifts. Moreover, the two tandem Fabry-Perot interferometers provide very high quality of the transmitted spectra, suppressing spurious peaks associated to the periodicity of the Airy function, leaving visible only two instrumental peaks (i.e. *ghosts*) at the edge of the FSR.

The two ghosts are then exploited for the calibrating procedure of the acquired spectra. The distance between the mirrors of the interferometers can be varied from 0.8 mm to 10 mm, therefore spanning a wide range of FSR, from few GHz to 180 GHz. This allows the detection of both SAWs with very small frequency shifts and BWs.

B.3 Scanning Electron Microscopy and Energy-Dispersive X-ray Spectroscopy

Scanning Electron Microscopy (SEM) is an electrons-based microscopy techniques which eploits an electron beam, focused on the surface of the sample, to obtain information about surface topography and composition. The electrons colliding with the sample surfaces are called *primary electrons*. The interaction between the specimen and this electrons probe results in *backscattered electrons* (BSE), *secondary electrons* (SE) and X-rays. BSE are produced by elastic scattering events between the electrons and sample's nuclei. Since the sattering cross section depends directly by the atomic number of the nuclei (i.e. $\propto Z^2$), BSE can give qualitative information about samples composition. In particular, the higher the Z, the more BSE are produced. Since the energy of the primary electrons can be increased by applying high accelerating voltages, they can penetrate inside the material, so that BSE can probe the specimen well below its surface. SE, instead, are produced by inelastic scattering events between primary electrons and bounded electrons to target nuclei as ionization products. If the energy of the impinging electron is sufficiently high, a SE can be kicked out. Usually, SE are characterized by an energy of $\approx$ 50 eV. In order to reach the detector, these electrons must have an energy higher than the material work function. For this reason, due to their low energy, that can further decrease when crossing the specimen, only SE produced in first nanometers of the material can be detected. This makes the detection of SE particularly suitable to highlight surface morphology. Finally, if a primary electron collides with an electron of inner shells, as ionization products, the excited atoms can relax by emitting characteristic X-rays or Auger electrons. The X-rays can thus be collected and analyzed in order to detect characteristic lines proper of specifc elements that are present in the probed region. Energy X-ray Dispersive Spectroscopy (EDXS) thus relies on the collection of these X-rays and provides quantitative information about the chemical composition of the specimen.

The SEM exploited in this work is a high resolution Field Emission-SEM Zeiss Supra 40 based on the Gemini column, equipped with an Oxford EDXS spectrometer. The accelerating voltage ranges from 1 kV to 30 kV. The sample holder is connected with five software-controlled motors (x, y, z, rotation and tilt). The EDXS detector is a solid-state Si-Li detector protected by a Be window. The energy resolution of the detector is $\approx$ 10 eV. Quantitative composition analysis is automatically done with INCA Analysis software for homogeneous samples. For inhomogeneous, as in the case of multilayers, the acquired data must be analyzed by proper models that consider the real geometry (one of this model, which has been exploited for this thesis, has been developed during a PhD thesis at NanoLab [206]).

B.4 Raman Spectroscopy

Raman spectroscopy exploits, as in the case of Brillouin spectroscopy, a laser source to probe the vibrational properties of the sample. In particular, Raman scattering is due to the inelastic collision between an incident laser photon with a low frequency phonon of the material. Raman spectroscopy thus probes the vibrational and rotational modes of crystals or molecules. Due to the inelastic scattering, the energy of the photons changes, giving rise to frequency shifts (i.e. peaks) that are related to the modes active in the analyzed material. The presence of peaks in the collected spectra are due to a certain lattice vibration modes, which are coupled with the electromagnetic field generated by the laser source, that induces a dipole moment within the molecule based on its polarizability. The intensity of peak is thus proportional to the polarizability change. However, not all the vibrational modes can couple with the electromagnetic field. Selection rules indicate which modes are Raman active. Generally, pure metals do not show any Raman-active modes. However, if these metals show some lattice defects, impurities and a certain oxidation degree, Raman signal can be present. Therefore, Raman spectroscopy is exploited in this thesis to obtain information about the crystalline structure and the oxidation degree of W based coatings.
In a Raman spectroscopy set-up, the sample is illuminated by a laser beam. The diffused light passes through a monochromator, which selects the light that has undergone a frequency shift. This part of light is then spectroscopically analyzed. In this thesis a Renishaw In-Via Raman spectrometer is used. The laser operates at λ = 514.5 nm. The spectra are acquired by a 1800 greeds/mm grating, a super-notch filter (cut-off at 100 cm^{-1}) and a Peltier cooled CCD camera, allowing spectra resolution of about 3 cm^{-1}. The laser power is set at 1 mW in order to avoid thermal modifications of the samples.

B.5 X-ray Diffraction spectroscopy

X-ray Diffraction spectroscopy (XRD) is a non destructive technique which can be exploited to derive information about the specific phase present in the probed area, as well as structural properties, such as crystallite size or preferential orientations. The X-ray probing source is diffracted by the crystalline planes of the material, constructively interfering when the Bragg's law is satisfied (i.e. $n\lambda = 2d_{hkl}sin\theta_{hkl}$, where d_{hkl} is the distance between crystallographic planes identified by the Miller indexes hkl, and θ_{hkl} is the the angle between these planes and the incident X-ray beam).
The XRD set-up exploited for the measurements of this thesis consists in Panalytical X'Pert Pro X-ray diffractometer, which uses a monochromatic copper Kα radiation (λ 0.154 nm) and works in the *Bragg-Bretano* θ/2θ configuration.

List of Figures

List of Tables

Bibliography

[1] K. Krane, *Introductory nuclear physics*, Wiley, New York, (1988).

[2] Lawson, J. D. *Some criteria for a power producing thermonuclear reactor*, Proc. Phys. Soc. Lond. B 70, 6–10 (1957).

[3] Nuckolls, J. et al., *Laser compression of matter to super-high densities: thermonuclear (CTR) applications*, Nature 239, 139–142 (1972).

[4] Betti. R and O. A. Hurricane, *Inertial-confinement fusion with lasers*, Nature 12, pp. 435 (2016).

[5] Betti, R. et al., *Thermonuclear ignition in inertial confinement fusion and comparison with magnetic confinement*, Phys. Plasmas 17, 058102 (2010).

[6] Kishony, R. & Shvarts, D. *Ignition condition and gain prediction for perturbed inertial confinement fusion targets*, Phys. Plasmas 8, 4925–4936 (2001).

[7] Atzeni S. & Meyer-ter-vehn J., *The Physics of Inertial Fusion* (Clarendon, 2004).

[8] O. A. Hurricane et al., *Fuel gain exceeding unity in an inertially confined fusion implosion*, Nature 506, 343-348 (2014).

[9] J. Ongena et al., *Magnetic-confinement fusion*, Nature Physics 12, pp. 398 (2016).

[10] S. Sudo et al., *Scalings of energy confinement and density limit in stellarator/heliotron devices*, Nucl. Fus. 30, pp. 11 (1990).

[11] J. Sapper et al., *Stellarator Wendelstein VII-AS: Physics and Engineering Design*, Fusion Technology 17 1, (1990).

[12] M. Keilhacker et al., *High fusion performance from deuterium tritium plasmas in JET*, Nucl. Fusion, 39, 209-234 (1999).

[13] J. Wesson and D.J. Campbell, *Tokamaks*, International series of monographs on Physics, OUP Oxford, (2011).

[14] D. Stork, *Neutral beam heating and current drive systems*, Fusion Engineering and Design 14, 111-133 (1991).

[15] D.Q. Hwang and J.R. Wilson, *Radio frequency wave applications in magnetic fusion devices*, Proceedings of the IEEE, 69 pp. 1030-1043 (1981).

[16] D. Mazon et al., *As Hot as It Gets*, Nature Physics 12, 14–17 (2016).

[17] Kulsrud, *MHD description of plasma*. Princeton University, 1980.

[18] Zohm, H. *Magnetohydrodynamic Stability of Tokamaks* (Wiley, 2015).

[19] Kirk, A. et al. *Structure of ELMs in MAST and the implications for energy deposition*, Plasma Phys. Control. Fusion 47, 315 (2005).

[20] Baylor I. R. et al., *Pellet Injection Technology and Application to Mitigate Transient Events on ITER*, in Proc. 25th IAEA Fusion Energy Confin. FIP/2-1 (IAEA 2014).

[21] I. H. Hutchinson, *Principles of Plasma Diagnostics*, Cambridge University Press, 2005.

[22] L. Bertalot et al., *Fusion neutron diagnostics on ITER tokamak*, 2nd International workshop on fast neutron detectors and applications (2011).

[23] K. Tomabechi et al., *ITER Conceptual Design*, Nucl. Fusion 31, pp. 1135 (1991).

[24] *Progress in ITER Physics Basis*, Nucl.Fusion 47, S1 - S414 (2007); corrigendum 48, 099801(2008).

[25] http://www.iter.org

[26] Wirth B.D et al., *Fusion materials modeling: Challenges and opportunities*, MRS BULLETIN 36 (2011), pp 216.

[27] Materials Assessment Report G 74 MA 10 01-07-11 W, Ch 2.2 Tungsten, ITER, 2001.

[28] A. Hasegawa, et al., *Neutron irradiation effects on tungsten materials*, Fusion Eng. Des. (2014), http://dx.doi.org/10.1016/j.fusengdes.2014.04.035

[29] T. Tanno et al., *Effects of transmutation elements on neutron irradiation hardening effects*, Materials Transactions, 48 pp. 2399-2402 (2007).

[30] J.W Coenen et al., *Plasma-wall interaction of advanced materials*, Nuclear Materials and Energy (2016), http://dx.doi.org/10.1016/j.nme.2016.10.008

[31] D. Nishijima et al., *Formation mechanism of bubbles and holes on tungsten surface with low-energy and high-flux helium plasma irradiation in NAGDIS-II*, J. Nucl. Mater. 329333, part B (0) (2004) 1029 - 1033. Proceedings of the 11th International Conference on Fusion Reactor Materials (ICFRM-11)

[32] B.N. Singh et al., *Nucleation of helium bubbles on dislocations, dislocation networks and dislocations in grain boundaries during 600 MeV proton irradiation of aluminium*, J. Nucl. Mater., 125 (3) (1984) 287 - 297.

[33] J. Roth et al., *Recent analysis of key plasma wall interactions issues for ITER*, Journal of Nuclear Materials 390–391 (2009) 1–9.

[34] A.S. Kukushkin et al., *Effect of neutral transport on ITER divertor performance*, Nucl. Fus. 45 (2005) 608.

[35] G. F. Matthews, *Material migration in divertor Tokamaks*, J. Nucl. Mater 337-339 (2005) 1-9.

[36] M Mayer et al., *Erosion and deposition in the JET divertor during the first ILW campaign*, Phys. Scr. T167 (2016) 014051 (9pp).

[37] Roth J et al, *Recent analysis of key plasma wall interactions issues for ITER*, J. Nucl. Mater. 390 (2009) pp. 1 - 9.

[38] Widdowson A et al., *Material migration patterns and overview of first surface analysis of the JET ITER-like wall*, Phys. Scripta T159 (2014).

[39] R. a. Pitts et al., *A full tungsten divertor for ITER: Physics issues and design status*, J. Nucl. Mater. 438 (2013) S48-S56

[40] R. Benz et al., *Thermal Shock Testing Of Ceramics With Pulsed Laser Irradiation*, Journal of Nuclear Materials 150 pp. 128 (1987).

[41] J. Linke et al., *Performance of different tungsten grades under transient thermal loads*, Nucl. Fusion 51 (2011) 073017 (6pp).

[42] G. Pintsuk et al., *Investigation of tungsten and beryllium under short transient events*, Fusion Eng. Des. 82 (2007) 1720.

[43] T. Hirai et al., *R&D on full tungsten divertor and beryllium wall for JET ITER-like wall project*, Fusion Engineering and Design 82 (2007) 1839-1845.

[44] J. Pamela et al., *An ITER-like wall for JET*, J. Nucl. Mater. 363-365:1-11 (2007).

[45] R. Neu et al., *The tungsten divertor experiment at ASDEX Upgrade*, Plasma Physics and Controlled Fusion 38(12A):A165, (1996).

[46] Nakamura H et al., *Divertor experiment on particle and energy control in neutral beam heated JT-60 discharges*, Nucl. Fusion (28) pp.43 (1998).

[47] Philipps V et al. and Textor Team, *Molybdenum test limiter experiments in TEXTOR*, Nucl. Fusion 34 1417 (1994).

[48] R. Neu et al., *Plasma wall interaction and its implication in an all tungsten divertor tokamak*, Plasma Phys. Control. Fusion 49 (2007) B59-B70.

[49] A. Herrmann et al., *Solid tungsten Divertor-III for ASDEX Upgrade and contributions to ITER*, Nucl. Fusion 55 (2015) 063015 (7pp).

[50] R. Neu et al., *Tungsten as plasma-facing material in ASDEX Upgrade*, Fusion Engineering and Design 65 (2003) 367-374.

[51] https://www.ipp.mpg.de/16195/asdex

[52] http://www.fz-juelich.de/iek/iek-4/EN/Research/JET.html

[53] H. Maier et al., *Qualification of tungsten coatings on plasma-facing components for JET*, Phys. Scr. T138 (2009) 014031 (5pp).

[54] M. Merola et al., *Overview and status of ITER internal components*, Fusion Eng. Des. 89 (2014) 890 - 895.

[55] M. Merola et al., *Engineering challenges and development of the ITER Blanket System and Divertor*, Fusion. Eng. Des., 96-97 (2015) 34 - 41.

[56] T. Hirai et al., *Use of tungsten material for the ITER divertor*, Nuclear Materials and Energy 9 (2016) 616-622.

[57] D. Guilhem et al., *Tungsten covered graphite and copper elements and ITER-like actively cooled tungsten divertor plasma facing units for the WEST project*, Phys. Scr. T167 (2016) 014066 (5pp).

[58] J. H. You et al., *European DEMO divertor target: Operational requirements and material-design interface*, Nuclear Materials and Energy (2016), http://dx.doi.org/10.1016/j.nme.2016.02.005

[59] J. N. Brooks et al., *Plasma-surface interaction issues of an all-metal ITER*, Nucl. Fusion 49 (2009) 035007 (6pp).

[60] Y. Ueda et al., *Research status and issues of tungsten plasma facing materials for ITER and beyond*, Fusion Engineering and Design 81 (2014) 901-906.

[61] Loewenhoff et al., *Combined Steady State and High Cycle Transient Heat Load Simulation With Electron Beam Facility JUdITH 2*, PhD Thesis, RWTH Aachen, Germany,2012.

[62] M.Y. Ye et al., *Blister formation on tungsten surface under low energy and high flux hydrogen plasma irradiation in NAGDIS-I*, J. Nucl. Mater. 313-316, 72-76 (2003).

[63] W.Wang et al., *Blister formation of tungten due to ion bombardment*, J. Nucl. Mater. 299 (2001) 124.

[64] M. S. Abd El Keriem et al., *Helium-vacancy interaction in tungsten*, Phys. Rev. B 47, 14771 (1993).

[65] M.J. Baldwin et al., *Helium induced nanoscopic morphology on tungsten under fusion relevant plasma conditions*, Nucl. Fus. 48 035001 (2008).

[66] A. Baron-Wiechec et al., *First dust study in JET with the ITER-like wall: sampling, analysis and classification*, Nucl. Fusion 55 (2015) 113033 (7pp).

[67] Balden M. et al., *Collection strategy, inner morphology, and size distribution of dust particles in ASDEX Upgrade*, Nucl. Fusion 54 073010 (2014).

[68] E. Fortuna-Zalesna et al., *Studies of dust from JET with the ITER-Like Wall: Composition and internal structure*, Nuclear Materials and Energy (2017), http://dx.doi.org/10.1016/j.nme.2016.11.027

[69] V. Rohde et al., *Wall conditioning in ASDEX Upgrade*, Journal of Nuclear Materials 363-365 (2007) 1369-1374.

[70] B. Lipschultz et al., *Influence of boronization on operation with high-Z plasma facing components in Alcator C-Mod*, Journal of Nuclear Materials 363-365 (2007) 1110-1118.

[71] N.Ohno et al., *Surface modification at tungsten and tungsten coated graphite due to low energy and high fluence plasma and laser pulse irradiation*, Journal of Nuclear Materials 363–365 (2007) 1153–1159

[72] J. Matejicek et al., *ELM-induced arcing on tungsten fuzz in the COMPASS divertor region*, J. Nucl. Mater. 492, 204-212 (2017).

[73] W. Han et al., *Mass flow facilitates tungsten blistering under 60keV helium ion implantation*, Nucl. Fusion 57 (2017) 076022 (6pp).

[74] D. Maisonnier et al., *Power plant conceptual studies in Europe*, Nucl. Fusion 47 (2007).

[75] K. Wittlich et al., *Damage structure in divertor armor materials exposed to multiple ITER relevant ELM loads*, Fusion. Eng Des. 84, 1982-1986 (2009).

[76] A. Kreter et al., *Linear Plasma Device PSI-2 for Plasma-Material Interaction Studies*, Fusion Science and Technology, 68:1, 8-14 (2015).

[77] P. Majerus et al., *The new electron beam test facility JUDITH II for high heat flux experiments on plasma facing components*, Fusion Engineering and Design 75-79 (2005) 365-369.

[78] J. Linke, *Testing of plasma facing materials and components*, 13th PFMC Workshop / 1st FEMaS Conference, Tutorial Course, Rosenheim, 09. 13.05.2011

[79] C. Grisolia et al. *In-situ tokamak laser applications for detritiation and co-deposited layers studies*, Journal of Nuclear Materials 363-365 (2007) 1138-1147

[80] A. Maffini et al., *Laser cleaning of diagnostic mirrors from tungsten-oxygen tokamak-like contaminants*, Nucl. Fusion 56 (2016) 086008 (9pp)

[81] S. Kajita et al., *Plasma-assisted laser ablation of tungsten: reduction in the ablation power threshold due to bursting of holes/bubbles*, Appl. Phys. Letters 91, 261501 (2007).

[82] S. Kajita et al.,*Reduction of laser power threshold for melting tungsten due to subsurface helium holes*, Journal of Applied Physics 100, 103304 (2006).

[83] A. Suslova et al., *Recrystallization and grain growth inducedbyELMsliketransientheatloads in deformed tungsten samples*, Scientific Reports 4 (2014) 6845, doi:10.1038/srep06845.

[84] N Farid et al., *Experimental simulation of materials degradation of plasma-facing components using lasers*, Nuclear Fusion 54, (2013).

[85] P. Wang et al., *Deuterium retention in tungsten films deposited by magnetron sputtering*, Phys. Scr. T159 (2014) 014046 (6pp).

[86] E. Vassallo et al., *Effects of Nitrogen Concentration on Microstructure of Tungsten Coatings Synthesized by Plasma Sputtering Method*, J Fusion Energ (2015) 34:1246-1251.

[87] M. H. J. t Hoen et al., *Deuterium retention and surface modifications of nanocrystalline tungsten films exposed to high heta flux plasma*, J. Nucl. Mater., 463:989-992, 2015.

[88] D. Dellasega et al., *Nanostructured and amorphous-like tungsten films grown by pulsed laser deposition*, Journal of Applied Physics 112, 084328 (2012).

[89] A. Pezzoli, *Tungsten-based coatings for magnetic fusion research: damage and hydrogen retention*, PhD Thesis, Politecnico di Milano, 2016, Italy.

[90] A. Pezzoli et al., *Thermal annealing and exposure to divertor-like deuterium plasma of tailored tungsten oxide coatings*, Journal of Nuclear Materials 463, 2015, 1041-1044.

[91] C. Ruset et al. *The impact of thermal fatigue and carbidization on the W coatings deposited on CFC tiles for the ITER-like wall project at JET*, Fusion Engineering and Design 88 (2013) 1690-1693.

[92] E. Besozzi, D. Dellasega, A. Pezzoli, C. Conti, M. Passoni, M.G. Beghi, *Amorphous, ultra-nano- and nano-crystalline tungsten-based coatings grown by Pulsed Laser Deposition: mechanical characterization by Surface Brillouin Spectroscopy*, Materials and Design 106, (2016) 14 -21.

[93] E. Besozzi, D. Dellasega, A. Pezzoli, A. Mantegazza, M. Passoni and M. G. Beghi, *Coefficient of thermal expansion of nanostructured tungsten based coatings assessed by substrate curvature method*, Materials and Design 137, 192-203 (2018).

[94] D. Dellasega, V. Russo, A. Pezzoli, C. Conti, N. Lecis, E. Besozzi, C.E. Bottani, M.G. Beghi and M. Passoni, *Boron films produced by high energy Pulsed Laser Deposition*, Materials and Design 134, 35 - 43 (2017).

[95] E. Besozzi, A. Maffini, D. Dellasega, V. Russo, A. Pazzaglia, A. Facibeni, M.G. Beghi and M. Passoni, *Nanosecond laser pulses for mimicking thermal effects on nanostructured tungsten-based materials*, Nuclear Fusion 58, (2018) 036019.

[96] E. Soczkiewicz, *Velocity of Rayleigh surface waves and Poisson's ratio of a medium*, Proc. SPIE 3581, Acousto-Optics and Applications III (1998).

[97] R.J. Jimnez Riobo et al., *Elastic properties by Brillouin spectroscopy of solgel (Pb,Ca)TiO3 films*, J. Appl. Phys. 85 (1999) 7349.

[98] F.G. Ferre et al., *The mechanical properties of a nanocrystalline Al2O3/a-Al2O3 composite coating measured by nanoindentation and Brillouin spectroscopy*, Acta Mater. 61 (2013) 2662-2670.

[99] M.G. Beghi et al., *Combined surface Brillouin scattering and x-ray reflectivity characterization of thin metallic films*, J. Appl. Phys. 81 (1997) 672.

[100] T. Blachowicz et al., *Crystalline phases in the GeSb2Te4 alloy system: Phase transitions and elastic properties*, J. Appl. Phys. 102 (2007) 093519.

[101] G.A.F. Seber, C.J. Wild, *Nonlinear regression*, Wiley Interscience, 2003.

[102] G.N. Greaves et al., *Poissons ratio and modern materials*, Nat. Mater. 10 (2011) 823-837.

[103] G. Grimvail, *Thermophysical properties of materials* (Chap. 3) North-Holland Physics Publishing, 1986.

[104] B.T. Bernstein, *Elastic Properties of Polycrystalline Tungsten at Elevated Temperature*, J. Appl. Phys. 33 (1962) 2140.

[105] F. C. Marques et al., *Stress and thermomechanical properties of amorphous hydrogenated germanium thin films deposited by glow discharge*, J. Appl. Phys. 84, 3118 (1998).

[106] S. Lei et al., *Measurement of residual stress on TiN/Ti bilayer thin films using average X-ray strain combined with laser curvature and nanoindentation methods*, Mater. Chem. Phys. 199(15) (2017), pp. 185-192.

[107] R Huang et al., *Apparatus for measuring local stress of metallic films, using an array of parallel laser beams during rapid thermal processing*, Meas. Sci. Technol. 21 (2010) 055702 (9pp).

[108] M. M. de Lima et al., *Coefficient of thermal expansion and elastic modulus of thin films*, J. Appl. Phys. 86, 4936 (1999).

[109] N. Woehrl et al., *Investigation of the coefficient of thermal expansion in nanocrystalline diamond films*, Diam. Relat. Mater. 18 (2009) 224-228.

[110] R. Knepper and S. P. Bakera,*Coefficient of thermal expansion and biaxial elastic modulus of β phase tantalum thin films*, Appl. Phys. Letter. 90, 181908 (2007)

[111] S. Dutta et al., *Estimation of boron diffusion induced residual stress in silicon by wafer curvature technique*, Mater. Lett. 164(1) (2016), pp. 316-319.

[112] E. Chason, *A kinetic analysis of residual stress evolution in polycrystalline thin films*, Thin Solid Films 526 (2012) 1-14.

[113] G. Stoney, *The Tension of Metallic Films Deposited by Electrolysis*, Proceedings of the Royal Society of London. Series A, Containing Papers of a Mathematical and Physical Character 82, no. 553 (1909), 172-75.

[114] G.C.A.M. Janssen et al., *Celebrating the 100th anniversary of the Stoney equation for film stress: Developments from polycrystalline steel strips to single crystal silicon wafers*, Thin Solid Films 517 (2009) 1858-1867.

[115] R. Shayduk, V. Vonk, B. Arndt, D. Franz, J. Strempfer, S. Francoual, T. F. Keller, T. Spitzbart, and A. Stierle, Nanosecond laser pulse heating of a platinum surface studied by pump-probe X-ray diffraction, Applied Physics Letters 109, 043107 (2016).

[116] T. Kundu, *Mechanics of elastic waves and ultrasonic nondestructive evaluation, in Ultrasonic Nondestructive Evaluation*, edited by T. Kundu, CRC Press, Boca Raton, FL, (2004), chapter 7.

[117] Chen J.K. et al., *Modeling of femtosecond laser-induced non-equilibrium deformation in metal films*, International Journal of Solids and Structures 39 (2002) 3199-3216.

[118] J K Chen et al., *Comparison of one-dimensional and two-dimensional axisymmetric approaches to the thermomechanical response caused by ultrashort laser heating*, J. Opt. A: Pure Appl. Opt. 4 (2002) 650-661.

[119] A. Quarteroni, *Numerical Models for Differential Problems*, Springer-Verlag Mailand, MS&A, 2014.

[120] Noda N. et al., *Thermal Stresses* 2000 (Rochester, NY: LastranCorp.).

[121] Lin E. X., *Laser Pulse Heating*, 1999 Proceedings of the 1999 Particle Accelerator Conference, New York, 1429-1431 (doi 0-7803-5573-3/99/$10.001999 IEEE) .

[122] Carslaw & Jaeger, *Conduction of Heat in Solids*, (2nd ed.) Oxford Univ. Press, New York (1959).

[123] Boumedine H. et al., *Von mises stress for two-dimensional elasticity problems*, Scripta Materialia 34 (1996) 401-406.

[124] Arakcheev A.S. et al., *Theoretical investigation of crack formation in tungsten after heat loads*, J. Nucl. Mater. (2015) 463 246-249.

[125] Li C. et al., *Thermal stress analysis on the crack formation of tungsten during fusion relevant transient heat loads*, Nucl. Mater. Energy (2017) 1-6.

[126] Koch-Bienemann E., Berg L. and Czack G. 1987 Gmelin *Handbook of Inorganic Chemistry (Tungsten)* vol Suppl A3 (Berlin: Springer).

[127] Gustafson P., *Evaluation of the thermodynamic properties of tungsten*, Int. J. Thermophys. 6 1985 395.

[128] Werner W. S. M. et al., *Optical constants and inelastic electron-scattering data for 17 elemental metals*, J. Phys Chem Ref. Data 38 (2009) 1013-1092.

[129] Liu X. et al., *Experimental and numerical simulations of ELM-like transient damage behaviors to different grade tungsten and tungsten alloys*, J. Nucl. Mater. 463 (2015) 166-169.

[130] Kajita S. et al., *Sub-ms laser pulse irradiation on tungsten target damaged by exposure to helium plasma*, Nucl. Fusion 47 (2007) 1358-1366.

[131] Wirtz M. et al., *Comparison of the thermal shock performance of different tungsten grades and the influence of microstructure on the damage behaviour*, Phys. Scr. T145 (2011) 014058.

[132] Orii T. et al., *Target system for fabrication and control of magnetic metal content in diluted magnetic semiconductors by pulsed-laser deposition*, Vac. Sci. Tech. A 22, (2004) 2096.

[133] D.B. Chrisey, G.K. Hubler, *Pulsed Laser deposition of Thin Films*, 1994 by John Wiley and Sons, Inc.

[134] D. Dellasega et al., *Nanostructured High Valence Silver Oxide Produced by Pulsed laser Deposition*, Appl. Surf. Sci. 255 (10), (2009) 5248 - 5251.

[135] E. Irissou et al., *Influence of the expansion dynamics of laser-produced gold plasmas on thin film structure grown in various atmospheres*, J. Appl. Phys. 94, (2003) 4796.

[136] B.R. Braeckman, P. Djemia, F. Tétard, L. Belliard, D. Depla, *Impurity-controlled film growth and elastic properties of CoCrCuFeNi thin films*, Surface & Coatings Technology 315 (2017) 475-483.

[137] D. Riabinina, et al., *Influence of pressure on the Pt nanoparticle growth modes during pulsed laser ablation*, J. Appl. Phys. 108, (2010) 034322.

[138] M. Passoni et al., *Nanostructured rhodium films produced by pulsed laser deposition for nuclear fusion applications*, J. Nucl. Mater. 404, (2010) 1 - 5.

[139] B. Koslowski et al., *Oxidation of preferentially (1 1 1)-oriented Au films in an oxygen plasma investigated by scanning tunneling microscopy and photoelectron spectroscopy*, Surf. Sci. 475, (2001) 1 - 10.

[140] G. Alcala et al., *Mechanical properties of amorphous anodic alumina and tantala films using nanoindentation*, Nanotech. 13, (2002) 451 - 455.

[141] M.Q. Jiang and L.H. Dai, *Short-range-order effects on intrinsic plasticity of metallic glasses*, Phil. Mag. Lett. 90, No. 4, (2010) 269 - 277

[142] Y.Q. Wang et al., *Size- and constituentdependent deformation mechanisms and strain rate sensitivity in nanolaminated crystalline Cu/amorphous CuZr films*, Acta Mater. 95, (2015) 132 - 144.

[143] Christopher A. et al., *Mechanical behavior of amorphous alloys*, Acta Mater. 55, (2007) 40674109

[144] M. Bonelli et al., *Structural and mechanical properties of ta-C films grown by pulsed laser deposition*, Europhys. Lett., 50 (4), pp. 501–506 (2000).

[145] V. Teixeira, *Residual stress and cracking in thin PVD coatings*, Vacuum 64 (2002) 393–399.

[146] T. Ganne et al., *Cracking behaviour of PVD tungsten coatings deposited on steel substrates*, Acta Mater. 50 (2002) pp. 4149-4163.

[147] J.M. Lackner et al., *Structural, mechanical and tribological investigations of pulsed laser deposited titanium nitride coatings*, Thin Solid Films 453-454 (2004), pp. 195-202.

[148] C. Cibert et al., *Properties of alumin oxide thin films deposited by pulsed laser deposition and plasma enhanced chemical vapour deposition*, Thin Solid Films 516 (2008) pp. 1290-1296.

[149] A. Portinha et al., *Residual stresses and elastic modulus of thermal barrier coatings graded in porosity* Surface & Coatings Technology 188 - 189 (2004) 120 - 128.

[150] F. C. Nix and D. MacNair, *The Thermal Expansion of Pure Metals. II: Molybdenum, Palladium, Silver, Tantalujm, Tungsten, Platinum, and Lead*, Phys. Rev. 61 (1942), pp. 64.

[151] M. M. de Lima et al., *Coefficient of thermal expansion and elastic modulus of thin films*, J. Appl. Phys. 86, 4936 (1999).

[152] K. Lu and M. L. Sui, *Thermal Expansion Behaviours in Nanocrystlline Materials with a wide grain size range*, Acta metall. mater. Vol. 43, No. 9, pp. 3325-3332, 1995.

[153] F. C. Marques et al., *Thermal expansion coefficient of hydrogenated amorphous carbon*, Appl. Phys. Lett. 83, (2003) pp. 3099.

[154] R. Daniel et al., *Size effect of thermal expansion and thermal/intrinsic stresses in nanostructured thin films: Experiment and model*, Acta Mater. 59 (2011) pp. 6631-6645.

[155] R. Birringer and H. Gleiter, in *Advance in Materials Science*, Encyclopedia of Materials Science and Engineering (edited by R. W. Cahn), p. 339. Pergamon Press, Oxford (1988).

[156] H. J. Klam et al., *The thermal expansion of grain boundaries*, Acta metall. 35, pp. 2101 (1987).

[157] A. E. Mag-isa et al., *Coefficient of Thermal Expansion Measurements for Freestanding Nanocrystalline Ultra-Thin Gold Films*, Int. J. Preci. Eng. Man. 15, No. 1, pp. 105-110 (2014).

[158] H. Y. Tong et al., *The structure and properties of nanocrystalline* $Fe_{78}B_{13}Si_9$ *alloy*, J. Non-Cryst. Solids 150, (1992) pp. 444 - 447.

[159] J. Hay, *Measuring Substrate-Independent Properties of Dielectric Films*, Agilent Technologies, 2006.

[160] D. C. Miller et al., *Thermo-mechanical properties of alumina films created using the atomic layer deposition technique*, Sensor. Actuator. A 164 (2010) pp. 58-67.

[161] Y. Zoo et al., *Investigation of coefficient of thermal expansion of silver thin film on different substrates using X-ray diffraction*, Thin Solid Films 513 (2006) 170-174.

[162] Chaplot, S. et al., *Thermodynamic Properties of Solids*, Wiley-VCH, pp. 197-199, 2010.

[163] J. Bhattarai et al., *The passivation behavior of sputter-deposited W-Ta alloys in 12M HCl*, Corr. Sci. 40, (1998) 757 - 779.

[164] M. Muzyk et al., *Phase stability, point defects, and elastic properties of W-V and W-Ta alloys*, Phys. Rev. B 84, (2011) 104 - 115.

[165] J.F. Yang et al., *Manufacture, microstructure and mechanical properties of W-Ta-N nano-structured hard films*, Appl. Surf. Sci. 258, (2012) 7849 - 7854.

[166] M. Rieth et al., *Tungsten as a Structural Divertor Material*, Adv. Sci. Tech. Vol 73 (2010) 11- 21.

[167] S. Wurster et al., *Fracture behaviour of tungsten-vanadium and tungsten-tantalum alloys and composites*, Journal of Nuclear Materials 413 (2011) 166-176.

[168] T. Kundu, *Mechanics of elastic waves and ultrasonic nondestructive evaluation, in Ultrasonic Nondestructive Evaluation*, edited by T. Kundu, CRC Press, Boca Raton, FL, (2004), chapter 10.

[169] F. Di Fonzo et al., *Synthesis and characterization of tungsten and tungsten oxide nanostructured films*, Catalysys Today 116(1):69 - 73, 2006.

[170] A. Bailini, F. Di Fonzo, M. Fusi, C.S. Casari, A. Li Bassi, V. Russo, A. Baserga, C.E. Bottani, *Pulsed laser deposition of tungsten and tungsten oxide thin films with tailored structure at the nano- and mesoscale*, Applied Surface Science 253 (2007) 8130-8135.

[171] A. Baserga, V. Russo, F. Di Fonzo, A. Bailini, D. Cattaneo, C.S. Casari, A. Li Bassi, C.E. Bottani, *Nanostructured tungsten oxide with controlled properties: Synthesis and Raman characterization*, Thin Solid Films 515 (2007) 6465-6469.

[172] X. Sun, et al., J. Alloys Compd. (2010), doi:10.1016/j.jallcom.2010.03.155

[173] O. S. Heavens. *Optical Properties of Thin Films*, Butterworth, London (1955).

[174] Born, M.; Wolf, E., *Principles of optics: electromagnetic theory of propagation, interference and diffraction of light*, Oxford, Pergamon Press, 1964.

[175] N.M.G. Parreira et al., *Synthesis, structural and mechanical characterization of sputtered tungsten oxide coatings*, Thin Solid Films 510 (2006) 191 - 196.

[176] T. Polcar, N.M.G. Parreira, A. Cavaleiro, *Tungsten oxide with different oxygen contents: Sliding properties*, Vacuum 81 (2007) 1426-1429.

[177] J. L. Enriquez-Carrejo, M. A. Ramos, J. Mireles-Jr-Garcia, A. Hurtado-Macias, *Nano-mechanical and structural study of WO_3 thin films*, Thin Solid Films 606 (2016) 148-154.

[178] R. Daniel, K.J. Martinschitz, J. Keckes, C. Mitterer, *The origin of stresses in magnetron-sputtered thin films with zone T structures*, Acta Materialia 58 (2010) 2621-2633.

[179] G. Soto et al., *Tungsten nitride films grown via pulsed laser deposition studied in situ by electron spectroscopies*, Applied Surface Science 214 (2003) 58-67.

[180] S. Veprek et al., *Superhard nanocrystalline W2N/amorphous Si3N4 composite materials*, Journal of Vacuum Science & Technology A 14, 46 (1996).

[181] A. Lahav et al., *Measurement of thermal expansion coefficients of W, WSi, WN, and WSiN thin film metallizations*, Journal of Applied Physics 67, 734 (1990).

[182] V.V. Aleksandrov et al., *Experimental evidence of the transformation of the Rayleigh surface phonon in CaF2/GaAs(1-11) heterostructures of the accelerating type*, J. Phys.: Condens. Matter 6 (1994) 1947-1954.

[183] O. Lefeuvre et al., *Surface wave dispersion beyond cutoff for a fast layer on a slow substrate*, Appl. Phys. Lett. 72 (7) (1998) 856-857.

[184] C. C. Klepper et al., *Amorphous boron coatings produced with vacuum arc deposition technology*, J Vac. Sci. Technol. A 20 (2002) 725. doi:10.1116/1.1464844.

[185] AR Oganov et al., *Ionic high-pressure form of elemental boron*, Nature. 457 (7231) (2009) 863-7.

[186] D. Music et al., *Elastic modulus of amorphous boron suboxide thin films studied by theoretical and experimental methods*, J. Appl. Phys. 93 (2) (2003) 940-944.

[187] G. Kumar et al., *Embrittlement of Zr-based bulk metallic glasses*, Acta Mater. 57, (2009) 3572 - 3583.

[188] Hong Jong-Sung et al., *Rapid thermal annealing effects on the properties of plasma-enhanced chemical vapor deposited tungsten films*, J. Appl. Phys. 70, (1991) 2366.

[189] Wu Chia-Ching et al., *Effects of tungsten thickness and annealing temperature on the electrical properties of W-TiO2 thin films*, Ceram. Inter. 38, (2012) 223 - 227.

[190] Ling Zhang et al., *Effects of annealing temperature on the crystal structure and properties of electroless deposited NiWCrP alloy coatings*, Appl. Surf. Sci. 255, (2008) 1686 - 1691.

[191] G. Ouyang, X. L. Li, X. Tan and G. W. Yang, *Size-induced strain and stiffness of nanocrystals*, Appl. Phys. Lett. 89, 031904 (2006).

[192] L. Liang, M. Li, F. Qin and Y. Wei, *Temperature effect on elastic modulus of thin films and nanocrystals*, Philosophical Magazine Vol. 9 , No. 8, (2013) 574 - 583.

[193] Li L. and Aubertin M., *A general relationship between porosity and uniaxial strength of engineering materials*, Can. J. Civ. Eng. 30 (2003) 644-658.

[194] H. Demiryont and Kenneth E. Nietering, *Tungsten oxide films by reactive and conventional evaporation techniques*, Appl. Optics 28, 1989.

[195] J. Gabrusenoks et al., *Infrared and Raman spectroscopy of WO3 and CdWO4* Electrochimica Acta 46 (2001) 2229-2231.

[196] S. Hayashi et al., *Phase Transitions in Gas-Evaporated WO 3 Microcrystals: A Raman Study*, J. Phys. Soc. Jpn. 61, 916 (1992).

[197] T. Polcar et al., *Tungsten oxide with different oxygen contents: sliding properties*, Vacuum 81 (2007) 1426-1429.

[198] Lian Y. et al., *Thermal shock performance of CVD tungsten coating at elevated temperatures*, J. Nucl. Mater. 455 (2014) 374-375.

[199] Lian Y. et al, *Influence of surface morphology and microstructure on performance of CVD tungsten coating under fusion transient thermal loads*, Appl. Surf. Sci. 390 (2016) 167-174.

[200] E. Salje and G. Hoppmann, High Temp.-High Press. 12, 213 (1980).

[201] A. G. Souza Filho et al., *Pressure effects in the Raman spectrum of WO_3 microcrystals*, Phys. Rev. B, 62 (2000) pp. 3699.

[202] S. Boire-Lavigne et al., *The relationship between the microstructure and thermal diffusivity of plasma-sprayed tungsten coatings*, J. Thermal Spray Tech. 4(3) (1995) 261.

[203] Niu Y. et al., *Microstructure and thermal property of tungsten coatings prepared by vacuum plasma spraying technology*, Fusion Eng. Des. 85 (2010) 1521-1526.

[204] J.M Vaughan, *The Fabry Perot Interferometer*.

[205] J.R.Sandercock, in Proc. 7th Int. Conf. on Raman Spectroscopy, Ottawa 1980.

[206] A. Pazzaglia, *Innovative targets for enhanced laser-plasma ions acceleration*, Politecnico di Milano, currently at 2^{nd} year of PhD.